

# Lightweight Materials R&D Program

2013

VEHICLE TECHNOLOGIES OFFICE

This document highlights work sponsored by agencies of the U.S. Government. Neither the U.S. Government nor any agency thereof, nor any of their employees, makes any warranty, express or implied, or assumes any legal liability or responsibility for the accuracy, completeness, or usefulness of any information, apparatus, product, or process disclosed, or represents that its use would not infringe privately owned rights. Reference herein to any specific commercial product, process, or service by trade name, trademark, manufacturer, or otherwise does not necessarily constitute or imply its endorsement, recommendation, or favoring by the U.S. Government or any agency thereof. The views and opinions of authors expressed herein do not necessarily state or reflect those of the U.S. Government or any agency thereof.

---

# CONTENTS

|  |            |
|--|------------|
| <b>ACRONYMS AND ABBREVIATIONS</b> .....  | <b>xi</b>  |
| <b>I.0 INTRODUCTION</b> .....  | <b>1</b>   |
| <b>II.0 THE EV EVERYWHERE GRAND CHALLENGE</b> .....  | <b>5</b>   |
| II.1. Background.....  | 5          |
| II.2. 2013 Highlights .....  | 6          |
| II.3. Planned Activities.....  | 11         |
| <b>III.0 AUTOMOTIVE METALS</b> .....   | <b>12</b>  |
| III.1. R&D Fundamental Study of the Relationship of Austenite-Ferrite Transformation Details to Austenite Retention in Carbon Steels—Oak Ridge National Laboratory (ORNL) .....                | 12         |
| III.2. Properties and Manufacturability—Pacific Northwest National Laboratory (PNNL) .....   | 19         |
| III.3. Modeling and Computational Materials Science (PNNL) Mechanistic–Based Ductility Prediction for Complex Magnesium (Mg) Castings .....  | 51         |
| III.4. Multi-Material Enabling—Oak Ridge National Laboratory (ORNL) .....  | 58         |
| III.5. Multi-Material Enabling—Pacific Northwest National Laboratory .....   | 80         |
| III.6. Industrial Scale-Up of Low-Cost Zero-Emissions Magnesium by Electrolysis—INFINIUM, Inc. ....  | 90         |
| III.7. Development and Demonstration of a Magnesium-Intensive Vehicle Front-End Substructure—United States Automotive Materials Partnership (USAMP) LLC .....                                  | 93         |
| III.8. Integrated Computational Materials Engineering Approach to Development of Lightweight 3GAHSS Vehicle Assembly (ICME 3GAHSS) .....   | 103        |
| <b>IV.0 CARBON FIBER AND POLYMER COMPOSITES</b> .....  | <b>112</b> |
| IV.1. Low-Cost Carbon Fiber Development—Oak Ridge National Laboratory .....  | 112        |
| IV.2. Carbon Fiber Technology Facility—Oak Ridge National Laboratory.....  | 123        |
| IV.3. Development and Commercialization of a Novel Low-Cost Carbon Fiber—Zoltek Companies, Inc. ....   | 127        |
| IV.4. Predictive Engineering Tools for Injection-Molded Long-Carbon-Fiber Thermoplastic Composites—Pacific Northwest National Laboratory .....   | 135        |
| IV.5. Low Cost Carbon Fiber Composites for Lightweight Vehicle Parts—Materials Innovation Technologies LLC .....   | 139        |
| IV.6. Validation of Carbon Fiber Composite Crash Models Via Automotive Crash Testing—USAMP, LLC .....  | 148        |
| <b>V.0 CROSSCUTTING</b> .....  | <b>161</b> |
| V.1. Demonstration Project for Multi-Material Lightweight Prototype Vehicle as Part of the Clean Energy Dialogue with Canada—Vehma International of America, Inc. and Ford Motor Company ..... | 161        |
| V.2. Safety Data and Analysis—Lawrence Berkeley National Laboratory.....   | 173        |

## List of Figures

|  |    |
|--|----|
| Figure I-1: 35% lignin/PAN precursor fiber Scanning Electron Microscope image showing uniform micro-porosity and 1500 meter spools of lignin/PAN carbon fiber ready for shipment. ....   | 2  |
| Figure I-2: Potential applications of components with features represented by the complex 3-D part in an automotive body structure. ....   | 2  |
| Figure I-3: High Angle Annular Dark Field Scanning Transmission Electron Microscope cross-section image of film formed on AZ31B magnesium alloy after exposure to water with elemental maps of Al, O, Mg, and Zn. Note the apparent segregation of the Zn to the metal-oxide interface. ....   | 3  |
| Figure I-4: Successful stamped aluminum tailor welded blank using 2.0 mm and 1.2 mm 5182 aluminum alloy sheets. ....   | 3  |
| Figure I-5: Yield Strength versus Uniform Elongation for a variety of steel types. ....  | 4  |
| Figure II-1: Demonstration “front-end” structure employing dissimilar metals as indicated. ....  | 6  |
| Figure II-2: Three Dimensional Representative Volume Element of BAO QP980 Steel—(Green = Martensite, Blue = Austenite and Red + Yellow = Ferrite). ....  | 7  |
| Figure II-3: Inside the Carbon Fiber Technology Facility. ....   | 8  |
| Figure II-4: The materials, part fabrication, modeling and assembly methodologies used in the Structural Composite Underbody were refined and utilized in the Chevrolet Spark EV battery enclosure. ....   | 9  |
| Figure II-5: Photo of the three vehicles tested (BEV, HEV, and ICE). ....  | 10 |
| Figure II-6: Vehicle Road Load vs. Vehicle Weight with respect to base vehicle. ....   | 10 |
| Figure III-1: Schematic diagram of the three-dimensional (3D) micro-diffraction. The beam is incident at 45° to the sample surface. Diffracted beams are collected at the detector. ....   | 14 |
| Figure III-2: The effect of initial microstructure and heating rate on the non-equilibrium ferrite/martensite ( $\alpha+\alpha_M$ ) to austenite ( $\gamma$ ) transformation in a DP980 steel observed by in situ neutron diffraction measurement. (a) 3°C/s heating rate, (b) 30°C/s heating rate. ....   | 14 |
| Figure III-3: The effect of heating rate on the non-equilibrium phase transformation in tempered martensite predicted by the phase transformation model developed in this project. ....  | 15 |
| Figure III-4: The relationship between fracture elongation and yield strength in steels and fabricated multilayered steels. ....   | 15 |
| Figure III-5: Depth-dependent inverse lattice parameter $Q_{317}$ for austenite layer at load 0 (a) and under load 2 (b) and intensity profiles at three different depths at load 0 (c) and at load 2 (d). The depths are shown by arrows in the (a) and (b) frames. Depth along the beam for the austenite layer is from the martensite/austenite interface. Vertical dashed lines in (c) and (d) and horizontal dashed lines in (a) and (b) mark the reference Q value for the austenite. ....   | 16 |
| Figure III-6: Depth-dependent inverse lattice parameter $Q_{345}$ for martensite top layer at load 0 (a) and under load 2 (b) and intensity profiles at three different depths at load 0 (c) and at load 2 (d). The depths are shown by arrows in the (a) and (b) frames. Depth along the beam for the top martensite layer is from the sample surface. Vertical dashed lines in (c) and (d) and horizontal dashed lines in (a) and (b) mark the reference Q value for the martensite sample. .... | 17 |
| Figure III-7: Stress-strain curves for the first heat Q&P steels. ....   | 21 |
| Figure III-8: (a) Histogram of 400 hardness data obtained from nano-indentation tests of MAT1–3, (b) different features observed from the microstructures of Q&P steels, and (c) average hardness values for the different features of MAT1–3. ....  | 22 |
| Figure III-9: (a) Schematic of experimental setup for in-situ HEXRD tests under uniaxial tension. Phase stresses and austenite transformation kinetics as function of macro strain for (b) MAT1 and (c) MAT2. ....   | 22 |
| Figure III-10: Microstructures of MAT1. (a) SEM, (b) grain orientation map, (c) phase map and (d) finite element (FE) model (green: austenite(19%); red: untempered martensite(20%); grey: tempered martensite(44%); blue: bainite(18%)). ....   | 22 |
| Figure III-11: (a) Original and (b) modified input stress-strain curves for the constituent phases and austenite stability ( $\Gamma_c$ ) for MAT1 model and (c) comparison of macroscopic responses of MAT1 model based original and modified material parameters. ....   | 23 |

|  |    |
|--|----|
| Figure III-12: (a) Tensile test setup for second heat Q&P steel samples and (b) comparison of stress-strain curves between MAT1, MAT5, and MAT8. ....  | 23 |
| Figure III-13: (a) PNNL's room-temperature FLD for AA7075-T6 at different strain-rate using plane-strain specimen geometry; (b) Thyssenkrupp data on predicted strains in a cold-stamped steel B-pillar. ....  | 26 |
| Figure III-14: Theoretical FLD (preliminary estimates) for AA7075-T6 as a function of strain-rate. ....  | 27 |
| Figure III-15: Strain-rate vs. strain in plane-strain specimens of W-temper AA7075 (RD = rolling direction). ....  | 27 |
| Figure III-16: (a) Influence of material pre-strain on safe and fracture strains for half dog-bone samples trimmed with 10 percent clearance in the Longitudinal Direction (LD); (b) tensile elongation results for samples subjected to 5% x 0% pre-strain in LD and trimmed with 0 to 20° cutting angles at 5 to 40 percent clearances. .... | 30 |
| Figure III-17: The procedure to integrate the 2D edge geometry of the trimming model into a 3D half dog-bone tensile sample. ....  | 30 |
| Figure III-18: The initial plastic strain mapped onto the half dog-bone tensile sample for different cutting clearances: (a) 10 percent, (b) 32 percent, (c) 43 percent, and (d) 60 percent. ....  | 31 |
| Figure III-19: (a) The predicted equivalent plastic strain contours for fractured samples of different clearances (2–60 percent); (b) images of samples taken before final fracture of the half dog-bone samples tensile stretched after being trimmed with different clearances. ....   | 31 |
| Figure III-20: Multiple edge cracking: (a) observed by SEM, (b) predicted for different clearances. ....   | 32 |
| Figure III-21: (a) The calculated tensile true stress-true strain curves for samples with different shearing clearances from 2 to 60 percent; (b) the calculated elongations for samples of different models in comparison with experimental observations featuring nominal (Nom) or calibrated (Cal) clearances. ....                         | 32 |
| Figure III-22: An example of models for 43 percent trimming clearance (a) before and (b) after the burr is removed. Simulation results of models after burr removed (c) stress-strain curves and (d) elongations. ....   | 33 |
| Figure III-23: Fine 15 nm Zr-rich dispersions (black particles) formed in the commercial ZK60A alloy interacting with dislocations. ....   | 36 |
| Figure III-24: Script and blocky eutectic constituent particles found in the Mg <sub>2</sub> Si alloy book mold casting. ....  | 36 |
| Figure III-25: Schematic of the novel high-shear extrusion system used for the production of tubular products. ....  | 37 |
| Figure III-26: Examples of 7 mm OD by 0.5 mm wall tubular extrusions made by high-shear extrusion. ....  | 37 |
| Figure III-27: Energy absorption curves for 6061 Al, rapidly solidified ZK60A (processed during FY2012) and high-shear Mg <sub>2</sub> Si extrusion showing that the energy absorption was similar, which indicates the potential for a mass improvement of at least 20 percent with rapid solidification or high-shear extrusion. ....        | 38 |
| Figure III-28: Backscattered scanning electron micrographs of the grain sizes in (a) Mg <sub>2</sub> Si and (b) ZK60A after high-shear extrusion. ....   | 38 |
| Figure III-29: Contributions of several deformation mechanisms to the strengthening of AZ31 magnesium during compression. ....   | 38 |
| Figure III-30: Predicted and experimentally determined stress-strain curve for AZ31 tested in compression. The inflection in hardening near 0.04 strain is attributed to the change in the relative contributions of twinning and prismatic slip due to evolving texture. ....   | 38 |
| Figure III-31: Schematics of two fracture modes of particles when subject to an applied stress when under hydrostatic stress. Mode 1 develops porosity, while Mode 2 porosity is healed by shear in the matrix. ....   | 39 |
| Figure III-32: Stresses and orientations required to model particle fracture using the traction tensor theory and Paris' Law. ....   | 40 |
| Figure III-33: Failure modes of particles under hydrostatic stress using the traction tensor theory. Under ideal processing, principal stresses should be kept within Mode II to develop fine particle sizes with minimum porosity. ....   | 40 |
| Figure III-34: Optical (a) and backscattered scanning electron (b) micrographs of the microstructure of the as-extruded Mg <sub>2</sub> Si alloy. Note the presence of coarse intermetallics in (a) of similar size to the as-cast structure and the very fine particles less than 1 μm and the lack of script structure in (b). ....          | 41 |
| Figure III-35: Solid model of A-pillar component (~650 mm overall component length). ....  | 47 |
| Figure III-36: Forming model simulation of preforming of the A-pillar component showing areas of high strain (up to 36 percent). ....  | 48 |

|   |    |
|---|----|
| Figure III-37: Forming model showing final A-pillar component shape with flanging outlined in purple. The white outlined area is material that will be formed into a second attachment flange. ....   | 48 |
| Figure III-38: Views of forming tools during fabrication at Magna SCFI. ....  | 49 |
| Figure III-39: Secondary electron images of 5-mm-thick (a) AM40 and (b) AM70. Light gray portions are $\beta$ phase, gray are $\alpha$ Mg, dark gray are Al-rich Mg solid solution, black are pores. ....   | 53 |
| Figure III-40: Representative tensile curves from each condition. ....  | 53 |
| Figure III-41: The influence of aluminum content and plate thickness on (a) yield strength, (b) strain at fracture (ductility), (c) Young's modulus, and (d) fracture strength. ....  | 54 |
| Figure III-42: (a) Different-sized models with different-sized large pores in the center and different ductility governing factors depending on the large pore size and model size; (b) different-sized models with a large pore at different locations from the edge. (L = model size; D = large pore size; d = distance from edge) ....                       | 54 |
| Figure III-43: Comparisons of the computational results for large-sized pore effects (a) with those of the models without the surrounding small pores and (b) with experimental results and (c) comparison of the the computational results for the location effects of large-sized pore with experimental results and possible threshold for edge effect. .... | 55 |
| Figure III-44: Microstructure models of (a) AM40 and (b) AM70 validated with experimental measurements. ....  | 55 |
| Figure III-45: Comparison of AM40 sample with 8 percent connected $\beta$ and AM70 sample with 21 percent clumped $\beta$ . ....  | 55 |
| Figure III-46: (a) Comparison of the test and predicted mean elongation (b) box plot of elongation variation. ....  | 56 |
| Figure III-47: Phase-field-predicted dendritic microstructure and its interaction with gas pores during solidification of high-pressure die-casting process. ....   | 56 |
| Figure III-48: Potentiodynamic curves generated in RT DI water saturated $Mg(OH)_2$ [Unocic 2013]. ....   | 61 |
| Figure III-49: Specific mass change data after immersion in RT DI water [Unocic 2013]. ....   | 61 |
| Figure III-50: Preliminary SIMS sputtering rate through films formed by 4 h immersion in RT $^1H_2^{18}O$ water followed by 20 h immersion in $^2H_2^{16}O$ water ( $D_2O$ ). ....  | 61 |
| Figure III-51: (a) HAADF-STEM image of the film cross section formed on AZ31B after immersion in RT DI water for 24 h. (b) EDS x-ray maps of Al, Mg, oxygen, and Zn [Unocic 2013]. ....   | 62 |
| Figure III-52: HAADF-STEM image of the cross-section of the film formed on E717 after exposure for 48 h in RT DI water. Higher magnification images of the precipitates present in the MgO film in conjunction with associated EDS Zn and Zr elemental maps [Unocic 2013]. ....   | 62 |
| Figure III-53: Schematic of the IR thermography-based RSW quality inspection system. ....   | 64 |
| Figure III-54: Correlation of weld nugget size vs. real-time IR thermal signatures for 3T boron steel welds. The "IR Signatures" are separate conditions calculated using ORNL proprietary software. They indicated portions of the data used for image analysis. ....  | 65 |
| Figure III-55: Real-time IR-predicted weld size vs. destructive measurement for (a) the same types of 3T boron steel welds used in Figure III-55 and (b) all different types of welds. ....   | 65 |
| Figure III-56: Correlation of weld nugget size and thickness vs. post-weld IR thermal signatures for 3T boron steel welds. ....   | 66 |
| Figure III-57: Post-weld IR-predicted weld size and thickness vs. destructive measurement for the same types of 3T boron steel welds used in Figure III-56. ....  | 66 |
| Figure III-58: Post-weld IR-predicted weld size and thickness vs. destructive measurement for all of the different types of welds collected so far in the project. ....   | 66 |
| Figure III-59: Post-weld IR-measured weld shape vs. cross section of destructive measurement (on the faying surface): (a) good weld and (b) weld with irregular shape. ....   | 67 |
| Figure III-60. (a) Representative welding pattern in auto body structures, (b) special weld fatigue specimen configuration, and (c) appearance of actual weld fatigue testing specimen adopted in this project. ....  | 69 |
| Figure III-61: Comparison of weld fatigue lives of a baseline ER70 weld versus the new filler wire developed in FY 2013. ....   | 70 |
| Figure III-62: Improvement of weld fatigue lives through an innovative mechanical stress management technique developed in FY 2013. ....  | 70 |

|  |     |
|--|-----|
| Figure III-63: ORNL prototype IR furnace with lamps above and below for heat treating flat castings (a and b) and bimetallic joints (c and d). (d) The bimetallic joint showing the steel tube (left) with an end cap buried in an Al casting (right).                             | 73  |
| Figure III-64: The measured temperature in a flat plate during an IR heating with the prototype furnace.   | 74  |
| Figure III-65: Cross-section of an as-cast joint. Note the gaps above the weld bead of the end cap to the steel tube (see green arrow at F) and cast Al, as well as below the deformed end cap.  | 74  |
| Figure III-66: The residual stresses as a function of distance from the interface for the as-cast and conventional T5 (182°C/4 h) samples.   | 75  |
| Figure III-67: Drawing of the bimetallic part showing heated surfaces and shielded portions of the component.  | 75  |
| Figure III-68: Temperature (°C) distribution for the (a) Al and (b) steel portions of the joint. In (a), the surface shown in the front is the symmetry plane, and the top surface is shown facing toward the IR heat source.  | 76  |
| Figure III-69: Temperature evolution at points B, E, and F (see Figure III-65) as a function of time. (A) and (B) are experimental data. (C) is the model prediction.  | 76  |
| Figure III-70: Boundary conditions for the thermomechanical model for the steel. (a) Pressure and temperature evolution within the Al during the die-casting process and (b) contact between Al and steel cap used to assess the capabilities of the thermomechanical steel model. | 77  |
| Figure III-71: (a) Temperature profile right before air-gap formation and (b) displacement in the direction along the tube axis, near room temperature (magnified 3×).   | 77  |
| Figure III-72: Deformation and displacement in the radial direction through a vertical cross-section of the steel near the edge (deformation magnified 3×).  | 77  |
| Figure III-73: Stress distribution through a vertical cross section of the steel near the edge for the (a) axial component and (b) hoop component (deformation magnified 3×).  | 78  |
| Figure III-74: (a) Temperature distribution and variation as a function of time at two locations and (b) joint temperature contours where location A represents the near contact area with the die and location B is near the rivet tip.   | 82  |
| Figure III-75: A comparison between the (a) model prediction and the (b) actual experimental joint of a 2 mm to 2 mm AZ31 SPR joint made at 300°C.   | 83  |
| Figure III-76: A representative image of an AZ31 SPR joint with no tail side cracking observed. This particular joint was prepared at ~200°C.  | 83  |
| Figure III-77: Representative images of the (a) tail pull-out and (b) rivet shear out failure modes observed of the AZ31 SPR joints under lap shear loading.   | 84  |
| Figure III-78: Four tool designs used for the design of experiment testing representing the types of changes made to pin and shoulder geometries.  | 87  |
| Figure III-79: 3D surface profiles for weld #1 (left) and weld #2 (right) obtained from high magnification optical measurement.  | 88  |
| Figure III-80: An as-stamped AA5182 welded blank with 2.0- to 1.2-mm dissimilar thickness sheets.  | 88  |
| Figure III-81: Bottom (left) and top (right) view of the MFERD Phase III shock tower of AM60B SVDC showing changes from Phase II casting.  | 96  |
| Figure III-82: Phase III demonstration structure.  | 96  |
| Figure III-83: Design of shear deformation-inducing tensile coupons for acquisition of AM60B magnesium yield-surface information for the condition of zero triaxiality.  | 97  |
| Figure III-84: Loading configuration of AM60B shock tower for finite element modeling and crashworthiness testing.   | 97  |
| Figure III-85: Geometry of partial “coach peel (CP)” sample and its fatigue life plot. A data point from fatigue studies of a Phase II demonstration structure (designated “ST”) is plotted for comparison with the prediction.  | 98  |
| Figure III-86: Nomenclature for friction-stir linear (lap) weldments and corresponding lap-shear strengths for joints in AZ31 sheet material.  | 98  |
| Figure III-87: ZE20 novel Mg alloy lower rails produced by Mag Specialties.  | 99  |
| Figure III-88: Adaptable insert concept.   | 100 |

|  |     |
|--|-----|
| Figure III-89: Electron micrograph of developing $\beta$ -phase precipitates in AZ91D magnesium and 3D platelet growth characteristics deduced from such observations as a function of ageing time. The results are compared with predictions from phase field simulations and show good correlation. ....   | 101 |
| Figure III-90: Target 3GAHSS Properties. ....  | 106 |
| Figure III-91: Three Dimensional Representative Volume Element of BAO QP980 Steel—(Green = Martensite, Blue = Austenite and Red + Yellow = Ferrite). ....  | 109 |
| Figure III-92: Baseline Assembly: Side Structure Part Details. ....  | 109 |
| Figure IV-1: Single filament cross section during conventional oxidative stabilization process. [3, 4]. ....   | 114 |
| Figure IV-2: Progress on the construction of the 1 ton/year plasma oxidation oven (large reactor). ....  | 115 |
| Figure IV-3: (a) The MAP line after rotating the applicator. Microwave coupling is now from below. (b) The MAP line exit feed-throughs shown fully strung with five tows in the horizontal configuration. ....   | 119 |
| Figure IV-4: Mechanical properties from selected MAP runs. The orange, red, and cyan points are from three 5-tow runs. Fiber properties in the shaded region meet or exceed programmatic targets. The large variance is the result of single-filament mechanical testing. ....   | 119 |
| Figure IV-5: Current density shown inside the plasma column for two different values of plasma conductivity. ....  | 120 |
| Figure IV-6: Tow orientations within MAP applicator. (a) Orientation in pre-2012 multi-tow experiments. Heating is very uneven. (b) Tow orientation after applicator rotation for five-tow experiment. Inner tows are processed less than the outer tows. (c) Current tow orientation. (d) Recent data at each position before reconfiguration. .... | 120 |
| Figure IV-7: Improved microwave energy and enhanced plasma hardware. This approach, here demonstrated with a single unit, should allow improved energy deposition control for industrial scale-up. ....  | 121 |
| Figure IV-8: Kaltex strand tensile strength. Each diamond symbol represents a set of test data for a sample set processed during different weeks. The photo is the Kaltex tow in the first oxidation oven. ....  | 125 |
| Figure IV-9: Lignin / PAN precursor fiber spools. ....   | 130 |
| Figure IV-10: Commercial Precursor Fiber Sample. ....  | 130 |
| Figure IV-11: Commercial Precursor Fiber Sample. ....  | 131 |
| Figure IV-12: Heater coil in pre-stretching bath saturated with non-soluble residue during commercial spinning trial. ....   | 131 |
| Figure IV-13: Lignin / PAN precursor color changes during oxidation. ....  | 131 |
| Figure IV-14: Spools of lignin / PAN carbon fiber. ....  | 131 |
| Figure IV-15: 1500 meter spools of lignin / PAN carbon fiber ready for shipment. ....  | 132 |
| Figure IV-16: SEM of 25% lignin / PAN carbon fiber. ....   | 132 |
| Figure IV-17: SEM of 25% lignin / PAN carbon fiber. ....   | 132 |
| Figure IV-18: Precursor Fiber Sample # 420. ....   | 133 |
| Figure IV-19: Toyota's complex 3D automotive structure that will be injection-molded from long-carbon-fiber/PP and long-carbon-fiber/PA6,6 compounds. ....   | 137 |
| Figure IV-20: Potential applications of components with features represented by the complex part (Figure IV-19) in an automotive body structure. ....  | 137 |
| Figure IV-21: The body-in-white (BIW) unit cost of an automobile body is dependent on the materials of construction (steel vs. carbon fiber composite), the cost of carbon fiber, and the production volume. ....  | 142 |
| Figure IV-22: Fifty-inch wide production roll goods line. ....   | 143 |
| Figure IV-23: Typical roll of nonwoven roll goods material made from reclaimed CF. ....  | 143 |
| Figure IV-24: Proterra electric bus for urban transit market. ....   | 144 |
| Figure IV-25: Molded rocker panel made from reclaimed CF and PET fiber roll goods. ....  | 144 |
| Figure IV-26: Molded upper door trim for Ford Escape front door made from reclaimed CF/natural fiber/polypropylene roll goods. ....  | 145 |
| Figure IV-27: Molded upper door trim with cover stock. ....  | 145 |
| Figure IV-28: Large 3-DEP <sup>®</sup> machine. ....   | 146 |
| Figure IV-29: CFD model showing fluid flow fields in large 3-DEP <sup>®</sup> forming tank. ....   | 146 |
| Figure IV-30: Upper and lower plenum preforms made of reclaimed CF after 40-second forming cycle. ....   | 146 |

|   |     |
|---|-----|
| Figure IV-31: Set-up of sled-on-sled system used for all high-speed test modes.....   | 150 |
| Figure IV-32: Schematic of top-view of four completed high-speed tests.....   | 151 |
| Figure IV-33: Schematic of side view of four completed high-speed tests.....  | 151 |
| Figure IV-34: Impact force vs. time comparing discrete measurements from load cells with calculated force using Newton's Second Law from mass and acceleration.....   | 151 |
| Figure IV-35: Graph of sled system displacement vs. time, comparing film analysis with double integrated acceleration from accelerometers for a full-frontal impact test.....                               | 151 |
| Figure IV-36: Tensile strength and modulus for 2x2 twill fabric at 0/90 orientation and quasi-isotropic orientation, and for carbon fiber SMC with all plies at 0° and with plies crossed at 0 and 90°..... | 152 |
| Figure IV-37: Crush Can Shape Concepts.....   | 155 |
| Figure IV-38: Force-Displacement Curves for the 12 Composite Concepts.....  | 155 |
| Figure IV-39: P7 Unstable Crush Mode a) Initial Crush b) Unstable Crush.....  | 156 |
| Figure IV-40: P12 Crush Mode.....   | 156 |
| Figure IV-41: Force-Displacement Curves for 30 mph Angular Impact.....  | 157 |
| Figure IV-42: "Peel" Crush Can Failure Mode (Adapted from Mamalis et al., 1997).....  | 158 |
| Figure V-1: MMLV BIW cast node architecture, common to both Mach-I and Mach-II vehicle designs.....   | 162 |
| Figure V-2: Mach-I Prototype Vehicle Build Status.....  | 163 |
| Figure V-3: Vehicle Assembly enables utilization of an existing body shop that integrates pre-coated subassemblies processed independent of the Class A components.....                                     | 165 |
| Figure V-4: Mach-I BIW.....   | 166 |
| Figure V-5: Mach-I Body Panels.....   | 166 |
| Figure V-6: Mach-I Chassis and Bumper Components.....   | 167 |
| Figure V-7: Engine weight savings investigations.....   | 167 |
| Figure V-8: Transmission weight savings investigations.....   | 168 |
| Figure V-9: Carbon Fiber seat back and cushion structures.....  | 168 |
| Figure V-10: Carbon fiber instrument panel cross-car beam.....  | 168 |
| Figure V-11: Aluminum brake under test.....   | 169 |
| Figure V-12: Photographs of tall/narrow prototype tire.....   | 169 |
| Figure V-13: Composite front spring at different loading conditions.....  | 170 |
| Figure V-14: Mach-II BIW "Concept Release.".....  | 171 |
| Figure V-15: 1994 and 2011 fatality risk per 10 billion miles traveled, by state.....   | 180 |
| Figure V-16: Estimated effect of control variables on societal fatality risk per mile traveled.....   | 182 |

## List of Tables

|   |    |
|---|----|
| Table II-1: For a 10% Reduction in Vehicle Mass.....  | 10 |
| Table III-1: Heat-treating parameters for four different first heat Q&P steels (MAT1–4).....  | 21 |
| Table III-2: Heat-treating parameters for second heat Q&P steel samples (MAT5–8).....   | 23 |
| Table III-3: X608 Aluminum Tensile Test Results for Warm Forming Temperatures.....  | 48 |
| Table III-4: A listing of heat treatment trials and corresponding YS, UTSs and elongations.....   | 74 |
| Table III-5: Preliminary joint strength results of AZ31 SPR joints under lap shear loading.....   | 83 |
| Table III-6: Process parameter details and properties from several welds in the study.....  | 87 |
| Table III-7: Project subject matter and team organization.....  | 95 |
| Table III-8: Comparison of maximum sustainable deformation loads for the shock tower component from experimental testing and modeling in LS-DYNA® using existing and newly devised material cards for AM60B die-cast magnesium..... | 97 |

---

|  |     |
|--|-----|
| Table III-9: Composition of ZE20 novel Mg alloy billet stock produced by Mag Specialties Inc. ....   | 99  |
| Table III-10: 3GAHSS Types .....   | 106 |
| Table III-11: DOE FOA Weight and Cost Targets.....   | 106 |
| Table III-12: Project Participants.....  | 107 |
| Table IV-1: 24k Textile PAN Results. Plasma oxidized (33 min), conventionally carbonized.....  | 115 |
| Table IV-2: Properties of 25% lignin / PAN carbon fiber.....   | 132 |
| Table IV-3: Mechanical Property Data from Prepreg Composite Panels.....  | 133 |
| Table IV-4. Comparison of Cured Composite Properties with those of Metals.....   | 141 |
| Table IV-5: Impact velocities for the 40% frontal offset test mode.....  | 150 |
| Table IV-6: Energy Absorption Comparison (35 mph Flat Frontal).....  | 156 |
| Table IV-7: Energy Absorption Comparison (30 mph Angular Impact).....  | 157 |
| Table IV-8: Energy Absorption Summary.....   | 158 |
| Table V-1: MMLV Mach-I Weight Comparison by System Against the DOE 2002 Baseline Average Sedan.....  | 171 |
| Table V-2: DRI 2-stage and alternate LBNL 2-stage estimates of the effect of mass or footprint reduction on U.S. societal fatality risk per crash (crashworthiness/compatibility), crashes per VMT (crash frequency), and fatality risk per VMT..... | 175 |
| Table V-3: Comparison of DRI and LBNL estimated effect of mass, track width, or wheelbase reduction on U.S. societal fatality risk per crash, crash frequency per VMT, and fatality risk per VMT.....  | 177 |
| Table V-4: Estimated effect of mass or footprint reduction on 13-state crash frequency (crashes per VMT), under alternative regression model specifications.....   | 178 |
| Table V-5: Estimates for selected control variables from two linear regression models of societal fatality risk, using different dependent variables.....  | 180 |
| Table V-6: Control variables considered in the linear regression model.....  | 181 |
| Table V-7: Estimated effect of including two additional variables on the NHTSA baseline model of societal fatality risk per VMT, by vehicle type.....  | 183 |

## ACRONYMS AND ABBREVIATIONS

|         |   |
|---------|---|
| °C      | degrees Celsius   |
| °C/s    | degrees Celsius per second  |
| Ω       | symbol for ohms, a unit of electrical resistance  |
| μm      | micrometers (microns)   |
| 1000/s  | strain rate: the rate of two lengths, a dimensionless quantity. The strain rate is dimensionally the reciprocal of time measured in reciprocal of seconds (s <sup>-1</sup> ).               |
| 2D      | two dimensional   |
| 3D      | three dimensional   |
| 3-DEP™  | Three Dimensional Engineered Preform–Materials Innovation Technologies LLC proprietary net-shape, wet-laid nonwoven forming process   |
| 3GAHSS  | third generation advanced high strength steel   |
| 2T      | two layer   |
| 3T      | three layer   |
| 34-ID-E | An undulator beamline dedicated for X-ray micro/nano-diffraction activities at the Advanced Photon Source of the Argonne National Laboratory.   |
| 5xxx    | Series designation of aluminum alloyed with magnesium   |
| 6xxx    | Series designation for aluminum alloyed with <i>magnesium</i> and <i>silicon</i> , are easy to machine, and can be precipitation hardened, but not to the high strengths that 2000 and 7000 |
| 7xxx    | Series designation for aluminum alloyed with <i>zinc</i> , and can be precipitation hardened to the highest strengths of any aluminum alloy   |

### A

|                                |  |
|--------------------------------|--|
| ABAQUS                         | A software suite for finite element analysis and computer-aided engineering                |
| ABS                            | acrylonitrile butadiene styrene  |
| ACC                            | Automotive Composites Consortium   |
| ACC45TO60                      | Value for the time (in seconds) for the vehicle to accelerate from 45 to 60 miles per hour |
| AHSS                           | advanced high-strength steel   |
| AISI                           | American Iron and Steel Institute  |
| AIST                           | Association for the American Iron and Steel Technology                                     |
| Al                             | aluminum   |
| Al <sub>2</sub> O <sub>3</sub> | aluminum oxide   |
| ALC_DRUG                       | Term used for alcohol and drug use in crash models   |

|           |  |
|-----------|--|
| AM        | aluminum-magnesium*  |
| AMO       | Advanced Manufacturing Office  |
| APS       | Advanced Photon Source   |
| APT       | atom probe tomography  |
| ARPA-E    | Advanced Research Projects Agency–Energy   |
| ARRA      | American Recovery and Reinvestment Act of 2009AS   |
| ASM       | American Society for Metals  |
| ASME-MSEC | <i>American Society of Mechanical Engineers–Manufacturing Science and Engineering Conference</i> |
| ASMI      | Autodesk Simulation Moldflow Insight   |
| A/SP      | Auto/Steel Partnership   |
| ASPPRC    | Advanced Steel Processing and Products Research Center   |
| ASTM      | American Society for Testing and Materials   |
| AVTA      | Advanced Vehicle Testing Activity  |
| AWD       | all-wheel drive  |

### B

|           |   |
|-----------|---|
| BAO       | Baosteel Group Corporation  |
| BAO QP980 | Baosteel Europe quenching and partitioning advanced high strength steel       |
| bcc       | body centered cubic   |
| bct       | body centered tetragonal  |
| BEV       | battery electric vehicle  |
| BF-STEM   | bright field–scanning transmission electron microscopy                        |
| BIW       | body-in-white (a car body's sheet metal components have been welded together) |
| BU        | Brown University  |

### C

|                  |   |
|------------------|---|
| CAD              | computer aided design   |
| CAE              | computer aided engineering  |
| CAFE             | Corporate Average Fuel Economy  |
| Cal              | calibrated  |
| CANMET           | CANMET Materials Technology Laboratory  |
| Canmet-MATERIALS | A Canadian federal laboratory in the energy sector with a focus on research in metals and materials in automotive, energy distribution, and power generation. |
| CCCP             | Combined Constraint Crystal Plasticity  |
| CCD              | charged-coupled device  |

## Acronyms and Abbreviations

|                   |  |
|-------------------|--|
| C/D segment       | Euro Market Segment Classification   |
| CD-4              | Critical Decision 4  |
| CDM               | Continuum Damage Mechanics (model)   |
| Ce                | cerium   |
| CF                | carbon fiber   |
| CFD               | computational fluid dynamics   |
| CFE               | coefficient of thermal expansion   |
| CFRP              | carbon fiber reinforced polymer  |
| CFTF              | Carbon Fiber Technology Facility   |
| CGI               | compacted graphite iron  |
| Cl <sub>2</sub>   | chlorine   |
| cm <sup>3</sup>   | cubic centimeter   |
| CO <sub>2e</sub>  | carbon dioxide equivalent  |
| Co-DEP™           | Co-Deposited Engineered Preform- Materials Innovation Technologies LLC proprietary net-shape preform process of co-deposited structural and TP matrix fibers |
| COMSOL            | COMSOL Multiphysics is a finite element analysis, solver and simulation software / FEA software package for various physics and engineering applications,    |
| Conv.             | conventional   |
| CP                | coach peel   |
| CP <sup>2</sup> E | Close-Proximity Plasma Electromagnetic Heating   |
| CPFEM             | Crystal Plasticity Finite Element Model  |
| CPIE              | close proximity indirect exposure  |
| CRADA             | Cooperative Research and Development Agreement   |
| CRASURV           | Crash Survivability  |
| CSM               | Colorado School of Mines   |
| Cu                | copper   |
| CU                | Clemson University   |
| CUV               | crossover utility vehicle  |
| CV or CoV         | coefficient of variation   |
| CY                | calendar year  |

## D

|                  |                                     |
|------------------|-------------------------------------|
| D <sub>2</sub> O | deuterium oxide (heavy water)       |
| DAS              | data acquisition system             |
| DC               | direct current                      |
| DCS              | dendrite cell size                  |
| DFT              | Density functional Theory           |
| DI               | deionized (water)                   |
| DIC              | digital image correlation           |
| DICTRA           | diffusion controlled transformation |
| D-LFT            | direct long-fiber thermoplastic     |

|          |  |
|----------|--|
| DOE      | U.S. Department of Energy  |
| DMA      | dynamic mechanical analysis  |
| DP       | dual phase   |
| DRI      | Dynamics Research, Inc.  |
| DRIVE    | Driving Research and Innovation for Vehicle efficiency and Energy sustainability |
| DRYBRAKE | Value for the stopping distance (in feet) on a dry surface                       |
| DSC      | differential scanning calorimetry  |

## E

|         |  |
|---------|--|
| EBM     | Cosma's Eagle Bend Manufacturing, Inc. in Clinton, Tennessee |
| EBSD    | electron backscattered diffraction                           |
| EBTR    | Executive Board Technical Review                             |
| EDAG    | Engineering + Design AG (Corporation)                        |
| EDS     | energy dispersive spectrometry                               |
| EERE    | Office of Energy Efficiency and Renewable Energy             |
| e.g.    | exempli gratia (for example)                                 |
| EHF     | electro hydraulic forming                                    |
| EPA     | Environmental Protection Agency                              |
| ESC     | electronic stability control                                 |
| ESI     | Engineered Solutions, Inc.                                   |
| et. al. | abbreviation for "and others"                                |
| EV      | electric vehicle   |
| EVP     | Executive Vice President                                     |
| Expt.   | experimental   |

## F

|                 |  |
|-----------------|--|
| Ft <sup>2</sup> | square feet  |
| FARS            | Fatality Analysis Reporting System                               |
| FBCC            | front bumper and crash can                                       |
| fcc             | face centered cubic  |
| Fe              | iron   |
| Fe-C            | Iron-carbon (alloy)  |
| FEA             | finite element analysis  |
| FEAWD           | Finite Element All-Wheel Drive                                   |
| FEM             | finite element model, finite element method                      |
| FIB             | focused ion beam   |
| FLD             | forming limit diagram  |
| FMVSS           | Federal Motor Vehicle Safety Standards                           |
| FOA             | Funding Opportunity Announcement                                 |
| FOOTPRNT        | Value for the vehicle footprint (in square feet) in crash models |

## Acronyms and Abbreviations

|        |                                 |
|--------|---------------------------------|
| Fract. | Fracture                        |
| FSLW   | friction stir linear welding    |
| FSSW   | friction stir spot weld/welding |
| FSW    | friction stir welding           |
| FVF    | fiber volume fraction           |
| FWHM   | full width at half maximum      |
| FY     | fiscal year                     |

## G

|                           |   |
|---------------------------|---|
| G <sub>1c</sub>           | Double Cantilever Beam (test configuration) |
| G <sub>2c</sub>           | End Notch Flex (test configuration)         |
| g/cm <sup>2</sup>         | grams per centimeter squared                |
| g/cm <sup>3</sup> or g/cc | grams per centimeter cubed                  |
| GCIP                      | generic closure inner panel                 |
| Gen I                     | first generation                            |
| Gen II                    | second generation                           |
| Gen III                   | third generation                            |
| GHG                       | greenhouse gas                              |
| GM                        | General Motors Company                      |
| GMAW                      | gas metal arc welding                       |
| GPa                       | giga pascal                                 |
| Gsm                       | grams per square meter                      |
| GTM                       | Global Technology Meeting                   |

## H

|       |   |
|-------|---|
| H     | hour  |
| HAADF | high-angle annular-dark-field   |
| HB-2B | Beamline used to map stress distributions in complex parts produced by additive manufacturing |
| HEV   | hybrid electric vehicle   |
| HEXRD | high-energy x-ray diffraction   |
| HHINC | Value for household income in crash model   |
| HPDC  | high pressure die-cast  |
| HPVDC | high pressure vacuum die cast   |
| HSLA  | high-strength low alloy   |
| HSS   | high-strength steel   |
| HVAC  | heating, ventilating, and air conditioning  |

## I

|      |  |
|------|--|
| IAC  | International Automotive Components            |
| ICE  | internal combustion engine                     |
| ICME | integrated computational materials engineering |
| ICS  | Innovative Composite Solutions LLC             |

|               |   |
|---------------|---|
| ICWE          | integrated computational weld engineering       |
| i.e.          | id est (that is; in other words)                |
| IIHS          | Insurance Institute for Highway Safety          |
| ILSS          | interlaminar shear strength                     |
| Inc.          | Incorporated                                    |
| Int. or Intl. | International                                   |
| IP            | instrument panel (beam)                         |
| IP            | intellectual property                           |
| IR            | infrared  |
| ISIJ          | International Science and Investigation Journal |
| ISO           | International Organization for Standardization  |
| ISV           | Internal State Variable (model)                 |
| IVAD          | ion vapor assist deposition                     |

## J

|                 |   |
|-----------------|---|
| J               | joule   |
| Intl J Dam Mech | International Journal of Damage Mechanics             |
| JOM             | Journal of The Minerals, Metals and Materials Society |

## K

|                    |                                  |
|--------------------|----------------------------------|
| KeV                | kilo electron volt               |
| kg                 | kilogram                         |
| kJ                 | kilojoules                       |
| kN                 | kilonewton                       |
| KPM                | Kingston Process Metallurgy Inc. |
| Ksi or ksi or kpsi | kilopound per square inch        |
| kWh                | kilowatt-hour                    |

## L

|          |   |
|----------|---|
| L/100 km | liters per 100 kilometer  |
| lb       | pound   |
| LBNL     | Lawrence Berkeley National Laboratory   |
| LCCF     | low-cost carbon fiber   |
| LCM      | liquid compression molding  |
| LD       | longitudinal direction  |
| LDH      | limiting dome height  |
| Lge      | Litres in gasoline equivalent terms; energy unit to be able to compare and add different fuels such as gasoline and diesel. Unless otherwise specified, fuel economy figures are expressed in Lge/100km |
| LFT      | long fiber thermoplastic  |
| LCA      | life cycle analysis   |
| LLC      | limited liability company   |

## Acronyms and Abbreviations

|          |   |
|----------|---|
| LPPM     | low pressure semi-permanent mold  |
| LPSPM    | low pressure permanent mold (casting process)   |
| LS-DYNA® | A general-purpose finite element program capable of simulating complex real world problems used by the automobile, aerospace, construction, military, manufacturing, and bioengineering industries. |
| LTT      | low-transformation-temperature  |

## M

|                                  |   |
|----------------------------------|---|
| m                                | meter   |
| M                                | million   |
| M2/M4                            | milestones 2 and 4  |
| m/min                            | meters per minute   |
| MagGen™                          | INFINIUM Inc. process for clean magnesium production  |
| MAGPASS-COAT®                    | A process for the chrome-free passivation of magnesium-based materials.                           |
| MANEUVER,                        | Value for the maximum speed (in miles per hour) a vehicle obtained on the avoidance maneuver test |
| MAO/MCC                          | Micro-Arc Oxidation/Micro-Arc Ceramic Composite   |
| MAP                              | microwave-assisted plasma   |
| Mater.                           | Materials   |
| Max                              | maximum   |
| MC                               | Monte Carlo   |
| MD                               | molecular dynamics  |
| MENA                             | Magnesium Elektron North America  |
| MFERD                            | Magnesium Front End Research and Development  |
| MFG                              | Molded Fiber Glass Companies  |
| Mg                               | magnesium   |
| MgAl <sub>2</sub> O <sub>4</sub> | magnesium aluminate   |
| MgCl <sub>2</sub>                | magnesium chloride  |
| MgCO <sub>3</sub>                | magnesium carbonate   |
| MgO                              | magnesium oxide   |
| Mg(OH) <sub>2</sub>              | magnesium hydroxide   |
| Mg <sub>2</sub> Si               | magnesium silicide  |
| MHz                              | megahertz   |
| MIG                              | metal inert gas   |
| MIT-LLC                          | Material Innovation Technologies, LLC   |
| mm                               | millimeter  |
| MMLV                             | multi material lightweight vehicle  |
| MMT                              | million metric tons   |
| Mn                               | manganese   |
| Mo                               | molybdenum  |

|      |                                       |
|------|---------------------------------------|
| MOST | Ministry of Science and Technology    |
| Mpa  | megapascal                            |
| mph  | miles per hour                        |
| MPS  | Material and Process Selection (Team) |
| MSF  | Multi-Scale Fatigue (model)           |
| MSU  | Michigan State University             |
| MY   | model year                            |

## N

|       |  |
|-------|--|
| NaCl  | sodium chloride                                |
| NaOH  | sodium hydroxide                               |
| NCAP  | New Car Assessment Program                     |
| NCF   | non-crimped fabric                             |
| NCMS  | National Center for Manufacturing Sciences     |
| NDA   | non-disclosure agreement                       |
| NDE   | nondestructive evaluation                      |
| NETL  | National Energy Testing Laboratory             |
| NF    | natural fiber                                  |
| NHTSA | National Highway Traffic Safety Administration |
| Ni    | nickel   |
| NIST  | National Institute of Standards and Technology |
| nm    | nanometer (10 <sup>-9</sup> meter)             |
| Nom   | nominal  |
| NRCan | Natural Resources Canada                       |
| NRC   | National Research Council                      |
| NVH   | noise, vibration, and harshness                |
| NWU   | Northwestern University                        |

## O

|                 |   |
|-----------------|---|
| <sup>18</sup> O | Oxygen-18 is a natural, stable isotope of oxygen and one of the environmental isotopes. |
| OCP             | open-circuit potential  |
| OEM             | original equipment manufacturer   |
| OM              | optical microscopy  |
| ORNL            | Oak Ridge National Laboratory   |
| OSO             | Oak Ridge Site Office   |
| OVERWT00        | Value for the mass reduction in heavier-than-average cars                               |

## P

|        |  |
|--------|--|
| PA     | polyamide                                      |
| PACCAR | Paccar Inc. (formerly Pacific Car and Foundry) |

## Acronyms and Abbreviations

|           |   |
|-----------|---|
| PAM-CRASH | A general purpose explicit finite element computer program for nonlinear dynamic analysis of structures in three dimensions |
| PAN       | polyacrylonitrile   |
| PC        | polycarbonate   |
| PCTHISPD  | Term for the fraction of vehicles on high-speed roads used in crash model   |
| PCTLGPU   | Term for the fraction of vehicles in Fatal Analysis Reporting System that are large pickups used in crash model             |
| PCTLT     | Term for the fractions of vehicle registrations that are light trucks in crash model  |
| PE        | predictive engineering (when referring to a modeling tool)  |
| PE        | polyethylene (when referring to a thermoplastic fiber)  |
| PET       | polyethylene terephthalate  |
| PEV       | plug-in electric vehicle  |
| PFM       | Progressive Failure Models  |
| PHS       | press hardened steel  |
| PNNL      | Pacific Northwest National Laboratory   |
| PP        | polypropylene   |
| PPAP      | Production Part Approval Process  |
| PPF       | pulse pressure forming  |
| PPS       | polyphylene sulfide   |
| pregreg   | pre-impregnated (composite fibers)  |
| Proc.     | Proceedings   |
| PSC       | Project Steering Committee  |
| PSI       | pounds per square inch  |
| PSP       | processing-structure-property   |
| PTC       | Project Technical Committee   |
| PTFE      | polytetrafluoroethylene   |

## Q

|           |  |
|-----------|--|
| Q1, Q2    | First and second quarter of a year   |
| Q&P       | quenching and partitioning   |
| $Q_{hkl}$ | The inverse interatomic spacing for a certain crystallographic direction ( $hkl$ ) |
| QI        | quasi-isotropic  |
| QM        | quality mapping  |
| QPF       | quick plastic forming  |

## R

|         |   |
|---------|---|
| $R_a$   | roughness of surface  |
| R&D     | research and development  |
| RADIOSS | A multidisciplinary finite element solver developed by Altair Engineering |

|         |   |
|---------|---|
| RCF     | Re-engineered carbon fiber  |
| RD      | rolling direction   |
| RE      | rare earth  |
| RED     | Term used for a crash that occurred in primarily Republican (red) state used in crash model   |
| RESTUSE | Term used for amount of driver rest used in crash model   |
| RF      | radio frequency   |
| RIVTAC® | Bollhoff technology that is particularly suitable for joints of aluminum, steel, plastics, non-ferrous metals as well as for mixed joints, multiple-layer joints and hybrid joints of these materials |
| RMX     | Formerly ReMaxCo Technologies   |
| RPM     | revolutions per minute  |
| RS      | retreating side   |
| RSW     | resistance spot welding   |
| RT      | room temperature  |
| RUC     | representative unit cell  |
| RURAL   | Value for county population density in crash model  |
| RVE     | representative volume element   |

## S

|       |  |
|-------|--|
| s     | second(s)  |
| SAE   | Society of Automotive Engineers  |
| SAMPE | Society for the Advancement of Material and Process Engineering  |
| SANS  | small angle neutron scattering   |
| SAZ   | shear affected zone  |
| SBIR  | Small Business Innovation Research   |
| SBMS  | Standards Based Management System  |
| SCFI  | Stronach Centre for Innovation   |
| Sci.  | science  |
| SD    | standard deviation   |
| SEA   | specific energy adsorption   |
| SEM   | scanning electron microscope   |
| Si    | silicon  |
| Sim.  | simulated  |
| SIMS  | secondary ion mass spectrometry  |
| SMC   | sheet molding compound   |
| Sn    | tin  |
| S-N   | <i>S-N curve</i> , also known as a <i>Wöhler curve</i> . A graph of the magnitude of a cyclic stress ( $S$ ) against the logarithmic scale of cycles to failure ( $N$ ). |
| SNS   | Spallation Neutron Source  |

## Acronyms and Abbreviations

|            |   |
|------------|---|
| SOP        | Standard Operating Procedures             |
| SoW or SOW | Statement of Work                         |
| SPF        | super plastic forming                     |
| SPR        | self-pierce riveting, self-piercing rivet |
| STEM       | scanning transmission electron microscope |
| SUV        | sports utility vehicle                    |
| SVDC       | super vacuum die cast                     |

## T

|             |  |
|-------------|--|
| T5          | Temper designation for cooled from hot working and artificially aged (at elevated temperature)     |
| T6          | Temper designation for solution heat treated and artificially aged aluminum alloy                  |
| T-direction | transverse direction   |
| TBTU        | trillion British Thermal Units   |
| Tech.       | technology   |
| TEM         | transmission electron microscopy   |
| TGA         | thermal gravimetric analysis   |
| TCMG2       | Thermo-Calc Software magnesium-based alloys database   |
| TMS         | The Minerals, Metals and Materials Society   |
| tonne       | A metric ton equal to 2,204.6 pounds   |
| TPO         | tail pull-out  |
| TRC UTC     | Transportation Research Board University Transportation Center                                     |
| TRIP        | transformation-induced plasticity  |
| TWB         | tailor-welded blanks   |
| TWB LLC     | TWB Company LLC, manufactures tailor welded products for the automotive industry in North America. |
| TWIP        | Twinning Induced Plasticity  |
| TYP         | type (ply type for modeling)   |

## U

|          |   |
|----------|---|
| UD       | unidirectional  |
| UHSS     | ultra-high strength steels                                |
| UHP      | ultra-high purity   |
| UIUC     | University of Illinois at Urbana Champaign                |
| UM       | University of Michigan                                    |
| UNDRWT00 | Value for the mass reduction in lighter-than-average cars |
| UPA      | units per annum   |
| U.S.     | United States of America                                  |
| USAMP    | United States Automotive Materials Partnership            |

|       |   |
|-------|---|
| USCAR | United States Council for Automotive Research |
| UTS   | ultimate tensile strength                     |
| UV    | ultraviolet                                   |

## V

|          |  |
|----------|--|
| VE       | vinyl ester  |
| VIN      | vehicle identification number                            |
| viz.     | videlicet (it may be seen; evidently; clearly)           |
| VUMAT    | vectored user material                                   |
| VMM      | Virtual Manufacturing Models                             |
| VMT      | vehicle miles of travel                                  |
| VMTWTFFA | Value for vehicle miles traveled weight factor           |
| VP       | Vice President   |
| VPSC     | viscoplastic-self-consistent                             |
| vs.      | versus   |
| VTO      | Vehicle Technologies Office/Vehicle Technologies Program |

## W

|     |   |
|-----|---|
| W   | Temper designation for aluminum alloy that is solution heat treated only. W is a relatively soft intermediary designation that applies after heat treat and before aging is completed |
| WI  | Work Instructions   |
| WSU | Wayne State University  |

## X

|     |                                  |
|-----|----------------------------------|
| XPS | x-ray photoelectron spectroscopy |
| XRD | x-ray diffraction                |

## Y

|    |                |
|----|----------------|
| yr | year           |
| YS | yield strength |

## Z

|      |   |
|------|---|
| ZE20 | A melt containing 2 percent zinc and 0.2 percent cerium and the balance magnesium by weight |
| Zn   | zinc  |
| Zr   | zirconium   |

---

## I.0 INTRODUCTION

As part of the U.S. Department of Energy's (DOE's) Vehicle Technologies Program (VTO), the Lightweight Materials (LM) activity focuses on the development and validation of advanced materials and manufacturing technologies to significantly reduce light and heavy duty vehicle weight without compromising other attributes such as safety, performance, recyclability, and cost. Because it takes less energy to accelerate a lighter object, replacing cast iron and traditional steel components with lightweight materials such as high-strength steel, magnesium, aluminum, and polymer composites can directly reduce a vehicle's fuel consumption. For example, a 10% reduction in vehicle weight can result in a 6%–8% fuel economy improvement. Reducing vehicle weight has other benefits such as allowing cars to carry advanced emissions control equipment, safety devices, and integrated electronic systems without becoming heavier. Lightweight materials are especially important for improving the efficiency and range of hybrid electric, plug-in hybrid electric and electric vehicles because they offset the weight of power systems such as batteries and electric motors.

In the short term, vehicle weight reduction is possible through the application of materials such as advanced high strength steels (AHSS) and aluminum alloys; automotive alloys and processes within these material families already exist however further improvement is necessary to enable greater weight reduction while also addressing implementation technology gaps in joining, modeling, and recycling. In the longer term, even greater weight savings are possible through the use of magnesium alloys and carbon fiber composites. However, more extensive R&D is needed to address implementation barriers, improve the performance of these materials, and reduce their costs.

Research and development work conducted within the Lightweight Materials activity is broken down into three categories: Properties and Manufacturing, Multi-material Enabling, and Modeling and Computational Materials Science (CMS). Work within Properties and Manufacturing aims to improve properties (such as strength, stiffness, or ductility) and manufacturability (such as material cost or production rate) of a variety of metal and polymer composite materials. Integrating components into a vehicle system while avoiding joining, corrosion, and other compatibility issues presents a significant challenge to the introduction of new, lightweight materials; work within Multi-Material Enabling targets novel processes, designs, materials, and technologies that enable assembly of disparate material systems into lightweight structures. CMS and Integrated Computational Materials Engineering (ICME) continue to mature as important disciplines for lightweight materials development and deployment. Work within Modeling and CMS engages broadly on topics ranging from model development and validation to framework deployment and ICME driven development of new materials. In support of the President's Materials Genome Initiative<sup>1</sup> and the Vehicle Technologies Office objectives, much of this work emphasizes application on integrated computational and experimental techniques towards more rapid development and deployment of lightweight automotive materials.

### Carbon Fiber and Polymer Composites

Carbon fiber (CF) reinforced polymer composites have the potential to reduce component weight by more than 60% however there are significant technical and cost barriers to their widespread introduction onto vehicles. The cost of input material (precursor) and the carbonization process contribute significantly to the total cost of CF hence significant focus has been provided to these areas. Focus on low cost carbon for both the precursor (Zoltek lignin/polyacrylonitrile (PAN)) and the advanced processing (Oak Ridge National Laboratory (ORNL) plasma oxidation and microwave assisted plasma (MAP)) show progress in both lower cost precursors as well as in lower cost oxidation of the precursor and conversion of the oxidized precursor to CF. Figure I-1 shows the desired uniform micro-porosity achieved in 35% lignin/PAN precursor fibers and spools of lignin/PAN carbon ready for shipment.

---

<sup>1</sup> <http://www.whitehouse.gov/mgi>.

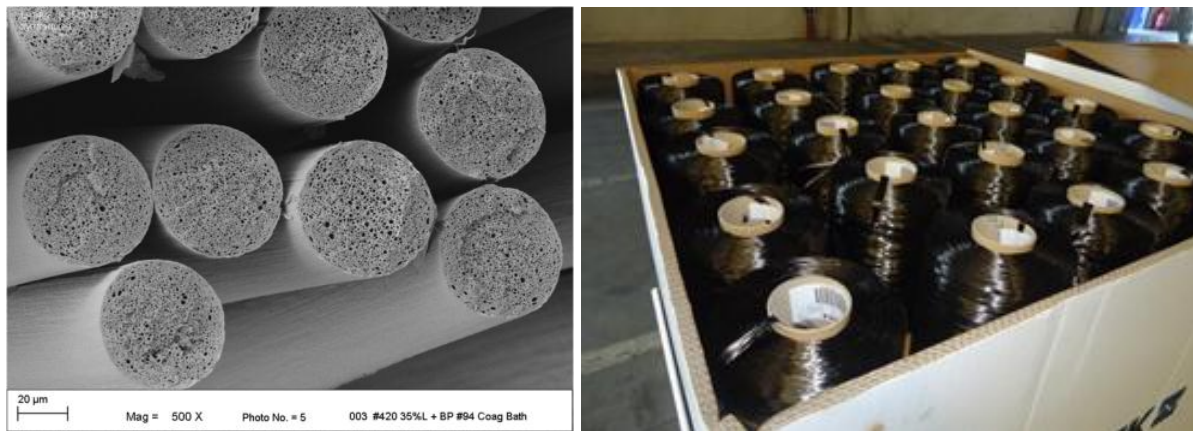


**Figure I-1: 35% lignin/PAN precursor fiber Scanning Electron Microscope image showing uniform micro-porosity and 1500 meter spools of lignin/PAN carbon fiber ready for shipment.**

The process improvements continue to enable validation of successfully converting larger volumes (tows) of precursor to carbon at faster rates ORNL is working on a project to scale and transition low cost CF technology through the ORNL Carbon Fiber Technology Facility (CFTF). ICME focused projects include validation of models for long carbon fiber injection molding processing of a complex 3-D part. Figure I-2 shows a candidate part and possible use for the 3-D validation of long fiber injection molding models.

In addition, USAMP's plan for validation of crash models for CF composites show preliminary results on the steel bumper baseline. The analysis of crash data on vehicles at Lawrence Berkeley National Laboratory (LBNL) continues to provide insight into the impact of size and weight on crashes.

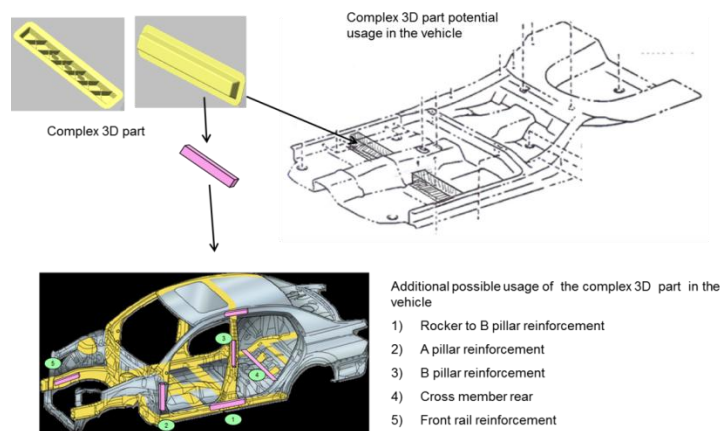


**Figure I-2: Potential applications of components with features represented by the complex 3-D part in an automotive body structure.**

## Magnesium Alloys

Magnesium (Mg) alloys, with the lowest density of all structural metals, have the potential to reduce component weight by greater than 60%. However, significant technical barriers limit the use of Mg to approximately 1% of the average vehicle by weight. These barriers include high raw material cost and price volatility, relatively low specific stiffness, difficulty in forming sheet at low temperatures, low ductility of finished components, and a limited alloy set, among others. In addition, using Mg in multi-material systems introduces joining, corrosion, repair, and recycling issues that must be addressed. This year's report features results from several projects addressing key Mg technology gaps. Researchers at Pacific Northwest National Laboratory (PNNL), working with industry partners, have demonstrated a non-rare earth (RE) containing Mg extrusion alloy and process along with a novel microstructure modeling approach that correctly predicts the experimentally measured properties. A PNNL, Ford, and the University of Michigan team has developed a microstructure-based modeling framework for predicting ductility in Mg die-castings (a notoriously difficult property to predict) and are continuing to improve the model through validation and incorporation of new features. ORNL researchers continue to apply tremendous expertise and leverage world-class characterization equipment towards an improved understanding of corrosion processes in Mg alloys. Figure I-3 shows project results characterizing film structure and chemical segregation in surface films after water exposure.

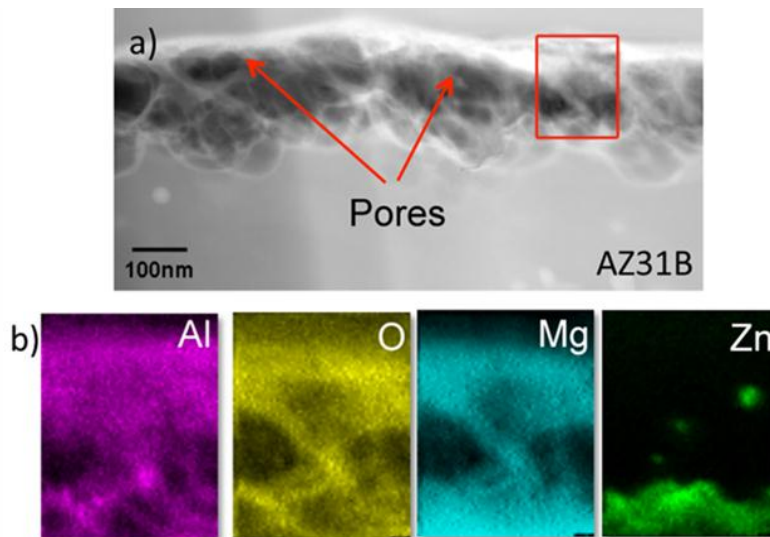


**Figure I-3: High Angle Annular Dark Field Scanning Transmission Electron Microscope cross-section image of film formed on AZ31B magnesium alloy after exposure to water with elemental maps of Al, O, Mg, and Zn. Note the apparent segregation of the Zn to the metal-oxide interface.**

At a higher level, the Magnesium Intensive Vehicle Front End project (a partnership with Ford, GM, Chrysler, a large team of universities and suppliers, and partners in Canada and China) has made considerable progress towards the construction and testing of Mg-intensive, multi-material vehicle substructures, setting the stage for wider adoption of Mg in the vehicle supply chain. These projects, and additional projects and activities targeting Mg technology development, can be found in the following chapters.

### Aluminum Alloys

Aluminum (Al) alloys represent a middle-ground in the structural light metals spectrum. Years of development within the aerospace, construction, and automotive industries have led to a well-developed and reasonably well understood alloy and processing set. Applications of Al within automotive design include hoods and panels, power train components, and even entire vehicle body-in-white (BIW) structures. There are several of barriers to the increased use of Al in vehicle weight reduction applications such as material cost, room temperature formability, and limitations within the existing manufacturing infrastructure. As with Mg, the addition of significant amounts of Al to the automotive manufacturing stream presents added multi-material challenges in joining, corrosion, paint and coatings, repair, and recycling. This report includes an update on a project with PNNL, GM, Alcoa, and TWB LLC seeking to develop and transition a commercially viable tailor welded blank (TWB) manufacturing process using friction stir welding to produce Al blanks. The team reports outstanding progress towards tooling and process designs for higher welding speed and deployment of the technology to commercial producers of automotive materials. As shown in Figure I-4, the team has successfully stamped TWBs requiring considerable deformation.

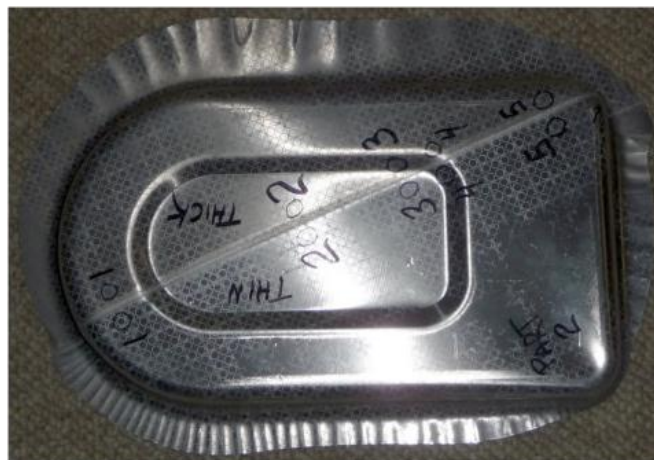


**Figure I-4: Successful stamped aluminum tailor welded blank using 2.0 mm and 1.2 mm 5182 aluminum alloy sheets.**

A project team from PNNL and PACCAR Technical Center has demonstrated a clever combination of hot and cold forming to yield aerodynamic structural components for heavy-duty truck cabs that could replace shape molding compound (SMC) at a considerable weight savings. The project team reports technology transition activities focused on producing prototype parts at a tier 1 supplier here. Further projects supporting wider adoption of lightweight aluminum alloys can be found in this report.

### Advanced High Strength Steel (AHSS)

Conventional iron and steel alloys are prominent in existing vehicle architectures, making up about 45% of the weight of a vehicle. Despite the relatively high density of iron based materials, the exceptional strength and ductility of advanced steels offers the potential for efficient structural designs and reduced weight. Application of a new generation of AHSS has the potential to reduce component weight by up to 25%, particularly in strength limited designs. Steel components are also generally compatible with existing manufacturing infrastructure and vehicle materials, making them a likely candidate for near-term weight reduction. Steel development and research in the LM activity is focused on introducing the so-called “3<sup>rd</sup> generation advanced high strength steels (3G AHSS)”. As shown in Figure I-5<sup>2</sup>, 3G AHSS are targeted to properties in between 1<sup>st</sup> and 2<sup>nd</sup> generation AHSS with high strength, improved ductility, and low cost.

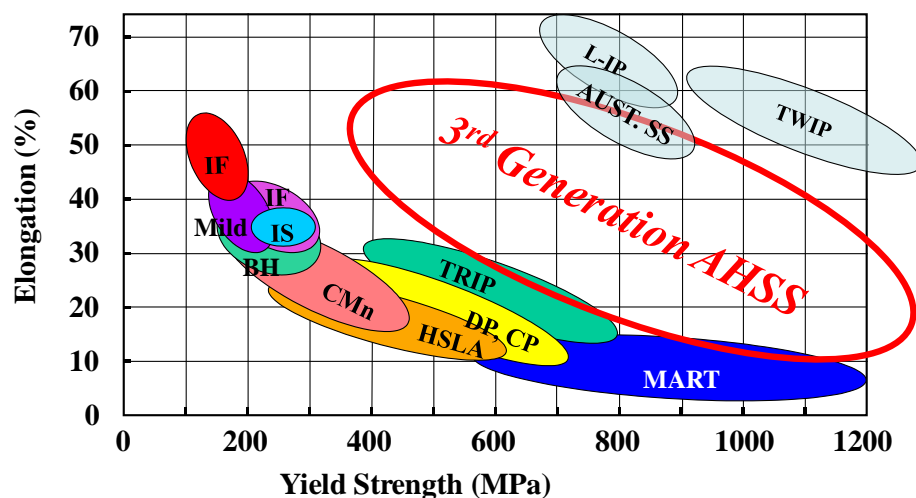


Figure I-5: Yield Strength versus Uniform Elongation for a variety of steel types.

New in 2013, the Integrated Computational Materials Engineering for Advanced High Strength Steel (ICME-AHSS) project represents a significant step for both the ICME and AHSS communities. The project team, consisting of Ford, GM, Chrysler, 6 major steel suppliers, and several universities, is working to develop a combined experimental-modeling framework that can be used to more rapidly and effectively discover steel alloys and processes with 3<sup>rd</sup> generation properties. This report features and updates on the ICME AHSS project and discussion of the path forward, as well as updates on other steel projects in the VTO portfolio.

### Looking Forward

The following reports provide a detailed description of the activities and technical accomplishments of the Lightweight Materials activity during the 2013 Fiscal Year. The work shown here has produced technologies that make today's vehicles more efficient, safe, and affordable. In collaboration with industry, universities, and national laboratories, VTO continues to develop the next generation of lightweight components. These efforts are building the foundation of technologies—and technology manufacturers—that tomorrow's vehicles need to achieve ultra-high efficiency and resulting reductions in petroleum use and greenhouse gas emissions.

<sup>2</sup> Auto/Steel Partnership, [www.autosteel.org](http://www.autosteel.org).

## II.0 THE EV EVERYWHERE GRAND CHALLENGE

### II.1. Background

In March 2012, President Obama announced the *EV Everywhere* Grand Challenge—to produce plug-in electric vehicles (PEVs) as affordable and convenient for the American family as gasoline-powered vehicles by 2022. Realizing the promise of PEVs is one of the grand challenges of this era. Today, our transportation system is still dependent on internal combustion engines (ICE) and oil. In fact, 93% of our transportation fuel is derived from petroleum and much of this is imported. PEVs can decouple personal mobility from oil, cut pollution and help build a 21<sup>st</sup> Century American automotive industry that will lead the world.

America is the world's leading market for electric vehicles and is producing some of the most advanced PEVs available today. Consumer excitement and interest in PEVs is growing—in 2012, PEV sales in the U.S. tripled, with more than 50,000 cars sold, and a PEV (the Chevrolet Volt) beat all other vehicle models in Consumer Reports' owner satisfaction survey for the second time. In 2013, PEV sales are on pace to nearly double prior year sales, with nearly 100,000 annual sales of PEVs projected.

PEVs have won critical acclaim with awards such as 2011 World Car of the Year (Nissan Leaf), 2013 Motor Trend Car of the Year (Tesla Model S) and 2012 Green Car Vision Award Winner (Ford C-MAX Energi). To maintain this leadership, strong growth in the U.S. PEV sector will need to continue.

The Department of Energy (DOE) developed an *EV Everywhere* "Blueprint" document that provides an outline for technical and deployment goals for PEVs over the next five years [[http://www1.eere.energy.gov/vehiclesandfuels/electric\\_vehicles/pdfs/everywhere\\_blueprint.pdf](http://www1.eere.energy.gov/vehiclesandfuels/electric_vehicles/pdfs/everywhere_blueprint.pdf)]. DOE will pursue these targets in cooperation with a host of public and private partners. The technical targets for the DOE PEV program fall into four areas: battery R&D; electric drive system R&D; vehicle lightweighting; and advanced climate control technologies. Some specific goals include:

- Cutting battery costs from their current \$500/kWh to \$125/kWh
- Reducing the cost of electric drive systems from \$30/kWh to \$8/kWh
- Eliminating almost 30% of vehicle weight through lightweighting

These numbers represent difficult to reach "stretch goals" established in consultation with stakeholders across the industry—including the *EV Everywhere* workshops held during the summer and fall of 2012. When these goals are met, the

levelized cost of an all-electric vehicle with a 280-mile range will be comparable to that of an ICE vehicle of similar size. Even before these ambitious goals are met, the levelized cost of most plug-in hybrid electric vehicles—and of all-electric vehicles with shorter ranges (such as 100 miles)—will be comparable to the levelized cost of ICE vehicles of similar size. Meeting these targets will help to reduce the purchase price for plug-in electric vehicles

The *EV Everywhere* Blueprint document also describes the deployment programs related to charging infrastructure and consumer education. Efforts to promote home, workplace, and public charging can also help speed PEV deployment.

#### **EV Everywhere Technical Targets**

DOE defined *EV Everywhere* technology targets using an analytical framework that evaluated the performance of component technologies as well as vehicle cost and performance. We synthesized data about future vehicle potential by using expert projections of component technology to create virtual vehicles of the future via computer modeling and simulation. The range of vehicle costs and efficiencies made possible a comparison of the degree to which the portfolio of these technologies must progress, in both performance and cost terms, to yield PEVs that are cost-competitive, as measured by the initial vehicle purchase price and the fuel expenditure accrued over a 5-year ownership period. Ultimately, an analysis of this balance yielded technical targets at the technology progress frontier: *EV Everywhere* targets are consistent with what experts see as very aggressive but still possible within the *EV Everywhere* timeframe.

The complete set of *EV Everywhere* technical targets are presented in the Blueprint document. The specific technical targets that pertain to lightweight materials are as follows:

#### **Vehicle Lightweighting 2022 Targets**

| E                             | Body | Interior | Chassis/<br>Suspension | Total<br>Vehicle |
|-------------------------------|------|----------|------------------------|------------------|
| Weight<br>Reduction<br>Target | 35%  | 5%       | 25%                    | 30%              |

## II.2. 2013 Highlights

### Magnesium Front End Research and Development

*Extending the utility of magnesium as a lightweighting material through study of advanced alloys, manufacturing and assembly processes, and mitigation of galvanic corrosion in dissimilar-metal joints.*

#### United States Automotive Materials Partnership LLC (USAMP)

USAMP's achievements in developing large, integrated all-magnesium alloy subassemblies comprised of high-integrity die castings and wrought forms have previously been reported. Such large-scale, lightweight substructures are capable of advancing the 50% vehicle weight reduction goal of the U.S. DRIVE's Materials Tech Team. This undertaking, collectively known as "Magnesium Front-End Research and Development" (MFERD), has also included an international partnership with magnesium researchers in Canada and China.

In the course of this broad effort, a number of key technical challenges have arisen, and constitute major thrusts of the current work.

**Challenge 1:** For widespread application, magnesium-intensive substructures will ultimately need to incorporate and interface with dissimilar materials such as steel and aluminum.

Tasks to provide and assess joining of such dissimilar metals, as well as protecting against galvanic corrosion were initiated. In FY 2013, these tasks have demonstrated successful aluminum-magnesium joints using both friction stir welding (upper rail) and self-piercing rivets (lower rail). Figure II-1 portrays the dissimilar-metal joints in the current embodiment of the demonstration structures. Adaptation of both technologies was enabled by fundamental advances in the metallurgy of the weld zone and deformation characteristics of magnesium in selected material stack-ups. Additionally, testing has begun on approaches developed for thwarting localized galvanic attack of magnesium adjacent to coated steel self-piercing rivets.

**Challenge 2:** Improving deformation properties of magnesium alloys for purposes of component fabrication and performance.

In FY 2013, a novel ZE20 magnesium extrusion grade was selected for evaluation, cast into billets and extruded into prototype lower rail profiles as shown in Figure II-1. These profiles will be used to evaluate crashworthiness, corrosion and fatigue properties of both the alloy and structure.

**Challenge 3:** Durability of magnesium-to-magnesium and magnesium-to-dissimilar metal joints.

In 2013 several improvements were made to computer-aided engineering tools used to predict joint failure in large structures through application of algorithms assessing localized structural stresses, which, in turn, can then be employed in conventional estimates of fatigue durability.

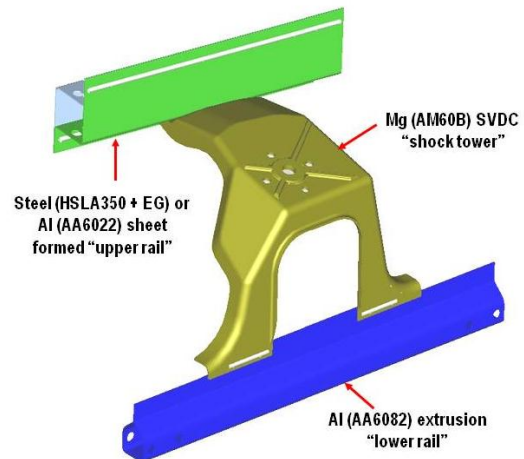


**Figure II-1:** Demonstration "front-end" structure employing dissimilar metals as indicated.

## Integrated Computational Materials Engineering (ICME) Approach to Development of Lightweight 3GAHSS

*Demonstrating the applicability of Integrated Computational Materials Engineering for the development and deployment of third generation advanced high strength steels (3GAHSS) for improved vehicle lightweighting*

### United States Automotive Materials Partnership

Professor Farhang Pourboghraat of Michigan State University (MSU), working with Professor Sharvan Kumar and Dr. Hassan Ghassemi Amaki of Brown University (BU) under the leadership of Dr. Louis Hector Jr. of General Motors, has developed an initial three dimensional (3D) representative volume element (RVE) which is statistically equivalent to the actual microstructure of a third generation advanced high strength steel (3GAHSS) based on BAO QP980 steel (see Figure II-2). The development of an accurate computer representation of this microstructure is impressive considering the complexity of this 3GAHSS, which consists of multiple dispersed microstructural phases such as soft ferritic, metastable austenite, and hard martensitic.

Mechanical properties for steel sheet are based on the composite response of all microstructural phases to strain. When sufficiently strained, such as during the forming of a vehicle component, the austenitic phase in the BAO QP980 transforms to a harder, less ductile martensitic phase. This transformation dramatically changes the material properties of the steel, which if not well understood can limit the extent to which 3GAHSS can be exploited to reduce vehicle mass and cost.

Accurate representation of the size, shape, distribution and volume of the individual phases, will enable computer modelers to assess the response of individual phases to strain. This in turn will enable improved computer simulations to determine the possible shapes that can be formed from 3GAHSS and subsequent component performance in a vehicle. This work is essential for designers tasked with producing lighter weight 3GAHSS structures that have similar or better performance than other (e.g., more costly) steels.

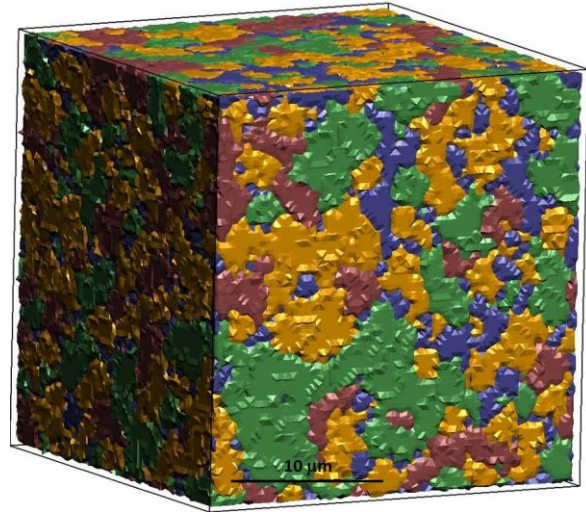


**Figure II-2: Three Dimensional Representative Volume Element of BAO QP980 Steel—(Green = Martensite, Blue = Austenite and Red + Yellow = Ferrite).**

This development is the first known implementation of 3D RVEs in an ICME program, where less accurate 2D images have been previously used to model nonferrous alloys. 3D RVEs are a fundamental improvement, not only to the 3GAHSS ICME project, but to ICME modeling in general. It is expected that future enhancements to 3D RVEs will reduce requisite testing for generating constitutive material parameters necessary for ICME models and minimize errors in ICME model simulations. Future work in the 3GAHSS ICME project is to validate 3D RVEs, and once validated, integrate them into an ICME model.

## Carbon Fiber Technology Facility (CFTF)

*The fully operational Carbon Fiber Technology Facility is a key resource for scaling and transferring lower cost carbon fiber technologies from the laboratory to the carbon fiber industry.*

## Oak Ridge National Laboratory (ORNL)

ORNL is leading research and development efforts in lightweight materials for transportation, with a focus on lower cost carbon fiber (CF) which would be available at a target price of \$5-7 per pound. ORNL has demonstrated, at a laboratory scale, CF can be produced using alternative precursors such as textile grade polyacrylonitriles, polyolefins, and lignins. ORNL is also developing lower-cost methods for converting precursors into CF including atmospheric plasma oxidation and microwave-assisted plasma carbonization. In order to commercialize these technologies, their viability must be proven on a continuous basis at near industrial scale.

The Carbon Fiber Technology Facility (CFTF), funded with funds provided by the *American Recovery and Reinvestment Act of 2009 (ARRA)* by the DOE's Vehicle Technologies Office (VTO). The CFTF is designed to scale up low-cost CF technologies and move them into the marketplace. During 2013 the CFTF was commissioned and is now fully operational with operating funds provided jointly by AMO and VTO.

The CFTF offers a flexible, highly instrumented CF line for demonstrating advanced technology scale-up and producing market-development volumes of prototypical CFs made from alternative precursors. The CFTF is intended to bridge the gap between laboratory research and commercial-scale deployment of low-cost CF technologies. The CFTF is capable of producing up to 25 tons of CF a year. In addition to a conventional conversion line, CFTF has a melt-spun precursor fiber production line with a rated capacity of 65 tons per year. The 42,000 ft<sup>2</sup> facility has the capacity for expansion, including the addition of an advanced technology conversion line based off of technologies currently being developed at ORNL.

Recently the CFTF has:

- Successfully determined a conversion process for a textile based polyacrylonitrile (PAN) precursor
- Melt blow lignin mat precursor at large scale
- Processed industrial grade CF precursor with strengths as high as 550 ksi
- Filed two invention disclosures
- Implemented a worker training program to develop a future work force for the CF industry
- Began working with industrial partners to supply carbon fiber as part of the AMO Manufacturing Demonstration Facility



Figure II-3: Inside the Carbon Fiber Technology Facility.

## Structural Composite Underbody—Going Forward

*The findings from the Automotive Composites Consortium Structural Composite Underbody project were used for the rapid commercialization of the Chevrolet Spark EV battery enclosure.*

### USAMP Automotive Composites Consortium (ACC)

The ACC Underbody project designed, built, analyzed, and tested an automotive underbody capable of carrying the crash loads of a vehicle, while saving about 13 kg mass compared to the optimized high strength steel underbody in the donor vehicle. Minimizing the mass of this structure required a number of thickness zones in the part, ranging from 1.8 mm to 5.4 mm.

The underbody was made from a coarse weave glass fabric coated with a vinyl ester resin in an SMC-like process. The prepreg was cut on an automated cutting table with patterns designed for minimal overlap to accommodate the complex thickness zones. These pieces were assembled into a preform and transferred to the compression molding tool. The part was assembled into a mock body-in-white, using composite-to-steel weld bonding (USCAR patents). The weld bonding used laser-cut holes in the composite for the welding. Adhesive was applied to the steel structure and to doubler strips with divots matching the hole pattern. These were placed on either side of the composite, and doubler welded to the steel structure, providing peel stoppers, and acting as fixturing during the adhesive cure. The composite/steel structure was then tested simulating the underbody loads that would have been seen in a 40 mph offset deformable barrier. The results showed that while the molded part was slightly thicker than design, our models predicted the behavior within tolerance.

**Spark EV:** When the Chevrolet Spark EV team found themselves in need of a new material for the two-piece structural battery enclosure a very short time from start of production, they saw an answer in the underbody. They used the coarse weave glass fabric/vinyl ester prepreg, further developing the resin system to virtually eliminate solvent emissions. The prepreg is then cut and placed on the tool with a laser-assist system, and the preform robotically placed in the mold.

After part cure and post processing, the battery tray is assembled to a lower steel structure, with the structural plates on the inside acting as the doublers. This used rivet bonding, similar to weld bonding. The change to this material was very rapid, because of the extensive research and development done by the ACC Underbody project.

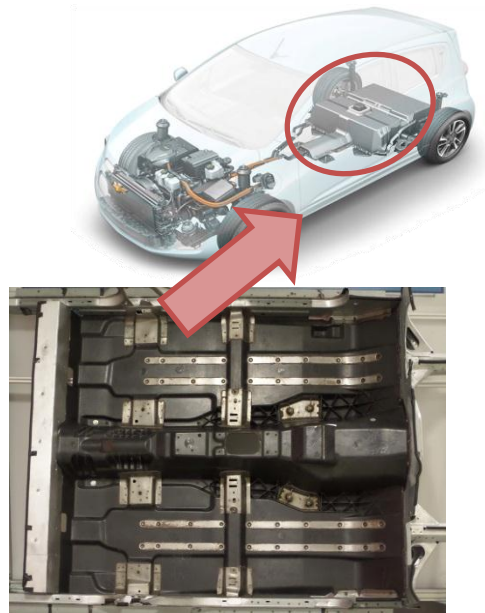


**Figure II-4: The materials, part fabrication, modeling and assembly methodologies used in the Structural Composite Underbody were refined and utilized in the Chevrolet Spark EV battery enclosure.**

## Vehicle Mass: Road Load & Energy Consumption Impact

Energy consumption decrease of 4% to 5% for a 10% Vehicle Mass reduction was quantified for three vehicle powertrain architectures: Internal Combustion Engine, Hybrid Electric, and Battery All-Electric.

### Idaho National Laboratory, Argonne National Laboratory, and ECotality North America

As part of the testing and data collection support to the U.S. Department of Energy (DOE), the Materials Technical Team (MTT), and DOE’s Advanced Vehicle Testing Activity (AVTA), the Idaho National Laboratory, Argonne National Laboratory, and ECotality North America test advanced technology vehicles in on-road fleets, on test tracks, and in laboratory settings in order to determine the real-world petroleum reduction potential of various advanced vehicle technologies.

The impact of vehicle mass on road load force and energy consumption for three vehicle powertrain architectures was measured through test-track coastdown testing and chassis dynamometer testing. Testing was conducted on a Ford Fusion V6 internal combustion engine vehicle (ICE), a Ford Fusion hybrid electric vehicle (HEV), and a Nissan Leaf battery electric vehicle (BEV). Testing was conducted at multiple 250 lb test weights for each vehicle. This study provides results for research, development, and modeling efforts.

Coastdown testing quantified the impact of vehicle mass on road load force to be a non-linear trend with respect to change in mass. For a 5% increase in mass, the road load force increases ~3% but for a 5% decrease in mass, the road load force decreases ~5%. This trend appears to be consistent across the three powertrain architectures (BEV, HEV, or ICE).

Chassis Dynamometer testing quantified the impact of vehicle mass on energy consumption. The largest impact of vehicle mass occurs during “stop & go” city and aggressive driving. For a 10% reduction in mass, a ~4% to ~5% decrease in percent energy consumption was measured across all powertrain architectures. However the conventional vehicle (ICE) has the largest decrease in net energy consumption (up to ~0.4 L/100km) during aggressive driving as compared to HEV or BEV.



Figure II-5: Photo of the three vehicles tested (BEV, HEV, and ICE).

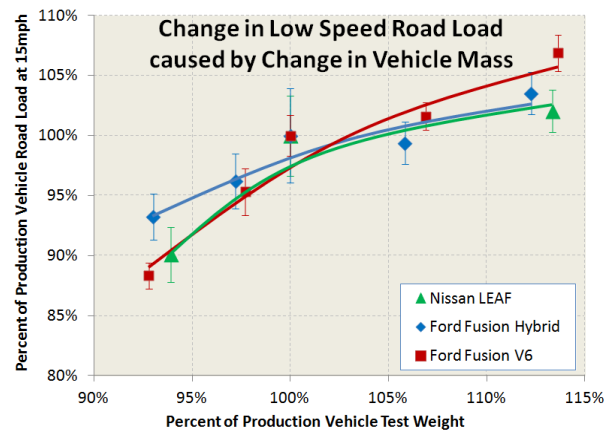


Figure II-6: Vehicle Road Load vs. Vehicle Weight with respect to base vehicle.

Table II-1: For a 10% Reduction in Vehicle Mass

| Driving type | Percent consumption reduction[%] |         |            | Energy consumption reduction [Lge/100km] |         |            |
|--------------|----------------------------------|---------|------------|--|---------|------------|
|              | City                             | Highway | Aggressive | City                                     | Highway | Aggressive |
| Conv. V6     | ~3.5%                            | ~3.0%   | ~4.5%      | ~0.35                                    | ~0.19   | ~0.40      |
| HEV          | ~2.5%                            | ~1.5%   | ~4.0%      | ~0.12                                    | ~0.06   | ~0.19      |
| BEV          | ~5.0%                            | ~0.1%   | ~2.5%      | ~0.08                                    | ~0.01   | ~0.10      |

## II.3. Planned Activities

Reducing the weight of a PEV can extend its electric range, reduce the size and cost of the battery, or achieve a combination thereof. In order for vehicle lightweighting to provide these benefits, lightweight metals and composites must be an attractive choice by meeting both cost and structural requirements. Materials properties related to mechanical behavior, crash response, and durability of vehicle structures must be improved. Moreover, techniques for predicting material behavior must be integrated with design methods to enable reduced cost, such as by minimizing input material quantities or decreasing cycle time.

The focus of these targets is to enable cost effective weight reduction for each of the systems of the vehicle that combined with compounding weight reduction in other systems and weight reduction for batteries and electric drive systems leads to a total vehicle weight reduction of almost 30%. For example, by 2022 we are seeking to reduce weight by 35% for the body structure, 25% for the chassis and suspension, and 5% for the interior. To achieve these targets for weight reduction, lightweight materials efforts must:

- Improve mechanical characteristics,
- Lower cost,
- Facilitate manufacturability,
- Provide solutions for cost effective joining and corrosion protection of multimaterial structures,
- Validate safety of lightweight designs, and
- Support design tools to facilitate faster development of new materials.

Lightweight material systems include carbon fiber composites, magnesium alloys, advanced high strength steel,

and aluminum alloys; and techniques to join combinations of these materials in a cost effective manner are also critical. Specific milestones seek to validate both that the material performance meets the system requirements and the cost to implement the material per pound of weight saved is acceptable.

In 2013, U.S. DRIVE updated its Materials Technical Team Roadmap. This Roadmap can be found at [http://www1.eere.energy.gov/vehiclesandfuels/pdfs/program/m tt\\_roadmap\\_august2013.pdf](http://www1.eere.energy.gov/vehiclesandfuels/pdfs/program/m tt_roadmap_august2013.pdf).

In support of the *EV Everywhere* Grand Challenge, DOE released a Funding Opportunity Announcement (FOA) in March 2013, soliciting proposals in the areas of energy storage, electric drive systems, lightweight materials, and auxiliary load reductions. DOE announced the selection of 38 awards from the FOA in September 2013. These projects, which were initiated in September 2013, will be described in more detail in next year's annual report, are as follows:

In the area of advanced lightweighting materials R&D, 15 projects were awarded, representing a DOE investment of \$10.2 million. Advanced materials are essential for reducing PEV weight, thereby reducing the size of the battery and electric drive system and extending the electric driving range of PEVs. These projects will conduct research on lightweight materials— such as advanced high-strength steel, magnesium and aluminum—that allow vehicle manufacturers to include electric drive components, electronic systems and emissions control equipment without increasing vehicle weight.

## III.0 AUTOMOTIVE METALS

### III.1. R&D Fundamental Study of the Relationship of Austenite-Ferrite Transformation Details to Austenite Retention in Carbon Steels—Oak Ridge National Laboratory (ORNL)

#### Zhili Feng (Principle Investigator)

Oak Ridge National Laboratory  
One Bethel Valley Road  
P.O. Box 2008, MS-6096  
Oak Ridge, TN 37831  
Phone: (865) 576-3797; Fax: (865) 574-4928  
E-mail: [fengz@ornl.gov](mailto:fengz@ornl.gov)

#### William Joost, Technology Area Development Manager

U.S. Department of Energy  
1000 Independence Avenue, S.W.  
Washington, DC 20585  
Phone: (202) 287-6020; Fax: (202) 856-2476  
E-mail: [William.Joost@ee.doe.gov](mailto:William.Joost@ee.doe.gov)

#### Partners:

Advanced Photon Source: Wenjun Liu, Ruqing Xu  
University of Tokyo: Mayumi Ojima, Junya Inoue,  
Toshihiko Koseki  
ORNL: Zhenzhen Yu, John Michael Vitek,  
Rozaliya Barabash

Contractor: Oak Ridge National Laboratory  
(ORNL)  
Contract No.: DE-AC05-00OR22725

#### Abstract/Executive Summary

The Advanced Photon Source and the Spallation Neutron Source (SNS), two of the most advanced materials characterization facilities available through the U.S. Department of Energy Office of Science, were used to characterize in situ (1) the austenite-ferrite phase transformation behavior under the rapid heating/cooling conditions typical of modern sheet steel production and (2) the microscopic deformation and failure processes in dual-phase advanced high-strength steels (AHSSs) and multilayered composite steels. In FY 2013, in situ neutron experiments were conducted at Oak Ridge National Laboratory's (ORNL) SNS for various heating and cooling conditions, focusing on the austenite formation kinetics and the effects of diffusion and homogenization of alloying elements on the transformation, which is a key variable in production of the first-generation AHSSs and the design of some third-generation AHSSs. A number of intriguing observations were obtained in the in situ

phase transformation experiments. For example, the experimental results seemed to suggest that the formation of austenite depends on both the heating rate and the initial microstructure. A phase transformation model for the non-equilibrium formation of austenite in the inter-critical temperature region was developed and applied to the steel experimentally studied, DP980, to correlate with the in situ neutron diffraction results to provide a fundamental understanding of the formation of austenite in dual-phase steels. This effort enables quantitative prediction on the effect of both heating rate and initial microstructure on the kinetics of non-equilibrium austenite formation.

Also in FY 2013, in collaboration with University of Tokyo, the synchrotron x-ray *micro-diffraction* technique was used to study the strain/stress partitioning of multilayer steel during tensile loading. This technique makes it possible to probe in situ the three-dimensional "distribution" of the microscopic strain distribution *within* the individual grains, thereby providing insights on the microscopic deformation incompatibility and stress partitioning between the hard and soft phases.

#### Accomplishments

- Successfully combined the in situ neutron diffraction measurement and numerical simulation to understand the non-equilibrium allotropic phase transformation behavior during inter-critical temperature annealing of a dual-phase AHSS DP980. (FY 2013)
- Investigated the stress partition and deformation inhomogeneity at both macro- and micro-scales in the newly developed multilayered composite steel during tensile loading. The respective advantages of in situ neutron diffraction and synchrotron x-ray micro-diffraction techniques were used to gain understanding of the mechanisms governing the exceptional combination of high strength and ductility in the composite steel. (FY 2013)

#### Future Directions

- Apply the novel experimental approach developed in this project to probe in situ the non-equilibrium allotropic phase transformations in AHSS under fast transient heating and cooling conditions relevant to steelmaking and auto-body structure manufacturing and joining.
- Correlate the in situ neutron and synchrotron experimental findings on deformation behavior with the polycrystalline

plasticity deformation and formability model for selected AHSSs.

### Technology Assessment

- Target: Develop science-based knowledge base and solutions to enable the development of future generation AHSSs (generation III (Gen III) and beyond) and the application (forming and joining) of the current generation of AHSSs.
- Gap: Fundamental understandings of the non-equilibrium phase transformation kinetics and the microscopic deformation incompatibility in AHSSs are quite limited.



### Introduction

Steel is an important material for body construction of motor vehicles. Generation I (Gen I) AHSSs are used greatly in today's vehicles with excellent crash management and other safety benefits, while offering considerable weight reduction opportunities. The steel research and development community is pursuing third generation (Gen III) AHSSs that will offer even greater potential for weight reduction and safety enhancement with manufacturability and affordability acceptable for future generation vehicles. The Gen III AHSSs would have the specific strength (strength-to-weight ratio) on a par with or even higher than those of aluminum alloys and magnesium alloys. Controlling cost will likely require that the Gen III AHSSs be no more than modestly alloyed compared to Gen I AHSSs and capable of being produced within existing steel mill infrastructures.

The Gen I AHSSs and several promising Gen III AHSS concepts rely on allotropic phase transformation (i.e., decomposition of austenite to various low temperature phases) and solution strengthening to achieve a balance of strength and ductility. This approach stems from the unique and versatile phase transformation characteristics of the Fe-C alloy system: by varying the amounts of alloying elements and controlling the thermo-mechanical processing routes in steel making, the volume fraction, grain size, and morphologies of different phases can be tailored to meet the strength and ductility specifications of different grades of steels. The resultant microstructures produced in such manner are essentially a mixture of hard phases such as martensite/bainite and soft phases such as ferrite/retained austenite, with the sizes of the constituent phases on the order of micrometers ( $10^{-5}$ – $10^{-6}$  m). Such dual phase AHSSs exhibit greatly improved strength. However, the ductility of the AHSSs sometimes falls far less than the rule of mixtures because of the incompatible deformation phenomenon. Under load, plastic strains are preferably accumulated in the soft phase grains under continuous loading. The localized strain concentration in soft phase grains causes nucleation and coalescence of micro-voids at the grain boundaries, which accelerates fracture during deformation.

The primary aim of this project is to use unique facilities like the Advanced Photon Source (APS) and the Spallation

Neutron Source (SNS), available through the U.S. Department of Energy Office of Science, to in situ characterize (1) the austenite-ferrite phase transformation behavior under the rapid heating/cooling conditions typical of modern sheet steel production and (2) microscopic and macroscopic deformation and failure processes in dual phase AHSSs and multilayered composite steels. The fundamental knowledge on the phase transformation and deformation/failure will provide the scientific underpinnings to support the on-going development of Gen III AHSSs at steelmakers, auto original equipment manufacturers (OEMs), and research organizations.

### Approach

AHSSs use highly engineered and carefully controlled thermo-mechanical processing routes to achieve the desired microstructures<sup>1</sup>. The phase transformation processes are complex and non-equilibrium in nature, and knowledge of the kinetics is very limited because of models to predict the influence of variants. A novel in situ neutron diffraction experimental approach was designed to directly measure and quantify the non-equilibrium phase transformation processes in bulk materials with sub-second temporal resolution under the fast heating and cooling conditions representative of AHSS thermo-mechanical processing<sup>2,3</sup>. The use of deep penetration neutrons eliminates the complications of the surface effects experienced in x-ray experiments. Furthermore, neutron diffraction directly detects and measures the different phases present in the material to eliminate the uncertainties in dilatometer measurement caused by the alloying element concentration induced volumetric changes associated with the non-equilibrium phase transformation<sup>3</sup>. In situ neutron experiments were conducted at the SNS at ORNL under various heating and cooling conditions, focusing on the heating austenite formation kinetics and the effects of diffusion and homogenization of alloying elements on the transformation, which is a key variable in production of the Gen-I AHSSs and the design of some Gen III AHSSs.

In FY 2013, a phase transformation model for the formation of austenite of dual-phase steels in the intercritical temperature region was developed based on computational thermodynamics software for diffusion controlled transformations (DICTRA). This model was used to correlate with the in situ neutron diffraction results to provide the fundamental insights on the diffusion-controlled carbon partitioning on formation of austenite in dual-phase steels.

There have been a number of studies on the macroscopic strain/stress partitioning between different phase constituents in polycrystalline alloys. For example, in situ synchrotron x-ray and neutron diffraction experiments measure the lattice strains of the respective constituent phases at different stress levels. Since the gage volume typically ranges from  $\text{mm}^3$  to  $\text{cm}^3$ , the lattice strains measured from these diffraction experiments are macroscopic ones averaged over hundreds to thousands grains. They are unable to resolve the microscopic strain variations inside a grain. In this work, the synchrotron x-ray micro-diffraction technique was used to probe, in situ, the three-dimensional (3D) "distribution" of the microscopic strain distribution in a newly developed multilayered composite steel

with an exceptional combination of high strength and ductility<sup>4</sup> under tensile loading to provide insights on the stress partitioning between the soft and hard layers, especially in the vicinity of layer interface. A special differential aperture x-ray microscopy technique was applied to probe the microscopic deformation process underneath the surface<sup>5,6</sup>. The basis experimental setup is shown in Figure III-1. The in situ microscopic deformation study was conducted at the high-energy x-ray micro-diffraction beam 34 ID-E beam line of the APS at Argonne National Laboratory. The macroscopic strain level within the sample gage section was determined by digital imaging correlation method.

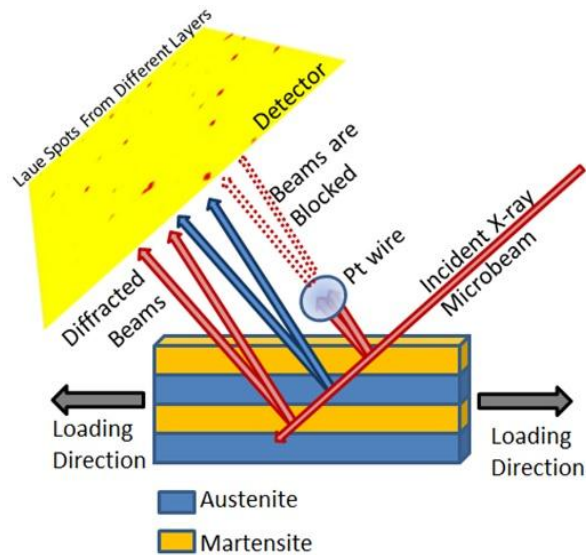


Figure III-1: Schematic diagram of the three-dimensional (3D) micro-diffraction. The beam is incident at 45° to the sample surface. Diffracted beams are collected at the detector.

## Results and Discussion

**The non-equilibrium phase transformation behavior.** The in situ neutron diffraction measurement of the on-heating phase transformation in the intercritical temperature region is shown in Figure III-2. A number of intriguing observations were obtained. The experimental results revealed that the formation of austenite depends on both the heating rate and the initial microstructure.

The as-received DP980 steel had a mixture of martensite and ferrite phases. Based on scanning electron microscopy, the martensite plate spacing was about 0.5  $\mu\text{m}$ , which can be considered as the spacing for the nucleation and growth of austenite in the model. To evaluate the effect of initial microstructure on the kinetics of non-equilibrium phase transformation, the DP980 steel was subjected to a heat treatment to increase the spacing up to  $\sim 2 \mu\text{m}$ . This resulted in a noticeable change in the kinetics of austenite formation at the 30°C/s heating rate but not for the case of the 3°C/s heating rate.

A phase transformation model for the formation of austenite of dual-phase steels in the intercritical temperature region was developed to help understand the phase transformation kinetics and elucidate the influence of initial microstructure and thermo-mechanical process variants. In this model, the overall austenite formation can be divided into three stages in sequential order: (1) tempered martensite (ferrite + carbide) transforming to austenite; (2) when carbide is completely dissolved, residual ferrite in tempered martensite transforming to austenite; and (3) carbon-poor pro-eutectoid ferrite to austenite. The continuous dilution of carbon concentration in austenite grains during growth explains the continuous decrease in austenite lattice spacing in the early stage of phase transformation observed by in situ neutron diffraction measurement<sup>3,7</sup>, which was also reported in the FY 2012 annual report.

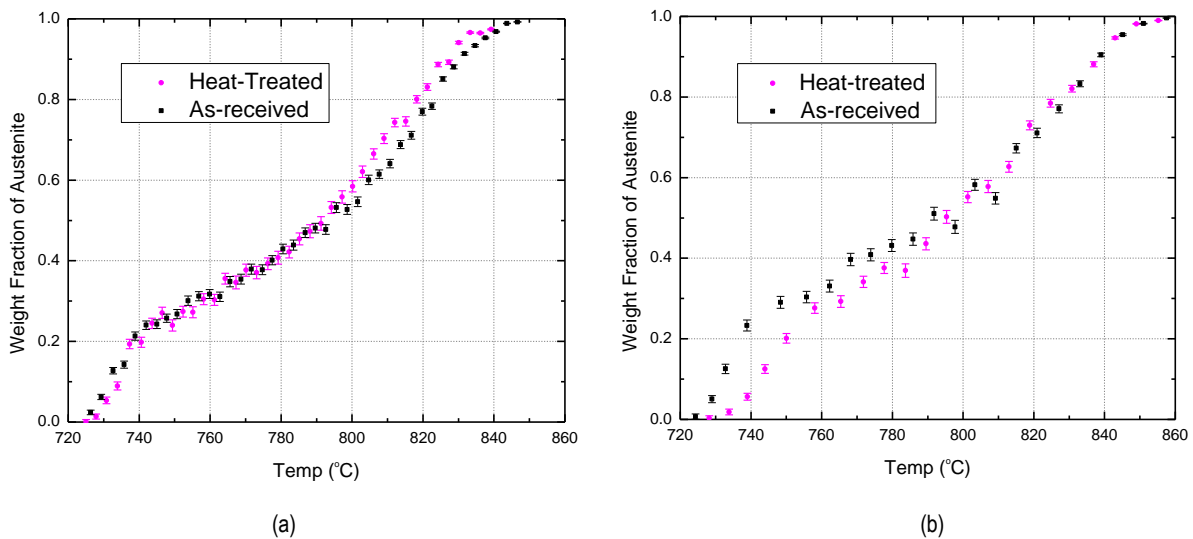


Figure III-2: The effect of initial microstructure and heating rate on the non-equilibrium ferrite/martensite ( $\alpha+\alpha_M$ ) to austenite ( $\gamma$ ) transformation in a DP980 steel observed by in situ neutron diffraction measurement. (a) 3°C/s heating rate, (b) 30°C/s heating rate.

The model predictions are summarized in Figure III-3. Overall, the model compared well with the in situ neutron diffraction results on the effects of both heating rate and the initial microstructure. More importantly, with the validity of the model verified by the in situ measurement, the model was used to gain some fundamental insights on the on-heating austenite formation in AHSSs. The model reveals that the nucleation and growth rates of austenite are much faster within tempered martensite than those in ferrite. Also, the phase transformation rate at stages I and II were strongly dependent on the martensite plate spacing. More specifically,

Figure III-3 shows the comparison of two heating rates, 3°C/s and 30°C/s. Under the slower heating rate, carbon diffusion is so fast that the martensite plate spacing does not have much influence. Under fast heating conditions (commonly associated with manufacturing and welding processes), the corresponding temperature increases by ~35°C as the martensite plate spacing increases from 0.05 to 2 μm for 50% of the complete phase transformation. Such information is critical for the process parameter design in the development and application of AHSSs.

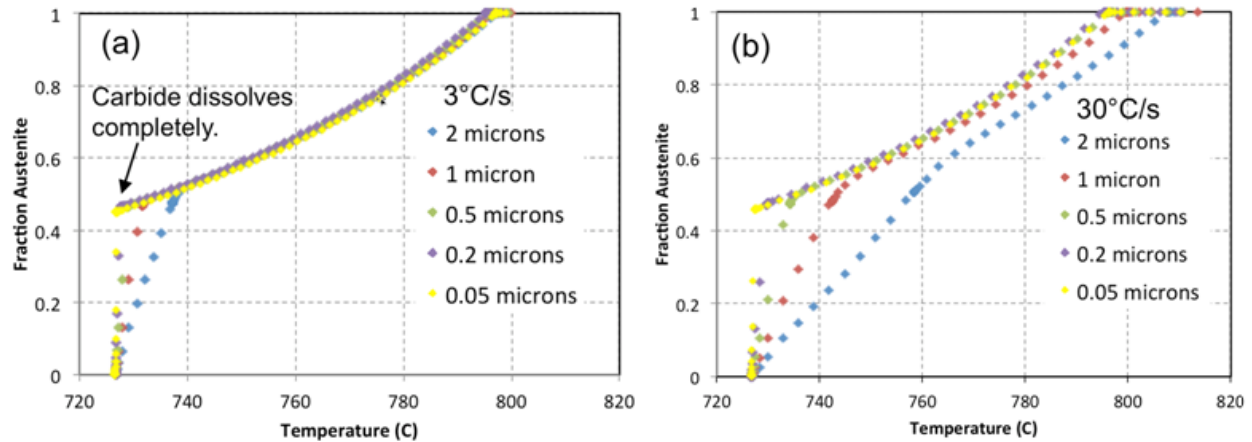


Figure III-3: The effect of heating rate on the non-equilibrium phase transformation in tempered martensite predicted by the phase transformation model developed in this project.

*In situ probing of microscopic deformation in multilayered steel.* Recently, multilayered composite steels consisting of alternating layers of hard and soft phases were developed by the University of Tokyo, Japan (collaborator in this project)<sup>4,8</sup>. The composite steels exhibit an excellent combination of high strength and ductility (Figure III-4), far beyond the general strength and ductility trade-off relationship in conventional AHSSs<sup>9</sup>. The deformation mechanisms governing such

mechanical behavior have not yet been fully understood, especially the stress partition kinetics at the layer interfaces. The micro-diffraction beam facility at APS allowed the investigation of microscopic strain/stress partitioning between the martensite and austenite layers in the multilayered composite steel during incremental tensile loading in the vicinity of layer interface.

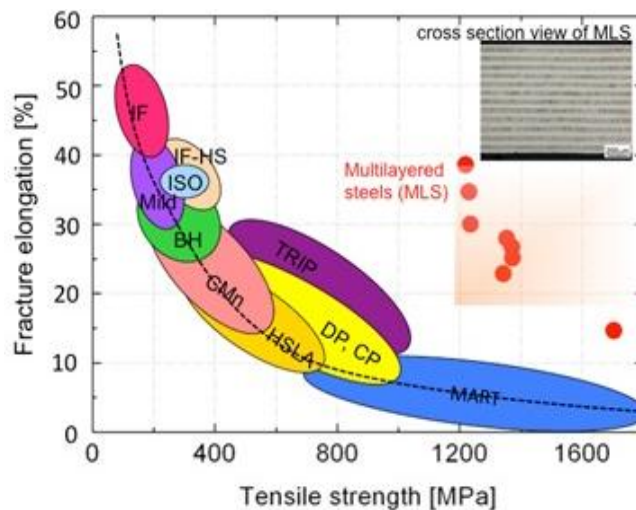


Figure III-4: The relationship between fracture elongation and yield strength in steels and fabricated multilayered steels.

Data from the in situ micro-diffraction deformation experiment are still being analyzed. Figure III-5 and Figure III-6 provide an initial glance of the results. In Figure III-5, the depth-dependent inverse lattice parameters  $Q_{hkl}$  are plotted as a function of the depth from the martensite/austenite interface in the austenite layer before loading (load 0) and under loading to a global strain level of 0.26% (load 2).  $Q_{hkl}$  can be considered as the inverse interatomic spacing for a certain crystallographic direction ( $hkl$ ):  $Q_{hkl} = 2\pi/d_{hkl}$ . Dotted lines represent the reference bulk martensite or austenite inverse lattice parameter. As shown in the figure, large strain gradient was observed in the austenite layer before loading. Compressive strain was observed in the austenite layer near the martensite/austenite interfaces in the as-manufactured composite steel since martensitic transformation involves significant volume expansion during quenching. During loading to a global strain level of 0.26%, strain distribution in the austenite layer becomes more homogeneous (Figure III-5b). Before and during loading, there was no significant change in the full width at half maximum (FWHM) of the intensity distributions (Figure III-5c and Figure III-5d) in the austenite layer. On the contrary, in the martensite layer, the FWHM of the intensity distributions at the very top of the martensite layer doubles under load 2 (e.g.,

comparing curve “1” in Figure III-6c and Figure III-6d), indicating the formation of strains and dislocations in the martensite layer during loading.

The preliminary findings from the in situ micro-diffraction deformation study suggest that during loading strains partitioned between martensite and austenite layers because of their differences in the capacity of plastic deformation. Austenite lattice has a significantly lower elastic limit compared with martensite. As a result, austenite grains located near the interfaces are very likely to deform plastically, while martensite grains are under elastic deformation. The strong bonding strength at the interface is the main reason for the effective stress partition, leading to the excellent combination of high strength and ductility.’

### Technology Transfer Path

The fundamental knowledge on the phase transformation and deformation/failure gained in this project will provide the scientific underpinnings to support the on-going development of Gen III AHSSs at steelmakers, auto OEMs, and research organizations.

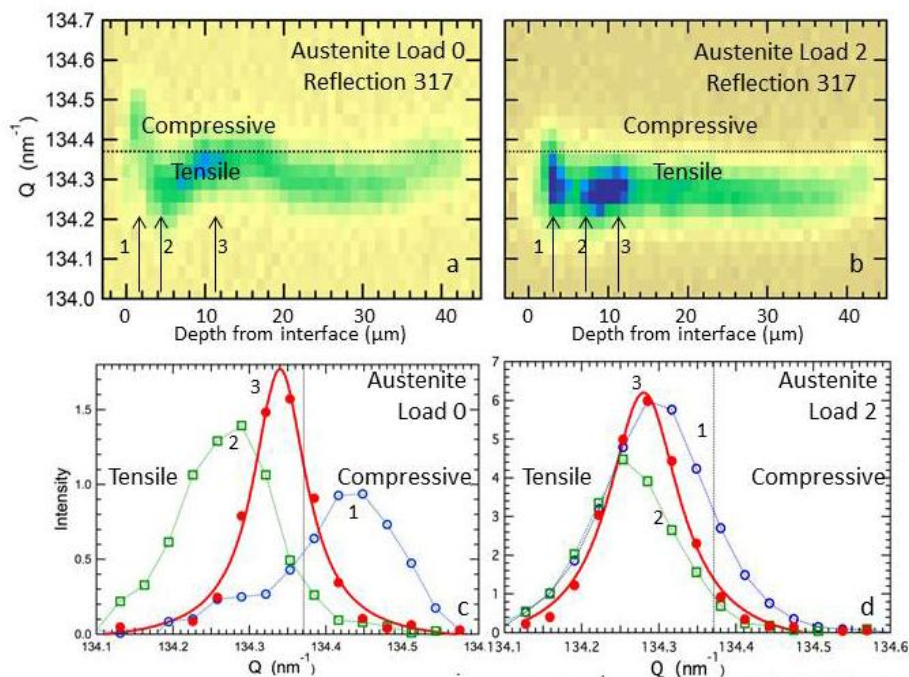


Figure III-5: Depth-dependent inverse lattice parameter  $Q_{317}$  for austenite layer at load 0 (a) and under load 2 (b) and intensity profiles at three different depths at load 0 (c) and at load 2 (d). The depths are shown by arrows in the (a) and (b) frames. Depth along the beam for the austenite layer is from the martensite/austenite interface. Vertical dashed lines in (c) and (d) and horizontal dashed lines in (a) and (b) mark the reference  $Q$  value for the austenite.

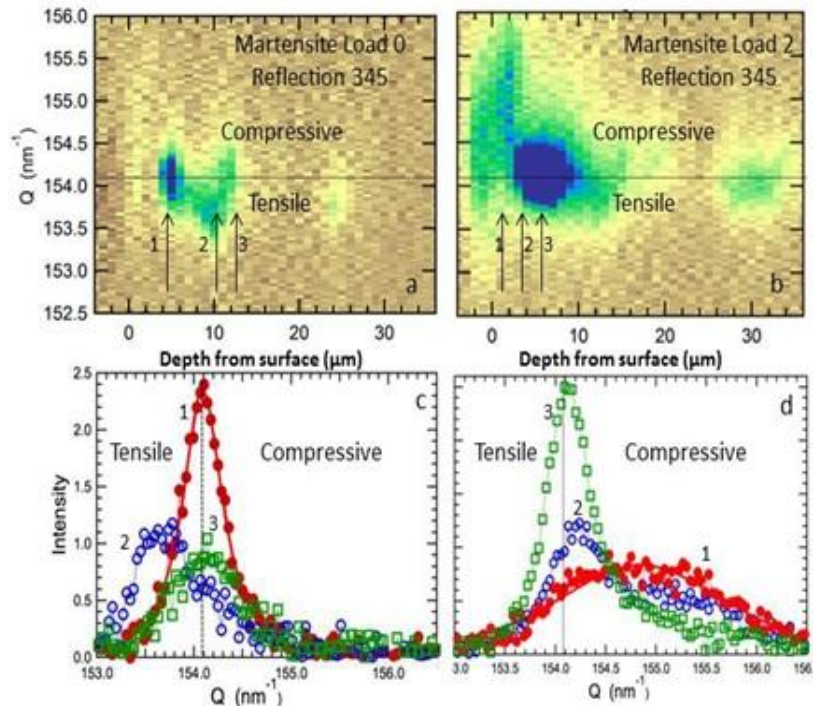


Figure III-6: Depth-dependent inverse lattice parameter  $Q_{345}$  for martensite top layer at load 0 (a) and under load 2 (b) and intensity profiles at three different depths at load 0 (c) and at load 2 (d). The depths are shown by arrows in the (a) and (b) frames. Depth along the beam for the top martensite layer is from the sample surface. Vertical dashed lines in (c) and (d) and horizontal dashed lines in (a) and (b) mark the reference  $Q$  value for the martensite sample.

## Conclusion

In FY 2013, the on-heating phase transformation in the intercritical temperature region of a dual-phase AHSS was successfully performed by in situ neutron diffraction and non-equilibrium phase transformation modeling. The effect of initial microstructure and heating conditions on the phase transformation behavior and the controlling kinetics were revealed. Synchrotron micro-beam diffraction experiments provided direct experimental evidence that highly nonuniform microscopic strain distribution develops within the multilayered composite steel during tensile loading. The strong bonding at the interface leads to the exceptional combination of high-strength ductility in the composite steels. Such efforts provide important insights for the development of next-generation AHSSs.

## Presentations/Publications/Patents

- Barabash, R.; Barabash, O.; Ojima, M.; Yu, Z.; Inoue, I.; Nambu, S.; Koseki, T.; Xu, R.; Feng, Z. 2013. Interphase Strain Gradients in Multilayered Steel Composite from Microdiffraction. *Met Mat Trans A*, DOI 10.1007/s11661-013-2100-5.
- Yu, Z.; Feng, Z.; An, K.; Yang, L.; Zhang, W.; Wang, Y. et al., 2013. In-situ Neutron Diffraction Study of Microscopic Deformation Processes and the Microstructure Effect in Advanced High-Strength Steels.

Invited Talk in *TMS 142nd Annual Meeting & Exhibition*; San Antonio, TX, Mar. 3-7.

- Yu, Z.; Barabash, R.; Barabash, O.; Liu, W.; Feng, Z. 2013. In-situ Probing of Microscopic Deformation Kinetics in Advanced High-Strength Steels. In *TMS 142nd Annual Meeting & Exhibition*; San Antonio, TX, Mar. 3-7. First prize of Yong Professional Poster Competition.

## References

- Wagoner, R.H. *Advanced High Strength Steel Workshop, organized jointly by National Science Foundation, Department of Energy and AISI*; Arlington, VA, Oct 23-26, 2006.
- Feng, Z. *Material Degradation Phenomena and Mitigation For Nuclear Reactor Life Extension, LDRD Program*, Oak Ridge National Laboratory, 2011.
- Yu, Z.; Feng, Z.; An, K.; Zhang, W.; Specht, E.D.; Chen, J.; Wang, X.L.; David, S. Comparative Study of Steel Phase Transformation Behavior by Dilatometry Method and In-Situ Neutron Diffraction. *Proc. 9th Int. Conference on Trends in Welding Research*; Chicago, IL, 2012.
- Inoue, J, Nambu, S, Ishimoto, Y, and Koseki, T, 2008. *Fracture elongation of brittle/ductile multilayered steel composites with a strong interface*. *Scripta Materialia*, 59(10):1055-1058

5. Larson, B.C.; Yang, W.; Ice, G.E.; Budai, J.D.; Tischler, J.Z. Three-dimensional X-ray structural microscopy with submicrometre resolution. *Nature* **2002**, *415*, pp. 887-890.
6. Liu, W.J.; Ice, G.E.; Larson, B.C.; Yang, W.G.; Tischler, J.Z.; Budai, J.D. The three-dimensional X-ray crystal microscope: A new tool for materials characterization. *Metall Mater Trans A* **2004**, *35A*, pp. 1963-1967.
7. Yu, Z.; Feng, Z.; Woo, W.; David, S. Application of In Situ Neutron Diffraction to Characterize Transient Material Behavior in Welding. *JOM* **2013**, *65*, pp.65-72.
8. Ojima, M.; Inoue, J.; Nambu, S.; Xu, P.; Akita, K.; Suzuki, H.; Koseki, T. Stress partitioning behavior of multilayered steels during tensile deformation measured by in situ neutron diffraction. *Scripta Mater.* **2012**, *66*, pp. 139-142.
9. Matlock, D.K. in Advanced High Strength Steel Workshop, *organized jointly by National Science Foundation, Department of Energy and AISI*: Arlington, VA, Oct 23-26, 2006.

## III.2. Properties and Manufacturability—Pacific Northwest National Laboratory (PNNL)

### **Dean Paxton, Field Technical Monitor**

Pacific Northwest National Laboratory  
902 Battelle Boulevard  
P.O. Box 999  
Richland, WA 99352  
Phone: (509) 375-2620  
E-mail: [dean.paxton@pnnl.gov](mailto:dean.paxton@pnnl.gov)

### **William Joost, Technology Area Development Manager**

U.S. Department of Energy  
1000 Independence Avenue, S.W.  
Washington, DC 20585  
Phone: (202) 287-6020  
E-mail: [william.joost@ee.doe.gov](mailto:william.joost@ee.doe.gov)

Contractor: Pacific Northwest National Laboratory  
(PNNL)  
Contract No.: DE-AC05-00OR22725 & DE-AC06-  
76RLO1830

### **Executive Summary**

The Properties and Manufacturability project consists of six tasks focused on research and development (R&D) activities advancing the basic mechanical properties, manufacturability, and cost of lightweight materials towards the levels needed for increased implementation in automotive applications. These tasks include the following:

- Microstructure and Deformation Fundamentals in Advanced Lightweight Materials
- Enhanced Room-Temperature Formability in High-Strength Aluminum Alloys Through Pulse Pressure Forming
- Aluminum Formability Extension Through Superior Blanking Process
- Non-Rare Earth High-Performance Wrought Magnesium (Mg) Alloys
- Mg Intensive Vehicle Developments
- Aerodynamic Lightweight Cab Structures

The following sections outline specific task work conducted at PNNL in the area of properties and manufacturability of lightweight metals. Each task supports one or more goals within the Properties and Manufacturability Agreement as outlined below.

## ACTIVITY AND DEVELOPMENTS

### Microstructure and Deformation Fundamentals in Advanced Lightweight Materials

#### Xin Sun (Principal Investigator)

Pacific Northwest National Laboratory  
Phone: (509) 372-6489; Fax: (509) 372-6099  
E-mail: [xin.sun@pnnl.gov](mailto:xin.sun@pnnl.gov)

#### David K. Matlock and John Speer (Principal Investigators)

Advanced Steel Processing and Products  
Research Center  
Colorado School of Mines  
Phone: (303) 273-3775; Fax: (303) 273-3016  
E-mail: [dmatlock@mines.edu](mailto:dmatlock@mines.edu)  
Phone: (303) 273-3897; Fax: (303) 273-3016  
E-mail: [jspeer@mines.edu](mailto:jspeer@mines.edu)

#### Accomplishments

- Completed electron backscattered diffraction (EBSD) test on the first heat quenching and partitioning (Q&P) steels to distinguish the phase fractions and morphologies. (FY 2013)
- Completed nano-indentation test with the first heat Q&P steels to quantify hardness differences for different phases. (FY 2013)
- Completed in-situ high-energy x-ray diffraction (HEXRD) test under uniaxial tensile condition with the first heat Q&P steels to determine the phase properties and austenite transformation kinetics. (FY 2013)
- Performed microstructure-based finite element analyses (FEA) on the first heat Q&P steels for property prediction and identified possible directions for property improvements. (FY 2013)
- Produced the second heat Q&P steels based on computational results for the first heat Q&P steels and completed tensile tests. (FY 2013)

#### Future Directions

- Develop a self-consistent viscoplasticity approach to determine the mechanical properties (i.e., phase stress-strain curves) of the constituent phases.
- Perform secondary ion mass spectrometry (SIMS) test on the Q&P steels to quantify C partition between retained austenite and the matrix phases for different partitioning time and duration.
- Perform further experiments and analyses with the second heat Q&P steels to understand the effects of heat-treating

parameters on the materials' phase properties and macroscopic properties.

- Develop new processing parameters based on the above results for further property improvement and produce the third heat steels.

#### Technology Assessment

- Target: Develop a 3<sup>rd</sup> generation advanced high-strength steel (3GAHSS) product with 1200 MPa ultimate tensile strength (UTS) and 30 percent total elongation.
- Gap: Reduced alloying and lower cost are important considerations for the development of 3GAHSS. In addition, automotive steel industry still lacks and overall understandings on key material parameters controlling the mechanical properties of AHSS.



#### Introduction

AHSS represent an important technology in efforts to reduce vehicle weight for improved fuel-efficiency and occupant safety. These steels have evolved with new alloying and processing strategies to tailor microstructures containing various mixtures of ferrite, martensite, bainite, and retained austenite. Following previous development of first and second generation AHSS, 3GAHSS concepts are being pursued to identify lower alloy steels that achieve ultra-high-strength properties in combination with formability sufficient for implementation in automotive production. Relative to the second generation steels, reduced alloying and lower cost are the focuses of these steels.

This project is focused on experiments and theoretical analyses based on microstructural-based modeling designed to improve the overall understanding of the variables which control austenite stability against straining, and thus mechanical properties of new AHSS products. The results of these analyses will be used to accelerate the development of 3GAHSS products. Steels with 1200 MPa UTS and 30 percent total elongation will be the property goal, along with a consideration of cost target of this class of material anticipated by the global automotive and steel industry. The proposed effort will also focus on improved understanding of the relationship between AHSS microstructural features and the effects of microstructure on global and local deformation mechanisms. Thus 3GAHSS developed in this effort will possess good localized deformation capacity for automotive forming and trimming operations.

## Approach

Because the Q&P process has been identified as a potential process to generate 3GAHSS properties (De Moor et al., 2011), the first round of material development focused on Q&P steels. In FY 2012, four different types of Q&P tensile samples which may be in 3GAHSS property range were produced based on the different chemical compositions and heat-treating parameters shown in Table III-1. Tensile test results for these steels are shown in Figure III-7. Based on the tensile test results and microstructure analyses (i.e., scanning electron microscopy (SEM)), MAT1–3 were selected for further experiments and analyses.

**Table III-1: Heat-treating parameters for four different first heat Q&P steels (MAT1–4).**

| Name | Chemistry      | Annealing (°C/sec) | Quenching (°C/sec) | Partitioning (°C/sec) |
|------|----------------|--------------------|--------------------|-----------------------|
| MAT1 | 0.3C-3Mn-1.6Si | 820/120            | 180/10             | 400/100               |
| MAT2 | 0.2C-3Mn-1.6Si | 840/120            | 250/10             | 400/10                |
| MAT3 | 0.2C-3Mn-1.6Si | 840/120            | 250/10             | 400/100               |
| MAT4 | 0.2C-3Mn-1.6Si | 725/120            | 185/10             | 450/10                |

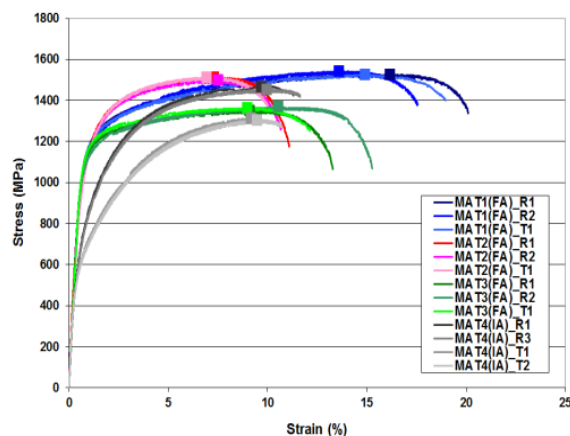


**Figure III-7: Stress-strain curves for the first heat Q&P steels.**

EBSD has been performed on the selected Q&P steels for quantifying different phase volume fractions. The orientation map and phase map from EBSD were used together with the SEM images for the same location in generating the microstructure-based finite element models of the Q&P steels. Nano-indentation tests were then performed with the selected Q&P steels to quantify the hardness values of the different constituent phases. The hardness data obtained from indentation tests were used to estimate the mechanical properties (i.e., phase stress-strain curves) of the constituent phases at the initial stage of the microstructure-based FEA. In a parallel effort, in-situ HEXRD tests under a uniaxial tensile condition were performed with the selected Q&P steels to obtain the volume fraction evolution of the austenite phase during the deformation process as well as to determine the mechanical properties for the constituent phases. A self-consistent viscoplasticity approach is currently being

developed to determine the mechanical properties of the constituent phases with improved accuracy. The phase mechanical properties determined with HEXRD can be compared with the hardness data from nano-indentation to establish possible correlations.

Next, microstructure-based FEA was performed for the selected Q&P steels. The input material parameters (e.g., phase mechanical properties, austenite stability) were determined by adjusting the initial values obtained from the tests (i.e., nano-indentation, HEXRD) and fitting the macroscopic response of the model to the experiments. Subsequently, the effects of various material parameters were computationally investigated to identify possible directions for property improvements. The second heat Q&P steels were produced based on the information from the computational investigation on the first heat Q&P steels.

## Results and Discussion

Figure III-8 shows the results obtained from nano-indentation tests with MAT1–3. As shown in Figure III-8(a), MAT1–3 shows different hardness distributions. For example, the constituents in MAT1 are, in general, softer than those in MAT3 (See also Figure III-8 (c)). As different features (i.e., A-D in Figure III-8(b)), depending on the etching response of each grain, were observed from the microstructures, average hardness values were obtained for the different features of MAT1–3 and plotted in Figure III-8(c). The average hardness values for the different features were used as initial information on the possible mechanical properties of some of the constituent phases (i.e., austenite, tempered martensite, untempered martensite) for the microstructure-based FEA. Figure III-9 (a) shows the experimental setup for the in-situ HEXRD tests under uniaxial tensile condition and some examples of results obtained for MAT1 (Figure III-9 (b)) and MAT2 (Figure III-9 (c)). As shown in Figure III-9, phase stress-macro strain curves were first obtained and then used as an approximation of the input mechanical properties for all of the constituent phases of the FEA. A self-consistent viscoplasticity approach is currently under development to determine the phase stress-strain curves for the constituents. Note in Figure III-9(b) and Figure III-9(c) that the austenite phase transforms gradually with the deformation process, which helps to enhance the ductility of these high-strength Q&P steels.

Figure III-10 shows the example of microstructure-based finite element (FE) modeling process of the complex-structured Q&P steels starting with the SEM image (Figure III-10(a)). First, an orientation map (Figure III-104(b)) from EBSD was used to generate the microstructure-based FE model. Phase maps (Figure III-10(c)) from EBSD and SEM images for the same location were then used to designate the austenite and untempered martensite, respectively, within the model. Nano-indentation results in Figure III-8(a) indicate that MAT1 has some soft grains (i.e., hardness: 2–4 GPa). These soft grains were considered in the model as the bainite grains (see Figure III-10(d)). Figure III-11 (a) shows the set of mechanical properties of the phases and

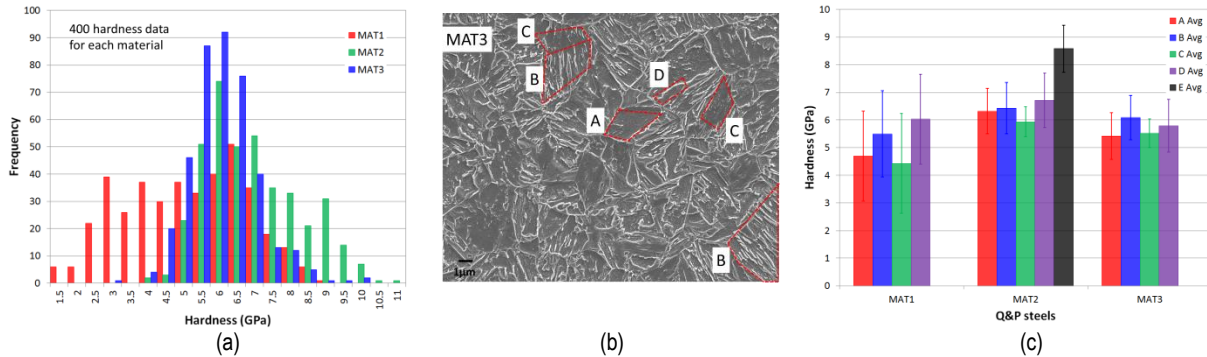


Figure III-8: (a) Histogram of 400 hardness data obtained from nano-indentation tests of MAT1–3, (b) different features observed from the microstructures of Q&P steels, and (c) average hardness values for the different features of MAT1–3.

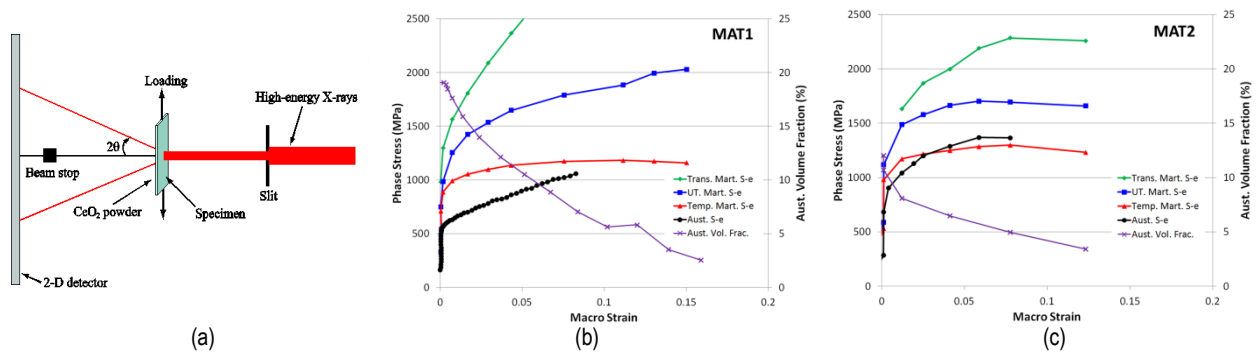


Figure III-9: (a) Schematic of experimental setup for in-situ HEXRD tests under uniaxial tension. Phase stresses and austenite transformation kinetics as function of macro strain for (b) MAT1 and (c) MAT2.

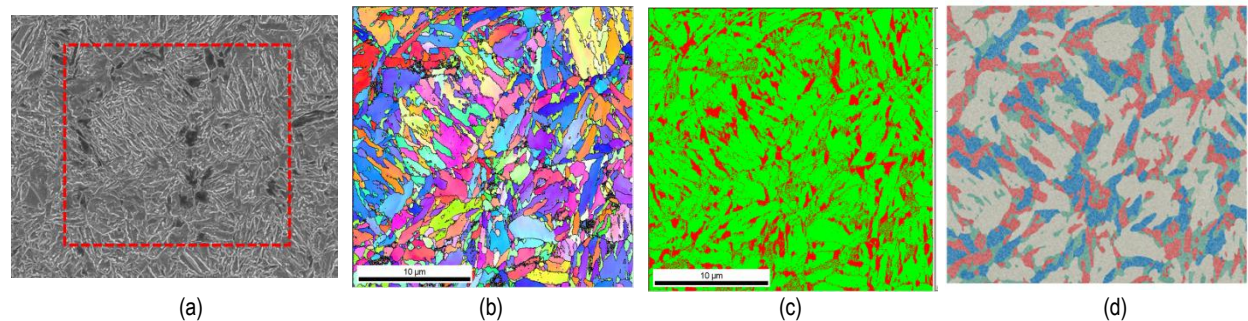


Figure III-10: Microstructures of MAT1. (a) SEM, (b) grain orientation map, (c) phase map and (d) finite element (FE) model (green: austenite(19%); red: untempered martensite(20%); grey: tempered martensite(44%); blue: bainite(18%).

austenite stability for MAT1 model, which were determined by adjusting the mechanical properties estimated from HEXRD tests (i.e., stress-strain curves in Figure III-9(b)) and fitting the macroscopic response of the model to the experiments, as shown in Figure III-11 (c). Note that the ultimate tensile strength (UTS) and elongation are of more interest in this study, and that initial yielding and hardening can be fitted to the experiment by fine tuning the initial plastic parts of mechanical properties of the constituent phases. The effects of various material parameters on the performance of Q&P steels were systematically investigated, and the results indicate that higher austenite stability ( $\Gamma_c$ ), less strength ( $K_i$ ) disparity between the phases, and higher hardening exponent ( $n_i$ ) of the matrix phases, etc. will help improve the overall properties. Figure III-11 (b) shows a new possible set of mechanical properties of the phases and austenite stability

based on computational results. Based on the MAT1 model, this new set of material parameters could result in improved properties as shown in Figure III 11(c).

New sets of Q&P heat-treating parameters were devised based on computational results of MAT1–3, and then applied to MAT1 (0.3C-3Mn-1.6Si) because this material showed the best property in the 3GAHSS property range. The second heat Q&P steels (i.e., MAT5–8) were produced and are listed in Table III-2. The new sets of heating parameters were used to increase the volume fraction and stability of austenite by varying quenching temperature, partitioning temperature, and time. As shown in Table III-2, according to x-ray diffraction (XRD) tests, three steels (i.e., MAT5, MAT6, and MAT8) have the high austenite volume fractions and high carbon

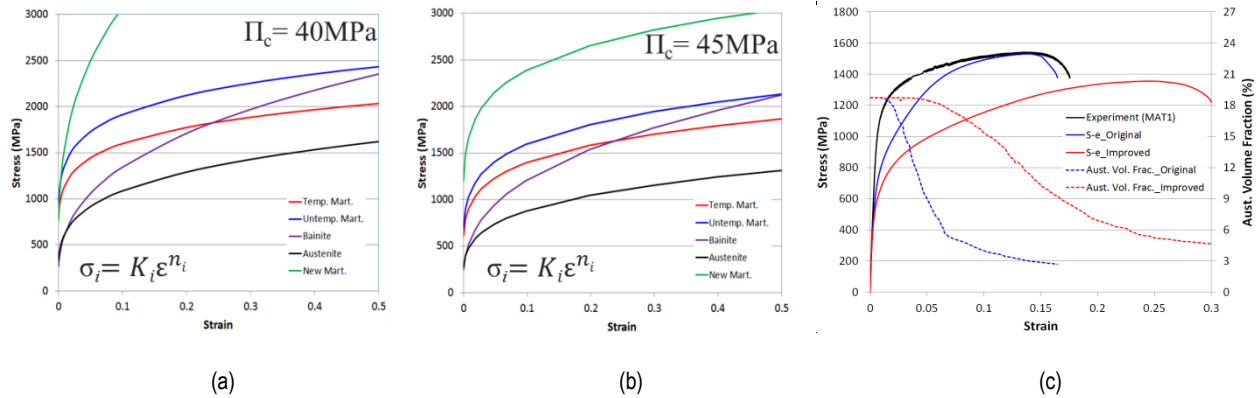
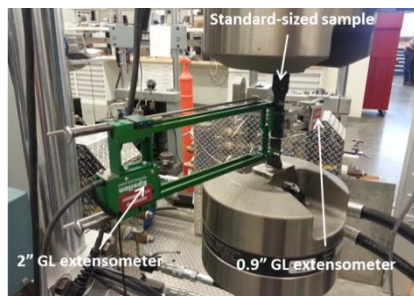


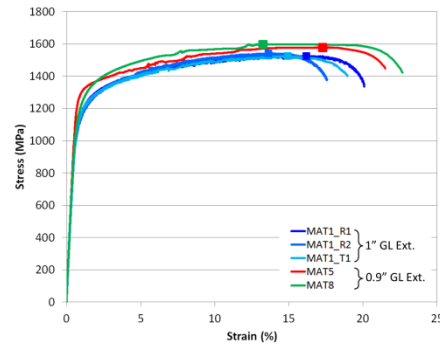
Figure III-11: (a) Original and (b) modified input stress-strain curves for the constituent phases and austenite stability ( $\Pi_c$ ) for MAT1 model and (c) comparison of macroscopic responses of MAT1 model based original and modified material parameters.

Table III-2. Heat-treating parameters for second heat Q&P steel samples (MAT5–8).

| Name | Chemistry      | Annealing (°C/sec) | Quenching (°C/sec) | Partitioning (°C/sec) | Retained Austenite (%) | Carbon Content (wt%) |
|------|----------------|--------------------|--------------------|-----------------------|------------------------|----------------------|
| MAT5 | 0.3C-3Mn-1.6Si | 820/120            | 180/10             | 425/100               | 25.2                   | 1.35                 |
| MAT6 | 0.3C-3Mn-1.6Si | 820/120            | 180/10             | 400/150               | 21.8                   | 1.39                 |
| MAT7 | 0.3C-3Mn-1.6Si | 820/120            | 180/10             | 375/100               | 6.9                    | 1.17                 |
| MAT8 | 0.3C-3Mn-1.6Si | 820/120            | 160/10             | 400/100               | 21.2                   | 1.28                 |



(a)



(b)

Figure III-12: (a) Tensile test setup for second heat Q&P steel samples and (b) comparison of stress-strain curves between MAT1, MAT5, and MAT8.

content in the austenite phase. Tensile tests were performed for the second heat Q&P steels. As shown in the test setup in Figure III-12(a), a small extensometer (i.e., 0.9" gauge length) was also used for measuring the strain to obtain comparable strain values to those found for first heat Q&P steels. Considering the slight difference in initial gauge length (i.e., 1" and 0.9" for first and second heat Q&P steels, respectively), the stress-strain curves for MAT5 and MAT8 in Figure III-12(b) still show improved total elongations (i.e., 2–3 percent) and increased UTS (i.e., ~50MPa). Additional experiments and analyses will be performed on MAT5 and MAT8 for further property improvement.

### Technology Transfer Path

The deliverables (procedures and data) of this project will be transferred to the original equipment manufacturer (OEM) participants and steel producers through the industry/university cooperative research center-Advanced Steel Processing and Products Research Center at Colorado School of Mines, during regularly scheduled semi-annual review meetings.

## Conclusions

Q&P steel was selected as the model steel for the development of 3GAHSS. In FY 2012, four different Q&P steels (i.e., first heat) were produced based on different chemical compositions and heat-treating parameters. Due to the small grain size and complex microstructures of the produced Q&P steels, various tests (e.g., SEM, EBSD, in-situ HEXRD, and nano-indentation) were performed to identify different phases and to find the mechanical strength of those phases. Test results were used in subsequent microstructure-based FEA to identify possible directions for property improvements. Computational results suggest that properties could be improved by realizing higher austenite stability, less strength disparity between the phases, and a higher hardening rate of the matrix phases. The second heat Q&P steels were produced based on the information from the computational results for the first heat Q&P steels. Two second heat Q&P steels show improved UTS and total elongation, possibly due to the increased austenite volume fraction and stability. This overall property improvement trend is quite encouraging. Additional experiments and analyses will allow further improvement in elongation and progress toward meeting specific project requirements.

## Presentations/Publications/Patents

1. Taylor, M.D., Choi, K.S., Sun, X., Matlock, D.K., Packard, C.E., Xu, L. and Barlat, F. Relationship between Micro- and Macro- Properties for Eight Commercial DP980 Steels. Submitted for publication in *Materials Science and Engineering A*, 2013.
2. Taylor, M.D., Matlock D.K., Speer J.G., and De Moor E. Effect of Microstructure on the Fracture Response of AHSS. In Semi-Annual Review Meeting of Advanced Steel Processing and Products Research Center, March 18-20, 2013, Golden, Colorado.
3. Taylor, M.D., Matlock D.K., Speer J.G. and De Moor E. Effect of Microstructure on the Fracture Response of AHSS. In Semi-Annual Review Meeting of Advanced Steel Processing and Products Research Center, September 23-25, 2013, Golden, Colorado.

## Reference

De Moor, E.; Speer, J.G., Matlock D.K., Kwak J.-H., and Lee S.B. Effect of Carbon and Manganese on the Quenching and Partitioning Response of CMnSi Steels. *ISIJ Intl.* **2011**, *51*, pp 137-144.

---

# Enhanced Room-Temperature Formability in High-Strength Aluminum Alloys Through Pulse-Pressure Forming (PPF)

---

## Richard W. Davies (Principal Investigator)

Pacific Northwest National Laboratory  
Phone: (509) 375-6474; Fax: (509) 375-6844  
E-mail: [rich.davies@pnnl.gov](mailto:rich.davies@pnnl.gov)

## Aashish Rohatgi (Principal Investigator)

Pacific Northwest National Laboratory  
Phone: (509) 372-6047; Fax: (509) 375-6448  
E-mail: [aashish.rohatgi@pnnl.gov](mailto:aashish.rohatgi@pnnl.gov)

- Gap: The strain-rates during PPF of sheet metals typically exceed 1000/s and the constitutive behavior of Al alloys can be quite different at strain-rates exceeding 1000/s, relative to their behavior at quasi-static rates. Further, PPF strain-rates can vary significantly during the course of deformation as a function of time and location on the workpiece. However, literature regarding strain-rates and strain-path during high-rate forming is generally lacking, which has hindered development of accurate and validated numerical models of high-rate forming processes.



## Accomplishments

- Demonstrated room-temperature formability improvements in AA7075-T6 through PPF to achieve safe major strains of ~20 percent (engineering) near plane-strain that are comparable to the strains predicted in a cold-stamped steel B-pillar.
- Constructed a theoretical forming limit diagram (FLD) of aluminum (Al) alloy AA7075-T6 as a function of strain-rate by using the constitutive data from the existing literature in combination with the Marciniak-Kuczynski method.

## Future Directions

Determine the formability of AA7075 in different tempers under pulse-pressure and quasi-static forming.

- Develop constitutive equations to describe the deformation behavior and formability of AA7075 in different tempers and under high strain-rates.
- Determine the combinations of initial temper, strain-rate during forming, and post-forming heat-treatment to achieve peak-aged (T6) equivalent strength in AA7075.
- Conduct a finite element model analysis to quantify the mass savings with the use of AA7075 in a candidate automotive part.

## Technology Assessment

- Target: Achieve 70 percent improvement in the room-temperature formability (near plane-strain) in 7xxx Al alloys.
- Gap: The room-temperature formability of Al alloys (e.g., 5xxx and 6xxx) in plane-strain typically does not exceed 25 percent while high-strength 7xxx alloys have almost no formability. An improvement of 70 percent or more can help make the formability of some Al alloys comparable to the formability of deep-drawing-quality steels, which possess plane-strain formability of ~45 percent. However, such formability enhancements in Al alloys are not possible without elevated temperatures due to their low strain-rate sensitivity at quasi-static rates during conventional room-temperature stamping.
- Target: Determine the strain, strain-rate, velocity, and strain-path of AA7075 as a function of time during PPF.

## Introduction

The goal of this project is to extend the room-temperature formability of high-strength Al alloys (e.g., 6xxx and 7xxx) to enable their use in structural automotive components conventionally made of steel. Such structural members are not typically fabricated in 6xxx and 7xxx Al alloys owing to the limited formability of these alloys under conventional room-temperature stamping conditions. In a prior project (DOE 2011), Pacific Northwest National Laboratory (PNNL) demonstrated that high-strain-rate forming (without a die) of AA5182-O Al alloy at room temperature can achieve safe strains ~2.5x times greater than those achievable under room-temperature quasi-static forming. Further, enhancement in safe strains can be as high as ~6 times when the forming process is performed inside a die. Similar formability enhancements were envisioned in heat-treatable, high-strength 6xxx and 7xxx alloys, enabling lightweight alternatives to steel structural members in automotive applications. However, further understanding is needed of the practical forming limits in PPF processes and their dependence upon process parameters and design. This project will quantify the deformation behavior of 6xxx and 7xxx Al alloys under PPF and develop validated constitutive relations to enhance understanding of high-rate forming processes and the resulting sheet metal formability.

## Approach

The work scope of this project was developed in conjunction with General Motors (GM) and Alcoa. Two Alcoa Al alloys, AA6022-T4E32 (1.2 mm) and AA7075-T6 (1 mm), were identified as representative high-strength, heat-treatable Al sheet alloys that, if sufficiently formable at room temperature, would be attractive candidates for automotive structural applications. Accordingly, in FY 2012 PNNL demonstrated an approximately 78 percent increase in the safe major strain at a minor strain of approximately -5 percent for AA6022 through PPF as compared to the safe strain at quasi-static strain-rate (DOE 2012). Therefore, the aim in FY

2013 was to determine if formability improvements could be obtained in AA7075 analogous to the improvements observed in AA6022. AA7075 sheets, in T6 and W tempers, were free-formed via PPF under plane-strain conditions. The W-temper sheets were prepared by subjecting the T6 temper sheets to solutionizing, quenching, and natural aging. The strain-rates during forming were quantified using PNNL's high-speed imaging plus a digital image correlation (DIC) system (Rohatgi et al., 2011, 2012, 2013). Post-deformation strains were quantified by the DIC method and corroborated by the conventional strain-grid technique. In addition, quasi-static bulge tests were performed in T6 temper to determine the baseline quasi-static formability under plane-strain conditions. The constitutive behavior of AA7075-T6 was estimated from literature data and implemented into a numerical model to predict its formability as a function of strain-rate.

### Results and Discussion

Figure III-13(a) shows the safe and unsafe incipient strains obtained by PNNL in AA7075-T6 (plane-strain specimen geometry) at quasi-static and high strain-rates. The maximum engineering strain-rate during high-rate forming was measured and found to be between 2000 and 4000/s. The data in Figure III-13(a) shows that the safe major strains during PPF and at minor strains from 0 to -3 percent, are as high as ~20 percent. By contrast, the corresponding safe major strains at quasi-static rates are on the order of a few percent only. Thus, the data in Figure III-13(a) shows that the room-temperature formability of AA7075-T6 can be enhanced, relative to its quasi-static formability, by deforming it at sufficiently high strain-rates.

Figure III-13(b) shows ThyssenKrupp's data (incar.thyssenkrupp.com) on the predicted strains in forming-critical areas of a cold-stamped steel ( $\sigma_{UTS} = 900$  MPa) B-pillar. The ThyssenKrupp data was provided to PNNL by our industrial partner (GM) with an interest in developing a B-pillar design using AA7075 that may be a lightweight alternative to a steel B-pillar. A comparison of Figure III-13(a) and Figure III-13(b) shows that near plane-strain conditions and at peak engineering strain-rates of ~2000-4000/s, PPF is capable of producing safe major strains of approximately 20

percent (engineering) that are comparable to the strains predicted in a cold-stamped steel B-pillar. A similarity in the safe strains in AA7075-T6 obtained via PPF and the predicted strains in a cold-stamped B-pillar suggests that the potential to replace steel with high-strength AA7075 exists and deserves further research.

A preliminary estimate of the FLD of A7075-T6 as a function of strain-rate was determined numerically using strain-rate constitutive data from the literature and the Marciniak-Kuczynski method. The predicted FLDs are shown in Figure III-14 and show that the formability of AA7075-T6 increases with increasing strain-rate and the predicted FLD at 2000 /s is in good qualitative agreement with experimental data in Figure III-13(a). Figure III-14 also suggests that a strain-rate of at least ~2000 /s is necessary to achieve forming strains in AA7075-T6 similar to those in a cold-stamped steel B-pillar (Figure III-13(b)).

The room-temperature formability of AA7075 at high strain-rates was also investigated in W tempers to determine if controlling the initial temper of the sheet could provide another means (i.e., in addition to strain-rate) to enhance the room-temperature formability of AA7075. Figure III-15 plots the strain-rate vs. strain for PPF-tested W-temper AA7075 that were either unaged (after solutionizing and quenching) or naturally aged for 5 days after solutionizing and quenching. The specimens did not fail and achieved strains (~15%) similar to the T6 specimens even though the maximum strain-rate (~1000 /s) was almost half the strain-rate achieved in T6 condition. Thus, the data in Figure III-15 suggests that a temper and strain-rate combination is possible that would produce sufficient formability in AA7075 suitable for cold-stamping a B-pillar and at strain-rate < 1000 /s. In an ideal scenario, the possibility exists to control the initial temper of AA7075 sheets such that the strain-rate necessary to achieve the desired formability is within the realm of cold-stamping itself. In such a scenario, AA7075 could be cold-stamped into a B-pillar just like steel. However, one would still need to consider post-forming heat-treatment to increase the strength of the formed part to T6 levels.

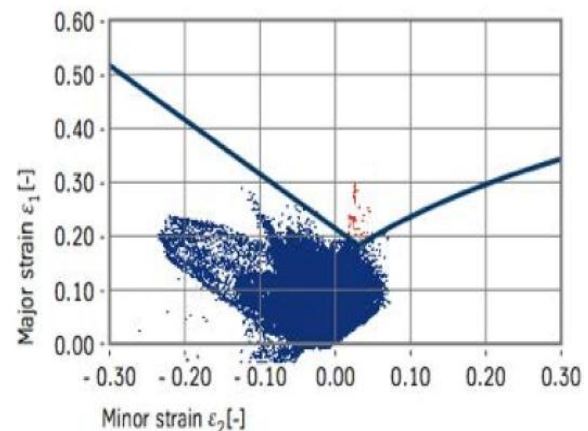
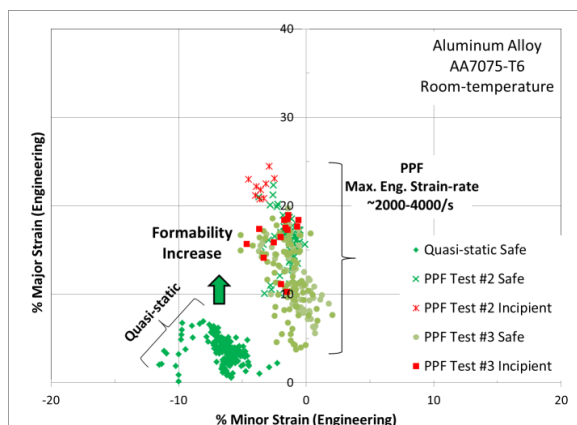


Figure III-13: (a) PNNL's room-temperature FLD for AA7075-T6 at different strain-rate using plane-strain specimen geometry; (b) ThyssenKrupp data on predicted strains in a cold-stamped steel B-pillar.

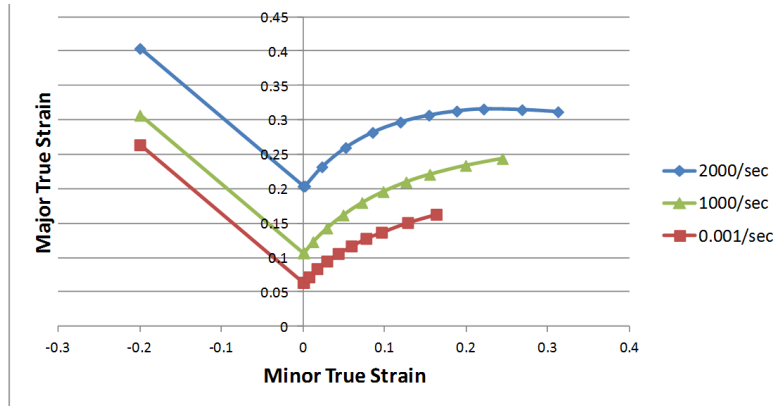


Figure III-14: Theoretical FLD (preliminary estimates) for AA7075-T6 as a function of strain-rate.

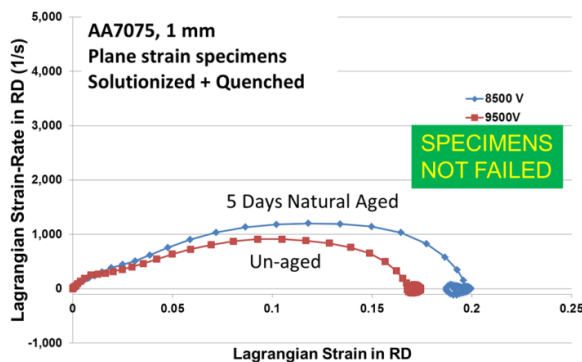


Figure III-15: Strain-rate vs. strain in plane-strain specimens of W-temper AA7075 (RD = rolling direction).

### Technology Transfer Path

PNNL will provide the results of the formability investigation and the constitutive equations for AA6022 and AA7075 to industry to enable automakers to identify which structural component features, currently not formable via cold-stamping, would be best candidates for high strain-rate forming. The team will also evaluate ways to deploy high-rate forming techniques for cost-effective industrial implementation.

### Conclusions

AA7075-T6 was subjected to electro-hydraulic forming experiments and preliminary results show enhanced formability at high strain-rates relative to its quasi-static formability. These results qualitatively mirror formability enhancements previously obtained in both non-heat-treatable (AA5182) and heat-treatable (AA6022) Al alloys.

The room-temperature formability of AA7075-T6 under plane-strain conditions was shown to be enhanced at engineering strain-rates of ~2000-4000/s. The resulting safe strains at such high strain-rates are comparable to the strains

predicted in a cold-stamped steel B-pillar. Thus, the potential to replace high-strength steel with high-strength AA7075 in a B-pillar for weight savings exists and merits additional research.

A theoretical model was developed to predict the dependence of room-temperature formability of AA7075-T6 as a function of strain-rate. The formability predictions of the model are in qualitative agreement with the experimental data.

Initial results on high-rate forming of W-temper AA7075 suggest the possibility of controlling the W-temper to enable its forming into a B-pillar at room-temperature and at lower strain-rates.

### Presentations/Publications/Patents

1. Rohatgi, A., Soulami, A., Stephens, E.V., Davies, R.W. and Smith, M.T. An investigation of enhanced formability in AA5182-O Al during high-rate free-forming at room-temperature: Quantification of deformation history, *In Press*, Journal of Materials Process Technology (2013). <http://dx.doi.org/10.1016/j.jmatprotec.2013.07.015>.
2. Rohatgi, A., Stephens, E.V., Davies, R.W., and Smith, M.T. An investigation of sheet metal deformation behavior during electro-hydraulic forming (EHF). In *Proc. ASME-MSEC 2013*, Paper no. 1129, June 10-14, 2013, Madison, Wisconsin.
3. Rohatgi, A. Enhanced Room-Temperature Formability in High-Strength Aluminum Alloys through Pulse-Pressure Forming (PPF). Presented at the 2013 U.S. Department of Energy Vehicle Technologies Program Annual Merit Review and Peer Evaluation Meeting, May 14-17, Arlington, Virginia.
4. Rohatgi, A., Stephens, E.V., Davies, R.W., and Smith, M.T. Sheet metal deformation behavior during electro-hydraulic forming (EHF). Presented at the ASME-MSEC 2013, June 10-14, 2013, Madison, Wisconsin.

## References

1. DOE. Pulse Pressure Forming of Lightweight Materials, U.S. DOE FY2011 Annual Report.
2. DOE. Enhanced Room-Temperature Formability in High-Strength Aluminum Alloys Through Pulse Pressure Forming, U.S. DOE FY2012 Annual Report.
3. Rohatgi, A., Stephens, E.V., Soulami, A., Davies, R.W. and Smith, M.T. Experimental characterization of sheet metal deformation during electro-hydraulic forming. *J. Mater. Process. Technol.* 2011, 211, pp. 1824-1833.
4. Rohatgi, A., Stephens, E.V., Davies, R.W., Smith, M.T. and Soulami, A. Electro-hydraulic forming of sheet metals: Free-forming vs. conical-die forming. *J. Mater. Process. Technol.* 2012, 212, pp. 1070-1079.
5. Rohatgi, A., Soulami, A., Stephens, E.V., Davies, R.W. and Smith, M.T. An investigation of enhanced formability in AA5182-O Al during high-rate free-forming at room-temperature: Quantification of deformation history, *In Press*, Journal of Materials Process Technology (2013). <http://dx.doi.org/10.1016/j.jmatprotec.2013.07.015>
6. [http://incar.thyssenkrupp.com/4\\_01\\_041\\_BS02\\_Umformen.html?lang=en](http://incar.thyssenkrupp.com/4_01_041_BS02_Umformen.html?lang=en), Cold-stamped B-pillar TPN-W 900, accessed and downloaded on 02/25/2013.

# Aluminum Formability Extension Through Superior Blanking Process

## Xin Sun and Richard W. Davies (Principal Investigators)

Pacific Northwest National Laboratory  
Phone: (509) 372-6489; Fax: (509) 372-6099  
E-mail: [xin.sun@pnnl.gov](mailto:xin.sun@pnnl.gov)  
Phone: (509) 375-6474; Fax: (509) 375-4448  
E-mail: [rich.davies@pnnl.gov](mailto:rich.davies@pnnl.gov)

## Sergey Golovashchenko (Principal Investigator)

Ford Motor Company  
Phone: (313) 337-3738; Fax: (313) 390-0514  
E-mail: [sgolovas@ford.com](mailto:sgolovas@ford.com)

## Accomplishments

- Performed new blanking experiments of AA6111-T4 aluminum (Al) sheets with different clearances. The influence of pre-straining and trimming angle on trimming quality and subsequent stretchability were studied.
- Trimmed sheet edges were characterized in terms of edge-cracking behaviors, sheared-edge roughness change with clearances, and burr height variation.
- A novel framework was developed to integrate the shearing-affected zone information of the trimming simulations into subsequent stretchability simulations.
- Performed three-dimensional (3D) tensile stretchability simulations of previously trimmed parts with the use of the developed computational framework. Predicted failure mode and ductility showed very good agreement with experiments with different cutting clearances.
- Using the new framework, the influence of deburring was studied. Consistent with experimental observations, the simulation results show that deburring do not influence tensile stretching behavior.

## Future Directions

- Determine work hardening behavior at large strains by accumulated rolling and tension tests.
- Conduct hole-punching and hole-expansion tests with various clearances.
- Simulate hole expansions with different punched-hole-edge conditions using the newly developed framework of integrating the hole-punching processes results into hole-expansion processes simulations.
- Demonstrate that the stretching formability can be improved by at least 50 percent with the use of optimized process parameters determined through modeling.

## Technology Assessment

- Target: Achieve 90 percent accuracy of the blanking simulations with experiments in terms of cut edge geometry.
- Gap: The simulations results of cut edge geometry are very close to experimental observations. For more precise prediction, more accurate damage parameters and plastic model at large strains are necessary.
- Target: Achieve 90 percent accuracy of the stretchability simulations with experiments in terms of the elongation to fracture.
- Gap: The predicted ductility is very close to experimental results. For more precise prediction, more accurate damage parameters and plastic model at large strains are necessary. An accurate account of the edge variability of previous trimmed sheets part is also required.



## Introduction

Automotive original equipment manufacturers (OEMs) and their Tier 1 suppliers have an extraordinarily high capital investment into their sheet-metal-forming facilities, equipment, and associated infrastructure. The ability to redirect these capital-intensive facilities from steel to Al component manufacturing would dramatically increase the widespread commercialization of Al sheet into vehicles. This project aims to enhance the overall formability of Al using the existing OEM capital infrastructure by developing enhanced processes for the blanking, piercing, and trimming operations to extend Al formability in the subsequent forming operations. The formability of the Al sheet in conventional automotive stamping is typically limited by the processes that prepare the blank for the stamping operation (i.e., blanking, piercing, and trimming). The overall formability and subsequent quality of the part is often limited by the height of burrs on a sheared surface, the microstructural damage imparted on the sheet, and the dimensional accuracy and the absence of splitting (Golovashchenko 2006; Golovashchenko 2008).

## Approach

In this project, we will further develop and mature a superior blanking process to enhance the room temperature formability of Al sheets with improvements on existing trimming infrastructures. The proposed approach is based on a new trimming method originally developed by Golovashchenko (Golovashchenko 2006; Golovashchenko 2008; Ilinich, et al., 2011) with various mechanisms of scrap/offal support, as well as extensions of the technology using other new and unique techniques. The goal of this work is to use a combined experimental and numerical approach to develop processing windows and parameters for preparation

of stamping blanks that achieve robust, extended ductility compared to conventionally trimmed blanks. Our activities in FY 2013 focused on developing the experimental validated modeling framework for accelerating the development and subsequent implementation of the superior blanking process.

### Results and Discussion

A simple tooling design was made for traditional and advanced trimming process. First, experimental studies were carried out to determine the influence of trimming parameters on the quality of sheared surface and its ability to stretch during the following flanging, hemming operations, and drawing of sheet metal work pieces. Optical microscopy (OM) and scanning electron microscopy (SEM) were used to examine the characteristics of the trimmed surface (e.g., the surface roughness and burr tip variation along the edge). A new optical system with a charge-coupled device (CCD) camera was created to monitor edge-crack initiation and propagation mechanisms to validate model predictions. In addition, edge cracks were carefully examined via SEM (see Figure III-16(a)). In industrial practice, pre-deformation is usually experienced before trimming. The effect of pre-strain on later trimming and stretching formability was studied experimentally (Figure III-16 (a)) for the case of 10 percent clearance. Separate from orthogonal cutting, angled

cutting (10° and 20°) was studied and found to positively affect later stretching formability; however, the trend of change with cutting clearances remained the same (Figure III-16(b)).

On the modeling side, the focus was to develop a framework for integrating blanking simulation results into the subsequent tensile stretchability studies (Hu, et al., 2013a). Accurate predictions of the trimmed edge conditions (e.g., plastic deformation, damage and geometric features) are essential to accurately predicting the edge stretchability of a previously trimmed part. This was accomplished in FY 2012. Hu et al., (2013b) described the detailed modeling procedures and material properties used in the trimming models. A three-dimensional (3D) finite element model was developed to represent the half dog-bone uniaxial tensile sample used by Golovashchenko (2008). The burr geometry of the predicted trimmed edge was obtained by post-processing the trimming simulation results to record the nodal coordinates of all the points on the cut edge after full separation of the part and scrap side (Figure III-17(a)). These results were later used to create the two-dimensional (2D) outline for this region, representing a cross-section of the 3D tensile model as illustrated in Figure III-17(b). The sketch was extruded into a 3D model (Figure III-17(c)), which was modified (using Abaqus/computer aided engineering (CAE)) to match the geometry of the half dog-bone sample (see Figure III-17(d)).

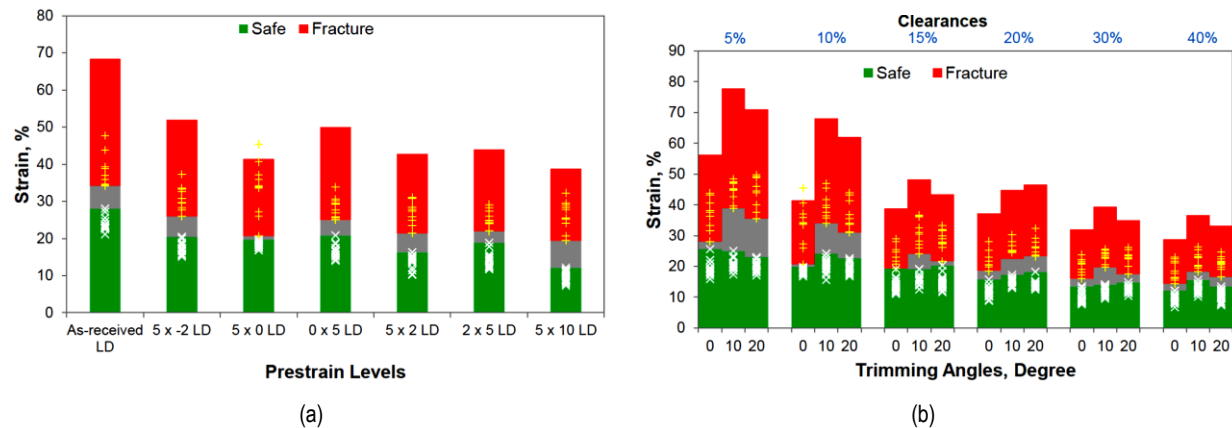


Figure III-16: (a) Influence of material pre-strain on safe and fracture strains for half dog-bone samples trimmed with 10 percent clearance in the Longitudinal Direction (LD); (b) tensile elongation results for samples subjected to 5% x 0% pre-strain in LD and trimmed with 0 to 20° cutting angles at 5 to 40 percent clearances.

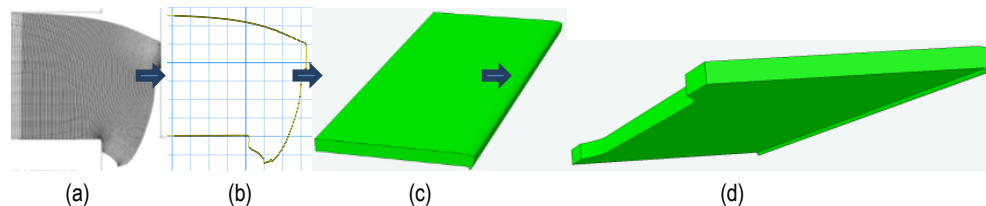


Figure III-17: The procedure to integrate the 2D edge geometry of the trimming model into a 3D half dog-bone tensile sample.

The trimming-model-predicted equivalent plastic strains at the sheared edge and in the shear affected zone (SAZ) were recorded and passed onto the 3D stretching model after interpolation. This was accomplished using the vectored user material (VUMAT) subroutine. Considering the fact that excessive plastic deformation induced by the trimming process contributes to the final edge fracture during the subsequent stretching process, the deformation contribution to initial damage ( $D_0$ ) was calculated by scaling the initial plastic strain of a material point by the maximum limit strain for uniaxial tension, e.g., 0.6 in the current work. Tensile stretching simulations were performed for six cutting clearances: 2, 10, 21, 32, 43, and 60 percent. Figure III-18(a,b,c, and d) illustrates examples of the mapped initial plastic strains for four representative cases (10, 32, 43, and 60% cutting clearances) where Taylor factor scaling was used. These mapped plastic strains contours show that the SAZ increases with cutting clearances. Figure III-19(a) shows the plastic strain contours of the fractured samples for different clearances calculated by finite element tensile stretch models. Clearly, the evolution of the calculated stretch failure modes is in line with experimental observation (Golovashchenko 2008). Samples with small cutting clearances tend to show shear-type failure. However, as cutting clearances increase, the shear-type failure gradually transitions into splitting-type failure for large cutting clearances. Figure III-19(b) features pictures of final fracture taken during a recent test of smaller gauge length samples. These pictures show that shear-type fractures are present in samples with trimming clearances less than

10 percent and that splitting-type failures are dominant for clearances larger than 20 percent. In current simulations, the predicted failure modes correspond quite well with experimental observations for various trimming clearances.

Experimentally, multiple cracks were observed along the edge of a fractured sample after tension of previously trimmed sheets with different clearances. Fine cracks were observed for clearances less than 10 percent across the trimming fracture zone and bottom edges near the final tensile fracture surface (Figure III-20(a)) and predictions of the cracks were made for the various clearances (Figure III-20(b)). Dense, small edge cracks were observed. Although fine cracks still exist for other clearances, large, major edge cracks exist at the bottom edge of the burr tips and the inter-crack distance becomes larger with increasing cutting clearances. Due to the coarse meshes used in these stretching simulations and use of element removal to represent material damage, the detailed features of fine and edge cracks could not be captured in the 3D tensile stretchability simulations because the actual crack opening, at initiation, is typically much smaller than the mesh size used. However, similar observations on multiple edge cracks were observed in the finite element simulations represented by element removal (see Figure III-19(b)). In Figure III-19(b), many evenly distributed, edge-damaged spots are visible on the trimmed edge with smaller clearances. With increasing trimming clearance, the hot spots become more discrete, and the predicted inter-crack distance increases.

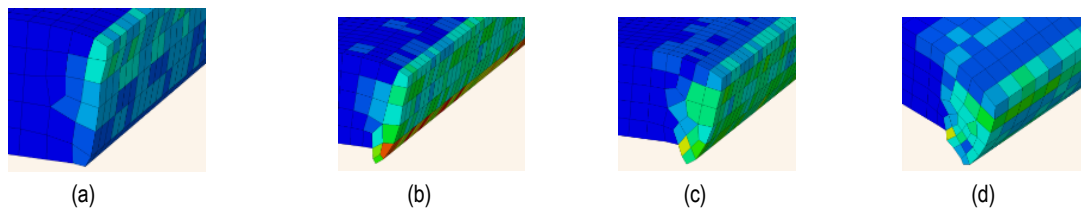


Figure III-18: The initial plastic strain mapped onto the half dog-bone tensile sample for different cutting clearances: (a) 10 percent, (b) 32 percent, (c) 43 percent, and (d) 60 percent.

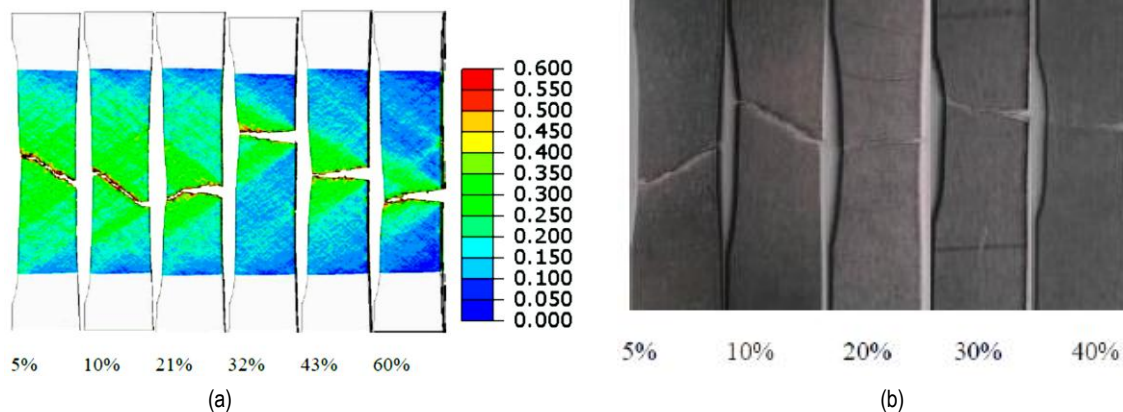


Figure III-19: (a) The predicted equivalent plastic strain contours for fractured samples of different clearances (2–60 percent); (b) images of samples taken before final fracture of the half dog-bone samples tensile stretched after being trimmed with different clearances.

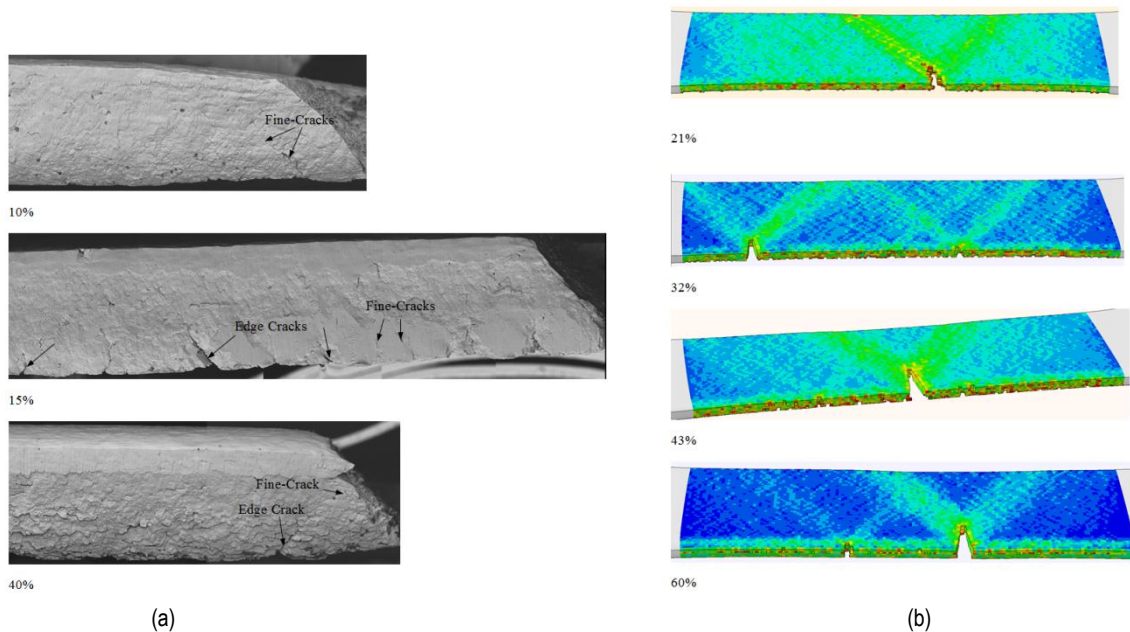


Figure III-20: Multiple edge cracking: (a) observed by SEM, (b) predicted for different clearances.

In Figure III-21(a), the calculated stress-strain curves of the models are shown for different cutting clearances. Figure III-21 (b) shows the comparison between the predicted tensile elongations and the experimental results reported by Golovashchenko (2008) for different shearing clearances: elongation decreases with clearances, and the decrease can be as much as 50 percent. The predicted elongations (i.e., the solid red line with solid diamond symbols in Figure III-21(b)) are slightly higher than the experimental results published by Golovashchenko (2006) (i.e., the black dashed line with empty upward triangles). However, the detailed trend of variation is close to experimental measurements. The clearance reported in the literature is the nominal clearance. The actual clearance may change at the end of cutting, and the changes can be

sizeable if the trimming tool is not stiff enough. Using calibrated clearances for the results of experimental measurements (Hu, et al., 2013), the calculated variation of tensile elongations stemming from finite element simulations is quantitatively close to the experiments (i.e., the solid red and black curves in Figure III-21(b)).

Although the process of deburring (burr removal) and/or sliver cleaning can be operationally costly, it has long been an industrial practice after trimming (Gillespie, 1999) for safety considerations, surface-quality considerations, and for possible improvement of the subsequent edge stretchability during forming. However, Adamzyck and Michal (1986) indicates that formability enhancement from deburring in

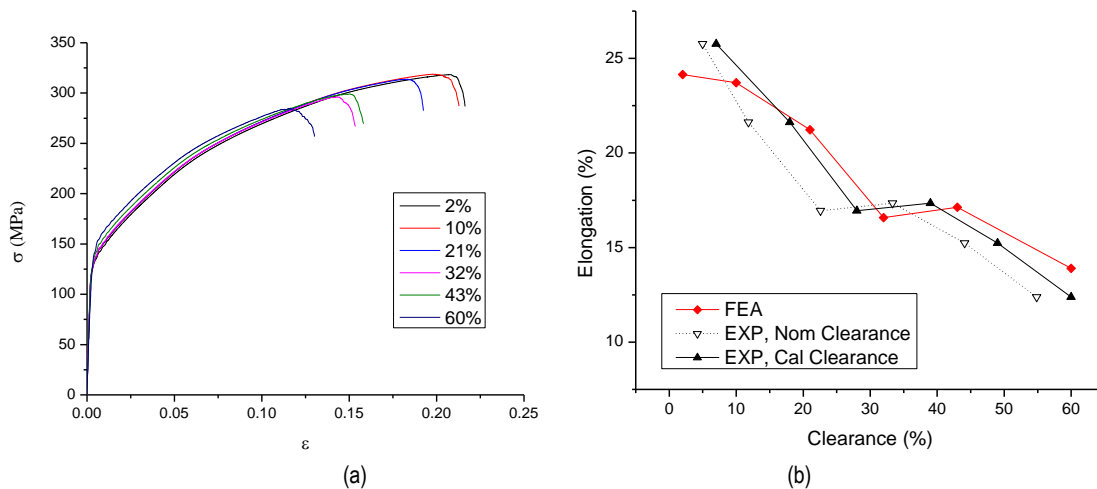


Figure III-21: (a) The calculated tensile true stress-true strain curves for samples with different shearing clearances from 2 to 60 percent; (b) the calculated elongations for samples of different models in comparison with experimental observations featuring nominal (Nom) or calibrated (Cal) clearances.

stretch forming of steel sheets is quite small. With the computational framework, PNNL virtually examined the separate effect of burr removal and examined its contribution, if any, to possible edge stretchability enhancement. The same material properties and stretching models for the trimming clearances discussed previously were used. Trimming-induced initial plastic strains were maintained in the models, but the burrs were numerically removed by adjusting the geometry of the lower trimmed edge (see Figure III-22(a) and Figure III-22(b)). Figure III-22(c) and Figure III-22(d) illustrate the predicted stress-strain curves and elongations at various clearances with burr removal. The results indicated that deburring has only a minute influence on tensile stretchability. In fact, ductility was slightly reduced for clearances of 2 to 21 percent and 43 to 60 percent. Meanwhile, elongation for clearances of 32 percent increased and a monotonic change of ductility was observed with trimming clearances. For most clearances, the planar failure modes were nearly the same as those shown in Figure III-18(a).

### Technology Transfer Path

Technology transfer of this project will be directly through Ford Motor Company and its Tier 1 suppliers. The broader commercialization of the technology through the Tier 1 suppliers will reach the entire automotive OEM industry.

### Conclusions

In FY 2013, Ford and Oakland University focused on new blanking experiments with AA6111-T4 Al sheets with different

clearances and on experimental characterizations of the sheared edge stretchability, edge crack initiation and propagation. PNNL focused on developing the validated integrated framework for carrying trimming simulation results into subsequent stretching operations. This was accomplished by post-processing the trimming simulation file with the use of a Python script, which records the geometry and deformation at the SAZ from the 2D plane-strain trimming model. The recorded geometric information was used to generate geometry and mesh of the 3D half dog-bone tensile stretchability models with the aid of the Abaqus/CAE pre-processing module. The deformation and damage information was interpolated into the stretching model with the use of a VUMAT.

With the developed framework, the tensile stretching formability of previously trimmed part was successfully predicted in terms of failure mode and elongations. These simulation results correlate very well with experimental observations. More studies using this framework indicated that deburring does not enhance the formability, but plastic deformation removal processes (e.g., annealing) can significantly improve the stretching formability of previously trimmed sheets

FY 2014 activities include hole-punching with various clearances and subsequent hole-expansion experiments and simulations for the newly developed framework. Advanced trimming process will be demonstrated in both simulation and experiments to show that at least 50 percent improvement of stretching ductility can be achieved at room temperature.

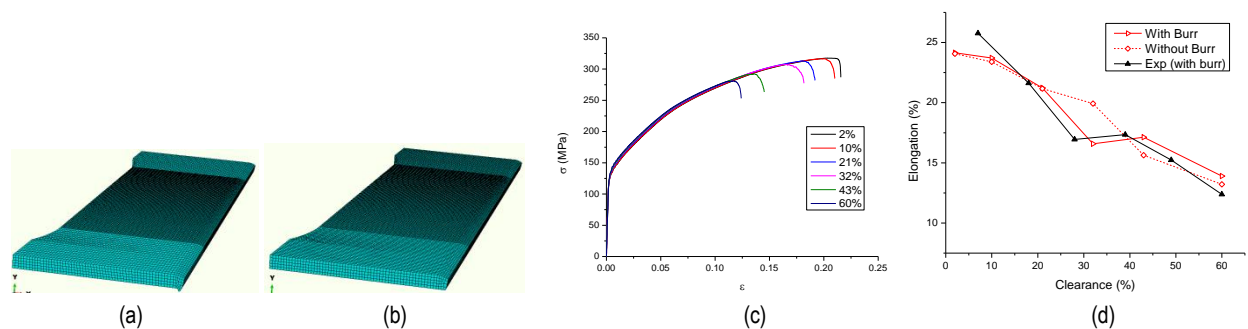


Figure III-22: An example of models for 43 percent trimming clearance (a) before and (b) after the burr is removed. Simulation results of models after burr removed (c) stress-strain curves and (d) elongations.

## References

1. Golovashchenko, S.F. A study on trimming of aluminum autobody sheet and development of a new robust process eliminating burrs and slivers. *International Journal of Mechanical Sciences* 2006, 48, 1384-1400.
2. Golovashchenko, S.F., Quality of Trimming and its Effect on Stretch Flanging of Automotive Panels *Journal of Materials Engineering and Performance* 2008, 17, 316-325.
3. Ilinich, A. M., Golovashchenko, S.F., Smith, L.M. Material anisotropy and trimming method effects on total elongation in DP500 sheet steel. *Journal of Materials Processing Technology* 2011, 211, 441-449.
4. Hu, X.H., Sun, X., Golovashchenko, S.F. Predicting Tensile Stretchability of Trimmed AA6111-T4 Sheets. Submitted to *Computational Materials Science* 2013.
5. Hu, X.H., Choi, K.S., Sun, X., Golovashchenko, S.F. Edge Fracture Prediction during Traditional and Advanced Trimming Processes for AA6111-T4 Sheets. In press, *ASME Journal of Manufacturing Science and Engineering* 2013.
6. Gillespie, L.K. *Deburring and Edge finishing Handbook*, Society of Manufacturing Engineers, Dearborn, MI 1999.
7. Adamczyk, R.D., Michal, G.M. Sheared edge extension of high-strength cold-rolled steels. *J. Applied Metalworking* 1986, 4, 157-163.

---

# Non-Rare–Earth High-Performance Wrought Magnesium Alloys

---

## Curt A. Lavender (Principal Investigator)

Pacific Northwest National Laboratory

Phone: (509) 372-6770

E-mail: [curt.lavender@pnnl.gov](mailto:curt.lavender@pnnl.gov)

## Tim Skszek

Magna Cosma International

Phone: (248) 689-5512

E-mail: [tim.skszek@cosmaeng.com](mailto:tim.skszek@cosmaeng.com)

## Accomplishments

- A series of magnesium (Mg) alloys were cast and extruded to produce high-performance Mg alloys with fine grain sizes.
  - Grain sizes appear to be less than 5  $\mu\text{m}$ .
  - Dispersions near 15 nm interact with dislocations.
- A Mg alloy containing no rare earth elements that was processed for fine grain size using a low-cost, high-shear extrusion process was shown to absorb energy similar to 6061Al
  - This is a 20 percent mass savings over 6061.
  - The mode of failure is different.
- Microstructural modeling has been initiated to help understand the behavior and predict energy absorption.
  - A new model for strength in Mg has been implemented using the phi theory.
  - Fracture of a hard second-phase particle during high-shear processing has been modeled.

## Future Directions

- Establish commercial goals for tubular Mg alloy extrusions and demonstrate high strength in prototypic-size components

## Technology Assessment

- Target: Develop high energy–absorption Mg alloys that do not contain rare earth elements and that can replace Al extrusions at a mass savings of 20 percent (based on density).
- Target: Use inverse process modeling to develop a low-cost process to produce microstructures required for high performance at a low cost, making Mg extrusion viable for automotive applications.
- Gap: Currently produced Mg alloys that possess high strength and ductility (energy absorption) use rare earth elements, which increase cost and are of limited supply, resulting in reluctance of the automotive industry to use Mg extrusions.
- Gap: The cost to produce high-performance Mg extrusion has prevented use in automotive applications.



## Introduction

The use of Mg in automotive applications for which extrusions would be preferred has been limited by the cost and energy absorption capacity of Mg. Applications like bumper beams, crush tips, intrusion beams, and shotgun tubes (among others) would present a significant vehicle-mass savings opportunity if they could be fabricated from Mg. Past projects that processed Mg for use in applications requiring energy absorption like that of Al required very slow extrusion rates (raising cost) or powder metallurgy processes requiring costly rapid solidification and rare earth alloying additions.

The purpose of this project is to develop and demonstrate low-cost wrought Mg alloys that do not rely on rare earth alloying elements for their strength, ductility, and energy absorption properties. A novel low-cost processing method, in conjunction with Mg alloys containing rare earth substitutes, will be developed to produce the microstructure and properties needed for the automotive applications in a cost-effective manner.

## Technical Approach

The project has been performed in three phases. In the first phase, the project team produced high-performance alloys using rare earth additions and rapid solidification to develop high-energy–absorbing microstructures that were used as model systems for non-rare earth alloys. The second phase of the project developed the microstructure found in Phase 1, using silicon (Si) additions and the ZK60A alloy, to produce high-performance alloys without rare earth additions. The third, and current, phase of the project will use an inverse process modeling method to develop a cost effective processing approach to produce the alloy with the energy absorbing properties.

The following technical steps have been completed:

- Produced rare earth-Mg alloy extrusions and performed mechanical tests comparing quasi-static tension and compression results to the Al alloy 6061 and the conventional Mg alloy AZ31.
- Evaluated energy absorption capability of the rare earth-Mg alloy via impact tests and compared to 6061 and AZ31.
- Evaluated—experimentally—the deformation mechanisms of the rare earth alloys using interrupted strain tests in tension and compression at room temperature.
- Developed a continuum-level model to predict microstructure evolution and mechanical deformation behavior of Mg alloys during processing. Validated using experimental data.
- Selected up to three alloys from the previous task, consolidated the materials by extrusion, and evaluated the non-rare earth alloys for strength and energy absorption

characterization, at both quasi-static and elevated strain-rate tension tests.

The following technical steps will be completed during the third and final phase:

- Produce sufficient material to provide partner Magna Cosma International with tubular extrusions that can be formed into shapes such as crush tips, roof structural support beams, etc., for testing and comparison to conventional materials.
- Develop the “Model Alloy” by implementing a statistical continuum mechanics model embedded with crystal plasticity. Use the model to predict grain size, dispersion, and textural effects.
- Use experimental data, crystal plasticity, inverse process path modeling, and laboratory trials to develop the necessary process to create the desired microstructure using an optimum low-cost, high-shear processing route.
- Prototype and demonstrate a small system that will produce extruded shapes by fracturing the coarse intermetallics and developing the strain needed for the fine grain size (as predicted by the inverse modeling) and provide the driving force for the subsequent extrusion.
- Magna Cosma International will evaluate extrusions produced by the system for formability. Billets produced by the process will be extruded at PNNL and subjected to formability tests using warm gas-pressure forming.

## Results and Discussion

The initial phase of this effort was to determine the microstructural characteristics of a rapidly solidified high-performance, rare-earth-containing Mg alloy and compare that to conventional alloys with similar processing. The project successfully demonstrated that a non-rare-earth alloy of similar grain size, ZK60A, could match the performance of the rare-earth-containing alloy. This behavior has been attributed to the fine grain size and the associated reduction in twinning. The next step of the project is to determine whether the same structure made by very costly rapid solidification could be produced using a novel extrusion method from a low-cost casting.

During this reporting period, efforts were focused on the demonstration of a high-shear extrusion process to produce fine grain size, modeling of the microstructure to predict the properties, and modeling of the high-shear process. In all activities, the objective was to use an alloy that did not contain rare earth elements or require costly processing such as powder metallurgy and rapid solidification, and as much as possible use an integrated computational material engineering approach to process and alloy selection.

Two alloys were chosen for the investigations: 1) ZK60A, which is a commercially available wrought alloy and 2) a custom cast alloy of Mg with 2 weight percent Si ( $Mg_2Si$ ). The ZK60A alloy was chosen because of ready commercial availability and contains very fine zirconium (Zr)-rich dispersions, shown here in Figure III-23, and when produced in fine grain sizes can possess energy absorption like that of 6061 Al (DOE 2012).

The alloy magnesium silicide ( $Mg_2Si$ ) was chosen because it contains an as-cast eutectic constituent phase,  $Mg_2Si$ , shown here in Figure III-24 that can be fractured to fine sizes during high-shear processing. For the extrusion demonstrations,  $Mg_2Si$  was cast by CANMET into a 50 mm by 300 mm by 600 mm book mold to allow for the formation of the  $Mg_2Si$  at a relatively slow solidification rate. From this book mold casting, billets were machined for extrusion. The ZK60A extrusion billets were machined from a 600 mm direct-chill cast ingot produced by Magnesium Elektron North America (MENA). The purpose of the respective castings was to verify that the constituent particles and as-cast structure would represent a low-cost full-scale commercial ingot and that the high-shear extrusion would be breaking down a commercially relevant as-cast structure.

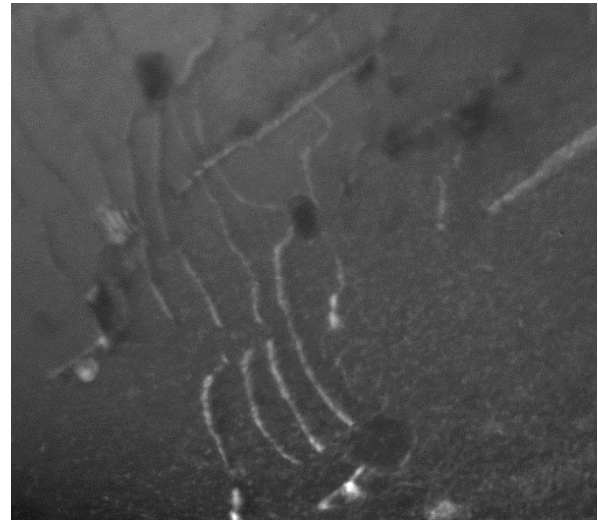


Figure III-23: Fine 15 nm Zr-rich dispersions (black particles) formed in the commercial ZK60A alloy interacting with dislocations.

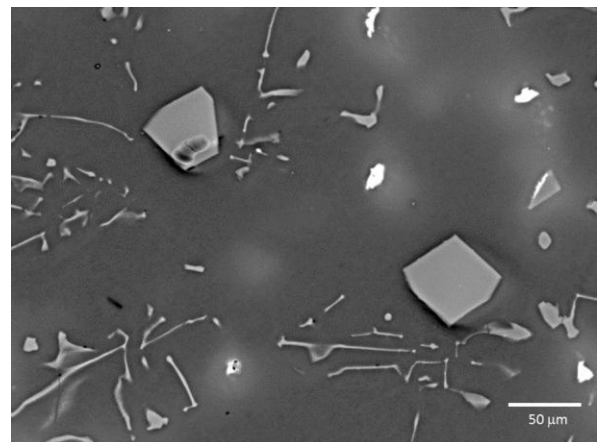
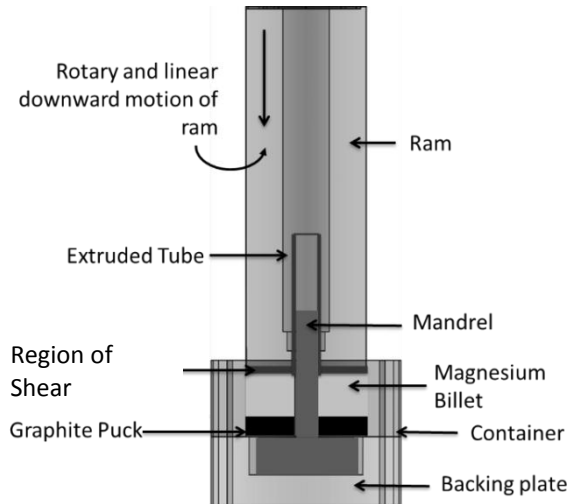


Figure III-24: Script and blocky eutectic constituent particles found in the  $Mg_2Si$  alloy book mold casting.

The high-shear extrusion process used for this activity is shown schematically in Figure III-25; the process closely resembles conventional indirect extrusion except that the ram, or die, is rotating while plunging. The extrusion system has been adapted to the PNNL friction-stir weld machine to allow

for accurate process control and gathering of torque and force data. The use of a mandrel in the extrusion process, to produce tubular cross-sections, is considered novel and is the subject of a provisional patent filed by PNNL to allow for reporting (Lavender et al., 2013); a formal filing has been initiated.



**Figure III-25: Schematic of the novel high-shear extrusion system used for the production of tubular products.**

Several extrusions were made during this period from  $Mg_2Si$  and ZK60A at a number of rates and were successfully processed into a 7 mm outside diameter by 0.5 mm wall tube approximately 250 mm in length, shown in Figure III-26. The tubes were extruded at rates from 75 mm/minute up to 4 m/minute. All materials were sound and possessed high strength; additional characterization is underway. Tube dimensions were very uniform: the outside diameter varied less than 0.1 mm over the entire length.

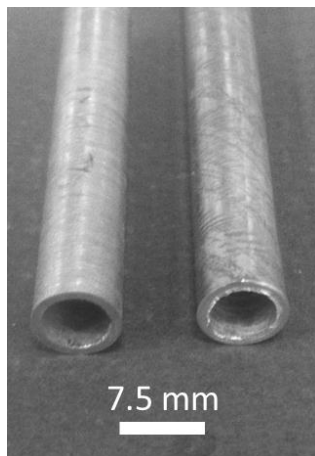


**Figure III-26: Examples of 7 mm OD by 0.5 mm wall tubular extrusions made by high-shear extrusion.**

The tubes were characterized for grain size and tested in compression to evaluate energy absorption. In the case of ZK60A and  $Mg_2Si$ , the energy absorbed was equivalent to that of the rapidly solidified powder metallurgy alloys produced during the previous reporting period and exceeded the energy

absorption of 6061, as shown by the energy absorption plots in Figure III-27. This data indicates the potential for a mass improvement of at least 20 percent with rapid solidification or high-shear extrusion. This high energy absorption is likely due to the fine grain size found in the extrusion, where the grain sizes for the  $Mg_2Si$  and ZK60A were approximately 3 to 5  $\mu m$ , as shown in Figure III-28. In Figure III-28(a), an arrow indicates the extrusion direction and a line at approximately 45 degrees follows a preferred flow direction in the  $Mg_2Si$ . This orientation effect was not observed in the ZK60A alloy and may be an indication of a difference in recrystallization behavior of the two alloys; further characterization is underway to explain the effect. This successful demonstration of the high-shear extrusion process has shown that a commercial-scale as-cast microstructure can be converted to a high strength, high-energy-absorption microstructure using a relatively simple process.

The modeling activities during this reporting period were focused in two areas: 1) modeling of the strength in Mg alloys and 2) modeling of the process conditions needed to fracture the primary intermetallics (eutectic constituents) into sizes fine enough to produce the fine grain sizes needed for high strength and energy absorption. The strength modeling was performed in collaboration with Dr. Said Azhi of the University of Strasbourg. In this case the strength of the Mg was simulated using the viscoplastic-self-consistent (VPSC) theory (Molinari et al., 1987) where an additional term was added to account for the anisotropic yield behavior in Mg. The term, called  $\phi$ , is a complex adaptation of several deformation theories that account for twinning, grain size and texture in predicting the strength of a magnesium alloy under plastic strain (Li et al., 2014). Using the  $\phi$  mode, the microstructural features of the alloy can be separated to determine the most important characteristic. Figure III-29 illustrates the use of the  $\phi$  model showing the activity of the various deformation modes with increasing compressive strain in AZ31 (all modes sum to 1.0 at any given strain). As shown by Figure III-29, the initial strength is derived from twinning and basal slip, which together account for 0.95 of the activity.

Twinning is a low energy event, and as observed in the predicted stress/strain curve of Figure III-30, the initial hardening is low. As the deformation proceeds, the texture is evolving and prismatic slip increases while twinning decreases, and the stress/strain curve predicted by the  $\phi$  model shows a higher rate of hardening at a true strain of  $\sim 0.04$ . As shown by Figure III-30, the  $\phi$  model predicted stress/strain closely correlates to the experimental results for compression of AZ31 sheet. The new  $\phi$  modeling approach is being incorporated into the project to guide development of the as-processed texture in the high-shear extrusion process to maximize strength and energy absorption. Preliminary indications are that  $Mg_2Si$  produces a different texture than the ZK60A alloy and the strength observed maybe influenced more by texture than grain size, whereas the ZK60A alloy is dominated by grain size. The implication is that the energy absorption for the  $Mg_2Si$  alloy may not be useful in complex shapes where applied stresses cannot be controlled as they can in a compression test. These data are new and the model appears to be a powerful tool for comparing materials.

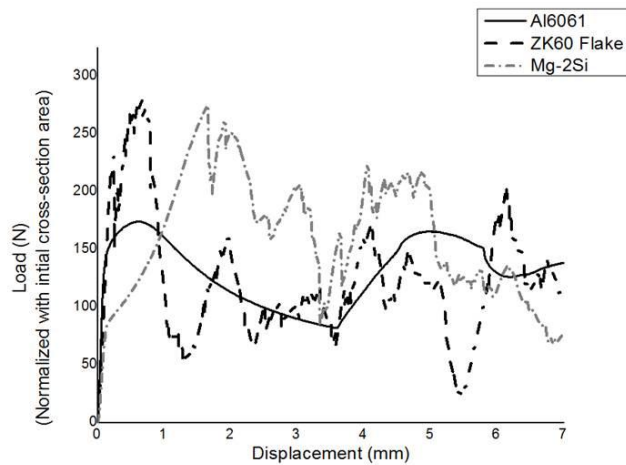


Figure III-27: Energy absorption curves for 6061 Al, rapidly solidified ZK60A (processed during FY2012) and high-shear Mg<sub>2</sub>Si extrusion showing that the energy absorption was similar, which indicates the potential for a mass improvement of at least 20 percent with rapid solidification or high-shear extrusion.

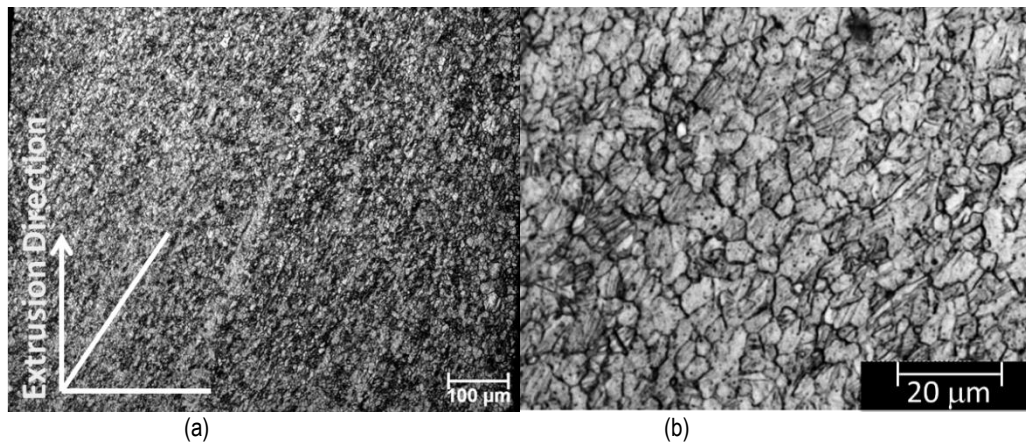


Figure III-28: Backscattered scanning electron micrographs of the grain sizes in (a) Mg<sub>2</sub>Si and (b) ZK60A after high-shear extrusion.

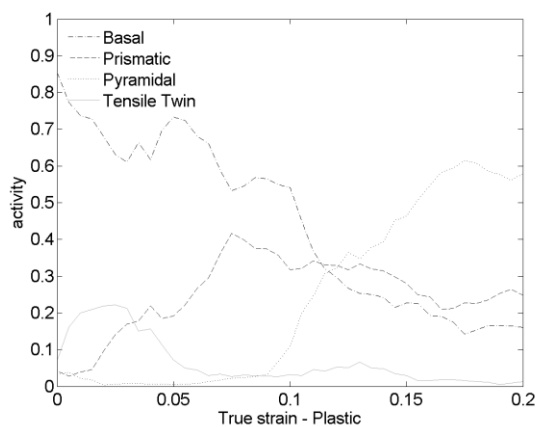


Figure III-29: Contributions of several deformation mechanisms to the strengthening of AZ31 magnesium during compression.

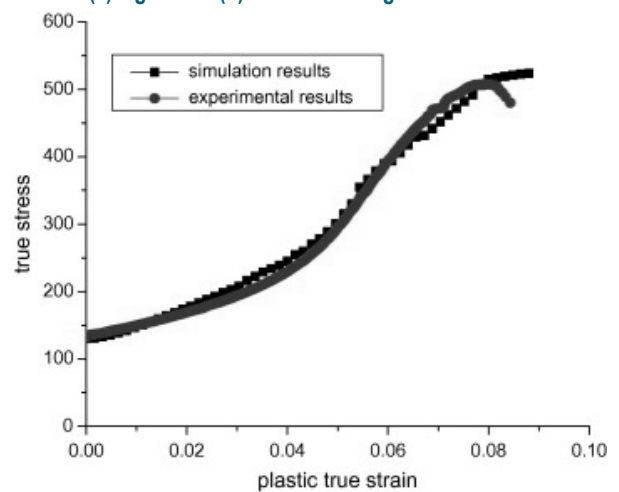


Figure III-30: Predicted and experimentally determined stress-strain curve for AZ31 tested in compression. The inflection in hardening near 0.04 strain is attributed to the change in the relative contributions of twinning and prismatic slip due to evolving texture.

The second modeling activity involves the fracture of secondary particles that are used to pin the grain boundaries and produce a fine grain size. In order to understand this process a new model has been developed to predict the fracture of particles under hydrostatic stress. The goal of the extrusion process is to fracture particles in shear under hydrostatic stress such that the particle is fractured without generating porosity. The desired fracture is shown as Mode II in Figure III-31, where the particle is fractured and the magnesium matrix fills in the resulting void, unlike Mode I where the particle is fractured and a void is created. The fracture process is simulated using traction tensors shown in Figure III-32 and is based on a model developed to predict fracture of aggregates in cement (Jeffery 1922). In Figure III-32, a particle of known orientation and aspect ratio is subjected to stresses in the  $x'$  and  $y'$  directions and fractures on plane S. The value of the model is twofold: 1) the model can predict the stress state (in terms of principal stresses  $\sigma_3$  and  $\sigma_1$ ) needed during the deformation to produce Mode 2 fracture, as shown by the shaded region labeled Mode II in Figure III-33, and 2) the method can predict the stress needed to fracture particles of given aspect ratio. The processing diagram can be implemented into a finite element model of the process and suggest what extrusion ratio, shear rate and extrusion rate are needed to remain in the Mode II field. This complex adaptation has not yet been done but is being

evaluated at Georgia Institute of Technology. At PNNL, an attempt was made to incorporate the traction tensor mode into the smooth particle hydrodynamic model, and although it predicted the extrusion forces and apparent strains, the model could not provide insight into extrusion conditions (Pan et al., 2013).

The traction tensor particle fracture theory was very useful and predicted that the blocky particles observed in the  $Mg_2Si$  book mold casting would require extremely high stress to fracture due to the aspect ratio of nearly unity; however, the model suggested that the script structure would fracture readily and produce fine particles on the order of the thickness of the eutectic constituent plate (much less than  $1 \mu m$ ). Interestingly, when the as-extruded structure of the  $Mg_2Si$  is examined, as shown in Figure III-34, there are large, blocky (aspect ratio near 1) intermetallics similar in size to those found in the book mold casting (Figure III-34a), no evidence that the script structure remains, and very fine particles (Figure III-34b) likely to be remnants of the script structure fractured during extrusion. This new model is useful in predicting particle fracture and must be integrated with a higher length-scale model that can predict the complex state of stress in the extrusion. The model also provides the evidence that shear alone will not refine the large intermetallics and the alloy must be modified to promote the formation of the script structure over the blocky phase.

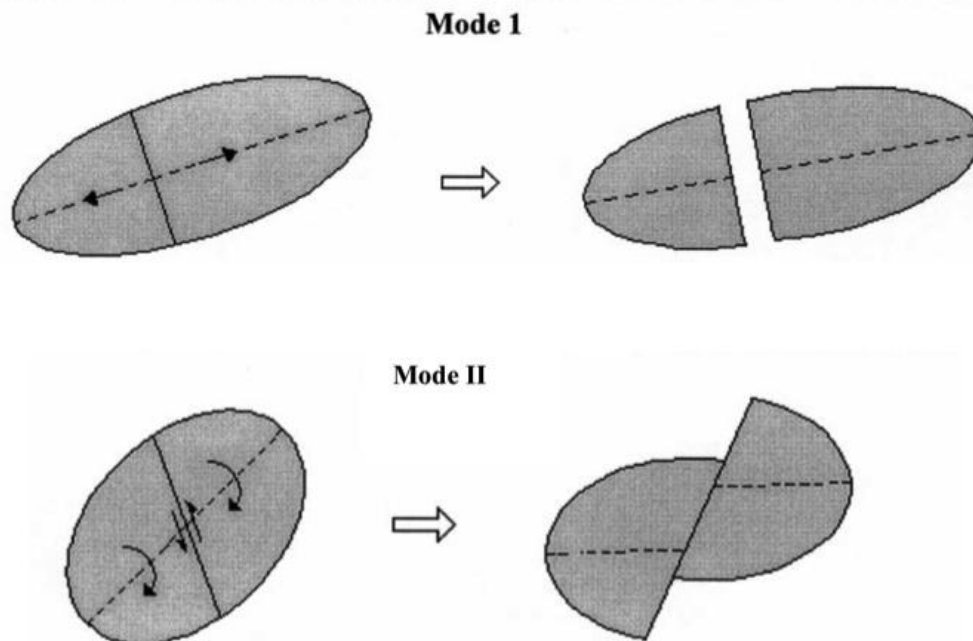


Figure III-31: Schematics of two fracture modes of particles when subject to an applied stress when under hydrostatic stress. Mode 1 develops porosity, while Mode 2 porosity is healed by shear in the matrix.

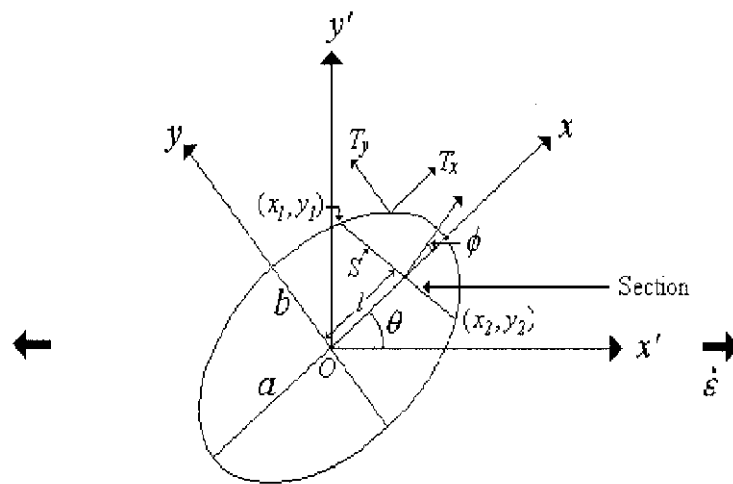


Figure III-32: Stresses and orientations required to model particle fracture using the traction tensor theory and Paris' Law.

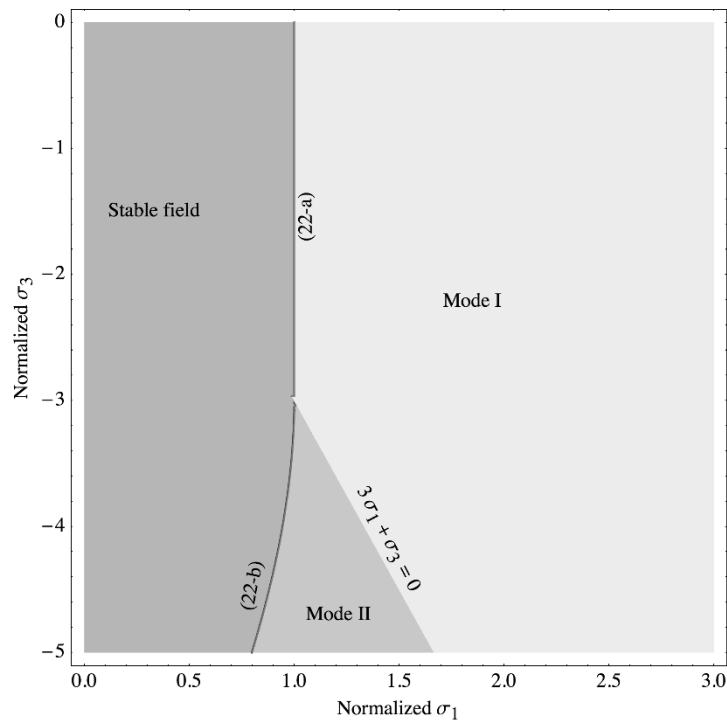
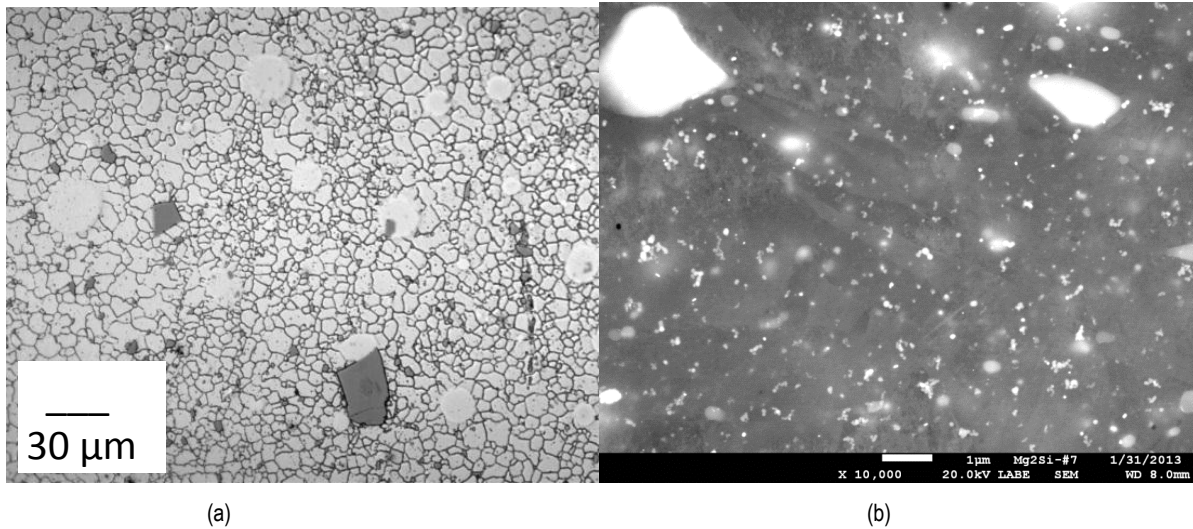


Figure III-33: Failure modes of particles under hydrostatic stress using the traction tensor theory. Under ideal processing, principal stresses should be kept within Mode II to develop fine particle sizes with minimum porosity.



**Figure III-34: Optical (a) and backscattered scanning electron (b) micrographs of the microstructure of the as-extruded Mg<sub>2</sub>Si alloy. Note the presence of coarse intermetallics in (a) of similar size to the as-cast structure and the very fine particles less than 1 μm and the lack of script structure in (b).**

### Technology Transfer Path

The technology transfer for this project will occur late in Phase 2 and during Phase 3. The initial phase will be focused on laboratory development and understanding the Mg alloys from a mechanistic standpoint. After the alloy is understood, the technology transfer will occur in two ways: 1) produce and deliver tubes to Magna Cosma for evaluation; and 2) transfer process knowledge to Transmet, Inc., and MENA. MENA has already contributed alloy feedstock for the high-shear extrusion processing and has played an active role in alloy selection.

Magna Cosma and MENA are cost-sharing partners in the project, and Georgia Institute of Technology and Transmet are subcontractors and were engaged in the project during the appropriate phases.

### Conclusions

A novel method for high-shear extrusion of tubular shapes was developed and demonstrated; a formal patent is to be filed.

A fine-grained Mg alloy containing no rare earth elements, ZK60A, was shown to absorb energy similar to Al alloy 6061 when processed using a commercially viable alloy and the novel high-shear extrusion process.

A new method called the phi model was developed to predict strength in magnesium alloys. Initial modeling results will be used as a guide for extrusion process development to produce desired grain size and texture for high energy absorption. Initial results indicate that the Mg<sub>2</sub>Si alloy may be absorbing energy due to a texture that is favorable for compression, whereas ZK60A appears to have an inherently more isotropic microstructure.

A method to predict the fracture of particles in combined stresses under hydrostatic stress was developed. The method

is used as a guide to select process conditions for extrusion and control the morphology of the eutectic constituent particles in the as-cast structure.

### References

1. DOE—U.S. Department of Energy. 2012. *Lightweight Materials 2012 Annual Report*. DOE/EE-0902, U.S. Department of Energy Vehicle Technologies Office, Washington, D.C. [http://www1.eere.energy.gov/vehiclesandfuels/pdfs/program/2012\\_lightweight\\_materials.pdf](http://www1.eere.energy.gov/vehiclesandfuels/pdfs/program/2012_lightweight_materials.pdf).
2. Molinari A, GR Canova and S Ahzi. 1987. "A self-consistent approach of the large deformation polycrystal viscoplasticity." *Acta Metallurgica* 35:12, 2983–2994. [http://dx.doi.org/10.1016/0001-6160\(87\)90297-5](http://dx.doi.org/10.1016/0001-6160(87)90297-5).
3. Li, DS, S Ahzi, S M'Guil, W Wen, C Lavender and MA Khaleel. 2014. "Modeling of deformation behavior and texture evolution in magnesium alloy using the intermediate  $\phi$ -model." *International Journal of Plasticity* 52:77–94. <http://dx.doi.org/10.1016/j.ijplas.2013.06.005>.
4. Jeffery GB. 1922. The motion of ellipsoidal particles immersed in a viscous fluid. *Proceedings of the Royal Society of London, Series A, Containing Papers of a Mathematical and Physical Character* 102(715):161-179.
5. Pan W, D Li, AM Tartakovsky, S Ahzi, M Khraisheh, and MA Khaleel. 2013. "A new smoothed particle hydrodynamics non-Newtonian model for friction stir welding: Process modeling and simulation of microstructure evolution in a magnesium alloy." *International Journal of Plasticity* 48:189-204. doi:10.1016/j.ijplas.2013.02.013. <http://www.sciencedirect.com/science/article/pii/S0749641913000582>.

## Publications

1. Pan W, D Li, AM Tartakovsky, S Ahzi, M Khraisheh, and MA Khaleel. 2013. "A new smoothed particle hydrodynamics non-Newtonian model for friction stir welding: Process modeling and simulation of microstructure evolution in a magnesium alloy." *International Journal of Plasticity* 48:189-204. doi:10.1016/j.ijplas.2013.02.013.
2. Li DS, S Ahzi, S M'Guil, W Wen, C Lavender and MA Khaleel. 2014. "Modeling of deformation behavior and texture evolution in magnesium using the intermediate phi model." *International Journal of Plasticity*, 52:77–94. <http://dx.doi.org/10.1016/j.ijplas.2013.06.005>.
3. Li D, V Joshi, CA Lavender, M Khaleel and S Ahzi. 2013. "Yield asymmetry design of magnesium alloys by integrated computational materials engineering" *Computational Materials Science* 79:448–455. <http://dx.doi.org/10.1016/j.commatsci.2013.06.045>
4. Li D, CA Lavender, EA Nyberg, X Sun, and MA Khaleel. 2011. "Modeling of Deformation Behavior of Multiphase Wrought Magnesium." Proceedings of The Minerals, Metals & Materials Society 2013 Conference, Orlando, FL. PNNL-SA-81747, Pacific Northwest National Laboratory, Richland, WA.
5. Li D, VV Joshi, CA Lavender, MA Khaleel and S Ahzi. 2013. "Yield Asymmetry Design and Crashworthiness Improvement of Magnesium Alloys by Integrated Computational Materials Engineering." Proceedings of The Minerals, Metals & Materials Society 2014 Conference, San Diego, CA. PNNL-SA-97063.

6. Joshi VV, S Jana, D Li, H Garmestani, EA Nyberg, and CA Lavender. 2013. "High Shear Deformation to Produce High Strength and Energy Absorption in Mg Alloys." In *Magnesium Technology 2014*. PNNL-SA-98774, Pacific Northwest National Laboratory, Richland, WA.

## Submitted for Publication

1. Tabei A, D Li, CA Lavender, and H Garmestani. 2013. *Effects of Morphology and Geometry of Inclusions on Two Point Correlation Statistics in Two Phase Composites*. PNNL-SA-95353, Pacific Northwest National Laboratory, Richland, WA.
2. Li D, and CA Lavender. 2013. Strengthening and Improving Yield Asymmetry of Magnesium Alloys by Second Phase Particle Refinement under Guidance of Integrated Computational Materials Engineering. PNNL-SA-98472, Pacific Northwest National Laboratory, Richland, WA.
3. Tabei A, D Li, CA Lavender, and H Garmestani. 2013. *Modeling of Precipitate Refinement in AZ31 Mg Alloy under Severe Plastic Deformation*. PNNL-SA-98501, Pacific Northwest National Laboratory, Richland, WA.

## Patent

Lavender, CA et al., Provisional Patent Application "Apparatus and Process for Formation of High-Shear Extrusion Structures," Battelle IPID 30343-E PROV.

---

## Magnesium-Intensive Vehicle Developments

---

### Eric A. Nyberg (Principal Investigator)

Pacific Northwest National Laboratory

Phone: (509) 375-2103; Fax: (509) 375-2186

E-mail: [Eric.Nyberg@pnnl.gov](mailto:Eric.Nyberg@pnnl.gov)

### Accomplishments

- Participated on the three-country collaborative, “Magnesium Front End Research and Development” (MFERD) project quarterly Project Technical Committee (PTC) teleconference calls.
- Participated on monthly teleconference calls with United States Automotive Materials Partnership (USAMP) Task Leaders and the U.S. Department of Energy (DOE).
- Coordinated the MFERD annual report including contracting the translation of the U.S. portion.
- Assisted in the organization of the annual project review meeting.
- Updated the [magnesium.pnl.gov](http://magnesium.pnl.gov) bibliographic database (2,700+ publications).

### Future Directions

- As part of the annual review meeting held in October 2013, each task determined the technical gaps in their area of interest. From these gaps, technical objectives were identified. Efforts to complete those technical objectives will be undertaken over the next 18 months. Preliminary plans to address the objectives were presented to the PTC and Project Steering Committee (PSC). The task teams will work together with their counterparts in China and Canada to accomplish these objectives. The international MFERD project is scheduled to conclude in 18 months and will be summarized in a final report.
- The U.S. PTC member will continue to oversee progress of the technical activities within the tasks, assist in editing the final report as needed, interact with the other PTC members, and provide input to the U.S. PSC member.
- Upon request from the DOE–Vehicles Technology (VT) office, provide general information as it pertains to magnesium and magnesium-intensive vehicles.



### Introduction

For magnesium to be used in structural and impact applications in a vehicle, property improvements in strength, ductility, and anisotropy (i.e., increased axial compressive yield strength) must be achieved. Currently, the ability to improve and predict the deformation behavior of magnesium alloys under impact is limited by low compressive strengths

and associated buckling. Through the efforts of many organizations and individuals, Phase I of a Canada-China-USA collaborative project, MFERD, launched in early 2007 to address the challenges for primary body applications of magnesium. The project is sponsored by Natural Resources Canada (NRCan), the Chinese Ministry of Science and Technology (MOST), the DOE, and USAMP, which is a partnership of Chrysler, Ford and General Motors. The goal of MFERD is to develop the enabling technologies in magnesium extrusion, sheet, high-integrity body casting, joining, and assembly and to enrich the knowledge base for magnesium corrosion protection, crashworthiness, fatigue and durability, noise, and vibration and harshness (NVH) performance.

Since its launch, MFERD project team has made remarkable progress. Phase I concluded in 2010. Phase II was initiated in 2011 with the design and construction of a unique demo structure. The structure was comprised of three magnesium components, each produced using different alloys and processes. The components were joined together using two state-of-the-art techniques for magnesium (i.e., friction stir welding and self-pierce riveting). In 2012, with the continued effort of a dedicated and reliable team, this multi-national program entered Phase III. The objectives over the next 3 years are to develop, construct, and test a magnesium-intensive vehicle front-end substructure. Beginning in Phase III, USAMP participation in the MFERD project was through a newly awarded DOE project titled, Demonstration Project to Develop and Construct a Magnesium-Intensive Vehicle Front-End Substructure (AMP-800).

### Approach

The U.S. PTC member, Eric Nyberg from PNNL, will continue to participate on quarterly MFERD teleconference calls. He will attend semi-annual/annual USAMP AMP-800 review meetings as they relate to the progress made contributing to the MFERD project. He will help compile and edit the U.S. contribution to the MFERD annual report. The final MFERD project review meeting will be held in the U.S. in May or June 2015. Mr. Nyberg will help organize and facilitate the meeting. Annually, Mr. Nyberg will attend one national and one international technical conference to stay abreast of the latest developments with magnesium technology and how they relate to multi-material vehicles.

Below are the major technical task areas from the MFERD project and the research activities identified during the annual project review meeting held in October 2013.

#### Crashworthiness

- Characterize advanced alloy.
- Determine multiple stress states and strain rates.

### Fatigue

- Characterize and model base materials and joint materials.
- Model the correlation between the fatigue of base material and the joints.

### Corrosion

- Further develop micro-arc oxidation and micro-arc composite ceramic coating and apply to the demonstration (“demo”) structures.
- Coat the demo structures and compare corrosion results.
- Evaluate surface treatments on fasteners.

### Extrusion

- Further develop advance extrusion technology optimizing heat of feed and exit stock to optimize mechanical performance.
- Receive, distribute, and evaluate new ZE20 alloy for other tasks (e.g., joining, crash, Integrated Computational Materials Engineering (ICME), and corrosion).
- Compare extrudability of ZE20 to traditional Al and Mg extrusion alloys.
- Ascertain modeling details for linking local mechanical properties to crash modeling.

### Sheet

- Address mechanisms controlling the formability of Mg alloys (e.g., activation/de-activation of slip systems when stamping a pre-heated blank using room temperature dies).
- Determine forming limits (e.g., forming limit diagrams, minimum radius).
- Develop better tools for simulations to predict formability.
- Establish hardening laws (stress vs. strain curves).
- Determine the asymmetry vs. anisotropy of deformation (Cazacu type yield functions).
- Failure criterion (pressure sensitive, ... ductile vs. shear).

### Casting

- Super high vacuum die casting:
  - Measure pressure in cavity.
  - Characterize die lube.
  - Investigate the benefit of vacuum.
- China and Canada will study at least one heat-treatable and one non-heat-treatable alloy for process/property correlations:
  - NZK alloy–China.
  - AE-44.2 or ZE 63–Canada.

### Joining

- Evaluate self-pierce riveting (SPR), including coated rivets for corrosion minimization.
- Develop advanced Friction Stir Welding (FSW) and Friction Stir Spot Welding (FSSW) techniques using new tool geometry and design.
- Understand the interfacial reactions occurring in fusion welding and minimize with interlayers.

- Predictive computer aided engineering (CAE) simulation of adhesively bonded joint.

### ICME

- Develop a refined local property model for AZ91D super vacuum die cast (SVDC) shock tower.
- Characterize the microstructure, microtexture, and macrotexture of ZE20.
- Create a visco-plastic self-consistent (VPSC) plasticity model based on initial texture and measured stress-strain data to obtain the material parameters of ZE20.
- Predict local flow stress and texture inside extrusion die and yield stress of the extrudate based on the predicted extrusion texture.

## Results and Discussion

PNNL staff participated in the U.S. annual meeting of the AMP-800 project where all U.S. project members discussed current progress and generated ideas for future research objectives. This meeting helped engage members from different tasks regarding cross-linking topics.

Technical results for AMP-800 were submitted to DOE in an annual report for the contract of the aforementioned “Demonstration Project.” Contributions specifically associated with PNNL efforts on the MFERD project include, but are not limited to, participation in quarterly PTC teleconference calls and monthly USAMP–DOE calls and his coordination of U.S. input to the MFERD annual review, including negotiating a subcontract for translation of the English-to-Chinese version of the U.S. annual report.

Through interaction on the MFERD project, Mr. Nyberg was able to suggest and co-author a paper on corrosion protection using the Micro-Arc Oxidation/Micro-Arc Ceramic Composite (MAO/MCC) coating technology developed in China. This paper (Zhang et al., 2013) was presented at the 70<sup>th</sup> Annual World Magnesium Conference, sponsored by the International Magnesium Association, which was held in May 19-21, 2013 in Xi’an, China and the proceedings published in July 2013.

In addition, [www.magnesium.pnl.gov](http://www.magnesium.pnl.gov), which is maintained by Mr. Nyberg, allows public access to useful information. The website was updated in 2013 and currently houses reference to over 2,700 documents on magnesium research.

## Technology Transfer Path

Technology transfer from this project comes in the form of direct application of magnesium in future automotive designs. The Big 3 U.S. automakers all have specific ideas on niche applications for magnesium. These applications are expected to increase in the next 18 months. Further, technology transfer occurs when subcontractors incorporate methods and materials developed by the project (e.g., advanced joining of dissimilar materials, corrosion mitigation strategies, and advanced alloys).

## Conclusions

This project is unique in its complex link with two other technical projects (MFERD and AMP-800). Bridging the information and communication between these projects has been a point of emphasis, as is providing timely and relevant feedback to the DOE on issues and significant progress. Ultimately, the success of this project will be measured with the conclusion of the other two projects, when the final MFERD summary report is issued.

## Presentations/Publications/Patents

1. Sadayappan, K., Shi, W., Logan, S., and Nyberg, E. 2012-2013 Annual Report: Canada-China-USA Collaborative Research and Development Project: Magnesium Front End Research and Development, 2013 Annual Working Meeting, University of Waterloo, Waterloo, Ontario, Canada, **October 2013**.
2. L. Zhang, B. Jiang, E. Nyberg, M. Liu, Y. Ge. "Characterization and Properties of Micro-arc Composite Ceramic Coatings on Magnesium Alloys," Proceedings of the 70th World Magnesium Conference, International Magnesium Association, **July 2013**.

# Aerodynamic Lightweight Cab Structure Components

## Darrell Herling and Mark T. Smith (Principal Investigators)

Pacific Northwest National Laboratory  
Phone: (509) 375-6905  
E-mail: [darrel.herling@pnl.gov](mailto:darrel.herling@pnl.gov)  
Phone: (509) 375-4478  
E-mail: [mark.smith@pnnl.gov](mailto:mark.smith@pnnl.gov)

## Nona Larson, Industrial Partner

PACCAR Technical Center  
Phone: (360) 757-5365  
E-mail: [nona.larson@paccar.com](mailto:nona.larson@paccar.com)

## Accomplishments

- PACCAR Technical Center engineering staff completed the design review and material specifications for the production A-pillar component that will be used to demonstrate the advanced forming process for an aerodynamic cab structure. The A-pillar component consists of left- and right-hand parts, and the complexity of the part exceeds the conventional forming limits of Al sheet alloys. As a result, the current part is produced from sheet molding compound (SMC) which has an approximate 40 percent weight penalty compared to Al.
- PNNL and PACCAR completed the selection of a Tier 1 supplier to develop the prototype A-pillar forming process, and placed a cost-shared subcontract with Magna Stronach Centre for Innovation (SCFI). Magna will develop tooling and the forming process capable of producing the A-pillar component and deliver 25 each of left- and right-hand A-pillar parts to PNNL/PACCAR.
- Magna completed the forming analysis and simulation of a hybrid hot-forming/cold-stamping process capable of forming the A-pillar component in the X608 Al alloy. Based on the forming analysis, a prototype forming tooling has been designed and is currently being fabricated.

## Future Directions

- Complete fabrication of prototype aerodynamic formed components and deliver 25 left- and right-hand A-pillar parts for testing by PACCAR.
- Conduct material property and finish-system characterization of formed prototype components to confirm the ability to meet PACCAR materials and manufacturing specifications.
- Establish production feasibility for Al components in conjunction with Magna SCFI and PACCAR.

## Technology Assessment

- Target: Develop an elevated-temperature hot-forming process, combined with a cold-finish forming process that

can increase the useable elongation and formability to the equivalent of over 40 percent for a 6000-series Al sheet alloy.

- Target: Demonstrate the feasibility of hot-forming complex Al sheet components requiring overall formability levels of up to 40 percent equivalent tensile elongation, while meeting mechanical property and finish requirements for exterior cab component applications.
- Gap: Current 6000-series Al sheet alloys have desirable strength levels and surface finish characteristics, but lack sufficient formability (>18–20 percent tensile elongation) to allow their use in the manufacture of many aerodynamic cab components and structures.
- Gap: Existing Al hot-forming processes typically result in formed sheet tensile properties below 100 MPa yield strength. This limits the use of hot-formed Al sheet in applications that require higher strengths (150 MPa) for long-term fatigue and dent resistance.
- Gap: Room-temperature (RT) Al forming processes result in mechanical properties with insufficient final-formed ductility. This limits its use in applications where residual ductility is required for riveting and hemming assembly operations.



## Introduction

The objective of this project is to demonstrate manufacturing methods for lightweight materials that will increase the efficiency of Class 8 trucks by enabling more widespread use of mass-saving Al and enabling aerodynamic styling through the use of a new approach to Al sheet forming. The project will develop forming technology that will enable Al sheet to replace sheet steel and molded fiberglass-reinforced composite panels and components, providing individual panel and component weight savings of approximately 40 percent.

## Approach

The project will use an elevated-temperature forming process, which has been developed at PNNL, to demonstrate enhanced formability in 6000-series Al alloy sheet. The high-ductility forming process will enable PACCAR member companies to design prototype cab components with aerodynamic features that would otherwise not be feasible to manufacture. PNNL will develop and optimize a hot-forming plus cold-forming process using sheet tensile specimens and PACCAR will evaluate surface conditions and corrosion behavior of formed specimens. Based on the selected process parameters, PNNL and PACCAR will design and build a prototype component for laboratory testing. The technology for the process developed at PNNL will be transferred to a Tier 1 supplier and project partner, Magna SCFI, who will build full-

scale prototype components. PACCAR will then finish the parts and perform durability testing (e.g., fatigue and corrosion testing). Planned technical steps and milestones include conducting elevated-temperature tensile tests at various strain rates on the alloy provided by PACCAR to develop a constitutive materials relation for use in forming analysis. These data will provide a basis for selection of the temperature and strain rates for subsequent forming trials.

The full-scale component will be modeled at Magna SCFI to determine the optimum forming process cycle. Magna SCFI will use forming simulations to design and fabricate tooling to demonstrate a hybrid hot preforming with room-temperature finish stamping capable of forming an aerodynamic A-pillar component for PACCAR's production Class 8 truck cab. PACCAR will perform surface-oxide characterization and evaluate the e-coat process development to insure good adherence through optimized parameters. Formed prototype A-pillar components will be delivered to PNNL for characterization and testing, including tensile and fatigue tests.

Based on successful forming and manufacturing process compliance of the prototype A-pillar parts, PACCAR will process the parts through the cab assembly and coating processes and perform component and on-cab testing. Component testing will include a durability test (possibly on a cab shake system); corrosion testing; and mechanical properties testing, including tension and fatigue testing.

## Results and Discussion

The second phase of this project has focused on demonstrating the hot/RT forming process on a three-dimensional prototypical A-pillar tray part that required levels of formability that exceed conventional Al sheet forming methods. A series of hot preforming experiments was conducted to evaluate different forming temperatures and post-forming cooling steps. These experiments narrowed the hot-forming step to two temperatures (500 and 540°C) and post-forming cooling by forced air or by water quenching. The hot-forming temperature combined with the post-forming cooling step was designed to re-solutionize the Al sheet so that after cold forming, the paint-bake (20 minutes at 180°C) heat-treatment response could be maximized. The cold-forming step was designed to input a minimum of 5 percent cold deformation in the majority of the formed component, as some level of RT deformation is important in promoting higher strengths in the final component after the paint-bake cycle. Results of this forming development work established several forming sequences and forming parameters that demonstrated significantly enhanced formability in X608 sheet and the ability to meet material yield strength requirements.

During the second half of FY2013, PACCAR evaluated several potential aerodynamic cab components for prototype demonstration of a hybrid Al sheet forming process. From this evaluation the A-pillar component was chosen for prototype development. A solid model of the A-pillar component is shown in Figure III-35. This component is currently manufactured as an SMC part because it cannot be formed

from the X608 Al sheet using conventional room-temperature stamping methods. The SMC component presents a number of drawbacks compared to an Al part, including a 40 percent increase in weight, and is not fully compatible with the series of assembly and finishing operations used in the cab assembly process.



**Figure III-35: Solid model of A-pillar component (~650 mm overall component length).**

After selection of the A-pillar component, PACCAR provided the computer-aided design package for the part to Magna SCFI for evaluation of candidate hybrid forming processes. In support of the Magna SCFI forming simulations of the Al truck A-pillar component, PNNL conducted a series of uniaxial tensile tests of the X608 Al sheet alloy at a series of candidate warm forming temperatures. This series of tests consisted of constant rate tensile test to determine the load/displacement and stress/strain behavior of the X608 alloy at room temperature and four elevated temperatures. The resulting stress/strain data was then utilized by Magna for development of the material constitutive models that provide input to the finite element-based forming simulation models. The tensile tests performed in support of the Magna forming simulation models were focused at a temperature range best characterized as the “warm” forming region. A summary of the tensile test results conducted by PNNL are provided in Table III-3, and the test results show several interesting trends for the X608 alloy at these lower forming temperatures. In particular, the 200 and 250°C test temperatures show an increase in yield strength over the as-received X608 room temperature test results. This increase in strength and corresponding decrease in tensile elongation is likely due to the rapid paint-bake response of the automotive-type sheet alloys. A typical paint bake cycle for these alloys is 20 minutes at 180°C, and in the tensile testing procedure, test specimens were heated at the selected test temperature for a minimum of 5 minutes prior to testing. At test temperatures higher than the standard 180°C paint bake temperature, the 5 minute heating appears to be sufficient to generate a significant age-hardening response in X608. For the higher test temperatures (300 and 350°C), softening occurs and the yields and ultimate strengths are significantly lower than room temperature, with somewhat higher final elongations. The higher temperature tensile test results were found to be consistent with previous PNNL tensile testing of the X608 alloy in the as-received condition. The test results also show that the lower “warm” forming temperatures (200 and 250°C) will result in much higher flow or forming stresses and lower elongations, and therefore will not offer enhanced formability.

**Table III-3: X608 Aluminum Tensile Test Results for Warm Forming Temperatures**

| Specimen Test Temperature (C) | Yield Strength (MPa) | Ultimate Tensile Strength (MPa) | Failure Strain (%) (1) |
|-------------------------------|----------------------|---------------------------------|------------------------|
| 20                            | 152.5                | 270.5                           | 22.6                   |
| 200                           | 273.2                | 330.5                           | 14.4                   |
| 250                           | 195.3                | 195.3                           | 15.5                   |
| 300                           | 113.2                | 118.7                           | 17.0                   |
| 350                           | 60.7                 | 69.0                            | 25.8                   |

(1) Elevated temperature failure strains calculated from specimen gage marks

A view of the initial preforming step of the forming model is presented in Figure III-36, showing areas of strain exceeding 35 percent, which would significantly exceed the limits for X608 during a conventional RT stamping operation.

Figure III-37 shows the model for the second forming stage of the hybrid process. During this step, the preformed component is placed in a second die and formed into the final shape, including forming of the flange features and the outer skin geometry. Based on actual forming trials scheduled for December (FY2014), additional flanging and trimming operations will possibly need to be incorporated into the forming process.

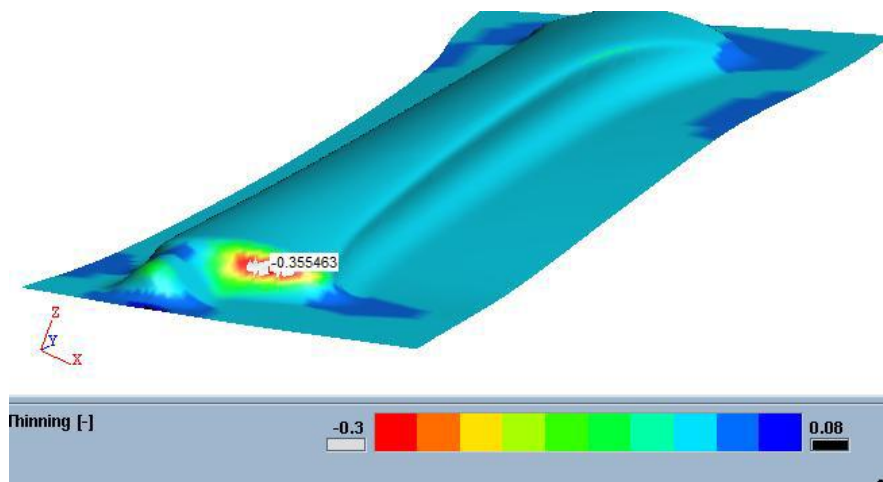


Figure III-36: Forming model simulation of preforming of the A-pillar component showing areas of high strain (up to 36 percent).

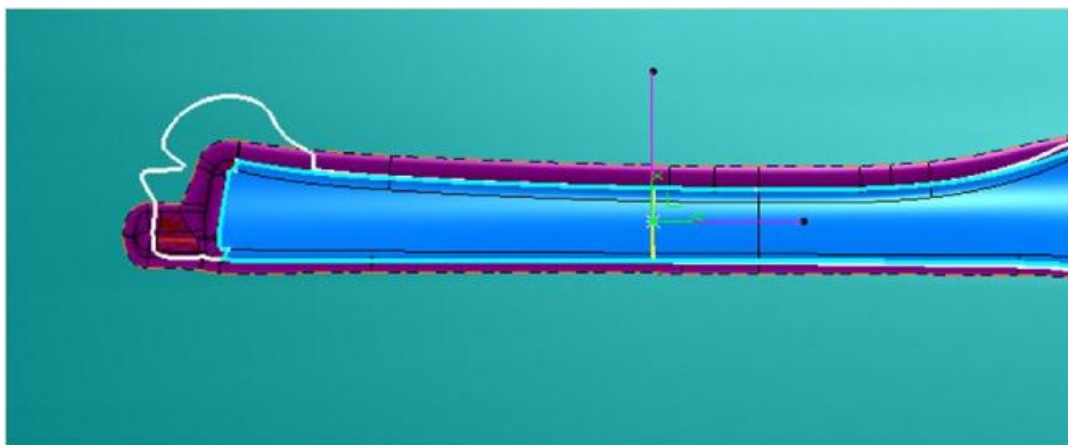


Figure III-37: Forming model showing final A-pillar component shape with flanging outlined in purple. The white outlined area is material that will be formed into a second attachment flange.

The hybrid forming process that is being developed by Magna SCFI will utilize a two-tool operation that includes a hot preforming step followed by either a reheating and final hot forming, or a final room-temperature stamping and flanging operation. Earlier work performed on tray shapes at PNNL indicated that some form of quenching or cooling from the 500–540°C temperature is needed to solutionize the X608 sheet after the warm-forming step, and that a final cold-

forming or coining step is needed to introduce some level of RT strain in the part to insure a proper heat treatment response during the paint-bake finishing step. PNNL has provided testing results from the laboratory stage of the project to Magna SCFI to assist in the development of their hybrid forming process. Figure III-38 shows pictures of the two-stage-forming tools during fabrication in the Magna SCFI machine shops.



Figure III-38: Views of forming tools during fabrication at Magna SCFI.

### Technology Transfer Path

This task is focused on demonstration of the development of a thermomechanical forming process that can achieve significantly enhanced levels of formability in Al sheet materials. PACCAR and its two truck companies have multiple applications in which high formability and good post-forming properties of the Al sheet would allow them to replace low-strength glass-fiber composites in highly shaped aerodynamic panels and components. The project includes participation by Magna SCFI, a major supplier of truck cab structures and components, which will facilitate transfer of the technology to a Tier 1 supplier.

### Conclusions

The current phase of this project is focused on demonstration of a prototype hybrid forming process by PACCAR's Tier 1 supplier, Magna SCFI. A cost-shared subcontract has been placed with Magna SCFI to develop a forming process suitable for truck-volume manufacturing rates and to deliver 25 sets of A-pillar components for evaluation by PACCAR and PNNL. Following evaluation of the A-pillar components, PACCAR will subject the components to a manufacturing demonstration that will include dimensional fit, assembly, and cab finishing process steps, and will evaluate approaches for component durability testing.

### Overall Conclusions

The Properties and Manufacturability project is focused on R&D activities advancing the basic mechanical properties, manufacturability, and cost of lightweight materials towards the levels needed for increased implementation in automotive applications. This project includes 6 different tasks and Principal Investigators that each address an aspect of this materials challenge and seek to fill technical gaps that limit implementation of lightweight materials solutions in current or planned automotive applications. The following highlights summarize the accomplishments of the tasks in this project:

The *Microstructure and Deformation Fundamentals in Lightweight metals* task is focused on experiments and theoretical analyses based on microstructural-based modeling designed to improve the overall understanding of the variables which control austenite stability against straining, and thus mechanical properties of new AHSS products.

- Completed characterization and property testing on the first heat Q&P steels.
- Performed microstructure-based FEA on the first heat Q&P steels for property prediction and identified possible directions for property improvements.
- Produced the second heat Q&P steels based on computational results for the first heat Q&P steels and completed tensile tests.

The task entitled *Enhance Room-Temperature Formability in High-Strength Aluminum Alloys using Pressure Forming* uses high-rate forming to demonstrate enhanced room-temperature formability in sheet metals beyond what is achievable by room-temperature quasi-static forming.

- Demonstrated room-temperature formability improvements in AA7075-T6 through PPF to achieve safe major strains of ~20 percent (engineering) near plane-strain that are comparable to the strains predicted in a cold-stamped steel B-pillar.
- Constructed a theoretical FLD of Al alloy AA7075-T6 as a function of strain-rate by using the constitutive data from the existing literature in combination with the Marciniak-Kuczynski method.

*The Aluminum Formability Extension Through Superior Blanking Process* task aims to enhance the overall formability of aluminum by developing enhanced processes for the blanking, piercing, and trimming operations to extend aluminum formability in the subsequent forming operations. The formability of the Al sheet in conventional automotive stamping is typically limited by the processes that prepare the blank for the stamping operation (i.e., blanking, piercing, and trimming). The overall formability and subsequent quality of the part is often limited by the height of burrs on a sheared surface, the microstructural damage imparted on the sheet, and the dimensional accuracy and the absence of splitting.

- Performed new blanking experiments of AA6111-T4 Al sheets with different clearances. The influence of pre-straining and trimming angle on trimming quality and subsequent stretchability were studied.
- A novel framework was developed to integrate the shearing-affected zone information of the trimming simulations into subsequent stretchability simulations.
- Performed three-dimensional (3D) tensile stretchability simulations of previously trimmed parts with the use of the developed computational framework. Predicted failure mode and ductility showed very good agreement with experiments with different cutting clearances.

*The Non-Rare Earth High-Performance Wrought Magnesium Alloys* task aims to develop high-energy absorption Mg alloys that do not contain rare earth elements

that can replace Al extrusions at a mass savings of 25% (based on density).

- A series of magnesium (Mg) alloys were cast and extruded to produce high-performance Mg alloys with fine grain sizes that appear to be less than 5  $\mu\text{m}$ .
- A Mg alloy containing no rare earth elements that was processed for fine grain size using a low-cost, high-shear extrusion process was shown to absorb energy similar to 6061 Al
- Microstructural modeling has been initiated to help understand the behavior and predict energy absorption.

*The Magnesium Intensive Vehicle Development* task provides technical and administrative leadership on the topic of magnesium materials research, specifically as the Technical Committee Chair-person for the U.S.-Canada-China collaborative Magnesium Front-End Research & Development (MFERD) project.

- Organized and participated in the October 2013 MFERD Annual Meeting in Waterloo, Ontario, Canada
- Produced the 2013 MFERD Project Annual Report, including Chinese translation.

*The Aerodynamic Lightweight Cab Structures* task is developing and will demonstrate an elevated temperature hot forming process, combined with cold finish forming that can increase the useable elongation and formability to over 40% for a 6000-series Al sheet alloy and demonstrate this in an A-pillar fabrication demonstration.

- PNNL and PACCAR completed the selection of a Tier 1 supplier to develop the prototype A-pillar forming process, and placed a cost-shared subcontract with Magna SCFI. Magna will develop tooling and the forming process capable of producing the A-pillar component and deliver 25 each of left- and right-hand A-pillar parts to PNNL/PACCAR.
- Magna completed the forming analysis and simulation of a hybrid hot-forming/cold-stamping process capable of forming the A-pillar component in the X608 Al alloy. Based on the forming analysis, a prototype forming tooling has been designed and is currently being fabricated.

### III.3. Modeling and Computational Materials Science (PNNL) Mechanistic-Based Ductility Prediction for Complex Magnesium (Mg) Castings

**Xin Sun (Principal Investigator)**

Pacific Northwest National Laboratory  
902 Battelle Boulevard  
P.O. Box 999  
Richland, WA 99352  
Phone: (509) 372-6489  
E-mail: [xin.sun@pnnl.gov](mailto:xin.sun@pnnl.gov)

**Mei Li, Industry Partner**

Ford Motor Company  
Phone: (313) 206-4219  
E-mail: [mli9@ford.com](mailto:mli9@ford.com)

**John Allison, University Partner**

University of Michigan  
Phone: (734) 615-5150; Fax: (734) 763-4788  
E-mail: [johnea@umich.edu](mailto:johnea@umich.edu)

**Dean Paxton, Field Technical Monitor**

Pacific Northwest National Laboratory  
Phone: (509) 375-2620  
E-mail: [dean.paxton@pnl.gov](mailto:dean.paxton@pnl.gov)

**William Joost, Technology Area  
Development Manager**

U.S. Department of Energy  
1000 Independence Avenue, S.W.  
Washington, DC 20585  
Phone: (202) 287-6020; Fax: (202) 856-2476;  
E-mail: [william.joost@ee.doe.gov](mailto:william.joost@ee.doe.gov)

Contractor: Pacific Northwest National Laboratory (PNNL)

Contract No.: DE-AC05-00OR22725 & DE-AC06-76RLO1830

**Abstract/Executive Summary**

An integrated experimental and multi-physics modeling approach was adopted to develop the ductility prediction capability for complex Mg castings. The FY 2013 focus included 1) casting preparation with the subsequent location-dependent microstructure and ductility characterization (University of Michigan), 2) microstructure-based finite element modeling considering both intrinsic and extrinsic ductility limiting factors (PNNL), 3) the quality mapping approach for ductility variation prediction using casting process simulations (Ford), and 4) phase-field simulation of

microstructure-pore interaction for magnesium castings (CANMET).

**Accomplishments**

- Completed tensile testing of as-cast magnesium plates with four different aluminum contents and two thicknesses and quantified the influence of aluminum content and thickness on modulus of elasticity, yield strength tensile strength, and elongation at failure. (FY 2013)
- Developed scanning electron microscopy (SEM) and x-ray diffraction (XRD) techniques to characterize the beta-phase volume fraction of the cast and solution-treated Mg alloys. (FY 2013)
- Conducted initial solution treatment study to investigate the influence of beta-phase on tensile properties. (FY 2013)
- Performed synthetic microstructure-based two-dimensional (2D)/three-dimensional (3D) finite element analyses and investigated the effects of large-sized pore and its location as well as the model size on the predicted ductility of Mg castings. (FY 2013)
- Developed microstructure-based intrinsic modeling framework for yield strength and initial hardening with lower length scale inputs, validated modeled predictions with experimental measurements, and examined the influence of  $\beta$ -phase volume fraction and morphology on initial hardening behavior of cast Mg alloys. (FY 2013)
- Examined the impact of different filling profiles on statistical variation of local ductility. (FY 2013)
- Initiated development of kinetic phase-field model to simulate the microstructure evolution and formation of dendritic structures during solidification. (FY 2013)

**Future Directions**

- Complete microstructure mapping for all conditions to be used for micro-mechanical model development.
- Quantify the influence of  $\beta$  phase on tensile properties via solution treatment dissolution studies.
- Determine the influence of machining on the local statistical variation in ductility for excised samples. The results will be used to determine the inherent statistical variation due to processing versus machining and will be incorporated in future models.
- Develop weak link analytical model for ductility and strength in Mg alloys by quantifying the hierarchy of effects of aluminum content, porosity,  $\beta$  phase, externally solidified crystals, thickness, and skin.

- Develop a plate bulge test to extend the results from tensile testing to component-like conditions and eliminate edge effects. Validate the models developed.
- Validate the microstructure-based modeling method based on actual pore distribution data with the incorporation of intrinsic ductility.
- Expand analysis with cohesive zone elements to incorporate failure and predict intrinsic ductility limit.
- Continue development and validation of kinetic phase-field model to simulate the microstructure evolution kinetics during rapid solidification.

### Technology Assessment

- Target: Develop a mechanistic-based ductility prediction method for high-pressure die casting with potential for less than 5 percent error.
- Gap: Conventional computational techniques and most phenomenological approaches have little or no capability for predicting ductility.



### Introduction

Mg castings have found increasing applications in lightweight vehicles because Mg and its alloys are the lightest metallic structural material. However, limited ductility is a critical technical hurdle hindering wider application of Mg castings in vehicle applications. It is well established that microstructure features (e.g., properties and distributions of porosity, brittle eutectic phases, and grain size) can significantly influence the ductility of Mg castings. However, these microstructure features vary from alloy to alloy, with different casting processes, and in different locations on a single casting (Chadha et al., 2007; Song et al., 2009). Although some commercial casting software and material models (Weiler and Wood, 2009a) are available for research of Mg castings, their predictive capabilities typically stop short of predicting the location-dependent stress versus strain behavior, particularly ductility. The purpose of this project is to develop an empirical casting process simulation tool and a mechanistic-based ductility predictive capability to provide a modeling framework applicable to future alloy design and casting process optimizations.

### Approach

The experimental casting was performed by Ford, and the subsequent mechanical and microstructural characterizations were performed at the University of Michigan. Plates with different aluminum contents were cast in eight different conditions and characterized through metallographic preparation. Tensile testing was conducted on samples cut from the plates. The data from the initial characterization will be used to map the microstructure and quantify microstructure features including the size and volume fraction of  $\beta$  phase and

other secondary phase features (e.g., pores and oxide inclusions).

In developing the mechanistic-based ductility prediction capability, two types of ductility limiting factors are considered: intrinsic and extrinsic. Intrinsic factors include features intrinsic to the specific Mg alloy (e.g., phase composition, grain size, morphology, volume fraction, and mechanical properties of the  $\alpha$ -Mg matrix and the eutectic  $\beta$  phase). Extrinsic factors come from the external processes applied to the alloy (e.g., casting and heat treatment processes); these include porosity, segregation, incomplete fill, hot tear and cold shut. The specific alloy and casting process determine both factors, which in turn influence the ductility of the final cast.

For the task on ductility prediction with extrinsic factors (i.e., porosity), our recent observations on the fracture surfaces of AM60 castings indicate that local areal pore fraction may not be the unique and primary factor in determining ductility. Extremely large pores and/or their locations were then considered as another possible ductility limiting factor. The effects of a large-sized pore, its location, and the computational model size on the ductility of Mg castings were subsequently investigated based on synthetic microstructure-based 2D/3D modeling method.

For the tasks on intrinsic ductility prediction of Mg castings, a series of synthetic microstructure samples were generated representing the morphology variations of  $\beta$  phase observed experimentally. Polycrystalline microstructure-based finite element analyses were conducted using the open source finite element package Finite Element All-Wheel Drive (FEAWD), and the effect of  $\beta$ -phase volume fraction and morphology were investigated. The predicted yield strength and initial hardening slopes were validated with representative tensile results from the AM40 and AM70 samples obtained from the experimental castings.

To provide a ductility prediction framework considering process variation, a quality mapping (QM) approach for mechanical properties, which includes both the mean value and the statistic variation of ductility, was developed by Ford. The QM equation for local ductility and yield strength for AM60 was refined using an additional criteria function generated from MAGMASOFT® casting simulations of the generic closure inner panel (GCIP). This model was validated on a production component.

### Results and Discussion

Metallography and tensile testing was completed for super vacuum die cast (SVDC) plates of two thicknesses (2.5 and 5 mm) and four compositions (4, 5, 6, and 7 wt% Al). SEM images of AM40 and AM70 samples are shown in Figure III-39. A significant increase in area fraction and connectedness in  $\beta$ -Mg<sub>17</sub>Al<sub>12</sub> was observed with increasing aluminum content from 4 to 7 wt%. Sections from the plates were also prepared for XRD. XRD whole pattern fitting was completed on detailed scans to measure the weight percent of  $\beta$ . Theoretical predictions for the weight percent of  $\beta$  formed

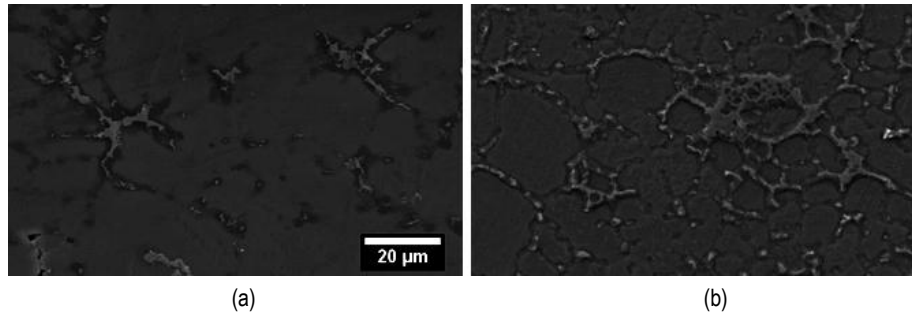


**Figure III-39: Secondary electron images of 5-mm-thick (a) AM40 and (b) AM70. Light gray portions are  $\beta$  phase, gray are  $\alpha$  Mg, dark gray are Al-rich Mg solid solution, black are pores.**

under equilibrium conditions were determined using ThermoCalc (TCMG2 database) for the AM alloys. The XRD-measured values of  $\beta$  were generally lower than those predicted using ThermoCalc.

Tensile testing on 18 samples for each of the 8 as-cast conditions was completed. A representative curve from each condition is shown in Figure III-40. In general, with increasing aluminum content, the ductility (elongation at failure) decreased, yield strength increased, fracture strength decreased, and Young's modulus increased. Note that the thickness dependent Young's modulus reported in Figure III-41(c) is derived from the measured stress-strain curves and subject to further verification. Figure III-41 shows that the effect of aluminum content on these properties was diminished in the thick (5-mm) plate.

In modeling consideration of the extrinsic ductility limiting factors, the size and location of a large pore was investigated. Figure III-42 shows the different-sized models with different large-sized pores at different locations used for the investigation. Figure III-43(a) shows the computational results for large-sized pore effects. Figure III-42(a) and Figure III-43(a) indicate that different ductility governing factors may dominate ductility depending on large pore size and the representative volume element (RVE) size of consideration. Within the valid region of the current modeling method ( $D/L < 13\%$ ), these computational results compare well with experimental observations reported in literature (see Figure III-43(b)). Figure III-43(c) shows the computational results for the location effects of large-sized pores together with experimental results. These results indicate that a threshold distance ( $d \approx 0.9\sqrt{D \cdot L}$ ) from the edge may exist within which a large pore begins to have significantly detrimental effects on sample ductility.

To investigate the impact of intrinsic microstructure features, a series of synthetic microstructures was generated with varying areal fractions and morphology of the  $\beta$  phase present. Polycrystalline finite element models representing AM40 and AM70 with different amounts of  $\beta$  phase present were generated.  $\alpha$ -phase material parameters were selected based on experimental measurements and varied from grain to grain while  $\beta$ -phase material parameters were extracted from first-principle calculations found in the literature (Wang et al., 2011). As shown in Figure III-44, for both AM40 and AM70, the microstructure-based intrinsic models captured the yield strength and initial hardening behavior accurately compared with experimental measurements obtained at University of Michigan. Additional analyses showed that the  $\alpha$ -phase parameters primarily controlled the initial yielding of the ensemble while the morphology and volume fraction of  $\beta$  phase primarily impacted the hardening slope.

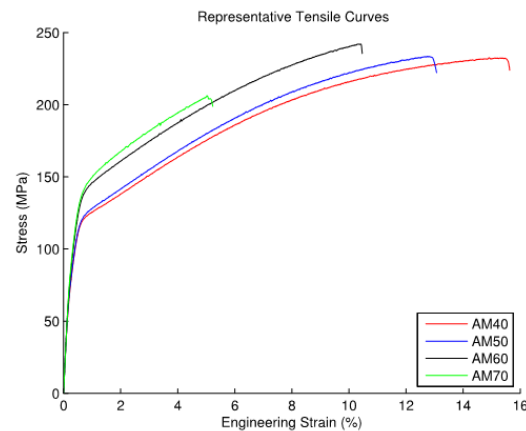


**Figure III-40: Representative tensile curves from each condition.**

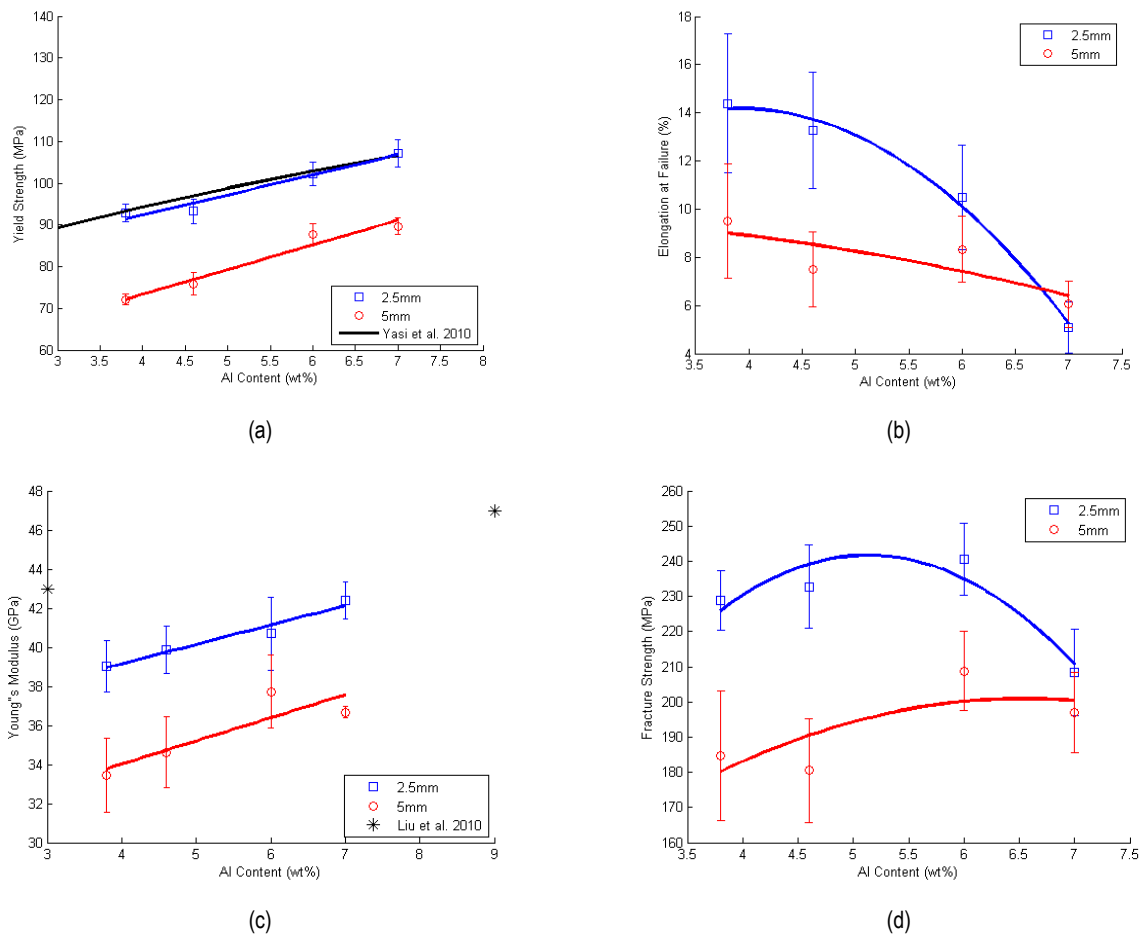


Figure III-41: The influence of aluminum content and plate thickness on (a) yield strength, (b) strain at fracture (ductility), (c) Young's modulus, and (d) fracture strength.

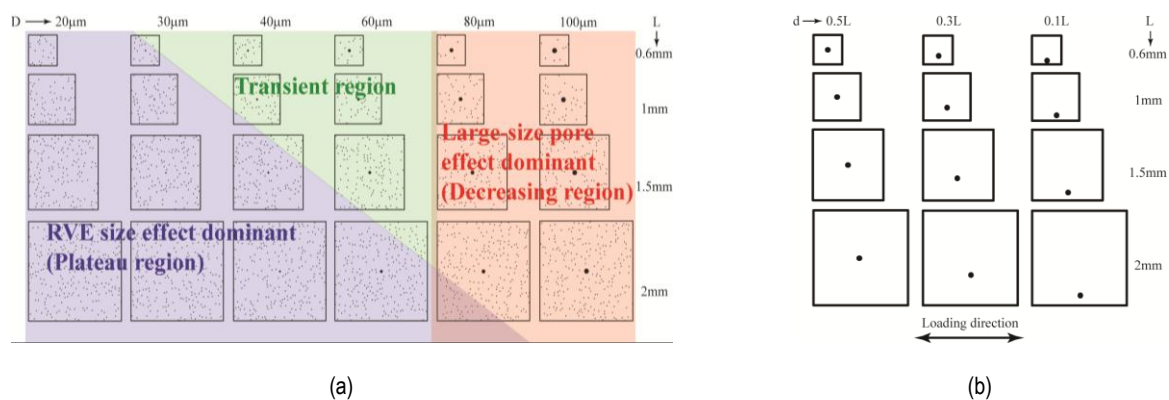
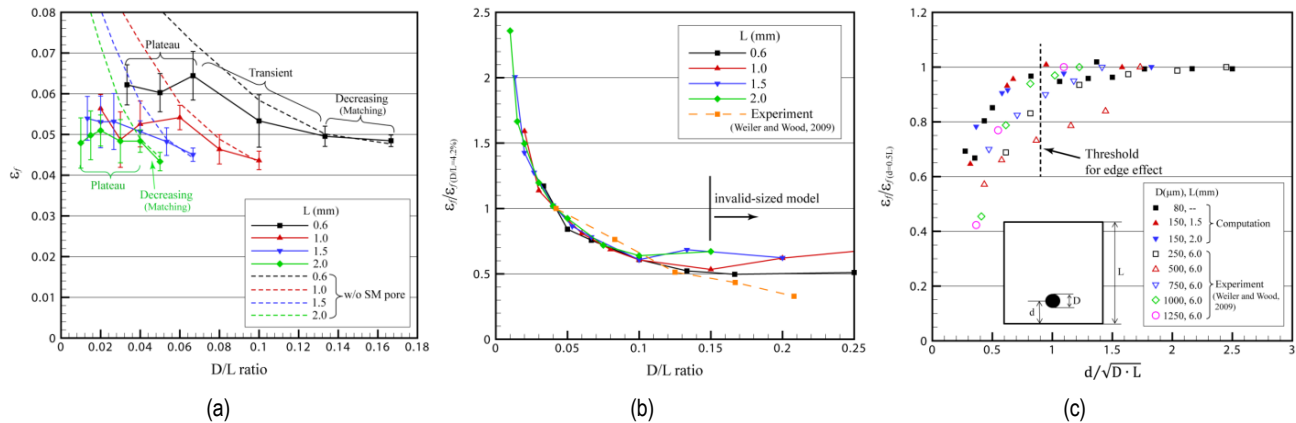
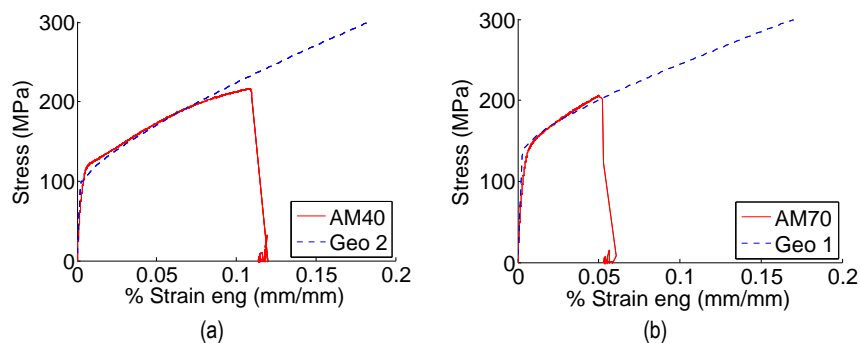


Figure III-42: (a) Different-sized models with different-sized large pores in the center and different ductility governing factors depending on the large pore size and model size; (b) different-sized models with a large pore at different locations from the edge. (L = model size; D = large pore size; d = distance from edge)



**Figure III-43: Comparisons of the computational results for large-sized pore effects (a) with those of the models without the surrounding small pores and (b) with experimental results and (c) comparison of the computational results for the location effects of large-sized pore with experimental results and possible threshold for edge effect.**



**Figure III-44: Microstructure models of (a) AM40 and (b) AM70 validated with experimental measurements.**

Next, the effects of  $\beta$ -phase morphology on predicted hardening behavior were investigated with a series of synthetic microstructures ranging from fully connected  $\beta$  phase network (i.e.,  $\beta$  phase along all cell boundaries) to thick, clumps of  $\beta$ , mimicking the reduction in connectedness observed with increased aluminum content, see Figure III-45(a) and (b). The predicted results shown in Figure III-45(c) indicate that a sample with lower areal fraction of  $\beta$  and a more connected morphology can result in a higher hardening slope than a sample with a higher overall areal fraction but a more clumped  $\beta$  morphology.

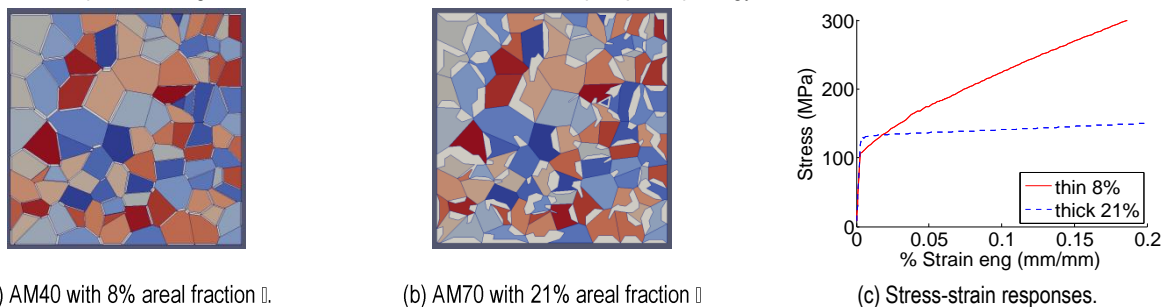


**Figure III-45: Comparison of AM40 sample with 8 percent connected  $\beta$  and AM70 sample with 21 percent clumped  $\beta$ .**

For the QM approach developed by Ford, the prediction of the mean values of elongation showed good agreement with experimental values, as shown in Figure III-46(a). However, significant statistical variation from the mean was observed in the tensile test results of excised samples for the same location across different castings of the GCIP from the same processing condition, i.e., Condition A in Figure III-46(a). A study was undertaken to determine if some of the variation could be coming from slight differences in the filling profile

during the production of individual castings in the course of a single run. MAGMASOFT® simulations were run using high, median, and low filling profiles to determine if differences in the output data would occur. Results showed that minor differences in the filling profile during the course of a production casting run can have an influence on the local ductility in a given location and may account for some of the local statistical variation.

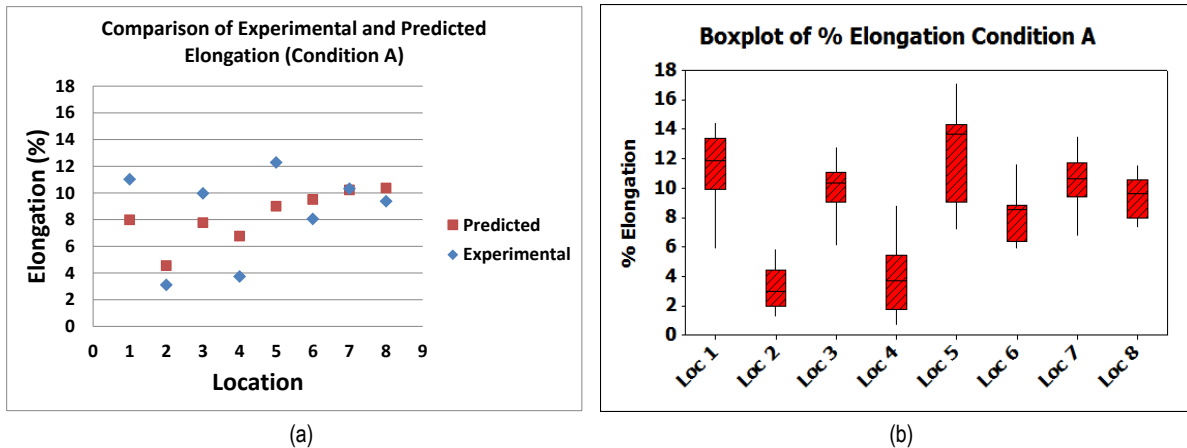


Figure III-46: (a) Comparison of the test and predicted mean elongation (b) box plot of elongation variation.

To explore the feasibility of more advanced computational tools to enhance the microstructure prediction capability of casting process simulation, the computational group CanmetMATERIALS has started developing kinetic phase-field models to simulate microstructure-pore interaction for magnesium alloys during solidification. CanmetMATERIALS is a Canadian federal laboratory in the energy sector with a focus on research in metals and materials in automotive, energy distribution, and power generation. This work builds upon prior work in phase-field simulations of magnesium, building modules which capture the non-equilibrium kinetics and gas pore formation and interaction with microstructure with a focus on high-pressure die-casting conditions (see Figure III-47).

### Technology Transfer Path

The deliverables of this project will be transferred to the original equipment manufacturers, casting producers and the broader lightweight materials and manufacturing community in the forms of technical reports, conference presentations/papers and peer reviewed journal publications. Industry can use the modeling methodology and results to improve performance of materials and manufacturing processes and reduce the number of prototypes needed to validate a design, saving time and cost.

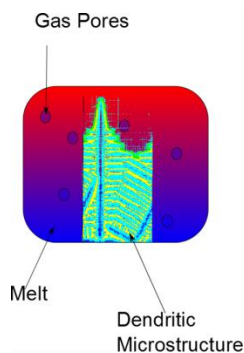


Figure III-47: Phase-field-predicted dendritic microstructure and its interaction with gas pores during solidification of high-pressure die-casting process.

### Conclusion

Impressive progress has been made on both experimental and modeling fronts in FY 2013 by project contributors from various institutions using a comprehensive approach. Tensile testing was completed for all conditions and the shape and volume fraction of  $\beta$ -Mg<sub>17</sub>Al<sub>12</sub> was quantified. In general, with increasing aluminum content, ductility decreased, yield strength increased, fracture strength decreased, and Young's modulus increased.

Modeling of extrinsic ductility limiting factors (i.e., the effects of a large-sized pore and its location) indicated that, depending on the large pore size and the model size, three different regions may exist: 1) large pore effect dominant region, 2) pore interaction dominant plateau region, and 3) pore interaction dominant transient region. The predictions indicate that near-edge large pores, if any, may possibly be a primary source for the wide variation of ductility of Mg castings. These predictions have been validated with experimental observations reported in the literature.

The intrinsic model was validated against experimental results. Analyses showed the typical increase in areal fraction of  $\beta$  phase increase hardness. However, the results also showed that for the same areal fraction, a more connected morphology increases initial hardening slope.

QM showed that minor differences in the filling profile during the course of a production casting run can have an influence on the local ductility in a given location and may account for some of the local statistical variation.

### Presentations/Publications/Patents

1. Barker, E.I., Choi, K.S., Sun, X., Deda, E., Allison, J., Li, M., Forsmark, J., Zindel, J., Godlewski, L. Microstructure Based Modeling of Cast Mg Alloys. Submitted to *Computational Materials Science*, 2013.
2. Choi, K.S., Li, D.S., Sun, X., Li, M. and Allison, J. Effects of Pore Distributions on Ductility of Thin-Walled High Pressure Die-Cast Magnesium. *SAE Technical Paper* no. 2013-01-0644, In SAE 2013 World Congress, April 16-18, 2013, Detroit, Michigan.
3. Choi, K.S., Sun, X., Li, D.S., Li, M. and Allison, J. Effects of Pore Distribution Features on Ductility of Mg Castings. In *2<sup>nd</sup> World Congress on Integrated Computational Materials Engineering*, July 7-11, 2013, Salt Lake City, Utah.
4. Choi, K.S., Barker, E.I. and Sun, X. Influence of a Large-Sized Pore and its Location and on Ductility of Thin-walled High Pressure Die Casting Magnesium, revision submitted to *Metallurgical and Materials Transactions A*, 2013.
5. Deda, E., Li, M., Zindel, J., Godlewski, J., Sun, X., Allison, J. Effects of aluminum content and plate thickness on the microstructure and tensile properties in AM series magnesium alloys. Poster presented at *TMS 2013 142nd Annual Meeting & Exhibition*, March 3-7, 2013, San Antonio, Texas.
6. Sun, X., Choi, K.S. and Li, D.S. Predicting the Influence of Pore Characteristics on Ductility of Thin-Walled High Pressure Die Casting Magnesium. *Materials Science and Engineering A* 2013, 572, pp. 45-55.

### References

1. Chadha, G., Allison, J.E. and Jones, J.W. The Role of Microstructure on Ductility of Die-Cast AM50 and AM60 Magnesium Alloys. *Metallurgical and Materials Transactions A* 2007, 38, pp. 286–297.
2. Song, J., Xiong, S.M., Li, M. and Allison, J.E. The correlation between microstructure and mechanical properties of high-pressure die-cast AM50 alloy. *Journal of Alloys and Compounds* 2009, 447, pp. 863-869.
3. Wang, J., Shang, S.-L., Wang, Y., Mei, Z.-G., Liang, Y.-F., Du, Y., Liu, Z.-K., First-principles calculations of binary Al compounds: Enthalpies of formation and elastic properties. *Calphad* 2011, 35 (4), 562-573.
4. Weiler, J.P. and Wood, J.T. Modeling fracture properties in a die-cast AM60B magnesium alloy I—Analytical failure model. *Materials Science and Engineering A* 527 (2009) 25-31.
5. Weiler, J.P., Wood, J.T., Modeling fracture properties in a die-cast AM60B magnesium alloy II—The effects of the size and location of porosity determined using finite element simulations. *Materials Science and Engineering A* 527 (2009) 32-37.
6. Yasi, J.A., Hector, L.G. Jr., Trinkle, D.R., First-principles data for solid-solution strengthening of magnesium: From geometry and chemistry to properties, *Acta Materialia* 58 (2010) 5704-5713.
7. Liu, Z.K., Zhang, H., Ganeshan, S., Wang, Y., Mathaudhu, S.N., Computational modeling of effects of alloying elements on elastic coefficients. *Scripta Materialia* 63 (2010) 686–691.

## III.4. Multi-Material Enabling—Oak Ridge National Laboratory (ORNL)

### **C. David Warren, Field Technical Monitor**

Oak Ridge National Laboratory  
1 Bethel Valley Road  
Oak Ridge, TN 37831  
Phone: (865) 574-9693; Fax: (865) 574-6098  
E-mail: [warrencd@ornl.gov](mailto:warrencd@ornl.gov)

### **William Joost, Technology Area Development Manager**

U.S. Department of Energy  
1000 Independence Avenue, S.W.  
Washington, DC 20585  
Phone: (202) 287-6020; Fax: (202) 856-2476  
E-mail: [William.Joost@ee.doe.gov](mailto:William.Joost@ee.doe.gov)

Contractor: Oak Ridge National Laboratory  
(ORNL)  
Contract No.: DE-AC05-00OR22725

Significant weight reduction in future vehicle structures will likely occur through the adoption of a variety of materials, including light metals. The obstacles to incorporating these materials include material cost and manufacturability. In addition, critical technologies are needed to enable the cost-effective performance necessary for application of these materials. Those technologies include multi-material joining, corrosion prevention, and nondestructive evaluation (NDE).

Corrosion of alternative candidate automotive materials is a factor that could potentially limit their adoption. Research is needed on mitigating the corrosion of magnesium (Mg), aluminum (Al), and high-strength steels (HSSs) in an automotive environment. Corrosion issues are even more critical for dissimilar material joints, especially when the materials to be joined have a significant difference in electrochemical potentials. Corrosion mitigation strategies are being developed. The quality of material joints is critical to their application. Nondestructive inspection methods for verifying joint integrity and material quality are needed. Those methods need to be rapid, reliable, repeatable, and easily integrated into automotive production plants. Additionally, strategies for mitigating residual stresses are critical to joint integrity.

This project consists of four tasks critical for the welding, inspection, and development of lightweighting metal structures with dissimilar metals: (1) develop an understanding of protective coating on Mg alloys; (2) develop a rapid, reliable spot weld inspection method for use in manufacturing plants; (3) improve the fatigue life of advanced HSS welds, and (4) design joints for Al-steel chassis structures.

## ACTIVITY AND DEVELOPMENTS

### Understanding Protective Film Formation by Magnesium (Mg) Alloys in Automotive Applications

**Michael P. Brady (Principal Investigator)**

Oak Ridge National Laboratory  
Phone: (865) 574-5153; Fax: (865) 576-5413  
E-mail: [bradymp@ornl.gov](mailto:bradymp@ornl.gov)

**Kinga A. Unocic (Principal Investigator)**

Oak Ridge National Laboratory  
Phone: (865) 574-0996; Fax: (865) 576-5413  
E-mail: [unocicka@ornl.gov](mailto:unocicka@ornl.gov)

**Bruce Davis, Partner**

Magnesium Elektron North America (MENA)  
Phone: (618) 709-502  
E-mail: [bruce.davis@magnesium-elektronusa.com](mailto:bruce.davis@magnesium-elektronusa.com)

#### Accomplishments

- Successfully completed advanced transmission electron microscopy (TEM) characterization of film formation by specimens under immersed aqueous conditions at ambient temperature as a function of exposure time (4–48 h) and alloy type (AZ31B, E717, and ultra-high purity (UHP) Mg). The objective was to elucidate the nanoscale film segregation tendencies of Al, rare earth (RE), zinc (Zn), and zirconium (Zr) alloy additions. (FY 2013).
- Successfully demonstrated secondary ion mass spectrometry (SIMS)/D<sub>2</sub><sup>16</sup>O and H<sub>2</sub><sup>18</sup>O isotopic tracer studies of film formation by Mg alloys under immersed aqueous and air-steam exposure conditions, providing new insights into film growth mechanisms and the relative penetration of hydrogen and oxygen species. (FY 2013)

#### Future Directions

- Expand advanced characterization by TEM to aqueous environments containing corrosive salt species to better understand how the salt species alter alloy addition segregation into the films.
- Complete in-progress aqueous and air-steam tracer studies. Attempt to expand tracer studies to aqueous environments containing corrosive salt species to better understand how the film growth mechanism is affected.
- Assess the potential of small angle neutron scattering (SANS) to provide new insight into film formation on Mg alloys and conversion coatings.
- Assess the feasibility of using atom probe tomography (APT) to provide 3-dimensional (3D) quantification of the chemistry at the atomic scale in bulk Mg alloy and in the

alloy–surface layer interface to characterize corrosion-driven alloy clustering or precipitation phenomena.

#### Technology Assessment

- Target: Gain improved understanding of protective film formation by Mg alloys and conversion coatings as a function of alloy chemistry and impurities, microstructure, and exposure conditions.
- Target: Provide a fundamental basis for design and optimization of new Mg alloys and/or conversion coating processes to improve corrosion resistance under automotive-relevant conditions.
- Gap: The lack of corrosion prevention strategies is a key factor limiting more widespread use of Mg alloys in automotive applications.
- Gap: Alloying has been shown to modify surface film performance; however, a detailed understanding of how and why is currently lacking. Such an understanding is needed to develop improved alloys and surface treatments/coatings to permit more widespread adoption of Mg alloys.



#### Introduction

Magnesium alloys are of great interest to automotive manufacturers because of their attractive combination of low density, good strength, amenability to casting, ease of recycling, and other qualities. A major obstacle to the widespread adoption of Mg alloys is susceptibility to corrosion [Song and Atrens 2007; Song 2005; Gray and Luan 2002]. Surface treatments and/or coatings are needed for many applications [Gray and Luan 2002]; these result in increased cost and can be a source of component durability issues. The inability of Mg alloys to establish a continuous, fully protective surface film under many exposure conditions is a key factor underlying their susceptibility to corrosive attack. Alloying and/or conversion coatings have been shown to modify surface film performance; however, a detailed understanding of how and why they do so is currently lacking. Such an understanding is needed to develop improved alloys and surface treatments and/or coatings to permit more widespread adoption of Mg alloys.

The goal of this effort is to improve understanding of how alloy composition, microstructure, and exposure conditions affect the establishment, continuity, nature, and growth of protective films on Mg alloys. To provide insight into film

formation, this project has employed advanced characterization techniques not previously widely applied to Mg surface film formation. The project is a systematic study of the formation of aqueous films and their evolution over time on two representative Mg alloy classes—the Mg-Al-Zn alloy AZ31B and RE- and zirconium-modified Elektron 717 (E717, based on a ZE10A type alloy)—relative to UHP Mg. These results will serve as baseline information for evaluating film formation in corrosive environments (e.g., salt species) and for modified alloy compositions and conversion coatings. Both bare, untreated Mg alloy surfaces and conversion-coated surfaces are being studied. The corrosion of Mg alloys has been the subject of intense research resulting in significant gains in the mechanistic understanding of both pure Mg and Mg alloys in recent years. These studies have identified the inability of Mg alloys to establish a continuous, fully protective surface film under many exposure conditions as a key factor underlying their susceptibility to corrosive attack. Deliverables in this project are related to the application, development, and suitability assessment of advanced characterization techniques to provide new insights into Mg alloy corrosion.

### Approach

Ambient corrosion of Mg differs from that of many corrosion-resistant structural alloy classes in that the protective surface films can become quite thick, on the order of tens to hundreds of nanometers, rather than the few nanometers typically encountered in stainless steels [Seyeux 2009; Hara 2007; Nordlien et al., 1997]. As a result, corrosion resistance is influenced not only by classical thin film electrochemical passivity considerations but also by thermodynamic and kinetic considerations typically encountered in thick film, high-temperature alloy oxidation phenomena.

The experimental approach merges methods used to study both ambient and high-temperature corrosion, leveraging extensive and unique expertise in these areas at Magnesium Elektron North America (MENA) and Oak Ridge National Laboratory (ORNL). World-class characterization capabilities available at ORNL will be used to more fully probe and understand the chemical, morphological, and structural features of the surface films formed on Mg alloys and conversion coatings as a function of alloy composition, microstructure, and exposure condition.

A major goal of the project is to assess which advanced characterization techniques are most amenable to providing new insights into film formation on Mg alloys. This is a key activity, as Mg alloys are notoriously difficult to work with. Sample procedure techniques must be developed, and not all proposed characterization approaches will prove effective. Advanced characterization approaches to be investigated include (1) development of ex situ focused ion beam (FiB) sample preparation and TEM of film/surface layer cross sections, (2) SIMS  $D_2^{16}O$  and  $H_2^{18}O$  tracer studies of Mg alloys/coatings under aqueous and gaseous vapor immersion conditions to gain insight into the growth aspects of the surface films, (3) ex situ neutron scattering (e.g., SANS, inelastic) to characterize Mg alloy surface film nanoporosity

and hydrogen species incorporation as a function of alloy composition and exposure condition, and (4) APT to provide 3D quantification of chemistry at the atomic scale in the bulk Mg alloy and near the alloy-surface layer interface to characterize corrosion-driven alloy clustering or precipitation phenomena.

Advanced TEM sample preparation techniques were successfully developed in FY 2012 and applied in FY 2013 to Mg alloy aqueous film formation as a function of exposure time and alloying additions. SIMS isotopic tracer techniques were also successfully developed and demonstrated in FY 2013 for film formation by Mg alloys under aqueous and air-steam exposure conditions.

### Results and Discussion

Cross-section TEM/scanning TEM data, supplemented by x-ray photoelectron spectroscopy (XPS), SIMS, scanning electron microscopy (SEM), and x-ray diffraction (XRD), were used to follow the evolution of the chemistry and structure of films formed on UHP Mg, AZ31B, and E717 immersed in room temperature (RT), high-purity deionized water (DI) water [Unocic et al., 2013]. The absence of galvanic second phases and the low impurity levels in the UHP Mg resulted in a lower open-circuit potential (OCP) than was found in commercial-purity Mg, AZ31B, and E717 alloys by potentiodynamic screening in RT DI water saturated with  $Mg(OH)_2$  (Figure III-48). However, this apparent benefit for UHP Mg did not cause it to maintain lower film growth rates (as measured by specific mass change vs. time) than the AZ31B and E717 alloys during longer-term 24, 48, and 200 h immersion exposures in RT DI water (Figure III-49). This result is attributed to the fact that alloying additions in AZ31B and E717 were segregated to the film and metal–film interface region, which had the beneficial effect of slowing longer-term film evolution and growth.

The films formed on all three materials in RT DI water primarily consisted of MgO; minor amounts of  $Mg(OH)_2$  and  $MgCO_3$  were detected primarily in the film surface regions. Film thickness was non-uniform and varied across the sample surface for all three alloy types and all the exposure times. However, after 48 h of exposure, the thickest film, with a maximum depth of  $\sim 10 \mu m$ , was observed on UHP Mg. The films formed after 48 h on AZ31B and E717 were much thinner, on the order of  $\sim 2\text{--}3 \mu m$  maximum depth, with AZ31B consistently yielding the thinnest films in cross-section imaging. Hydrogen was detected throughout the film thickness by SIMS in all three materials (Figure III-50), suggesting an in-progress inward hydration transition of the initially formed MgO into  $Mg(OH)_2$  at the water interface, with decreasing levels of hydration moving through the film thickness to the underlying metal. The SIMS data indicated possible penetration of hydrogen into the underlying metal, particularly for E717 and AZ31B. Preliminary analysis also suggested that the films were inward growing, with the  $^{18}O$  species introduced during the first 4 h of exposure remaining enriched near the outer film surface.

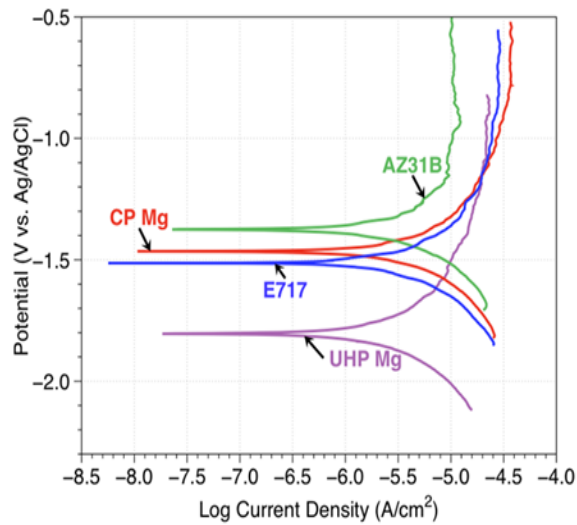


Figure III-48: Potentiodynamic curves generated in RT DI water saturated  $\text{Mg}(\text{OH})_2$  [Unocic 2013].

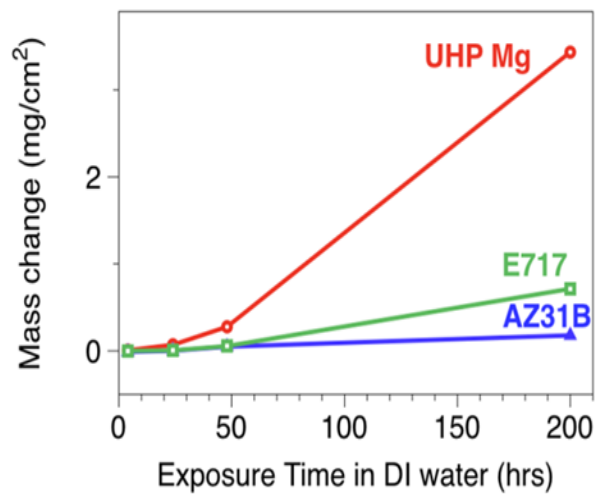


Figure III-49: Specific mass change data after immersion in RT DI water [Unocic 2013].

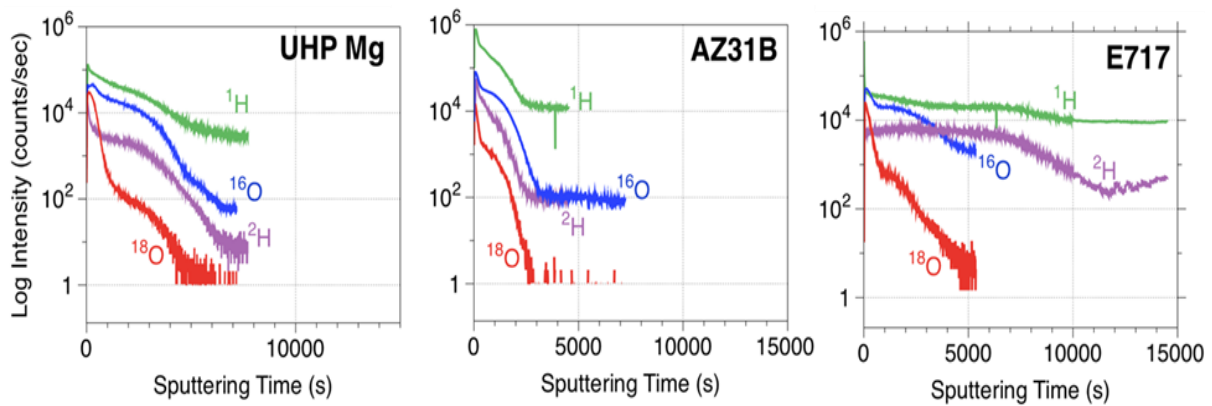


Figure III-50: Preliminary SIMS sputtering rate through films formed by 4 h immersion in RT  $^1\text{H}_2^{18}\text{O}$  water followed by 20 h immersion in  $^2\text{H}_2^{16}\text{O}$  water ( $\text{D}_2\text{O}$ ).

Figure III-51 presents a high-angle annular-dark-field (HAADF) image of the film cross-section formed on AZ31B after 24 h immersion in RT DI water. The image shows the structural appearance of the film throughout the entire thickness, with some porosity evident, and a bright underlying thin area at the film–metal interface indicative of heavier element segregation. EDS x-ray maps show that Al was present throughout the entire film thickness. XPS analysis confirmed that Al was present throughout the entire film thickness. XPS analysis confirmed that Al was present in the film in an oxidized state at a level of 4–5 atomic %. These data, combined with the electron diffraction analysis, indicate that the Al is likely incorporated in some fashion in the  $\text{MgO}$  phase, but likely not as discrete  $\text{MgAl}_2\text{O}_4$  or  $\text{Al}_2\text{O}_3$  phases. The EDS maps also show Zn enrichment at the metal–film interface, consistent with the bright thin area at the film–alloy interface region in the HAADF image. Several small Zn-containing precipitates were also observed within the film.

Cross-section HAADF–Scanning Transmission Electron Microscope (STEM) images of the film formed on E717 after 48 h immersion in RT DI water are shown in Figure III-52. Extensive Zn- and Zr-rich nanoprecipitates were observed in the film formed on E717. Using fast Fourier transform analysis, the precipitates were identified as  $\text{Zn}_2\text{Zr}_3$ . Similar  $\text{Zn}_2\text{Zr}_3$  precipitates were observed in the underlying alloy; they suggest that the  $\text{MgO}$  film was inward growing, consistent with the SIMS data, with the  $\text{Zn}_2\text{Zr}_3$  particles from the underlying metal entrapped in the growing  $\text{MgO}$  film as the corrosion proceeded inward. Enrichment of Zn at the metal–film interface was also observed for E717, similar to AZ31B. Enrichment of RE additions in E717 was also observed at the metal–film interface, but only in a local region near where a discrete RE-, Zr-, Zn-rich article was observed in the underlying metal near the metal–film interface.

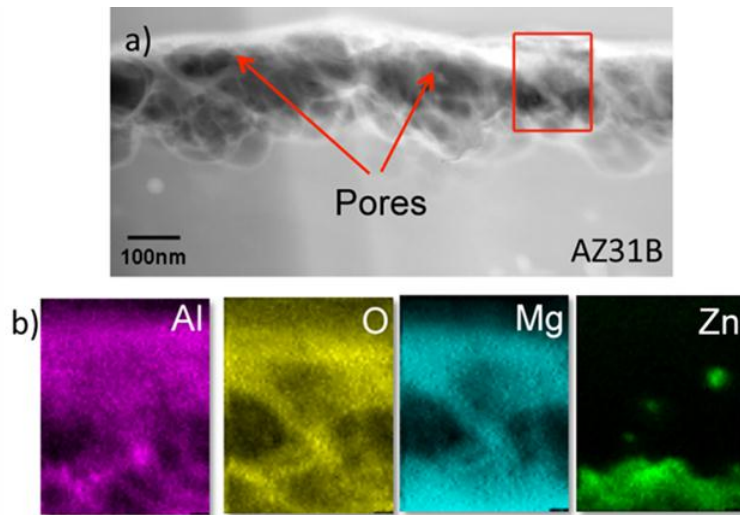


Figure III-51: (a) HAADF-STEM image of the film cross section formed on AZ31B after immersion in RT DI water for 24 h. (b) EDS x-ray maps of Al, Mg, oxygen, and Zn [Unocic 2013].

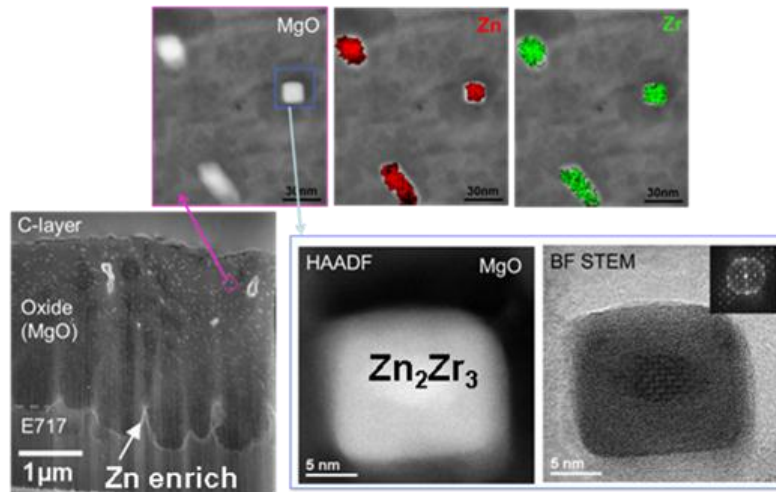


Figure III-52: HAADF-STEM image of the cross-section of the film formed on E717 after exposure for 48 h in RT DI water. Higher magnification images of the precipitates present in the MgO film in conjunction with associated EDS Zn and Zr elemental maps [Unocic 2013].

### Technology Transfer Path

Basic understanding of film formation on Mg alloys and its behavior in different environments will provide insight into how improvements can be made in designing and optimizing new Mg alloys and conversion coatings to improve corrosion resistance under automotive-relevant conditions. The current gap in basic understanding of film formation mechanics and kinetics, and the correlation with alloy chemistry and microstructure, is a key barrier to improved corrosion resistance to permit more widespread use of Mg alloys in automotive applications. Teaming with MENA, a leading Mg alloy producer, on this project will provide a direct path for incorporating insights from this effort into practice.

### Conclusions

The more protective film behavior for AZ31B in RT DI water is attributed to the presence of Al in the MgO film and enrichment of Zn at the metal-film interface. Although it is not as protective as AZ31B, E717 shows a slow film growth rate compared with UHP Mg that is attributed to Zn enrichment at the metal-film interface; the nanosize  $Zn_2Zr_3$  precipitates in the E717 film may also play a beneficial role. The film growth behavior established for UHP Mg, AZ31B, and E717 in RT DI water will serve as a baseline comparison condition for continued SIMS isotopic tracer studies in FY 2014. This research will also provide a baseline for the study of the effects of salt species on the film growth mechanism on AZ31B and E717, both bare and with conversion coatings.

---

# Online Weld Quality Monitor and Control with Infrared Thermography

---

## Zhili Feng (Principal Investigator)

Oak Ridge National Laboratory  
Phone: (865) 576-3797; Fax: (865) 574-4928  
E-mail: [fengz@ornl.gov](mailto:fengz@ornl.gov)

## Contributors:

Jian Chen, Ralph B. Dinwiddie and Wei Zhang, ORNL

## Accomplishments

- Completed real-time and post-weld infrared (IR) data collection on various resistance spot welds made of different steels, thickness gauges, coatings and stack-ups. (FY 2013)
- Refined the IR data analysis algorithm to accurately identify weld attributes, including weld nugget size, thickness, shape, and some welding defects (lack-of-fusion, excessive indentation, and welding expulsion). (FY 2013)
- Completed the first version of the automated inspection software and integrated it into the prototype system. (FY 2013)
- Performed a field demonstration of the prototype system to show its feasibility and robustness. (FY 2013)
- Developed the first prototype of a fully automated online real-time IR inspection system that meets the inspection requirements of a mass production environment and can be readily integrated into the existing production line. (FY 2012)
- Identified new IR signatures and refined IR data analysis algorithms with improved accuracy and reliability for both real-time and postmortem applications. (FY 2012)
- Generated a reference weld quality database consisting of nugget size, weld thickness (indentation depth), weld shape, and stuck welds and porosity for a wide range of steels, coatings, thicknesses, and stack-up configurations. (FY 2011)
- Demonstrated the overall satisfactory system performance for both real-time and postmortem inspection for a wide range of spot weld conditions under laboratory testing conditions. (FY 2011)

## Future Directions

- Conduct beta testing of both the real-time and postmortem prototype systems with additional welds made in an automotive assembly line production environment.
- Perform additional field demonstrations of the IR inspection expert system to confirm the feasibility and robustness of the system to original equipment manufacturers (OEMs) and other stakeholders.
- Discuss with automotive OEMs, including part suppliers, the potential for technology transfer and commercialization following beta testing.

## Technology Assessment

- Target: A spot weld quality inspection system based on IR thermography that can detect a stuck weld, weld nugget size (up to 0.2 mm resolution), and surface indentation (up to 0.1 mm resolution) in both the two-layer (2T) and three-layer (3T) stack-up configurations.
- Target: An inspection system that can meet or exceed the inspection cycle time requirements dictated by the mass production assembly line environment including (1) collection time of less than 2–3 s for online inspection, (2) collection time of less than 5–10 s for offline inspection, and (3) data analysis and decision making time of less than 1–2 s.
- Gap: Automated, robust, efficient IR image acquisition and analysis algorithms and hardware systems do not currently exist to determine weld quality within the targeted time period and with the necessary quality and weld attribute spatial resolution.



## Introduction

Resistance spot welding (RSW) is the most widely used technology for assembling auto body structures. Variations in welding conditions, part “fit-up,” and other production conditions inevitably occur in the complex, high-volume body-in-white (BIW) assembly process. These variations can result in out-of-tolerance joints that impair the quality and performance of the vehicle. The increased use of advanced high-strength steels (AHSSs) and other lightweight metals is expected to pose even more stringent requirements for joint quality. Despite extensive R&D efforts over the years, nondestructive weld quality inspection remains a critical issue for the auto industry, largely because of the unique technological and economic constraints of the auto production environment: any weld quality inspection technique must be fast, low-cost, and low in false rejection rate and must not interfere with the highly automated welding fabrication process. Currently, inspection systems that meet these requirements do not exist.

This project aims to develop a field-deployable, on-line weld quality monitoring method based on IR thermography. A distinct advantage of IR thermography as a non-destructive evaluation (NDE) tool is its nonintrusive and noncontact nature. This makes IR-based NDE especially attractive for highly automated BIW assembly lines

## Approach

The project consists of the following major tasks to achieve the project goal.

- Refine and optimize field-deployable IR measurement techniques that can reliably detect the characteristic

thermal signature patterns of various weld quality attributes both in real time and in postmortem online inspection.

- Develop robust IR image analysis software that can, in real time, analyze the IR thermal image for the characteristic signatures of various weld defects and weld joint configurations to provide a quantitative measure of the quality.
- Develop a prototype IR weld quality monitoring expert system (hardware and software) that is cost-effective and suitable for field demonstration.
- Validate and demonstrate the effectiveness and robustness of the technology for a wide range of spot welds made with different steel grades, coatings, thicknesses, and stack-up configurations with varying quality attributes (e.g., nugget size, indentation depth) commonly encountered in BIW production;
- Identify and work with potential industry entities for technology transfer and eventual commercialization.

A unique prerequisite for IR thermography-based NDE technology in automotive applications is that the surfaces of the materials and welds cannot receive any special treatment. All the development and testing in this project is on as-welded or as-received surfaces.

## Results and Discussion

In previous years, an initial version of an IR image acquisition system and a data analysis algorithm was developed that demonstrated its feasibility for both real-time (online) and post-weld (offline) inspection applications. A wide range of welds made with different steel grades, coatings, thicknesses, and stack-up configurations were produced. Welds with varying attributes (e.g., nugget size, indentation depth) were intentionally made by carefully controlling the

welding parameters. Tests showed that the system was able to positively quantify the weld nugget size, shape, and thickness and identify welding defects including lack-of-fusion and excessive indentation. The FY 2013 efforts were focused on three major areas: (1) further refinement of the data analysis algorithm, (2) integration of the automated inspection software with the prototype system, and (3) validation of the entire prototype system for various welding conditions.

Figure III-53 shows a schematic of an RSW quality inspection system for both real-time and post-weld NDE inspection. This system consists of (1) a computer with specially designed software for system control, data acquisition, and IR image analysis; (2) a low-cost IR camera; (3) input/output instruments for system control and synchronization; and (4) an auxiliary heating device (for post-weld inspection).

In FY 2013, additional real-time and post-weld image data were collected mostly for boron steels with different grades, thickness gauges, coatings, and stack-up configurations in current and future generations of lightweight vehicle structures. Various combinations of those steels in both 2T and 3T stack-up configurations were studied. The welding parameters were carefully controlled to produce welds with varying attributes (e.g., nugget size). Real-time IR images of spot welding were acquired during the experiment. The resulting welds were further analyzed using the post-weld inspection procedure.

A major technical achievement in this fiscal year was the addition of self-learning capability to the software. The system has the capability to automatically generate a weld quality database according to the destructively measured data, as well as the welding conditions specified by users, and later make quantitative predictions of weld attributes using such a database. In addition, severe welding expulsion (another type of welding defect) can be detected during real-time inspection.

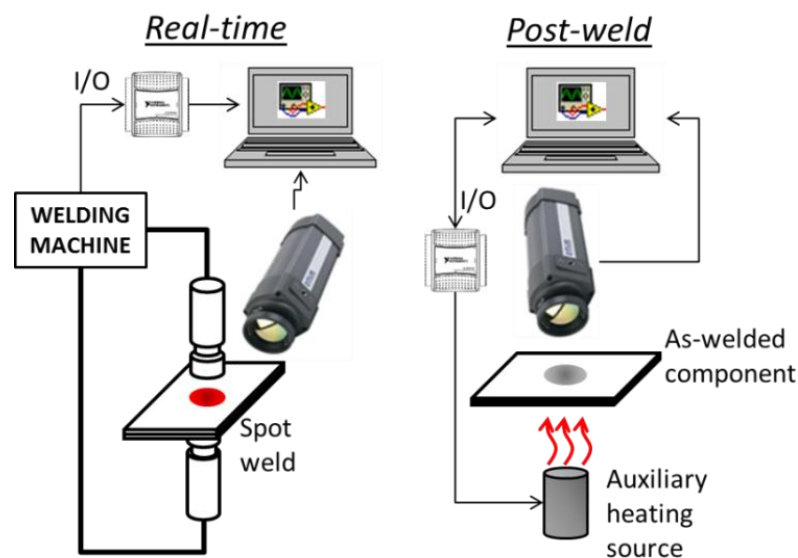


Figure III-53: Schematic of the IR thermography-based RSW quality inspection system.

**Real-time IR NDE.** During FY 2013, the image analysis algorithms for real-time IR inspection were further developed. The total time required for image collection and data analysis for each weld is 1.5~2.5 s, depending upon the material thickness and welding condition. Weld nugget size, weak stuck welds, and welding expulsion can be positively identified.

Figure III-54 shows a typical relationship between the weld nugget size and calculated IR thermal signatures, as well as the acceptable quality range and the defect range (welds made of 3T boron steel). This correlation is automatically generated when the system is operated in “training mode.”

With a correlation such as the quality database for inspecting the same types of welds (made of 3T boron steel under the same welding procedure), the weld nugget size can

be quantitatively determined when the system is running in inspection mode. After inspection, some of the welds were destructively opened. Figure III-55a shows the comparison between the IR-predicted weld nugget size and the destructively measured data. In the same manner, the real-time IR nugget size predictions for all other types of welds collected so far in the project are shown in Figure III-55b.

**Post-weld IR NDE.** Similar to real-time inspection, a weld quality database is also needed for post-weld inspection. Again, the database is automatically created when the system is in training mode with user-provided measurement data. The total time required for image collection and data analysis for each weld is about 3 s. Weld nugget size, thickness, stuck welds, and excessive indentation can be accurately measured.

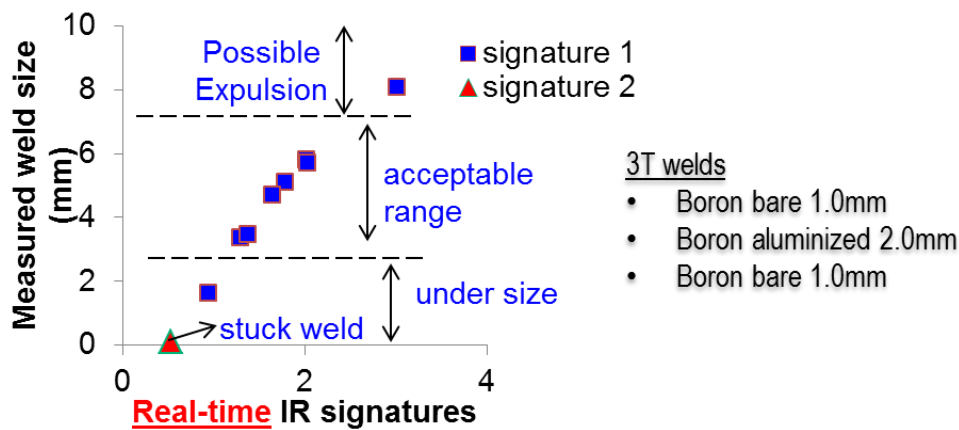


Figure III-54: Correlation of weld nugget size vs. real-time IR thermal signatures for 3T boron steel welds. The “IR Signatures” are separate conditions calculated using ORNL proprietary software. They indicated portions of the data used for image analysis.

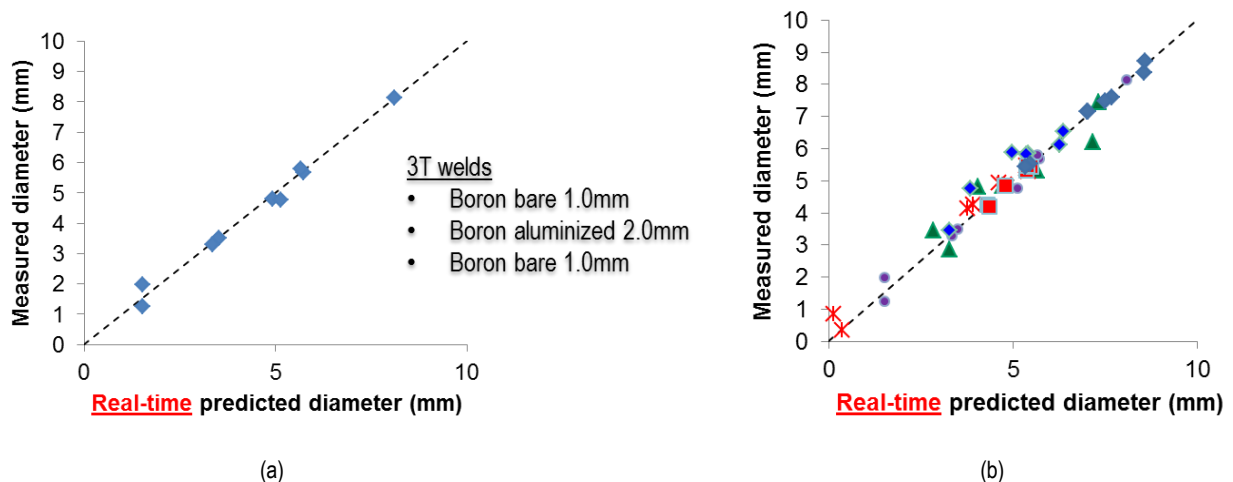


Figure III-55: Real-time IR-predicted weld size vs. destructive measurement for (a) the same types of 3T boron steel welds used in Figure III-55 and (b) all different types of welds.

Figure III-56 shows one of the databases for the 3T boron steel welds. The subsequent prediction results with such a database are also compared with destructively measured data shown in Figure III-57. The same comparison for all other welds collected in this project is plotted in Figure III-58.

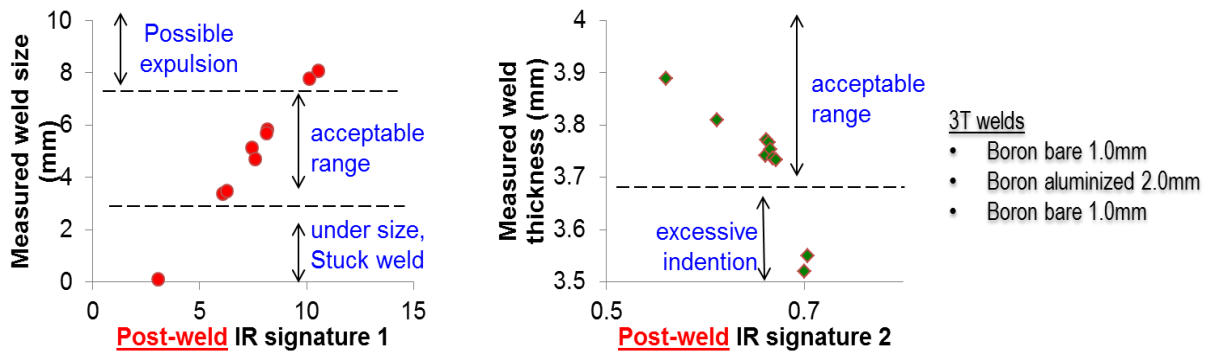


Figure III-56: Correlation of weld nugget size and thickness vs. post-weld IR thermal signatures for 3T boron steel welds.

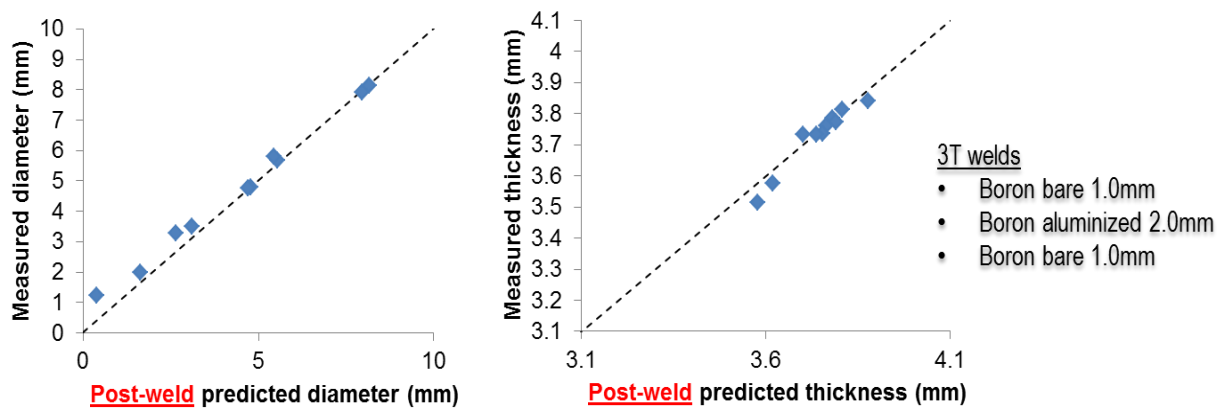


Figure III-57: Post-weld IR-predicted weld size and thickness vs. destructive measurement for the same types of 3T boron steel welds used in Figure III-56.

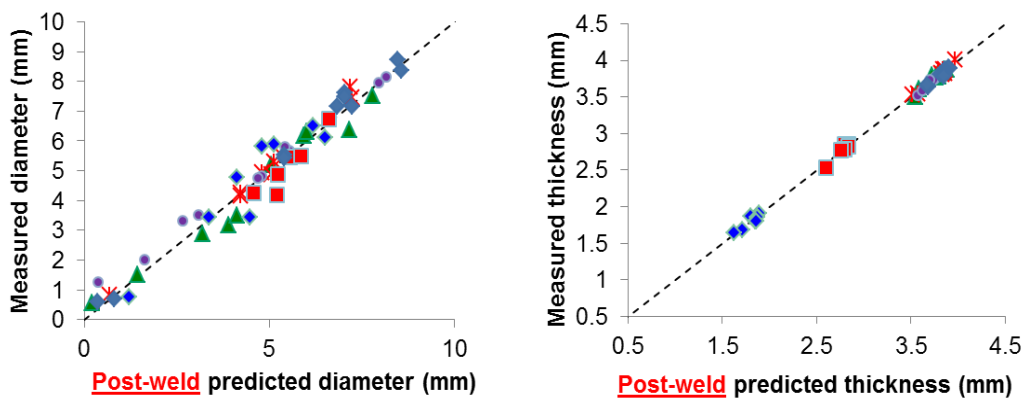


Figure III-58: Post-weld IR-predicted weld size and thickness vs. destructive measurement for all of the different types of welds collected so far in the project.

In addition, post-weld IR NDE can measure the weld nugget shape on the faying surface. Figure III-59 shows a comparison between the IR-measured results and the cross section of the destructive measurements.

### Technology Transfer Path

In June 2013, major automotive OEMs were invited to an onsite demonstration of the IR NDE prototype system in Detroit. GM, Ford, Chrysler, and Honda attended the meeting and demonstration. The automotive OEMs and their suppliers are very interested and willing to work further with ORNL. The first deployment partner has been identified—Cosma's Eagle Bend Manufacturing, Inc. (EBM) in Clinton, Tennessee. Further system testing and improvement will be carried out on EBM's production lines.

### Conclusions

Significant progress was made in FY 2013 toward the development of a cost-effective, robust, and accurate IR thermography-based system to quantitatively inspect spot weld quality in automotive manufacturing plants. Intelligent, automated software was developed and implemented in the system. An algorithm that was further refined shows that the inspection time for both real-time and postmortem applications is 3 s or less. Different types of welds using various materials, thickness gauges, stack-up configurations, and surface coatings have been tested. Results show that weld nugget size, thickness, lack-of-fusion defects, excessive indentation, and welding expulsion can be accurately measured or detected by the system.

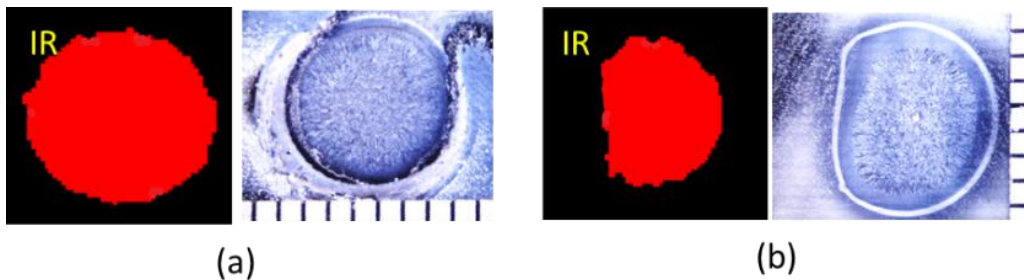


Figure III-59: Post-weld IR-measured weld shape vs. cross section of destructive measurement (on the faying surface): (a) good weld and (b) weld with irregular shape.

# Improving Fatigue Performance of AHSS Welds (ORNL-ArcelorMittal CRADA)

## Zhili Feng (Principal Investigator)

Oak Ridge National Laboratory  
Phone: (865) 576-3797; Fax: (865) 574-4928  
E-mail: [fengz@ornl.gov](mailto:fengz@ornl.gov)

## Benda Yan (Principal Investigator)

ArcelorMittal USA  
Phone: (219) 399-6922  
E-mail: [benda.yan@arcelormittal.com](mailto:benda.yan@arcelormittal.com)

### Contributors:

Wei Zhang, Dongxiao Qiao, Stan David, ORNL;  
Wenkao Hou, Steve Kelly, ArcelorMittal;  
Wesley Wang, ESAB

## Accomplishments

- Successfully demonstrated a new weld filler metal design approach and concept that could effectively control the stresses in the high-stress-concentration region of short stitch welds commonly used in auto body structures. Preliminary fatigue testing confirmed 3 to 5x weld fatigue improvement. (FY 2013)
- Successfully developed a mechanical stress management approach and demonstrated that such an approach improves weld fatigue life by 5 to 10x at the high-cycle-fatigue testing range that is more relevant to the durability of auto body structures. (FY 2013)
- Completed the initial fatigue testing of baseline welds fabricated with both conventional filler wire and low-transformation-temperature (LTT) filler wires to generate the applied stress magnitude against the number of cycles to failure (S-N) curves. (FY 2012)
- Completed the initial development of a weld thermal-metallurgical-mechanical model to gain an understanding of the effect of low-temperature phase transformation on the formation of compressive weld residual stresses at the fatigue-cracking-initiation region. (FY 2012)
- Developed a new weld fatigue testing specimen configuration that is essential to maintain the weld residual stress field representative of actual welded automotive body structures. (FY 2011)
- Completed a comprehensive survey of open literature to collect the published chemistry of LTT filler wires. Down-selected and produced three different types of baseline LTT filler wires. (FY 2011)

## Future Directions

- Measure the near-surface weld residual stress distribution in the baseline welds using techniques such as American Society for Testing and Materials (ASTM) hole-drilling, x-ray diffraction, and/or neutron diffraction.

- Study the phase transformation kinetics and associated lattice/volume change for LTT filler metals using thermal-mechanical testing in the Gleeble system and a novel approach of in situ neutron diffraction developed in a synergetic activity.
- Complete the development of a 3D weld residual stress model to determine the phase transformation effect at the weld start and stop regions where fatigue cracking initiation is typically observed in fatigue testing. Validate the 3D weld model using the experimental residual stress data.
- Develop the next generation of LTT filler metal chemistry with balanced properties of compressive surface stress, weld toe geometry, and resistance to fatigue cracking.

## Technology Assessment

- Target: Develop robust in-process weld fatigue life improvement technologies that can be used to join AHSS auto body structural components at costs acceptable to the auto industry.
- Gap: The weld fatigue strength in the as-welded condition does not increase in proportion to the yield/tensile strength of AHSSs. The insensitivity of weld fatigue strength to steel static strength is a major barrier for lightweighting through down-gauging for chassis and other load-bearing components.
- Gap: Current weld fatigue improvement techniques are mostly post-weld-based and add processing steps. The added steps are cost-prohibitive in the high-volume, mass production automotive environment and there exists large variability in the fatigue life achieved by the post-weld-based techniques.



## Introduction

Under a cooperative research and development agreement (CRADA), ORNL and ArcelorMittal USA are working together to develop the technical basis and demonstrate the viability of innovative technologies that can substantially improve the weld fatigue strength and the durability of auto body structures. Durability is one of the primary metrics related to designing and engineering automotive body structures. The fatigue performance of welded joints is critical to the durability of the body structure because the likeliest locations for fatigue failure are often at welds. Recent studies by the Auto/Steel Partnership (A/SP) Sheet Metal Fatigue Committee, the Department of Energy's (DOE) Lightweighting Materials Program, and others [Bonnen and Iyengar 2006; Yan et al., 2005; Iyengar 2008, Feng et al., 2008; Feng et al., 2009] clearly reveal that, unlike the base metal fatigue strength, the weld fatigue strength of advanced

high strength steels (AHSSs) is largely insensitive to the base metal composition, microstructure, and strength under typical welding conditions used in body in white (BIW) construction. The lack of an inherent weld fatigue strength advantage for AHSSs compared with conventional steels is a major barrier for vehicle weight reduction through down-gauging, as down-gauging leads to increases in stresses and so reduces durability under the same dynamic road loading conditions. In addition to AHSSs, a recent comparative study [Feng et al 2009] reveals that other lightweight materials such as Al and Mg alloys may not offer improved weld fatigue strengths on a specific weight basis. Therefore, solutions to improve the fatigue strength of welds are critical to BIW lightweighting.

### Approach

Instead of using post-welding techniques to improve weld fatigue strength, this project focuses on developing in-process weld technology as part of the welding operation. The overall goal is to develop effective ways to control and mitigate the key factors governing the fatigue life of AHSS welds, including weld residual stress, weld profile, and weld microstructure/chemistry. The project also fully utilizes state-of-the-art integrated computational welding engineering (ICWE), neutron/synchrotron imaging, other advanced residual stress measurement techniques, and the fatigue testing and microstructure analysis capabilities at ORNL and ArcelorMittal Global R&D to perform the research and development required.

The project will explore effective means to control and mitigate the key factors governing the fatigue life of AHSS welds, including weld profile, weld residual stress, and weld microstructure/chemistry. Two specific in-process approaches will be further developed. Both technical and economic issues unique to the automotive body structural welding environment have been identified and are being addressed. According to CRADA policy, specific details of the approaches will be released to the public at a later time.

### Results and Discussion

A special weld fatigue specimen configuration was designed to mimic the stitch weld pattern typical in automotive body and chassis structures. Figure III-60a shows the typical chassis and engine motor mount structures assembled using stitches of gas metal arc seam welds. Considering the representative weld pattern, a special weld fatigue specimen configuration was designed (Figure III-60b). This specimen is fabricated by placing a 50 mm long seam weld on the lap joint of two steel sheets, i.e., the most commonly used weld type in automotive structures. Moreover, the specimen contains both weld start and stop, which are the critical locations for fatigue cracking initiation. The special weld fatigue specimen configuration not only maintains the weld residual stress field representative of actual seam welds but also produces stress/strain conditions resembling those endured by vehicle structure welds under cyclic loading conditions.

In FY 2012, four different types of baseline LTT filler wires were down-selected and produced for welding and fatigue testing, based on a comprehensive open literature survey of the low-temperature phase transformation filler wire. Two of the LTT filler wires showed limited but promising improvements in weld fatigue life. ORNL's ICWE model was then used to analyze the effects of low-temperature phase transformation and other relevant welding and geometric factors on the weld residual stress distribution. The model was further utilized to understand the stress distribution under fatigue loading conditions to quantify the effects of new weld filler wire design. The weld modeling revealed that the weld start and stop regions of the stitch weld are high-stress-concentration sites under fatigue cyclic loading. The crater at the weld stop has less material to carry the load and so is particularly vulnerable to crack initiation. Indeed, failure analysis of fatigued welds, as well as in situ observation during fatigue testing, confirmed that the weld start and stop were the predominant fatigue-crack-initiation sites.

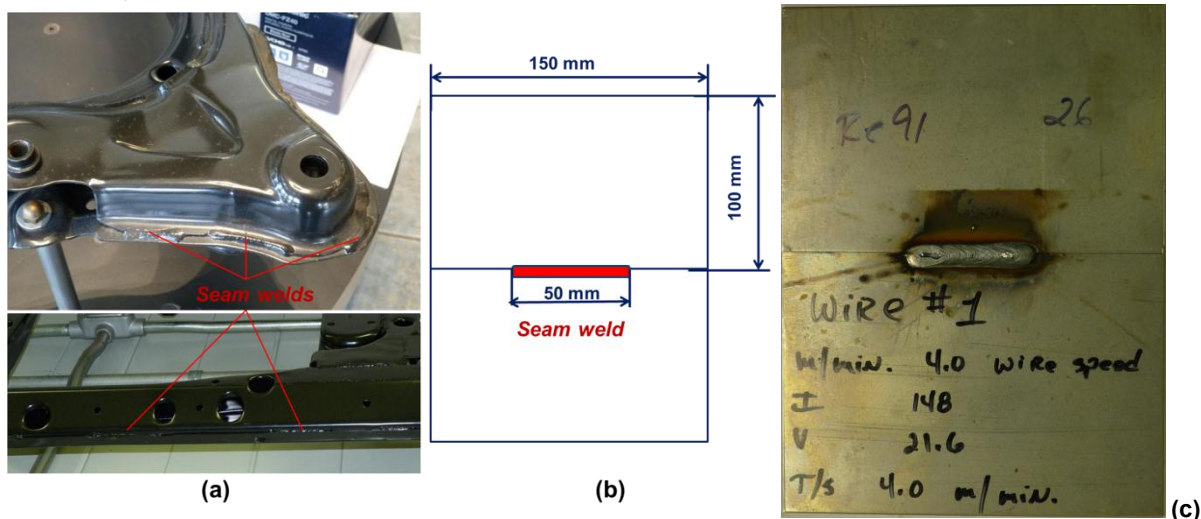


Figure III-60. (a) Representative welding pattern in auto body structures, (b) special weld fatigue specimen configuration, and (c) appearance of actual weld fatigue testing specimen adopted in this project.

Based on the results obtained in FY 2012, the FY 2013 research was focused on developing effective strategies to mitigate weld residual stresses in the weld start and stop region. This research resulted in two different promising approaches that showed dramatic improvement in weld fatigue lives.

In the first approach, a new filler wire design concept was used, which not only considered the effect of LTT on weld residual stress, but also considered other essential factors such as weldability, strength, and toughness in the chemistry formulation. Preliminary fatigue testing at medium load levels confirmed 3 to 5× weld fatigue improvement with this new filler wire design (Figure III-61). Testing of the new filler wire under other loading levels is currently being conducted.

In the second approach, a mechanical stress management technique was developed to mitigate the tensile residual stresses in the high-stress-concentration region of the stitch weld. This resulted in significant weld fatigue life improvement. Figure III-62 shows the fatigue testing results collected so far, for both DP590 and DP980. At the low-stress level that is more relevant to the durability of auto body structures, the improvement was between 5 and 10 times compared with the baseline reference cases using ER70-S filler wire, which is widely used in gas metal welding of AHSS auto body structures. In fact, at 2000 lb, the weld specimens with stress management did not break after 10 million cycles (marked as run-out in the figure) for DP590.

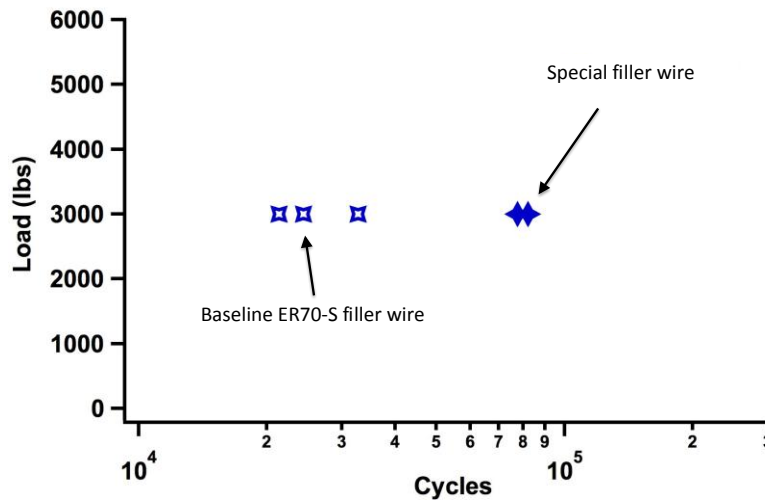


Figure III-61: Comparison of weld fatigue lives of a baseline ER70 weld versus the new filler wire developed in FY 2013.

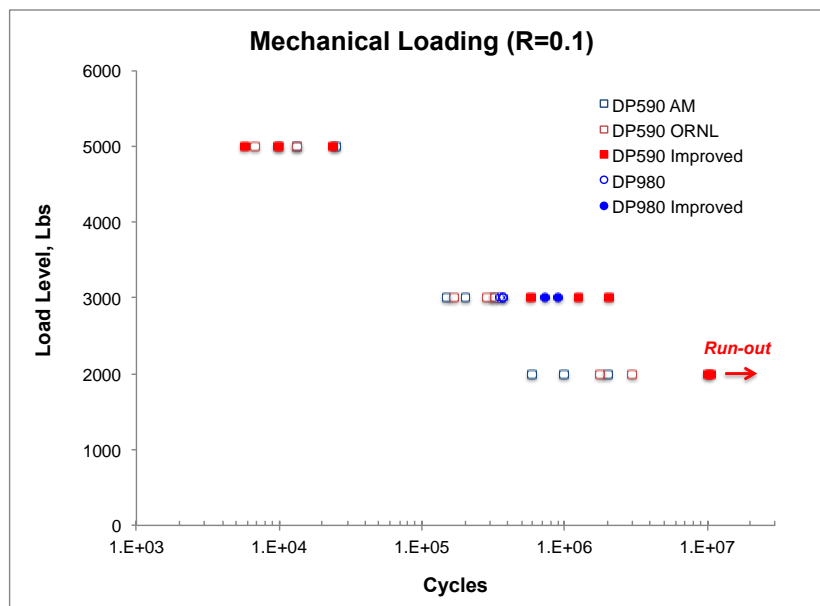


Figure III-62: Improvement of weld fatigue lives through an innovative mechanical stress management technique developed in FY 2013.

In FY 2013, high-energy synchrotron x-ray diffraction was used to determine the weld residual stress and the effect of the mechanical stress management technique. The mechanical stress management technique was indeed found to be able to considerably lower residual stresses, thereby providing the technical basis for the drastic life improvement in weld fatigue life that was observed.

### Technology Transfer Path

The primary technology transfer path is to work closely with the industry partners of the project—a major steel supplier and a major welding consumables manufacturer—that have the business interests and marketing capability to quickly commercialize the technology developed in this project. In addition, the findings and results from the project will be disseminated to automotive OEMs and other interested parties through the extensive communication channels established over the years.

### Conclusions

Weld fatigue life has been identified as one of the key technology barriers to widespread use of lightweight materials (AHSSs, Al and Mg alloys) for automotive body structure lightweighting. The technology developed in this project is expected to provide cost-effective, practical solutions to the automotive industry to address this critical issue. Significant technical progress was achieved in FY 2013. Weld fatigue life improvements of 3–5× and 5–10× were demonstrated using two different novel approaches to control and mitigate the weld residual stresses. These two approaches will be further refined and optimized, and technology commercialization strategies will be formulated in FY 2014.

---

# IR Heat Treatment of Cast Bimetallic Joints and Residual Stress Characterization

---

## Thomas R. Watkins (Principal Investigator)

Oak Ridge National Laboratory  
Phone: (865) 387-6472; Fax: (865) 574-3940  
E-mail: [watkinstr@ornl.gov](mailto:watkinstr@ornl.gov)

## Timothy W. Skszek (Principal Investigator)

Cosma Engineering  
Phone: (248) 786-2584; Fax: (248) 786-2583  
E-mail: [tim.skszek@vehmaintl.com](mailto:tim.skszek@vehmaintl.com)

### Contributors:

Adrian Sabau, Hebi Yin, Donald Erdman III, Wei Zhang,  
Gerald M. Ludtka, Pooron Josh, ORNL; Xiaoping Niu,  
Promatek Research Centre

## Accomplishments

- Fast casting samples treated with a modified T5 heat treatment method were delivered to Department of Energy (DOE). Using this T5 heat treatment method, the minimum performance requirements were met. Samples demonstrated a yield strength >172 MPa, ultimate tensile strength >243 MPa, and elongation >7%. (FY 2013)
- Completed 90% of the neutron residual stress data collection for a series of conventionally heat treated joints to determine conditions in which beneficial residual stresses are lost, and completed 85% of the data analysis. (FY 2013)

## Future Directions

- Complete thermomechanical modeling which is currently being conducted.
- Develop and document an Al T5 and modified Al T6 IR heat treatment method for bimetallic joints. Determine the minimum duration of time at temperature with IR heating required to maximize the yield strength, ultimate tensile strength, and elongation, as validated using similarly IR-processed flat samples. Complete the residual stress determination, modeling, and prototype assembly efforts.

## Technology Assessment

- Target: Complete and document both a modified T6 and a T5 heat treatment schedule for a bimetallic joint. Manufacture demonstration joints and validate that flat casting samples treated according to this schedule meet minimum performance requirements: modified T6: yield strength >250 MPa, ultimate tensile strength >310 MPa, elongation >8%; T5: yield strength >172 MPa, ultimate tensile strength >243 MPa, elongation >7%.
- Gap: Traditional heat treatment methods are either too time consuming or degrade the beneficial residual stresses in bimetallic joints.



## Introduction

The technical objective of this CRADA is to develop and model a heat treatment process based on IR heating of an Al casting and a bimetallic joint to produce a T5 temper in a shorter period of time than is currently achievable and, separately, to produce a modified T6 temper for improved mechanical properties without the loss of joint integrity. IR heat treatments have been demonstrated to provide reduced processing time, reduced energy requirements, and improved material properties of Al components, including strength and elongation, relative to convective thermal heat treatment methods.

This project addresses the DOE Vehicle Technologies Program Lightweighting Materials technology barrier “Joining and Assembly” by facilitating the use of lightweighting, high-performance materials that will contribute to the development of vehicles that provide better fuel economy yet are comparable in size, comfort, and safety to current vehicles. The project is focused on a specific application for a high-volume vehicle platform; however, the joining technologies and methods developed will be applicable to multiple joints throughout this and other vehicle architectures.

The bimetallic joints [Buchholz 2011] under consideration are part of the automotive front and rear cross-car structure, wherein a steel tube is enveloped by molten Al to form a joint. A novel IR heat treatment approach is being developed to tailor the temperature profile, after casting, to strengthen the Al, better manage the residual stresses, and achieve a superior joint. Fabrication and thermal processing of a bimetallic structure comprising two dissimilar materials presents processing challenges to mitigate, reduce, and optimize many materials issues, such as residual stresses, interfacial reactions, and altered properties.

The A356 alloy is one of the most used Al-Si-Mg casting alloys, especially in the T6 heat-treated condition, because the improvements in mechanical properties make this alloy suitable for load-bearing applications. The first stage of T6 heat treatment is a solution treatment at an elevated temperature (e.g., 540°C), which homogenizes the chemistry and dissolves any preexisting precipitates. At the end of the solution treatment, castings are typically quenched in water. This serves to retain the solute-rich homogeneous matrix chemistry, formed at high temperature, at room temperature. A subsequent aging treatment capitalizes on this super-saturated solid solution to generate controlled dispersions of very small strengthening precipitates within the matrix of Al grains.

## Approach

The project has been organized into three research areas: IR processing experiments and prototype assembly; characterization of castings and joints; and model development and validation. Two distinct sets of samples were examined: flat casting samples and sectioned bimetallic “joint-only” samples. Cosma supplied flat castings and joint-only samples under standard processing conditions (T5 and modified T6) as well as untempered/un-heat-treated flat casting and joint-only samples.

During Phase II of this project, a modified T5 heat treatment method for flat Al-Si-Mg castings (i.e., not bimetallic joints) was developed based on a combined computational and experimental approach. A prototype furnace and quenching scheme were assembled and ordered, respectively. Residual stresses were measured using neutron diffraction and subsequent data analyses were performed. A thermomechanical model for steel deformation during a heating schedule was developed, and a model for the bimetallic joint is being developed.

## Results and Discussion

### 1. IR processing experiments and prototype assembly

A prototype electric IR heating furnace from ORNL was employed to test novel IR heat treatments (Figure III-63). The

IR furnace consists of tungsten-halogen lamps located above and below the Al component part in an attempt to minimize the temperature distribution within the bimetallic part. To test the heat transfer capabilities of the prototype IR furnace, experiments were conducted using flat, 5 mm thick, A356 plates. These plates were placed horizontally on a quartz plate, as shown in Figure III-63a and Figure III-63b to facilitate heating from both sides of the plate. Three thermocouples were placed on the top and bottom and in the side of the plate sample to measure the temperature during the heat treatment. As shown in Figure III-64, the temperature of the plates reached 500°C in less than 2 min, as indicated by the thermocouple inside the plate. The data also show excellent temperature control during the experiment, with low overshoot and constant target temperature. For the future series of experiments, a quartz tube will be used to hold the bimetallic part in the furnace (see Figure III-63c and Figure III-63d). The bimetallic joint is pictured at the bottom of Figure III-63d.

### 2. Characterization of castings and joints

The series of additional flat casting samples that were heat-treated to a T5 temper were subsequently mechanically tested, and the yield strength (YS), ultimate tensile strength (UTS) and elongation were determined. Table III-4 lists the mechanical properties of these heat-treated flat castings. For each heat treatment, two tensile samples were machined and tensile tested.



Figure III-63: ORNL prototype IR furnace with lamps above and below for heat treating flat castings (a and b) and bimetallic joints (c and d). (d) The bimetallic joint showing the steel tube (left) with an end cap buried in an Al casting (right).

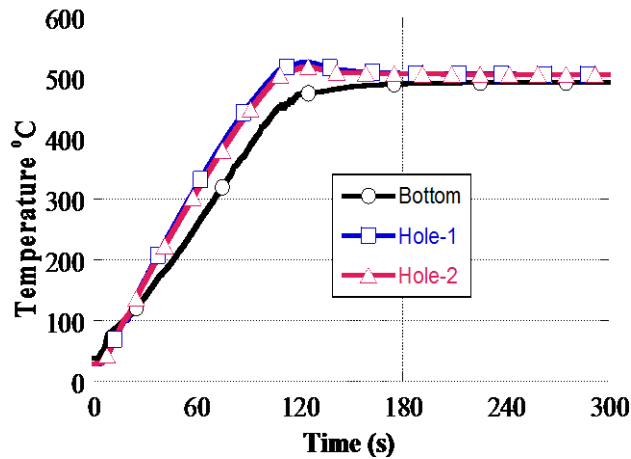


Figure III-64: The measured temperature in a flat plate during an IR heating with the prototype furnace.

Table III-4: A listing of heat treatment trials and corresponding YS, UTSs and elongations

| Heat treat # | Type | YS (MPa) | UTS (MPa) | Elongation (%) |
|--------------|------|----------|-----------|----------------|
| F1-A         | T5   | 186      | 279       | 9.5            |
| F1-B         | T5   | 186      | 276       | 10.3           |
| F2-A         | T5   | 172      | 273       | 11.1           |
| F2-B         | T5   | 165      | 266       | 11.8           |

YS = yield strength; UTS = ultimate tensile strength

Residual stresses play an important role in these joints. A series of conventionally heat-treated joints were examined using neutron diffraction to measure and map the residual stresses in the joint region. The measurements were

conducted at the High Flux Isotope Reactor at ORNL using the HB-2B beam line. The position of the (211) steel reflection and (311) Al reflection were measured in the radial, hoop, and axial directions. The experimental details are similar to those described in the literature (Johnson et al., 2012). Figure III-65 illustrates the steel tube with a welded end cap and Al joint cross section, as well as the neutron measurement locations. The casting temperature and pressure associated with the high-pressure casting process appears sufficient to deform the steel tube and end cap. Contact with the molten A356 Al alloy (600–650°C) and the pressure associated with the casting process results in a temperature increase in the steel component, drastically reducing the yield strength of the steel (NCMS 1997). Prior torsion test results have demonstrated a high joint strength in the steel-Al joint region.

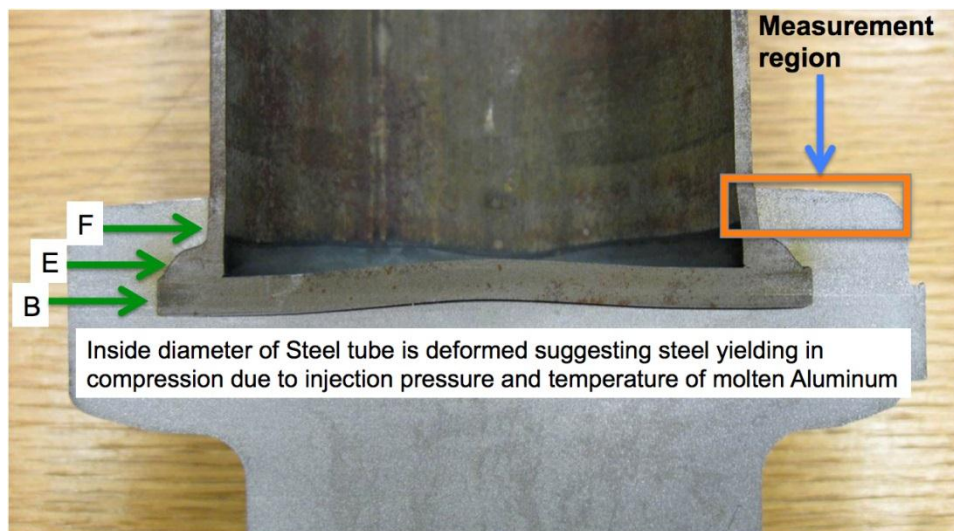


Figure III-65: Cross-section of an as-cast joint. Note the gaps above the weld bead of the end cap to the steel tube (see green arrow at F) and cast Al, as well as below the deformed end cap.

Figure III-66 shows the residual stresses in the as-cast and conventional T5 samples. In Figure III-66b, the tensile hoop strains in steel were reduced and became more compressive in nature after the T5 heat treatment. To date, nine heat treatment conditions have been measured and eight analyzed.

**3. Model development and validation**

**Modeling of heat treatment phenomena during radiant heating.** A computer aided design (CAD) model resembling the Al-steel joint was used to study the effect of IR heating on the temperature and stress distribution in the joint (see Figure III-67). A heat transfer model of the bimetallic part was completed, and a stress analysis model was developed in ABAQUS. Several details and main results are presented and discussed below.

**Heat transfer analysis of Al-steel joint.** Initially, a heat transfer analysis was conducted to ensure that appropriate temperature conditions would be imposed before the more complex thermomechanical simulations were conducted. The inputs to the heat transfer model included (1) finite element mesh; (2) thermophysical properties of the Al and steel; and (3) boundary conditions, such as surface heating sources and heat transfer losses due to natural convection, forced convection, and thermal radiation. The meshing of the

complex part was created so as to allow the flexibility to change the mesh resolution locally as needed for the next effort on stress analysis. The heat transfer model can be run using the in-house ORNL software or ABAQUS (Figure III-67).

The temperature distribution within the bimetallic joint was simulated during heating (Figure III-68). In Figure III-68a, the top surface of the Al part is directly heated by the IR lamps, whereas the steel tube is not directly heated and was actively cooled using compressed air, imposing a temperature gradient within the Al and steel part (Figure III-68b). The section at the small end, opposite from the tube insert end, achieved the highest temperature (Figure III-68a). The temperature gradient is evident on the symmetry plane, with lower temperatures toward the back surface of the component. The model indicates that the temperature is very uniform within the tube cap. To further assess the nonuniformity of the temperature within the Al portions of the joint, close to the steel-Al interface, the predicted temperature data were extracted at three locations. These are indicated with red circles and identified as “top,” “side,” and “back” (Figure III-68a). The temperatures at three points are labeled “B,” “E,” and “F” in Figure III-65 above. Figure III-69a and Figure III-69c indicate that a fairly uniform temperature distribution is predicted within the Al shoulder that wraps around the tube cap.

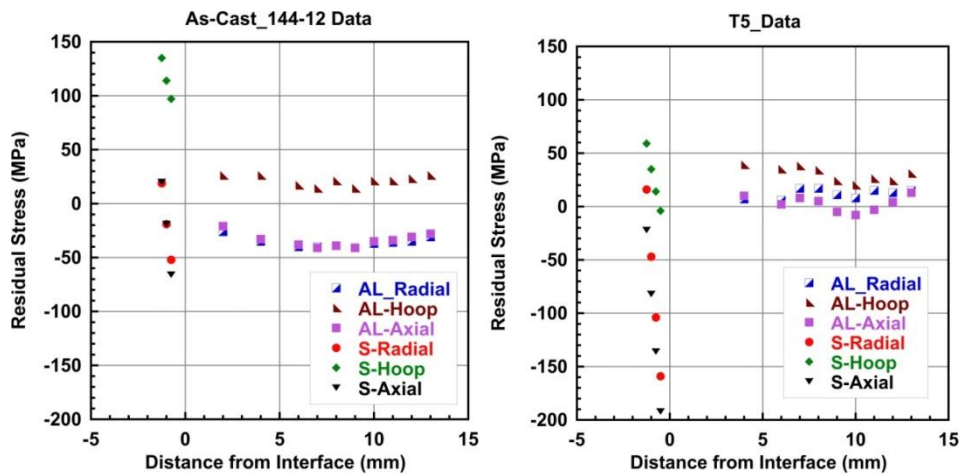


Figure III-66: The residual stresses as a function of distance from the interface for the as-cast and conventional T5 (182°C/4 h) samples.

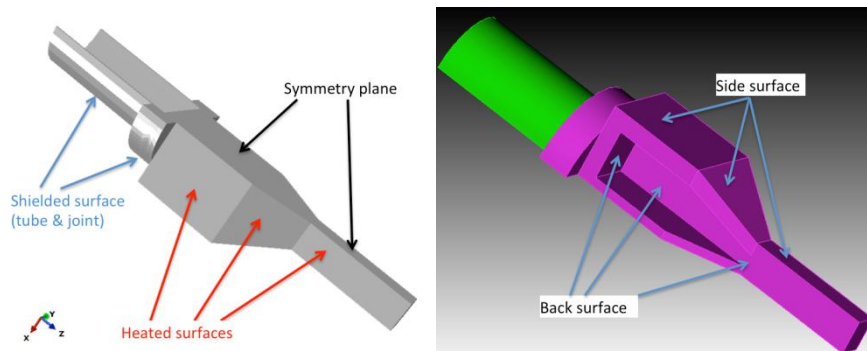


Figure III-67: Drawing of the bimetallic part showing heated surfaces and shielded portions of the component.

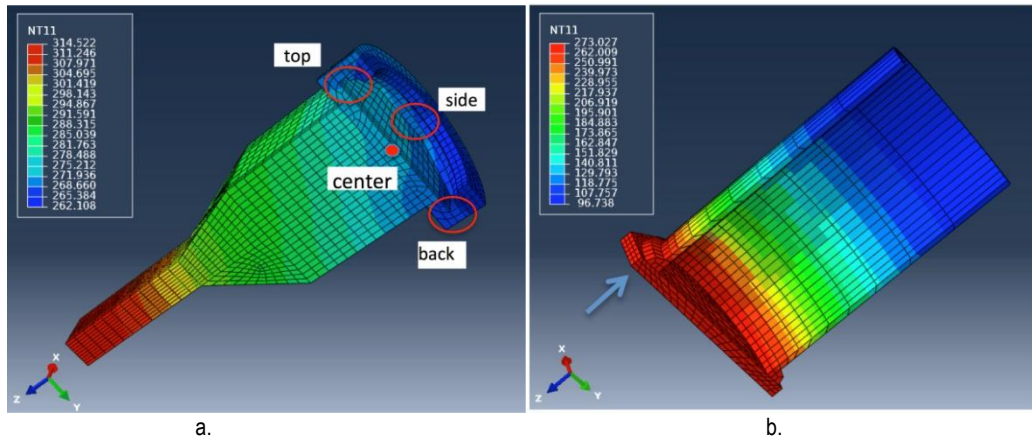


Figure III-68: Temperature (°C) distribution for the (a) Al and (b) steel portions of the joint. In (a), the surface shown in the front is the symmetry plane, and the top surface is shown facing toward the IR heat source.

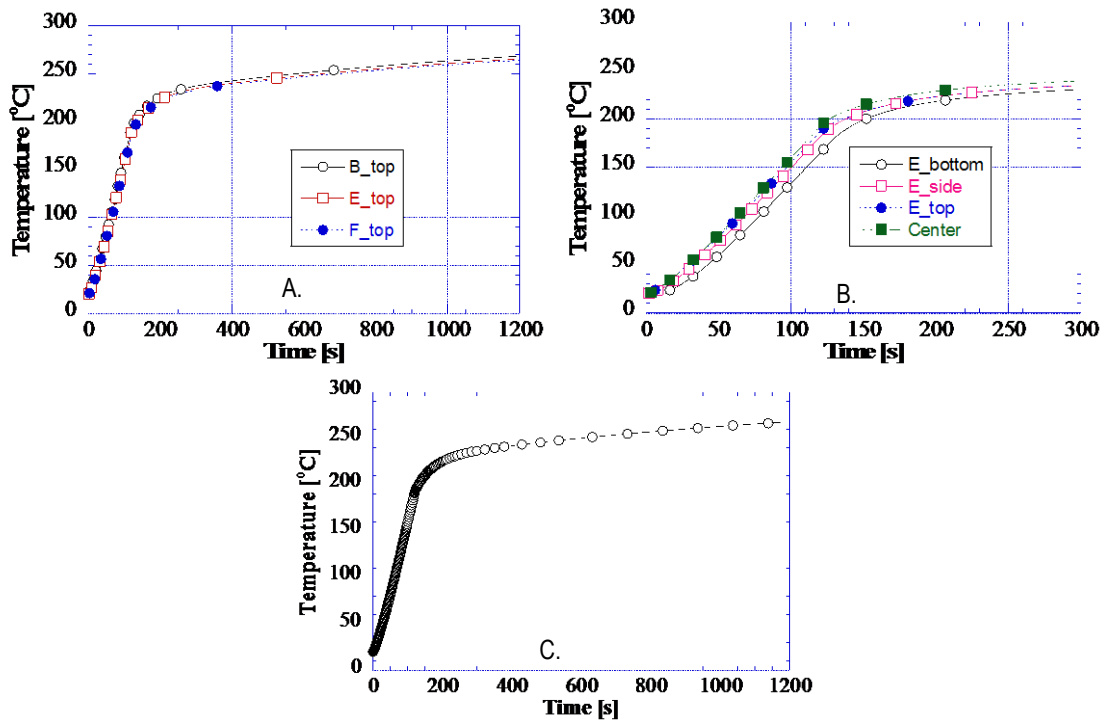


Figure III-69: Temperature evolution at points B, E, and F (see Figure III-65) as a function of time. (A) and (B) are experimental data. (C) is the model prediction.

**Thermomechanical modeling of Al-steel joint.** To obtain the residual stresses, the inelastic properties of both steel and Al must be considered, requiring a step-by-step evolution of the model to ensure that each part of the model is accurate. Thus as a first step toward the numerical simulation of the entire casting process and ensuing heat treatment, only the heating and deformation of the steel tube was conducted. The thermomechanical model was built in ABAQUS using the rate-independent isotropic hardening plasticity model for the steel. Temperature-dependent property data were used for both the elastic and plastic properties. A pressure-temperature schedule was used to simulate the pressure that would have been applied on the steel during casting of the Al part of the

bimetallic component as shown in Figure III-70. The pressure is applied on the cap and as well as around its circumference. The temperature profile at an instant right before the onset of air-gap formation that would have been forming between the Al and steel (Figure III-70a) is shown on a deformed steel component in Figure III-71a. The residual deformation of steel, which is shown in Figure III-71b (magnified 3× for clarity) at an instant near room temperature, is less than the deformation at high temperature. This result proves that the high pressure applied during die casting at 700°C is high enough to induce a permanent deformation of the steel cap, deformation that was also observed experimentally (Figure III-65).

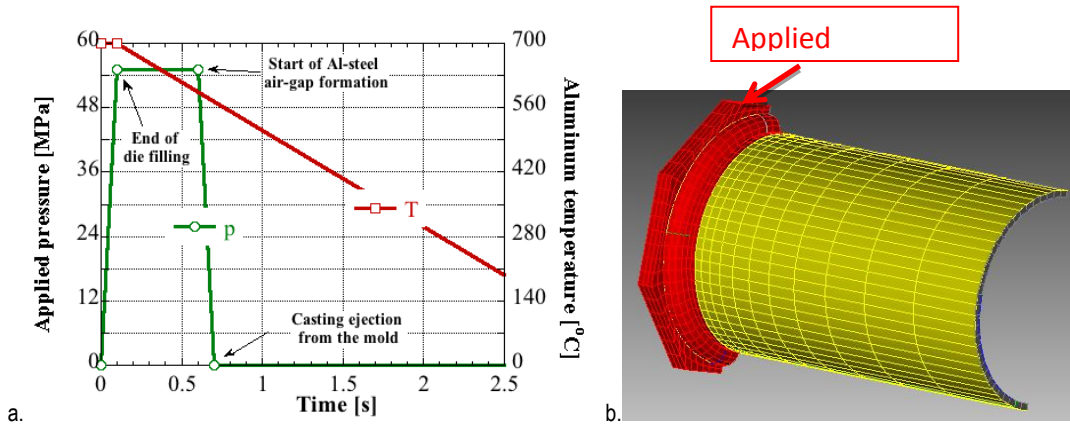


Figure III-70: Boundary conditions for the thermomechanical model for the steel. (a) Pressure and temperature evolution within the Al during the die-casting process and (b) contact between Al and steel cap used to assess the capabilities of the thermomechanical steel model.

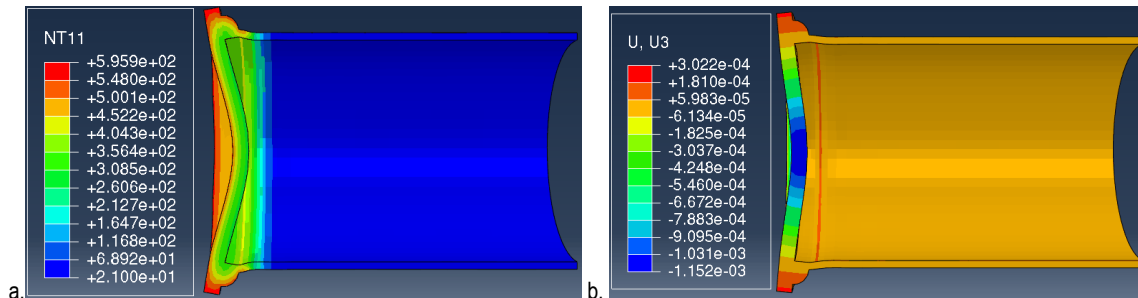


Figure III-71: (a) Temperature profile right before air-gap formation and (b) displacement in the direction along the tube axis, near room temperature (magnified 3x).

In Figure III-72, the deformation in the vertical/radial direction is shown in a detail located at the end of the weld, between the cap and cylinder. The distribution of the displacement in the radial direction and the overall deformation indicate that the steel tube adjacent to the weld bead shrank in the radial direction, which is also consistent

with the experimental observations. Based on these thermomechanical predictions, similar to those shown in Figure III-73, the residual stresses in the hoop, axial, and radial directions will be obtained at the same locations where neutron scattering experiments were conducted.

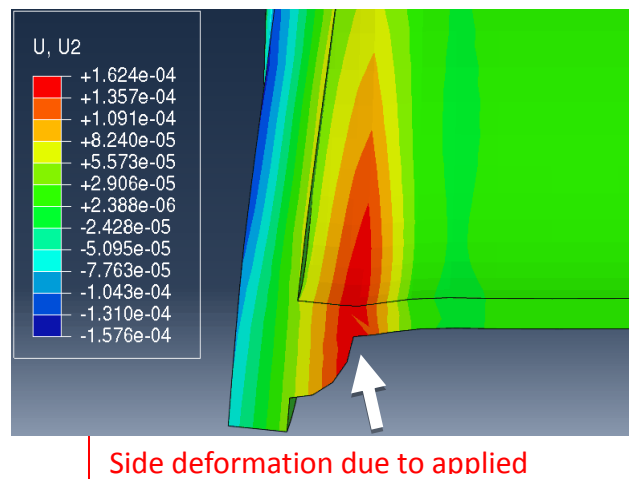


Figure III-72: Deformation and displacement in the radial direction through a vertical cross-section of the steel near the edge (deformation magnified 3x).

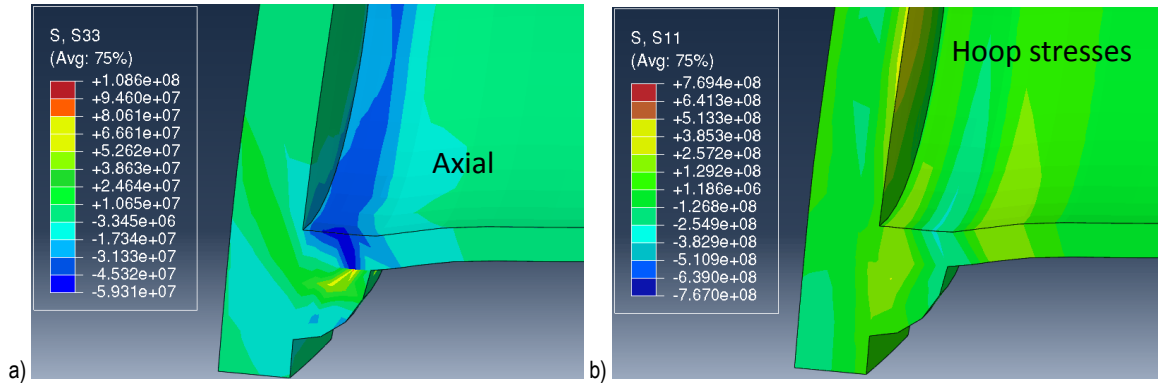


Figure III-73: Stress distribution through a vertical cross section of the steel near the edge for the (a) axial component and (b) hoop component (deformation magnified 3x).

### Technology Transfer Path

The primary technology transfer path for this effort is to work closely with the industry partner—Cosma—which has the business interests and marketing capability to quickly commercialize the technology developed in this project. The technology being developed is being put into use on a high-volume vehicle platform as the technology is developed.

### Conclusions

The purpose of this project is to investigate IR heat treatment to increase the yield strength and elongation of the cast Al portion of an Al–steel bimetallic joint to achieve improved material properties, resulting in a superior joint. T5 heat treatment experiments using IR processing are complete. Flat casting samples were heat-treated with an IR heating system. The mechanical properties of samples receiving IR-based T5 heat treatment developed as part of the project exceeded the minimum performance requirements. The use of an aging model developed by ORNL was critical to the development of the new IR-based T5 heat treatment. Modified T6 heat treatment experiments using IR processing are in progress. Characterization of bimetallic joints including torsion testing and residual stress measurement is nearly complete.

A pressure–temperature schedule was used to simulate die casting conditions for the Al part around the steel component. The computed residual deformation of the steel cap and cylinder is in qualitative agreement with the experimental data. From these thermomechanical data, the residual stresses in the hoop, axial, and radial direction will be obtained at the same locations where neutron scattering experiments were conducted.

### Conclusions

Research under this task has provided insights into the operating mechanisms of protective films on Mg alloys that provide the scientific community with guidance on the development of protective films and better alloys for reducing the corrosion behavior of future Mg alloys and the automotive parts manufactured from those alloys. Significant progress

was made in FY 2013 on the development of a cost-effective, robust, accurate IR thermography-based system to quantitatively inspect spot weld quality in automotive manufacturing plants. Intelligent and automated software was developed and implemented in the system and tested in automotive assembly plants. Significant technical progress was achieved in reducing the weld fatigue of AHSS joints by 3–10× using two novel approaches to control and mitigate weld residual stresses. IR-based heat treatment schedules were developed for T5 and T6, and these are being implemented in automotive production facilities.

### Presentations/Publications/Patents

1. Chen, J.; Feng, Z.; Wang, H.; and Zhang, W. “Non-destructive Inspections of Welds and Joints Using Infrared Imaging and Post-Weld Heating,” ORNL patent application, May 2011.
2. Chen, J.; Feng, Z.; and Zhang, W. “A Non-destructive and Real-time Inspection System for Monitoring Resistance Spot Welding Using Infrared Thermography,” ORNL patent application, August 2012.
3. Chen, J.; Zhang, W.; Yu, Z.; Wang, H.; and Feng, Z. “Automated spot weld inspection using infrared thermography,” presented at Trends in Welding Research 2012: The 9th International Conference, Chicago, 2012.
4. Chen, J.; Zhang, W.; Yu, Z.; and Feng, Z. “Automated spot weld inspection using infrared thermography,” in *Trends in Welding Research 2012: Proceedings of the 9th International Conference*, ASM International, 2013.
5. Chen, J.; Zhang, W.; and Feng, Z. “Resistance spot welding on-line inspection system based on infrared thermography,” presented at FABTECH 2012, Las Vegas.
6. Chen, J.; Feng, Z.; and Zhang, W. “An online infrared-based resistance spot weld inspection system,” presented at SAE 2013 World Congress.

7. D. Qiao et al., "The effect of martensitic phase transformation on weld residual stress distribution in steel sheet lap joints—A computational study," in *Trends in Welding Research 2012: Proceedings of the 9th International Conference*, Chicago, 2012.
8. Watkins, T. R.; Sabau, A. S.; Yin, H.; Erdman III, D. L.; Zhang, W.; Skszek, T. W.; and Niu, X. "Residual stress determination in cast bi-metallic joints," presented by T. R. Watkins at the TMS 2013 Annual Meeting, San Antonio, March 6, 2013.
9. Unocic, K. A., Elsentriecy, H. H., and Brady, M. P. "Characterization of film formation on commercial and model magnesium alloys," presented at the TMS 2013 Annual Meeting, San Antonio, March 4, 2013, to Magnesium Technology 2013 Symposium.
10. Unocic, K. A., Elsentriecy, H. H., Brady, M. P., Meyer III, H. M., Song, G-L, Fayek, M., Meisner, R. A. and Davis, B. "Transmission electron microscopy study of aqueous film formation and its evolution with time on magnesium alloys," submitted to *Corrosion Science*.
11. Yin, H.; Sabau, A.S.; Ludtka, G.M.; Skszek, T.W.; and Niu, X. "Yield strength prediction for rapid age-hardening heat treatment of aluminum alloys," presented by A. S. Sabau at the TMS 2013 Annual Meeting, San Antonio, March 5, 2013.
12. Yin, H.; Sabau, A. S.; Skszek, T. W.; and Niu, X. "Microstructure evolution modeling for solution treatment of aluminum alloys," presented by A. S. Sabau at the TMS 2013 Annual Meeting, San Antonio, March 5, 2013.
7. Hara, N., et al., 2007. "Formation and breakdown of surface films on magnesium and its alloys in aqueous solutions," *Corrosion Science* **49**(1), 166–175.
8. Iyengar, R. M. et al., 2008. "Fatigue of spot-welded sheet steel joints: Physics, mechanics and process variability," *Great Designs in Steel 2008*.
9. Johnson, E. M., Watkins, T. R., Schmidlin, J. E., and Dutler, S. A. 2012. "A benchmark study on casting residual stress," *Metall. Mater. Trans. A* **43A**(5) 1487–1496.
10. Lotus Engineering, Inc. 2010. "An assessment of mass reduction opportunities for a 2017–2020 model year vehicle program," March.
11. Moat, R. J. Stone, H. J., Shirzadi, A. A., et al., 2011. "Design of weld fillers for mitigation of residual stresses in ferritic and austenitic steel welds," *Science and Technology of Welding and Joining* **16**, 279–284.
12. NCMS (National Center for Manufacturing Sciences) 1997. *Predictive Model and Methodology for Heat Treatment Distortion, Phase I Project Summary Report*, January 1994–December 1997, Materials Properties Task Team, Oak Ridge, Tennessee.
13. Nordlien, J. H. et al., 1997. "A TEM investigation of naturally formed oxide films on pure magnesium," *Corrosion Science* **39**(8), 1397–1414.
14. O'Hara, B., and Shafer, P. 2011. "Honda Odyssey body development: Concept, styling, weight reduction, and safety," presented at the International Automotive Body Congress, November 2010.
15. Ohta, A. Matsuoka, K., Nguyen, N. T., et al., 2003. "Fatigue strength improvement of lap joints of thin steel plate using low-transformation-temperature welding wire," *Welding Journal* **82**, 78s–83s.
16. Seyeux, A., et al., 2009. "ToF-SIMS depth profile of the surface film on pure magnesium formed by immersion in pure water and the identification of magnesium hydride," *Corrosion Science* **51**(9), 1883–1886.
17. Song, G, and Atrens A. 2007. "Corrosion mechanisms of magnesium alloys," *Advanced Engineering Materials* **9**(3), 177–183.
18. Song, G-L. 2005. "Recent progress in corrosion and protection of magnesium alloys," *Advanced Engineering Materials* **7**(7), 563–586.
19. Unocic, K. A., Elsentriecy, H. H., Brady, M. P., Meyer III, H.M., Song, G-L., Fayek, M., Meisner, R. A., and Davis, B. 2013. "Transmission electron microscopy study of aqueous film formation and its evolution with time on magnesium alloys," submitted to *Corrosion Science*.
20. Yan, B., Lalam S.,H., and Zhu, H. 2005. "Performance evaluation of GMAW welds for four advanced high-strength steels," *SAE International*, paper no. 2005-01-0904.

## References

1. Barsoum, Z. and Gustafsson, M. 2009. "Fatigue of high strength steel joints welded with low temperature transformation consumables," *Engineering Failure Analysis* **16**, 2186–2194.
2. Bonnen, J. and Iyengar, R. M. 2006. "Fatigue of spot welds in low-carbon, high-strength low-alloy, and advanced high-strength steels and fatigue of fusion welds in advanced high-strength steels," *2006 International Automotive Body Congress*, pp. 19–30.
3. Buchholz, K. 2011. "Two-metal cradle from Cosma is production-ready," *Automot. Eng.* [online], *15*. <http://www.sae.org/mags/AEI/9505> (last accessed November 2013).
4. Feng, Z. Chiang, J. Kuo, M. Jiang C. and Sang, Y. 2008. "A new perspective on fatigue performance of advanced high-strength steel GMAW joints," *Sheet Metal Welding Conference XIII*, 2008.
5. Feng, Z., Sang, Y., Jiang, C., Chiang, J., and Kuo, M. 2009. "Fatigue performance of advanced high-strength steels (AHSS) GMAW joints," *SEA 2009 World Congress*, Detroit, paper 09M-0256.
6. Gray, J., and Luan, B. 2002. "Protective coatings on magnesium and its alloys—A critical review," *Journal of Alloys and Compounds* **336**(1–2), 88–113.

## III.5. Multi-Material Enabling—Pacific Northwest National Laboratory

### **Dean Paxton, Field Technical Monitor**

Pacific Northwest National Laboratory  
902 Battelle Boulevard, P.O. Box 999  
Richland, WA 99352  
(509)375-2620; Fax: (509)375-2186  
E-mail: [dean.paxton@pnnl.gov](mailto:dean.paxton@pnnl.gov)

### **William Joost, Technology Area Development Manager**

U.S. Department of Energy  
1000 Independence Avenue, S.W.  
Washington, DC 20585  
Phone: (202) 287-6020; Fax: (202) 856-2476  
E-mail: [william.joost@ee.doe.gov](mailto:william.joost@ee.doe.gov)

Contractor: Pacific Northwest National Laboratory  
(PNNL)  
Contract No.: DE-AC05-00OR22725 & DE-AC06-  
76RL01830

The purpose of SPR project is to provide a reliable mechanical joining technology for Mg joint applications and to enable the success of mechanical fastening of Mg by assisting the Mg SPR process development and cycle time through rivet process simulation and experimentation. This will be achieved by providing actual SPR joint performance data of Mg/Mg and Mg/dissimilar metal joints, so that more accurate data is applied to the overall structural design, and by developing process windows to provide design recommendations/guidelines for effective Mg SPR joining.

For the Al TWB project, the purpose is to develop the joining technology needed to demonstrate the fabrication of an aluminum tailor-welded component for an automotive door inner assembly that is currently made from steel, and demonstrate a greater than 40% mass savings. The project also aims to successfully transfer the production of aluminum TWBs into the automotive supply chain, thus enabling the rapid utilization of the technology in high-volume applications.

### Executive Summary

The Multi-Materials Enabling project consists of two tasks focused on research and development that can lead to greater implementation and manufacturing of multi-material lightweight components/systems in automotive applications. The tasks include the following: 1) Self-Pierce Riveting (SPR) Process Simulation, Analyses, and Development for Magnesium (Mg) Joints, and 2) High-Speed Joining of Dissimilar Alloy Aluminum Tailor-Welded Blanks (TWBs).

More energy efficient and environmentally friendly highway transportation is critical to reducing both the environmental impacts and energy consumption associated with transportation mobility. While transformational propulsion technologies and hybrid architectures show great promise in meeting such goals, these and other forthcoming solutions depend upon significant weight savings in passenger and commercial vehicles to fully capitalize on their potential to provide freedom of mobility without harmful emissions and dependence on foreign petroleum. Significant weight savings in the automotive fleet is likely to occur through the use of various advanced materials. While improvements in the properties, manufacturability, and cost of advanced materials are critical in achieving vehicle weight reduction, technologies that support the use of these materials in a multi-material system are equally important. Unlike a single material system, structures composed of different metals and polymer composites present significant challenges in areas such as joining, corrosion, recycling, and nondestructive evaluation. Work conducted in this agreement seeks to overcome these challenges by developing new techniques and preparing advanced technologies for a production environment.

## ACTIVITY AND DEVELOPMENTS

### Self-Pierce Riveting (SPR) Process Simulation, Analyses, and Development for Magnesium Joints

#### Elizabeth Stephens (Principal Investigator)

Pacific Northwest National Laboratory  
Phone: (509) 375-6836  
E-mail: [elizabeth.stephens@pnnl.gov](mailto:elizabeth.stephens@pnnl.gov)

#### Xin Sun, Co-Principal Investigator

Pacific Northwest National Laboratory  
Phone: (509) 372-6489  
E-mail: [xin.sun@pnnl.gov](mailto:xin.sun@pnnl.gov)

#### Eric Nyberg, Co-Principal Investigator

Pacific Northwest National Laboratory  
Phone (509) 375-2103  
E-mail: [eric.nyberg@pnnl.gov](mailto:eric.nyberg@pnnl.gov)

#### Dr. Siva Ramasamy (Principal Investigator)

Stanley Engineered Fastening  
Phone: (586) 949-0550  
E-mail: [siva.ramasamy@sbdinc.com](mailto:siva.ramasamy@sbdinc.com)

#### Accomplishments

- Numerically identified a temperature profile and heating mechanism for SPR joining. (FY 2013)
- Incorporated Stanley Engineered Fastening rivets and die geometries into the SPR modeling tool. (FY 2013)
- Prepared Mg SPR joints at elevated temperatures ranging from ~200 to 300°C with no tail side cracking. (FY 2013)
- Achieved joint strengths ranging from ~5.4 to 6.1 kN for 2 to 2 mm AZ31 SPR joints and joint strengths ranging from ~3.4 to 3.7 kN for 1 to 2 mm AZ31 SPR joints both under lap shear loading conditions. (FY 2013)
- Designed a custom heating system to implement into the elevated temperature joining process. (FY 2013)

#### Future Directions

- Integrate custom heating system into joining process.
- Prepare Mg joints with the implemented custom heating system and achieve target joint strength.
- Characterize SPR joint performance in terms of fatigue and corrosion.
- Disseminate modeling results via publications in peer-reviewed journals and conference presentations.

#### Technology Assessment

- Target: Create Mg SPR joints of similar and dissimilar materials under the guidance of SPR modeling tools established by the PNNL with no tail side cracking.
- Target: Produce Mg SPR joints with a minimum target joint strength of 1.5 kN \* t (substrate thickness).
- Gap: Mg alloys have low ductility at room temperature and when conventional SPR processing is used with magnesium, rivet tail end cracking occurs.
- Gap: Cracks in the SPR joint can be detrimental to the joint performance in terms of static and fatigue strength, as well as corrosion performance.



#### Introduction

Mg components offer a potential weight reduction of approximately 50 percent when substituted for the higher density or lower strength steel materials conventionally deployed in vehicles. Historically, poor joining methods for Mg components have limited their applications in vehicles. Over the years, a variety of joining technologies have been introduced into the automotive industry to achieve lightweight vehicle goals. SPR is potentially a viable method for joining similar and dissimilar metals involving Mg. SPR is a low energy consumption joining process with relatively low initial capital equipment cost. Because SPR is a mechanical joining process, the joint formation process involves large plastic deformation at the rivet tail end to ensure a mechanical interlock between the rivet material and the bottom sheet material. However, Mg alloys have low ductility at room temperature; thus, conventional SPR processing typically causes rivet tail end cracking. These cracks can be detrimental to the rivet performance in terms of static strength, fatigue strength, and corrosion performance.

#### Approach

This project is focused on developing and enabling the SPR process for joining Mg components in new vehicle applications to reduce vehicle weight through efforts established in a CRADA between PNNL and Stanley Engineered Fastening. This project aims to eliminate or substantially address key technical barriers in using SPRs in Mg-joining applications by using an integrated modeling and experimental approach. Barriers include tail side cracking of Mg sheet or castings due to the lack of ductility at room

temperature; lack of desired joint properties including corrosion at the joint; and lack of acceptable processing parameter windows. Further, the project will explore alternative/non-conventional rivet metals similar to the materials being joined to minimize the galvanic potential in the joint and an alternative joining method (i.e., clinching) that may further promote joining of Mg. Initial work has focused on the development of a numerical tool used to develop reliable Mg riveting process parameters through modeling and provide guidance in the development of joining process windows.

Phase 1 focuses on experimental validation of the modeling tool previously developed for Mg SPR joining using conventional rivet materials and geometries. This phase will experimentally validate the predicted results from the modeling tool to provide actual joint performance data (e.g., joint strength, fatigue strength, and corrosion performance) for the joint combinations evaluated. Phase 2 will focus on optimizing Mg SPR joints using the established modeling tool to investigate alternate rivet materials, including coatings or interlayers (e.g., adhesives). In addition, Phase 2 will address potential joint corrosion issues and optimize rivet geometry (i.e., shape and length) and die design to ensure joint integrity and performance. In addition, clinch joining, an alternate joining method that may be used alone or in conjunction with SPR, will be explored to investigate its potential to advance joining of Mg.

## Results and Discussion

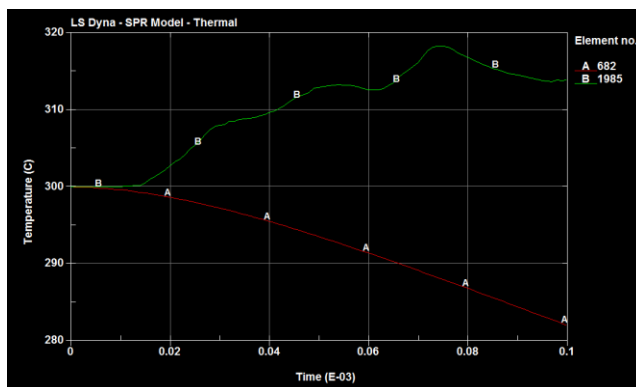
In FY 2013, efforts focused on improving the previously developed SPR finite element model (FEM) (e.g., adding thermal features and validating the predicted model joints with actual SPR joints made at elevated temperatures). Temperature is one of the most important parameters of the SPR process. Temperature is critical for determining the material properties of the sheet to be pierced. Hence, it is

important for the model to be able to capture the temperature gradient extending from one side of the sheet to the other side and from the top sheet to the bottom sheet. Temperature loss from the sheets is considered to result from three phenomenon: (1) heat conduction from the sheets to the die and to the clamping tool; (2) radiation of the sheets to the ambient surrounding; and (3) plastic work converted to heat resulting from plastic deformation near the rivet tip. These three phenomena were implemented into the model to aid and to ensure accurate material behavior at every location of the piercing area.

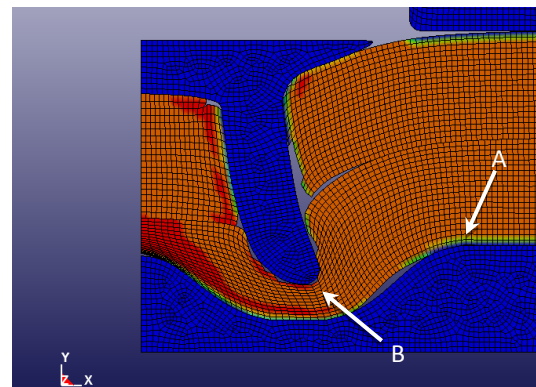
Figure III-74 shows the temperature distribution as a function of time and the joint area temperature contours during the riveting simulation at 300°C. Only temperature loss due to conduction and radiation is observed on the bottom sheet near the die (location A), whereas a rise of the temperature due to the plastic deformation is observed near the rivet tip (location B).

Stanley Engineered Fastening rivet and die geometries were incorporated into the thermo-mechanical FEM model. Simulations of the SPR process were then performed at room temperature and at elevated temperatures using those geometries. At temperatures ranging from 200 to 300°C, a good interlock of the rivet into the bottom sheet was observed, indicating a good joint. Better selection of rivet material properties at various areas of the joining zone attributed to this result.

Figure III-75(a) shows the predicted 2 mm to 2mm AZ31B SPR joint at 300°C using the newly incorporated geometries and the recently improved FEM model. Figure III-75(b) is a cross-section of the SPR joint made by Stanley Engineered Fastening using the same processing conditions. Good agreement is observed between the predicted joint using our FEM model and the actual joint made by Stanley Engineered Fastening.



(a)



(b)

Figure III-74: (a) Temperature distribution and variation as a function of time at two locations and (b) joint temperature contours where location A represents the near contact area with the die and location B is near the rivet tip.

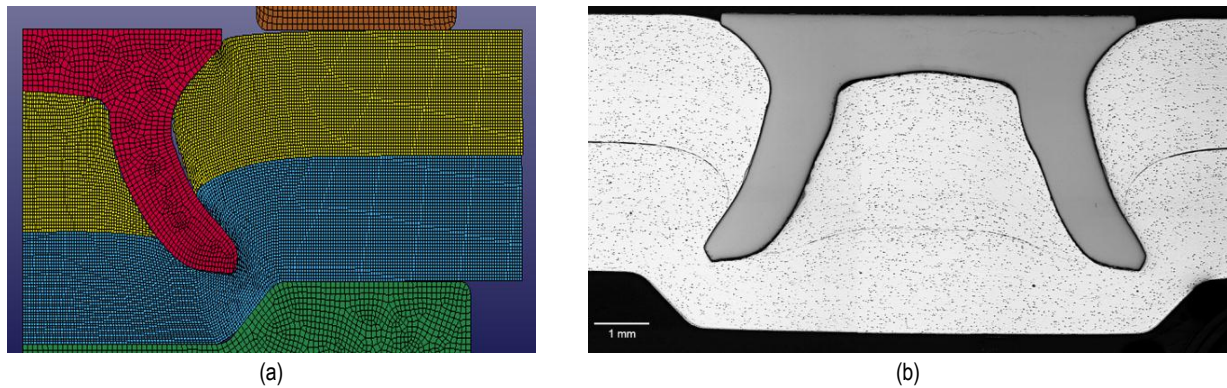


Figure III-75: A comparison between the (a) model prediction and the (b) actual experimental joint of a 2 mm to 2 mm AZ31 SPR joint made at 300°C.

To further validate the FEM model, 1 mm to 2 mm and 2 mm to 2 mm AZ31 SPR joints were prepared at room temperature and at elevated temperatures ranging from 100 to 300°C, as guided by the model. Conventional heating was used to perform the elevated joining. Varying rivet and die geometries were evaluated. No tail side cracking was observed on joints prepared at temperatures ranging from 200 to 300°C (see Figure III-76).

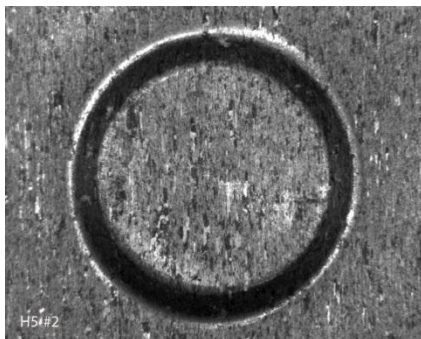


Figure III-76: A representative image of an AZ31 SPR joint with no tail side cracking observed. This particular joint was prepared at ~200°C.

Select processing conditions were performed on AZ31 lap shear coupons to assess the preliminary strength of joints prepared at 250 and 300°C. Under lap shear loading, joint strengths ranging from ~5.4 to 6.1 kN for 2 mm to 2 mm AZ31 SPR joints and from ~3.4 to 3.7 kN for 1 mm to 2 mm AZ31 SPR joints were achieved. Table III-5 summarizes the joint strength results and the observed failure modes. For the 2 mm to 2 mm AZ31 SPR joints, tail pull-out (TPO) was the primary mode of failure (Figure III-77(a)). For the 1 mm to 2 mm AZ31 SPR joints, shear out (i.e., rivet head pull-through) was the primary mode of failure. Figure III-77 shows representative images of the observed failure modes.

In addition, a preferred custom heating system was designed to be implemented into the elevated temperature joining process to better align with joining cycle times. Fabrication was completed at the end of FY 2013 and the unit is anticipated to be implemented in early FY 2014.

Table III-5: Preliminary joint strength results of AZ31 SPR joints under lap shear loading.

| AZ31 Stack-up | Specimen | Peak Load (kN) | Energy (J) at Peak Load | Failure Mode |
|---------------|----------|----------------|-------------------------|--------------|
| 2 mm to 2 mm  | 250-1    | 6.06           | -                       | Partial TPO  |
|               | 250-2    | 6.12           | 3.68                    | TPO          |
|               | 300-1    | 5.39           | 3.47                    | TPO          |
|               | 300-2    | 6.04           | 5.46                    | TPO          |
| 1 mm to 2 mm  | 250-3    | 3.67           | 0.70                    | Shear out    |
|               | 250-4    | 3.53           | 0.66                    | Shear out    |
|               | 300-3    | 3.41           | 0.66                    | Shear out    |
|               | 300-4    | 3.47           | 0.70                    | Shear out    |

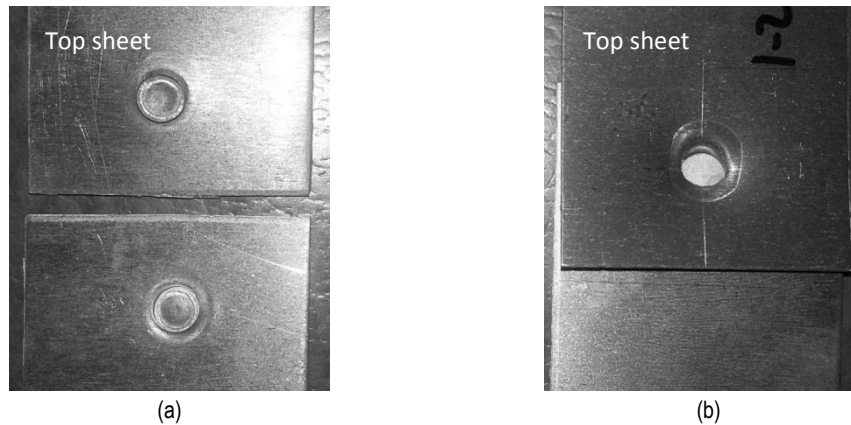


**Figure III-77: Representative images of the (a) tail pull-out and (b) rivet shear out failure modes observed of the AZ31 SPR joints under lap shear loading.**

### Technology Transfer Path

Technology transfer will occur throughout the project via close collaboration between PNNL and Stanley Engineered Fastening. The technology transfer approach includes the development of process equipment and processing parameters necessary to achieve successful Mg SPR joints.

### Conclusions

In this reporting period, the FEM SPR model was improved via the incorporation of thermal features to better assess material behavior during joining and incorporation of Stanley Engineered Fastening rivet and die geometries. Simulations performed using the improved model indicated that good interlock of the rivet into the bottom sheet material could be achieved at elevated joining temperatures ranging from 200 to 300°C without tail side cracking. The simulation results were further validated experimentally where efforts were spent assessing AZ31 joints created at both room temperature and at elevated temperatures ranging from 100 to 300°C. Promising, preliminary joint strength results of AZ31 SPR joints prepared at both 250 and 300°C indicate that the technology assessment targets may be met when the preferred heating system is implemented.

### Presentations

1. Stephens EV, A Soulami, EA Nyberg, and X Sun. 2013. "SPR Process Simulation, Analyses, & Development for Mg Joints Project Kick-off Meeting." Presented at Emhart Teknologies, Chesterfield, Michigan, February 2013.
2. Stephens EV, A Soulami, EA Nyberg, and X Sun. 2013. "2013 DOE Vehicle Technologies Program Review SPR Process Simulation, Analyses, & Development for Mg Joints." Presented at DOE Vehicle Technologies Annual Merit Review, Arlington, Virginia, May 2013.
3. Ramasamy, S, B Wilkins, B Kenyon. 2013. "SPR Process Simulation, Analyses, & Development for Mg Joints Internal Program Review." Presented at Stanley Engineered Fastening, Chesterfield, Michigan, September 2013.

# High-Speed Joining of Dissimilar Alloy Aluminum Tailor-Welded Blanks

## Yuri Hovanski (Principal Investigator)

Pacific Northwest National Laboratory  
Phone: (509) 375-3940  
E-mail: [yuri.hovanski@pnnl.gov](mailto:yuri.hovanski@pnnl.gov)

## Tom Luzanski (Principal Investigator)

TWB Company LLC  
Phone (734) 289-6468  
E-mail: [Tom.Luzanski@twbcompany.com](mailto:Tom.Luzanski@twbcompany.com)

## John Carsley (Principal Investigator)

General Motors  
Phone: (586) 986-2928  
E-mail: [john.carsley@gm.com](mailto:john.carsley@gm.com)

## Accomplishments

- Completed full design of experiment to quantify the measurable effects of tooling on formability and weld quality in high-speed friction stir-welded (FSW) TWBs of dissimilar thicknesses and alloy combinations. (FY 2013)
- Supported technology transfer by providing joining specification to TWB, LLC. Equipment was purchased and will be placed at the TWB, LLC facility in the first quarter of FY 2014. (FY 2013)
- Completed high-speed weld development at the PNNL for speeds up to 3 m/min in combinations of AA5182 and AA6022. (FY 2013)
- Prepared tooling and fixturing for continued high-speed development (3 to 6 m/min) and component production of the door inner welded blank at the General Motors (GM) and TWB, LLC facilities over the final year of the project. (FY 2013)
- Stamped hundreds of welded blanks using the TWB, LLC beaver tail die and characterized post-weld performance, draw depth, surface quality, and repeatability. (FY 2013)

## Future Directions

- High-speed weld development at the OEM and suppliers (3 to 6 m/min).
- Support technology transfer of welding and formability analysis to automotive supply chain.
- Probabilistic evaluation of alloy and thickness combinations that support component-forming models.
- Component production, stamping validation, and production durability testing of aluminum TWBs.
- Development of weld parameters for 5XXX to 7XXX series sections.

## Technology Assessment

- Target: Achieve friction stir weld speeds for aluminum TWBs in excess of 3 m/min with repeatable quality and surface finish.
- Gap: While conventional laser techniques are capable of welding at speeds from 4 to 10 m/min, linear speeds for friction stir welding have traditionally been below the 3-m/min range.
- Target: Develop capability for high-speed friction stir welding within the automotive supply chain by transferring high-speed friction stir welding techniques to at least one supplier that is capable of producing high-volume quantities of welded blanks.
- Gap: FSW is currently performed by only a few niche companies, none of which has the capability to support high-volume production.
- Target: Probabilistic analysis that supports formability modeling of tailor-welded components as a direct input, avoiding the complexity of direct phenomenological relations that currently do not exist.
- Gap: Modeling efforts of as-welded blanks lack the constitutive relationships needed to correctly predict the post-weld formability; however, probabilistic analysis inserted as an input may allow the modeling efforts to move forward based on statistically derived boundaries.
- Target: Full-size welded components that demonstrate modeled performance.
- Gap: Current modeling efforts do not accurately represent as-welded components; thus, a modeling effort needs to be fully verified with full-size component testing.



## Introduction

Strategic research and development investments over the last few decades have moved tailor-welded products from concept to reality. Several companies now produce dissimilar thickness panels, tailor-welded coils, and tailor-welded tube sections in a variety of steel alloys for use in many applications (e.g., door inners, shock towers, and floor pans). Use of the tailor-welded technology is increasing with greater demand for lightweight structures that reduce part count and lower cost. While automotive OEMs would like to expand the usage of tailor-welded technologies into aluminum alloys, current joining technologies significantly reduce the formability of the as-welded materials. Aluminum alloys have great potential for use in tailor-welded structures, and preliminary assessments show that the weight of numerous high-volume automotive components could be reduced by more than 40 percent.

While preliminary assessments demonstrate that tailor-welding technologies have the potential to reduce part count, cost, and weight, the joining technology needed to provide

adequate formability of the as-welded blank is not sufficiently developed to transfer the technology to any supplier. While several groups have shown the preliminary potential for FSW 5083 aluminum blanks of similar thickness, no weld schedules exist that can be modified or adapted for very dissimilar thicknesses (2:1 thickness ratios and greater) in dissimilar aluminum alloy combinations (e.g., 5000 series to 6000 or 7000 series aluminum alloys). To achieve weight savings in excess of 40 percent, weld parameters must be developed that enable multiple alloys to be joined in very dissimilar thickness sheet combinations while maintaining the majority of their original formability.

As the majority of data related to friction stir welding of Al TWBs is based around non-precipitation strengthened alloys (a material set that is very amenable to producing as-welded blanks with formability similar to the parent sheet) very little data has been produced relating the functional relationships between tool design, process parameters, fixtures, and alloy combinations. Joining dissimilar Al alloys has proved problematic, and successful implementation depends upon a much greater understanding of the influence of each of these factors on the formability of the tailor-welded component. Thus, further development of the FSW process in these form factors is necessary to provide a side-by-side comparison with other welding techniques.

Furthermore, previous pitfalls have hindered the progress of Al TWBs, as several groups have moved directly from welding to stamping without understanding the formability limits of the TWBs. This weld and stamp approach has proven problematic, as very little information on the usability of the as-welded component comes from the stamped part. Whether the part forms or fails provides little data as to whether the blanks will ultimately work in another application, and as such does not lead to a successful deployment path.

Predictive formability analysis has previously been developed and used at PNNL to determine the probabilistic forming limit for a weld blank. This approach, in conjunction with stamping models, has the potential to determine the overall probabilistic formability limits and provide an understanding of how they can be applied to numerous part geometries while avoiding the expense of the weld and stamp methodology.

The purpose of this project is to develop the functional relationships of factors driving the weld formability of both dissimilar thickness AA5182 as well as dissimilar alloy combinations. Furthermore, the best in class parameter set for each will then be analyzed to determine the probable forming limit, which will be used to model the overall stamping process. The process will be validated as the technology is transferred for actual part production, providing the tools needed to be able to further implement the process on other parts, geometries, and materials.

### Approach

To develop the joining technology needed to enable aluminum TWBs for high-volume automotive components, the work scope is divided into four main task areas. The first

focuses on the initial weld development for formability, including quantifying the effects of tool design and process parameters on formability. The second is designed to provide a comparison of the formability of aluminum welds produced via friction stir, laser, and laser-plasma welding. This task will ultimately lead to a decision gate that provides the information necessary to justify capital investments and product design using aluminum TWBs. The third task is divided into several areas that will emphasize preparing the process for commercialization. This includes pushing the process to higher linear weld speeds (up to 6 meters/min for solid state processes), tying probabilistic formability data into the component-forming models, and assisting the transfer of the weld process into a supplier's facility. That task will lead to the concluding task of producing actual production-ready coupons that will be stamped and tested by GM as a conclusion to the project efforts.

Efforts in FY 2013 focused on fully characterizing and quantifying the relationships between tool design and process parameters on post-weld formability. Having completed the first two tasks, the project team safely moved onto the third task, which focuses on technology transfer and commercialization. The data obtained in the first two tasks provided the information needed to machine designers and allowed TWB, LLC to fully engage in stamping welded blanks in various configurations.

### Results and Discussion

With the project approximately half completed, a significant amount of work was accomplished during FY 2013. The completion of a Taguchi design of experiment, quantifying the effects of tooling and processing parameters, met a milestone on the project that opened up progress on many of the final tasks. This statistical approach to analyzing parameters and tooling allowed for each factor to be independently quantified, while also evaluating the combined effects of multiple factors simultaneously (e.g., tooling features and rotational velocity). Examples of the tooling evaluated for this portion of the project are shown in Figure III-78, with specific probe and shoulder designs being shown in Figure III-78(a)-(d). Figure III-78(e) and (f) show a complete rendering of the tool and provide detailed design features necessary to duplicate the work. The alloy combinations in the design of experiments testing included dissimilar thickness AA5182 (2.0 to 1.2-mm) and dissimilar alloy AA5182 (1.2-mm) to AA6022 (2.0-mm). Each combination was investigated at weld speeds up to 3 meters/minute.

With a goal to systematically investigate the effects of various welding factors on the resulting weld quality and mechanical properties, the following control variables were evaluated: plunge depth, tool tilt, anvil tilt, the ratio of shoulder diameter to pin diameter, the number of shoulder scrolls, rotational velocity of the tool, pin features, and pin length. Welds were scrutinized based on surface quality, mechanical properties, and post-weld formability. Data from four of the weld conditions that yielded the highest strengths are shown in Table III-6.

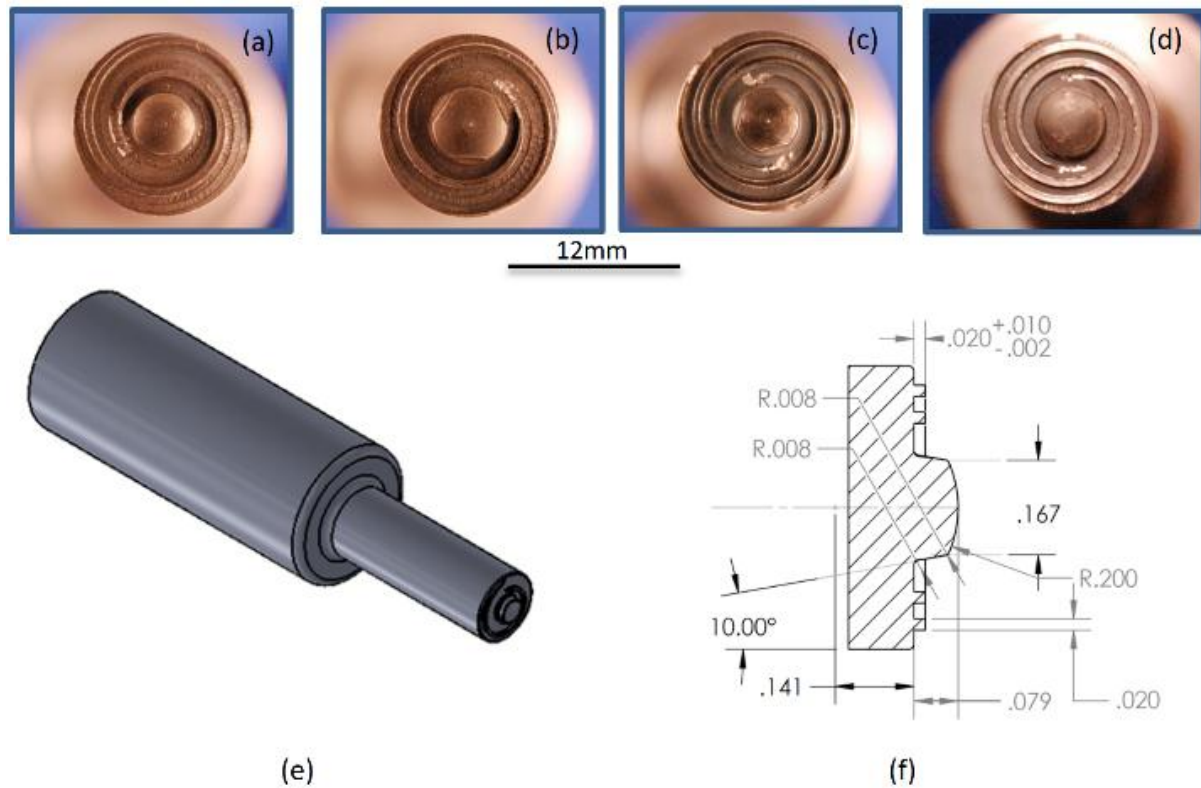


Figure III-78: Four tool designs used for the design of experiment testing representing the types of changes made to pin and shoulder geometries.

Table III-6: Process parameter details and properties from several welds in the study.

| # | Plunge Depth | Tool Tilt | Anvil Tilt | Shoulder/ Pin Ratio | Scroll | RPM  | Pin Feature | Pin Length | Strength, MPa | % Elong. | LDH   | R <sub>a</sub> , R <sub>max</sub> |
|---|--------------|-----------|------------|---------------------|--------|------|-------------|------------|---------------|----------|-------|-----------------------------------|
| 1 | Deep         | one       | tangent    | low                 | 2      | 1950 | flats       | 2          | 297.7         | 12.4     | 20.8  | 29.4, 33.7                        |
| 2 | Deep         | one       | less       | low                 | 1      | 1500 | taper       | 2          | 297.5         | 11.9     | 20.90 | 36.3, 47.8                        |
| 3 | Shallow      | zero      | tangent    | low                 | 1      | 1500 | flats       | 1.75       | 294.4         | 11.2     | 18.0  | 87.8, 96.3                        |
| 4 | Shallow      | one       | less       | high                | 1      | 1950 | taper       | 1.75       | 290.5         | 9.0      | 13.9  | 228.1, 197.4                      |

The R<sub>a</sub> and R<sub>max</sub> values indicated corresponds to the surface roughness of the weld crown measured using a high magnification optical method. Figure III-79 shows three-dimensional (3D) surface roughness profiles for welds #1 and #2, indicating key roughness parameters. Some variation in surface roughness is apparent between different weld parameter sets. Weld #1 produces the smoothest weld surface. Note that the surface roughness values are independent of the extent of the flash obtained during the weld.

Ultimately the main effects of each factor were quantified with respect to measurable outcomes. While the individual

effects of each factor were insightful, the combined effects were more helpful in understanding the relationships between tool design and process parameters on outcomes of the weld (e.g., dome height, surface roughness, and mechanical strength). Details on these outcomes are slated to be presented in several publications that are in process and too lengthy for discussion herein. However, the weld parameters most effective for welding AA5182 in dissimilar thicknesses of 2.0 and 1.2-mm are identified in Table III-6 as weld #1. This weld condition led to the smoothest weld condition with properties near the best achieved in every other measured category.

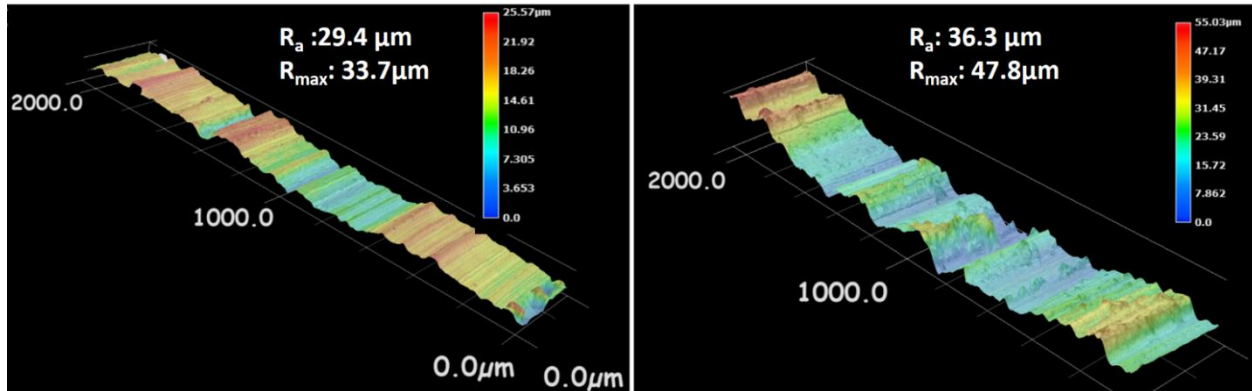


Figure III-79: 3D surface profiles for weld #1 (left) and weld #2 (right) obtained from high magnification optical measurement.

A significant number of welded blanks were stamped using a beavertail die set at TWB, LLC. This die accentuated the worst possible stamping conditions with the weld seam being placed on the outer corners of the die and the internal embossed section. The die was setup to allow for variable draw depths up to 36 mm, and proved an effective means of looking at overall weld quality, repeatability, and formability. See Figure III-80 for a representative stamping of a welded blank between 2.0 and 1.2-mm AA5182. While stampings were made from several welding processes, only FSW was able to weld blanks capable of the full draw depth of the beaver-tail die.

Based on the positive results from the design of experiments testing at speeds up to 3 meters/minute, the project team has designed fixtures and tooling to transfer the welding parameters to the R&D center at GM. Welding of full-size door panels will commence in FY14 at 3 meters/minute welding speed, and development will continue at velocities up to 6 meters/minute.

### Technology Transfer Path

Technology transfer into the high-volume automotive supply chain was a key task critical to the planning of the entire project. The project was designed to provide technological expertise from the researchers at PNNL who engage the entire supply chain, including the material provider, Alcoa; the high-volume automotive supplier, TWB, LLC; and the OEM, GM. With this team engaged from start to finish in the project, the technology will be developed and transferred using alloys and gauges already set for production quantities and quality sufficient to meet the demands of high-volume automotive production. A production line will be set up within the high-volume supplier's facility with quality and production standards in place, allowing full-size production components to be produced for testing by the automotive OEM.



Figure III-80: An as-stamped AA5182 welded blank with 2.0- to 1.2-mm dissimilar thickness sheets.

At the conclusion of the project, the entire supply chain should be staged and able to supply aluminum TWBs for high-volume production components. This path should effectively bridge the gap between development and utilization by intrinsically supporting industrial implementation.

## Conclusion

Completion of a statistical design of experiment approach to analyzing the effects of tool design and process parameters provided a means for quantifying their relationships on post-weld properties. The data obtained through the study evaluated hundreds of combinations of combined effects and ultimately bounded many of the parameters needed to be able to specify appropriate equipment designs for industrialization of the process. This process demonstrated a path to production for welding dissimilar thickness AA5182 and dissimilar alloy combinations of AA5182 and AA6022 at speeds up to 3 m/min.

A significant effort from the automotive supply chain provided interim evaluations of post-weld formability via stamping trials, which have prepared the work for moving to the final phase in component production. In combination with the modeling work that continues at PNNL, this data begins to bound the formability of each welded combination such that current modeling software may be adjusted to more accurately predict weld formability of aluminum welded blanks.

## Presentations/Publications/Patents

1. Hovanski, Y; Carsley, J; Pilli, S. P; Verma, R; Hartfield-Wunsch, S; Carlson, B; Eisenmenger, M. High Speed Joining of Aluminum Tailor-Welded Blanks for Automotive Applications. *In Proceedings of TMS Annual Meeting 2013*, San Antonio, Texas, March 2013.
2. Carsley, J.; Hovanski, Y.; Pilli, S.; Verma, R.; Hartfield-Wunsch, S.; Carlson, B.; Eisenmenger, M. High Speed Joining of Aluminum Tailor-Welded Blanks for Automotive Applications. *In Proceedings of Material Science and Technology 2012*, Pittsburgh, Pennsylvania, October 2012.

## III.6. Industrial Scale-Up of Low-Cost Zero-Emissions Magnesium by Electrolysis—INFINIUM, Inc.

### Adam C. Powell, IV (Principle Investigator)

INFINIUM, Inc.  
3 Huron Drive  
Natick, MA 01760  
Phone: (781) 898-3430  
E-mail: [apowell@infiniummetals.com](mailto:apowell@infiniummetals.com)

### Aaron Yocum, Project Officer

National Energy Technology Laboratory  
3610 Collins Ferry Road  
Morgantown, WV 26507  
Phone: (304) 285-4852  
E-mail: [Aaron.Yocum@netl.doe.gov](mailto:Aaron.Yocum@netl.doe.gov)

### William Joost, Technology Area Development Manager

U.S. Department of Energy  
1000 Independence Avenue, S.W.  
Washington, DC 20585  
Phone: (202) 687-6020  
E-mail: [william.joost@ee.doe.gov](mailto:william.joost@ee.doe.gov)

Contractor: INFINIUM, Inc.  
Contract No.: DE-EE0005547

### Abstract/Executive Summary

Direct electrolysis of magnesium oxide has been a dream of the magnesium industry for decades. Magnesium oxide is typically made from brines or sea water by reaction of dissolved  $MgCl_2$  with  $NaOH$  producing  $NaCl$  and insoluble  $Mg(OH)_2$ , which is removable by filtration. Heating the hydroxide then drives off its water to produce  $MgO$ . Today's chloride electrolysis plants must then use carbochlorination or hydrochlorination with chloride dehydration to produce pure anhydrous  $MgCl_2$ , and electrolyze that to produce  $Mg$  metal and  $Cl_2$  gas. Direct  $MgO$  electrolysis would save this  $MgCl_2$  production step, which is energy and capital intensive and can produce harmful dioxin and furan emissions.  $MgO$  electrolysis would also eliminate the need to contain chlorine which often escapes as a pollutant, and would use less energy also due to the lower formation enthalpy of  $MgO$  vs.  $MgCl_2$ .

The INFINIUM MagGen™ system performs this direct  $MgO$  electrolysis. This process dissolves  $MgO$  in a molten salt, then applies a DC potential across the salt, producing magnesium vapor at the cathode and oxygen gas at the zirconia-sheathed anode. The zirconia acts as a solid electrolyte which separates the magnesium and oxygen products, preventing back-reaction between them. The anode

is also protected from the harsh molten salt environment, enabling the use of a variety of inert anode materials. Zirconia is very selective, such that the oxygen by-product is much more pure than that produced by conventional inert anodes without zirconia protection, such as nickel ferrite.

The overarching objective of this project is to bring INFINIUM's MagGen™ primary magnesium production system from large laboratory demonstration to the threshold of industrial production. This efficient zero-emissions process makes high-purity magnesium directly from abundant domestically-produced industrial magnesia in a single step, with a high-purity oxygen by-product, and with condenser heat available for other uses.

Success of this project will prepare the technology for industrial implementation of this process, reducing the costs, energy use, and emissions associated with magnesium production, and helping vehicle manufacturers to realize their goals of reduced weight and increased vehicle efficiency. Improved vehicle recyclability may also result by increasing the value of post-consumer automotive scrap metal.

Toward those ends, this project's tasks during this period were as follows:

1. *Project Management and Reporting*
2. *Design, Build and Test Prototypes* Produce fully-featured prototypes designed to demonstrate all aspects of the process, one with a focus on maximum possible run time and the other at increasing scale
3. *Anode Optimization and Manufacturing* Optimize zirconia tube composition and structure for this novel application, and develop other components including low-cost charge transfer material and current collector.
4. *Test Magnesium Product Composition* Understand the source and disposition of impurities in the system to meet the requirements of automotive components
5. *Magnesium Plant Cost, Energy, Greenhouse Gas (GHG) and Other Emissions Modeling* Characterize these aspects of the process relative to current practices in automotive materials and magnesium competitors
6. *Magnesium Plant Design and Planning* Design the layout of a magnesium primary production plant based on the unique advantages and requirements of MagGen™ electrolysis cells.

### Accomplishments

- Alpha prototype furnace ran continuously from mid-July to late-October, 2448 hours, a new benchmark.
- Ran the longest electrolysis experiment with a single component assembly to date, with sustained tube integrity; set new benchmark for increasing tube life.

- Improved Alpha prototype to include a reconfigured modular condenser, new casting system with controlled cooling.
- Finalized cathode assembly design and began manufacturing for prototyping needs.
- Developed a new method for reliably hot-swapping cathodes and anodes in the Alpha prototype furnace while at 1150°C process operating temperature, including a mechanical tube loader.
- Completed fabrication and assembly of the Beta prototype, focused on scale-up magnesium production. Upgraded ventilation and power, began testing instrumentation and controls, and loaded salt.
- Manufactured custom zirconia tubes to meet most prototyping needs and maintained tube inventory of four different compositions. Purchased and installed large furnace for on-site sintering of 40 tubes per batch.
- Designed and fabricated prototype for testing electrolysis with seven different flux compositions simultaneously. Identified initial candidates for optimal tube performance and lifetime.
- Subcontractor Kingston Process Metallurgy (KPM) conducted short-term magnesium oxide electrolysis experiments using INFINIUM zirconia-sheathed anodes in a transparent crucible and furnace, producing visible magnesium vapor.
- KPM also performed experiments to selectively remove calcium from salt.
- In several areas, new experimental data and refined models are indicating much lower costs than initial estimates.
- Began a detailed COMSOL multi-physics model of fully-coupled heat and mass transfer and fluid flow with electrolysis in a single anode-cathode assembly.
- Detailed plant design narrative to refine capital and balance of plant cost estimates is nearly complete. The electrolysis cell house reaches good returns to scale in modules of about 3500-4000 tonnes/year, indicating ability to scale down to “minimills” at mines or customer sites.
- Submitted provisional and non-provisional utility patent applications.

### Future Directions

- Continue to run electrolysis in the alpha prototype for anode optimization experiments and increased uptime.
- Run electrolysis in the beta prototype to test scaling issues at high current and make magnesium metal for tensile testing and part fabrication.
- Finalize anode assembly design and scale up manufacturing. Verify anode plant design.

### Technology Assessment

- Target: Alpha prototype to achieve 50% of industry standard uptime.
- Gap: Traditional material handling is not suited for raw material feed in this application.

- Target: Beta prototype to achieve 20% increase in uptime over the FY2013 performance of the alpha prototype.
- Gap: Systems integration poses compatibility and scale-up challenges.
- Target: Down-select final methods for producing anode assembly components.
- Gap: Testing anode assemblies requires significant Alpha/Beta prototype access.



### Introduction

The objective of this project is to bring INFINIUM's MagGen™ primary magnesium production system from large laboratory demonstration to the threshold of industrial production. This zero-emissions, energy-efficient process makes high-purity magnesium from domestic industrial magnesia in a single step. By-products include high-purity oxygen gas and condenser heat, both available for other uses.

### Approach

The Alpha prototype is designed to run for as long as possible. The goal is to identify and ameliorate as many failure modes as possible at a small scale, then apply those lessons to future prototypes in order to maximize uptime at full scale production. The main system components to refine include the zirconia tube, anode, current collector, and condenser. The Beta prototype, with at least 10 times the production capacity of the Alpha, will test subsystems at larger scale and produce magnesium metal for tensile testing and part die-casting, and will have all required process features for a full industrial-scale unit.

### Results and Discussion

The full Alpha prototype is focused on maximizing uptime by improving component design and materials. Significant improvements were made to the anode-cathode assembly, current collector assembly and condenser. Additionally, INFINIUM has begun making high-quality zirconia tubes from several different compositions in order to increase tube lifetime and ultimately magnesium manufacturing uptime. The Alpha prototype has produced magnesium with 99.97% product purity, and current controls are predicted to produce even higher purity levels. Furthermore, modeling and experimentation has demonstrated excellent feasibility for recycling argon gases exiting the electrolysis cell.

Magnesium use in the automotive industry will reap significant fuel and energy savings. Modeling and calculations determined annual fuel savings from magnesium use at  $5.79 \times 10^9$  gallons of gasoline, equivalent to 724 TBTU, and reducing U. S. transportation emissions by 51.6 MMT CO<sub>2e</sub>. Annual energy savings from magnesium production ranges from 84-340 TBTU/year, reducing industrial emissions by 4.3-

45 MMT CO<sub>2</sub>e, depending on elasticity of magnesium demand.

During the course of this project, the technology will move from laboratory scale to prototype production systems. These prototype systems will be located at plants and/or customer sites to log sufficient uptime to demonstrate financially viable commercial production.

Additionally, INFINIUM will continue to collaborate with program partners to discuss implementing our technology and other advances, such as new sheet rolling and other technologies. Working with die casters and other parts suppliers, we will define future expectations and have deals in place when metal production ramps up.

## Conclusions

INFINIUM has met targets and overcome significant technical hurdles. Component design of the alpha prototype has steadily improved, resulting in longer system uptime, higher current efficiency, and much lower zirconia degradation in this process than before. Some of the biggest challenges at the Alpha prototype scale were solved or will be solved, and those solutions have been implemented in our already assembled Beta prototype. Great strides in analyzing zirconia tube compositions were made, which will likely lead to longer tube life and system uptime.

INFINIUM is well on its way to realizing the project's goal of scaling up the MagGen™ magnesium primary production system and achieving the vision of low-cost zero-emissions magnesium production.

## Presentations/Publications/Patents

1. A. Powell, "Clean Metal Production for a Clean Energy Future," Presentation to ARPA-E Program Managers December 4, 2012.
2. A. Powell, "Computer Modeling for Materials Science and Sustainability," *National Research Council Network for Emerging Leaders in Sustainability*, December 4, 2012.
3. A. Powell, "Magnesium in Transportation: Unlocking Limitless Potential Through Primary Production and Recycling," *ARPA-E A-TEME Workshop* January 31, 2013.
4. A. Powell, "Modeling Electrodeposition in Materials Process Operations," *TMS Annual Meeting Short Course*, March 3, 2013.

5. U. Pal, "Electrolytic Production of Metals from Oxides Dissolved in Molten Salts," *TMS Annual Meeting Symposium on High Temperature Electrochemistry*, March 4, 2013.
6. A. Powell, "Systems Engineering for Scale-Up of the INFINIUM™ MagGen™ Primary Magnesium Production System," *Reactive Metal Workshop* March 8, 2013.
7. U. Pal, "Low Carbon Footprint Process for Metals Production," *Reactive Metal Workshop* March 8, 2013.
8. Guan, X.; Zink, P.; Pal, U.; Powell, A. Recycling of Magnesium Alloy Employing Refining and Solid Oxide Membrane (SOM) Electrolysis. *Metall. Mater. Trans. B*. DOI: [10.1007/s11663-013-9797-9](https://doi.org/10.1007/s11663-013-9797-9) **2013**, 44, pp. 261–271.
9. Milshtein, J.; Gratz, E.; Pati, S.; Powell, A.; Pal, U. Yttria-Stabilized Zirconia Membrane Stability in Molten Fluoride Fluxes for Low-Carbon Magnesium Production by the SOM Process. *J. Min. Metall. B* DOI: [10.2298/JMMB120809005M](https://doi.org/10.2298/JMMB120809005M) **2013**, 49, pp. 183–190.
10. Guan, X.; Pal, U.; Powell, A. An Environmentally Friendly Process Involving Refining and Membrane-Based electrolysis for Magnesium Recovery from Partially Oxidized Scrap Alloy. *JOM*. DOI: [10.1007/s11837-013-0659-3](https://doi.org/10.1007/s11837-013-0659-3) **2013**, 65, pp. 1285–1292.
11. Guan, X.; Pal, U.; Gopalan, S.; Powell, A. LSM (La<sub>0.8</sub>Sr<sub>0.2</sub>MnO<sub>3-δ</sub>)-Inconel Inert Anode Current Collector. *J. Electrochem. Soc.* DOI: [10.1149/2.016311jes](https://doi.org/10.1149/2.016311jes) **2013**, 160, pp. F1179-F1186.
12. Uday B. Pal, Eric Gratz, Xiaofei Guan, Peter Zink, Soobhankar Pati, Adam C. Powell, John Strauss, Aaron Tajima and R. Steve Tucker, "Methods and Apparatuses for Metals Production, Separation and Recycling by Salt- and Argon-Mediated Distillation with Oxide Electrolysis, and Sensor Device Related Thereto," U.S. Patent Application 13/645,876, PCT Application PCT/US12/58882, filed October 5, 2012.
13. Adam C. Powell, John Strauss, R. Steve Tucker, J. Brodie Voellinger, "Low-Metal Inert Anode for High-Temperature Oxygen Separation," U.S. Provisional Patent Application 61/834,180 filed June 12, 2013.

## Reference

- Kippouros, G; Sadoway, D. A thermochemical analysis of the production of anhydrous MgCl<sub>2</sub>. *J. Light Metals* **2001**, 1, pp 111–117.

## III.7. Development and Demonstration of a Magnesium-Intensive Vehicle Front-End Substructure—United States Automotive Materials Partnership (USAMP) LLC

### James F. Quinn (Principle Investigator)

General Motors Research & Development Center  
30500 Mound Road  
Warren, MI 48090-9055,  
Phone: (586) 596-439; Fax: (586) 986-9204  
E-mail: [james.f.quinn@gm.com](mailto:james.f.quinn@gm.com)

### Joy H. Forsmark (Principle Investigator)

Ford Motor Company  
Ford Research and Innovation Center  
2101 Village Road  
Dearborn, MI 48124,  
Phone: (313) 845-3056  
E-mail: [jforsma5@ford.com](mailto:jforsma5@ford.com)

### Stephen D. Logan (Principle Investigator)

Chrysler Group LLC  
800 Chrysler Drive  
Auburn Hills, MI, 48326-2757  
Phone: (248) 512-9485; Fax: (248) 576-7490  
E-mail: [sl16@chrysler.com](mailto:sl16@chrysler.com)

### Aaron Yocum, Project Manager

National Energy Technology Laboratory  
3610 Collins Ferry Road  
Morgantown, WV, 26505  
Phone: (304) 285-4852  
E-mail: [aaron.yocum@netl.doe.gov](mailto:aaron.yocum@netl.doe.gov)

### William Joost, Technology Area Development Manager

U.S. Department of Energy  
1000 Independence Avenue, S.W.  
Washington, DC 20585  
Phone: (202) 287-6020; Fax: (202) 856-2476  
E-mail: [william.joost@ee.doe.gov](mailto:william.joost@ee.doe.gov)

Contractor: United States Automotive Materials  
Partnership LLC  
Contract No.: DE-EE0005660

### Abstract/Executive Summary

The goal of this project is the design, manufacture and evaluation of magnesium-intensive “demonstration” vehicle front end substructures, enabled through the application of

novel magnesium alloys, material processing, joining, finishing and computer-aided modeling techniques. The “demonstration” structure concept serves as a geometric platform for investigation of alternative materials and processes whereby computer aided design (CAD) renderings and fixtures for processing and testing are commonized. The structures will employ a central, super-vacuum die cast (SVDC) AM60B magnesium “shock tower” component to which upper and lower rail pieces are attached, reminiscent of structural archetypes seen in typical unibody vehicle front-end construction. A focal point of this work is the development and subsequent study of mixed-metal structures including galvanized steel and wrought aluminum to demonstrate multi-material joining and finishing techniques as well as exceptional structural/crash and durability performance (including fatigue and corrosion). The project includes efforts in the Integrated Computational Materials Engineering (ICME) of die-cast and wrought magnesium alloys and components fabricated from them.

### Accomplishments

- Concluded the design and component material selection for the multi-material demonstration structures.
- Produced formed high-strength low-alloy (HSLA) 350 galvanized steel and 6022-T4E40 aluminum sheet components for the upper rail portions of the structures.
- Obtained billet stock and experimental lower-rail extrusions of a new ZE20 extrusion grade of magnesium, showing acceptable extrusion speeds in comparison to baseline AZ31 magnesium.
- Confirmed capability for forming sound joints of AM60B magnesium to 6082-T4 aluminum (extrusion) using self-piercing rivets (SPR) without the necessity of preheating the magnesium.
- Procured unique ion-vapor assist deposition (IVAD) aluminized SPR rivets for comparative corrosion testing with various coating technologies. Developed an extensive designed experiment test matrix for assessment of rivet coatings and candidate corrosion protection for magnesium and mixed-metal joints.
- Identified a technological approach and enlisted a supplier to assess the effectiveness of various coatings to steel fasteners (principally self-piercing rivets) for use with magnesium.
- Demonstrated capability for producing friction-stir weld joints of 6022-T4 aluminum to AM60B magnesium with sufficient lap-shear strength (> 2 kN) for use in joining the upper rails to shock-tower castings.

- Refined computer aided engineering (CAE) durability models for all magnesium Phase II demonstration structures to enable improved predictions of fatigue failure location and durability.
- Demonstrated understanding of friction-stir weld tensile loading performance asymmetry associated with differentials of advancing/retreating interfacial hooking as it depends on material stacks in lap welds using this joining method.
- Commissioned a technology partner to further develop a unique joining technique (adaptable insert welding) to permit fastening of steel to magnesium.
- Commissioned a technology partner to develop a 3-D LS-DYNA® material card for die-cast AM60B magnesium as may be employed in thick-wall castings such as the shock tower.
- Conducted microstructural and ICME modeling studies of the continuous  $\beta$ -phase ( $Mg_{17}Al_{12}$ ) precipitation in the high aluminum content magnesium alloy AZ91D.
- Obtained initial SVDC AM60B shock tower castings for process validation and crashworthiness testing.

### Future Directions

- Acquire the remainder of the magnesium (super vacuum die castings) and aluminum component parts necessary for manufacture of the requisite quantities of demonstration structures for evaluation.
- Validate selected manufacturing processes (e.g., joining and surface finishing) that will ultimately be employed in the construction of the demonstration structures and select contractors for fabrication and finishing of the same.
- Construct the demonstration structures in two versions: steel upper rail structures and aluminum upper rail structures (both including the same AM60B SVDC shock tower and 6082-T4 aluminum extruded lower rail).
- Complete all durability and corrosion testing of the demonstration structures and document findings.
- Conclude ICME activities as pertain to both current demonstration structures as well as advanced materials (e.g., next generation magnesium alloys) which may be employed in future structures.

### Technology Assessment

- Target: **Design**. Create a design for a magnesium plus mixed material demonstration structure to evaluate candidate joining methods, durability and corrosion mitigation strategies while accommodating improved magnesium shock tower design. Design such demonstration structure for robust fixturing for durability testing.
- Gap: Apply lessons learned in Phase II to improve castability and SVDC part integrity.
- Target: **Crashworthiness**. Analytically predict peak load and displacement at peak load within 5% (or within test scatter band) of average of physical tests for magnesium AM60B SVDC components.

- Gap: Accurate 2D and 3D material property inputs for LS-DYNA® to permit finite element calculation of deformations of die-cast magnesium at high strain rates.
- Target: **Durability (Fatigue)**. Achieve capability for CAE prediction of fatigue life of similar and dissimilar metal joints with magnesium within a factor of two with respect to experimentally obtained values.
- Gap: Mechanistic models that permit transference of coupon load/cycles to failure data to structural stresses at joints in actual assemblies with complex geometries.
- Target: **Corrosion**. Achieve zero or minimal galvanic corrosion associated with coated, hardened steel self-piercing rivets in magnesium.
- Gap: Lack of analytical methods and coating technologies to isolate steel fasteners from surrounding magnesium or aluminum.
- Target: **Extrusion**. Mg extruded alloy with improved ductility over conventional AZ31/AM30 extrusion alloys (>12%) and more isotropic texture to improve performance in component level deformation testing and achieve higher extrusion speed.
- Gap: Further testing and characterization is required to determine if performance improvement of selected ZE20 extrusion alloy (27% ductility under uniaxial tension in laboratory testing) can be achieved at the component level. Comparison of extrusion speeds to baseline 6082 aluminum alloy.
- Target: **Casting**. Confirmation of the value of SVDC in improving the tensile and fatigue properties of die cast AM60B alloy. To date, a controlled, statistically significant study has not been completed to quantify the benefits.
- Gap: Lack of suppliers (of Mg alloy die castings with vacuum capability) to conduct such a study.
- Target: **Joining**. Identification and demonstration of joining technologies compatible with the dissimilar material combinations included in the present generation of demonstration structures and assemble approximately 200 structures by 5/31/14.
- Gap: For Aluminum-magnesium joints, there are consistent issues with generation of brittle intermetallic compounds of Al and Mg and reduction in joint strength. For galvanized steel-magnesium joints there are similar issues of incompatibility of the base metals as well as severe galvanic corrosion coupling prospects for iron and magnesium.



### Introduction

This project builds upon the learning from several prior and interrelated USAMP Magnesium Front End R&D (MFERD) projects. Hence, it is commonly referred to as “MFERD Phase III.” The overall effort is aimed at developing robust, enabling technologies permitting greater utilization of magnesium alloys in light-vehicle body structures, of which the “front end” substructure is exemplary [1]. The precursor projects included manufacture and evaluation of a number of

“all magnesium” demonstration structures employing both friction-stir welding and self-piercing rivets as the principal joining methods, with conversion coating and cathodic electrocoat as the protective finish. Conventionally-coated (i.e., Zn-Sn) self-piercing steel rivets, which, while offering substantial joint strength, had disadvantages of requiring preheating of the magnesium alloys used, and susceptibility to galvanic corrosion attack in regions adjacent to the rivets.

The current project considers front-end design alternatives with a common structural design envelope, but that employ “mixed” metal construction, specifically, galvanized HSLA 350 steel and wrought 6000 series aluminum in the form of sheet-fabricated components or high-strength extrusions. This approach addresses concerns from the earlier phases of the initiative, wherein commercially-available wrought grades of magnesium were more prone to early fracture, particularly in high-strain rate (i.e., crash) loadings and where integration of large magnesium structural castings to predominantly steel body-in-white structures is a more likely scenario. Previously-defined, knowledge-based and enabling technology disciplines are now primarily focused on dissimilar metal structures. The project does, however, maintain a substantial effort targeting the improvement and understanding of magnesium alloys at a fundamental level with the aims of reducing production cost and improving mechanical properties to be more competitive with current lightweighting materials such as aluminum. The project also exploits a longstanding (since 2007) international (U.S., Canada and China) cooperative effort aimed at

advancing the knowledge base and technologies required for greater use of magnesium alloys in automotive structures, leading to consequential reductions in greenhouse gas emissions and fuel consumption.

### Approach

This project is organized similarly to the prior USAMP efforts, principally by the technical or knowledge-based specialties shown in Table III-7. A similar organizational structure is also employed by the greater three-country effort focused on magnesium, wherein task titles refer to the working groups of each country.

### Results and Discussion

**Task 2—Design.** The subtasks are to design, build, and create CAD models of the demonstration structures for MFERD Phase III. The demonstration structure for MFERD Phase III utilizes the existing shock tower tooling from the previous project (DE-EE0003583). The shock tower casting design was modified to improve metal flow during casting, to add bosses for bolted joint studies, to add loading ribs for durability testing and to add a thickened edge section to reduce stress concentrations (Figure III-81). These changes reflect “lessons learned” from the prior works.

**Table III-7: Project subject matter and team organization.**

| Task | Title  | Remarks  |
|------|--|--|
| 1    | Project Administration                                   | maintain project financial records, reporting, purchasing and project management   |
| 2    | Design and Build   | CAD of structures, logistics, design   |
| 3    | Crashworthiness and Noise, Vibration and Harshness (NVH) | develop material deformation equations and CAE background  |
| 4    | Durability and Fatigue                                   | develop models for predicting fatigue life of structural joints; conduct durability testing of structures  |
| 5    | Corrosion and Surface Treatment                          | provide corrosion protective coatings for structures; develop methods for analysis and defeat of galvanic corrosion of magnesium in mixed metal structures   |
| 6    | Extrusion  | explore novel extrusion alloys to permit improved formability and component durability   |
| 7    | Low-cost Sheet and Forming                               | monitor developments in Mg sheet alloys; provide sheet-formed parts of aluminum and steel for demonstrations   |
| 8    | High-Integrity Casting                                   | continue development of the “super-vacuum” die casting process for magnesium and provide requisite castings for demonstration structures and test specimens. |
| 9    | Welding and Joining                                      | provide joining technologies for mixed-metal joints incorporating magnesium in the demonstration structures  |
| 10   | Integrated Computational Materials Engineering (ICME)    | continue development of computational tools for processing-structure-properties characterization of magnesium alloys   |

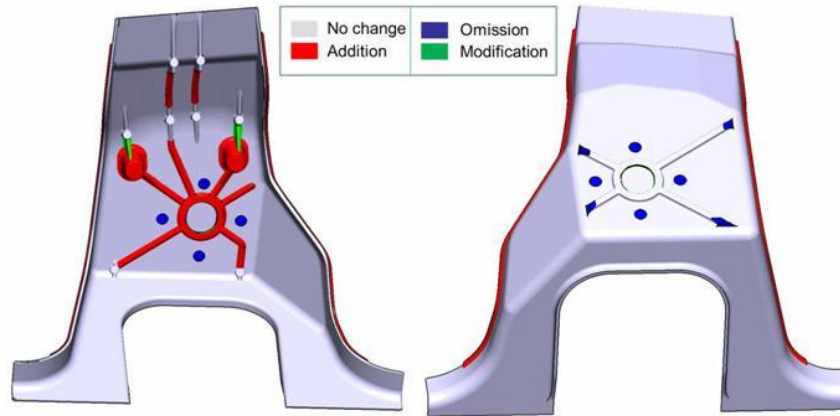


Figure III-81: Bottom (left) and top (right) view of the MFERD Phase III shock tower of AM60B SVDC showing changes from Phase II casting.

With the interest in mixed-material structures utilizing a central cast magnesium component, the Phase III demonstration structure has the magnesium AM60B die-cast shock tower joined to extruded and sheet aluminum or sheet steel, (Figure III-82). This strategy develops and demonstrates joining and surface treatments for magnesium castings as they may be integrated into dissimilar material vehicle structures.

The Task 2 (Design) Team coordinated the timeline for the demonstration structure builds and testing, which identified critical interactions between the teams, especially for joining, corrosion and durability. Additionally, an agreement was implemented (with Universal, Inc., Warren, MI) for storage and logistics of parts and coupons supporting the demonstration structure build and the testing by all the task teams. By calendar year end 2013 the Design Team intends to release the CAD renderings for the Phase III demonstration structures to all the task teams for their various uses.

**Task 3—Crashworthiness and NVH.** The task objectives are (1) improvement in the previously-devised LS-DYNA® material card for shell elements and (2) development of a comparable material card for solid elements to describe thicker sections of die cast AM60B in crash simulations. The improved LS-DYNA® material card incorporates (1) an automated procedure for calculating material parameters from stress-strain curves, (2) a nonlinear damage model, and (3) strain hardening in both tension and compression, reflecting the unique crystal plasticity behavior of magnesium alloys. The model for solid elements, however, does not currently include these nonlinear features. The supplier, Forming Simulation Technologies, Inc. began computer coding of these enhancements in August 2013 and coding will be completed by end of calendar 2013.

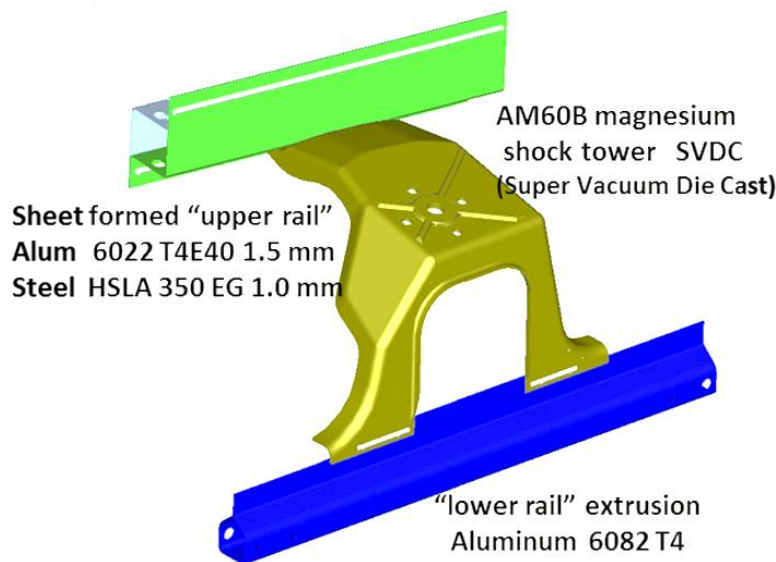


Figure III-82: Phase III demonstration structure.

The material model “card” for AM60B die cast magnesium in LS-DYNA® requires actual deformation data acquired for known points on the yield surface (e.g., pure shear). The pure shear specimens developed enable this type of data. Plans for securing both samples and experimental data were developed. A study was conducted to define suitable specimen geometries for pure shear testing. Two sample geometries proposed and modeled using the finite element method are shown in Figure III-83. Initiators were added to the samples to produce failures starting in the shear zones in these samples. The Phase III shock tower was selected as the component for material model validations. Both 2-D (shell) and 3-D (solid) finite element models of the shock tower were created during FY 2013. Trial runs on the 2-D model have been completed and compared to experimental deformation of the shock tower component (Table III-8). The model accurately predicted the locus of failure for static loading of the current shock tower design. Details for the modeling are shown in Figure III-84.

In addition to developing material property data for AM60 die cast magnesium, which has nominally isotropic yield and deformation properties, the team organized an approach to collect high strain-rate deformation data for the ZE20 grade of

extruded magnesium acquired for the current project phase. If ZE20 proves to be less prone to texture development during extrusion and exhibits more fine-grained and isotropic deformation properties, then its value in crash loading applications such as upper and lower rail components in the front end structure would be greatly enhanced. Such measurements are planned for completion in 2014.

**Task 4—Durability and Fatigue.** In Phase II, CAE stress analysis and material fatigue models were revisited to improve simulations of fatigue tests of all-magnesium demonstration structures joined by friction-stir welding and self-piercing rivets. A new finite element mesh was generated, based on actual geometry of the tested structures, which varied from the CAD data used in the first simulations. The new mesh eliminated the observed discrepancies including casting thickness and weld line lengths of the linear friction welds. The contact algorithm portraying the loading fixture was also improved to reflect the actual test configuration more precisely. This new CAE model was found to more accurately predict the locus of fatigue failure observed in testing of the actual structures, underscoring the importance of precise correlation between the physical structure and its CAD rendering.

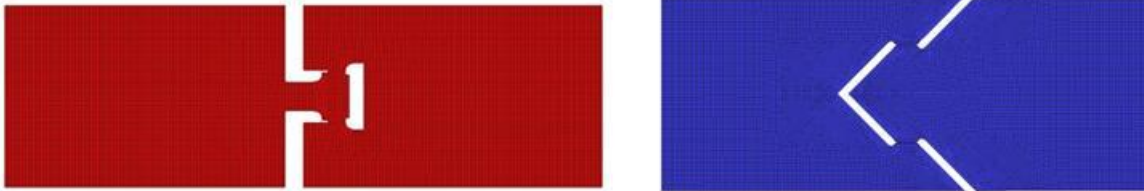


Figure III-83: Design of shear deformation-inducing tensile coupons for acquisition of AM60B magnesium yield-surface information for the condition of zero triaxiality.

Table III-8: Comparison of maximum sustainable deformation loads for the shock tower component from experimental testing and modeling in LS-DYNA® using existing and newly devised material cards for AM60B die-cast magnesium.

| MAT Model Type | Test  | MAT124 | MAT099 | NEW Mat Card |
|----------------|-------|--------|--------|--------------|
| Max Load       | 30.50 | 40.66  | 33.32  | 32.21        |
| % Difference   |       | 33.3%  | 9.2%   | 5.6%         |

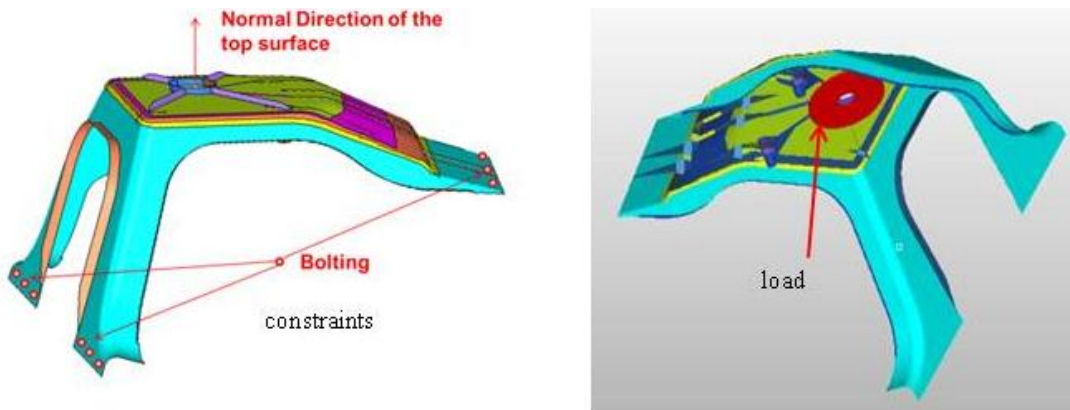


Figure III-84: Loading configuration of AM60B shock tower for finite element modeling and crashworthiness testing.

Structure specimens including riveted joints were obtained from the upper and lower rails of the demonstration structures (cf Figure III-82) for joints including AZ31 sheet to AZ31 sheet and AM60 die-casting to AZ31 extrusion. These component-level specimens, arranged in partial “peel” geometries (viz. Figure III-85) provided crucial data for CAE model validation beyond that normally obtained from lap-shear coupon samples. Figure III-85 shows the predictions of CAE models. The solid diagonal line represents perfect correlation and the dotted lines represent the “factor of 2” acceptable error bars for this type of simulation.

Friction Stir Linear Welded (FSLW) coupons were created to experimentally quantify the effect of the tool pin exit “keyhole” on fatigue behavior. Phase II demonstration structure durability tests suggested that most weld failures appeared to initiate at the keyholes. Fatigue tests aimed at detecting the influence of the keyhole confirmed that the coupons with the

keyhole actually did not exhibit a decrease in the number of cycles to failure, and in fact, rather exhibited a beneficial effect, probably akin to blunting of the advancing crack by the hole. Additionally, studies were conducted to quantify the effect of the sheet stacking orientation on friction-stir weld joint performance. Test coupons of AZ31 sheet were devised in two configurations: (1) with the top sheet adjacent to the retreating side (RS) and (2) with the top sheet adjacent to the advancing side (AS). Notable differences in both shear strength and fatigue life were observed for the different orientations of sheet stackup with respect to tensile load orientation with respect to direction of the tool motion that created the weldment. Retreating side loading led to both higher lap shear strength as well as greater fatigue life. Figure III-86 illustrates the nomenclature and differing lap-shear strength results for the two discrete orientations.

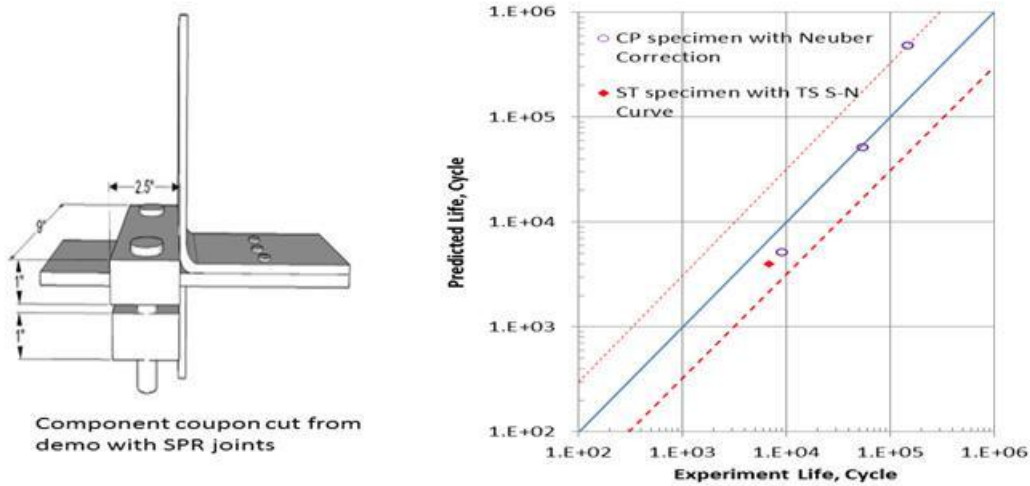


Figure III-85: Geometry of partial “coach peel (CP)” sample and its fatigue life plot. A data point from fatigue studies of a Phase II demonstration structure (designated “ST”) is plotted for comparison with the prediction.

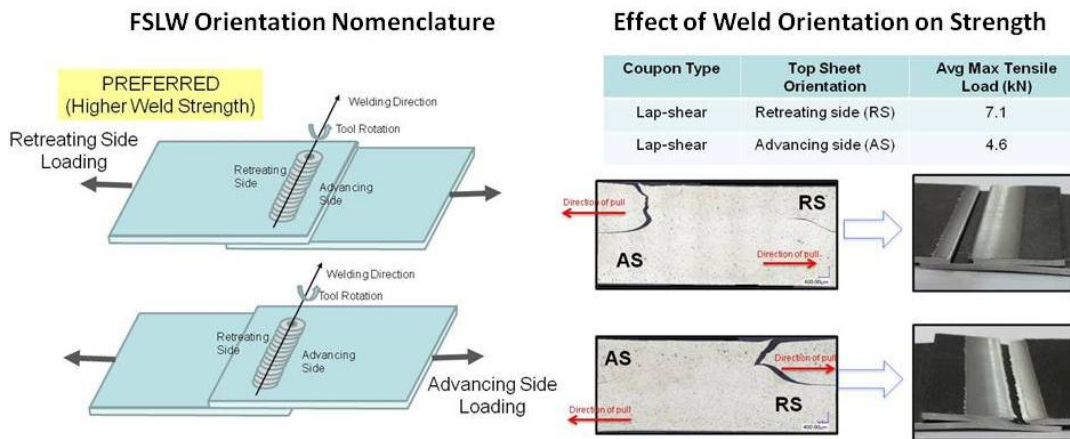


Figure III-86: Nomenclature for friction-stir linear (lap) weldments and corresponding lap-shear strengths for joints in AZ31 sheet material.

**Task 5—Corrosion and Surface Treatment.** The task team identified providers for pilot production of the cleaning, pretreatment and coating systems to be considered for the demonstration structures, as well as exploratory surface treatments at the coupon level. For steel/magnesium/aluminum versions of the structure, the pilot plant will employ PPG Industries' Zircobond® pretreatment with PPG Industries' Powercron® 590-534 cathodic electrocoat. For the aluminum/magnesium/aluminum versions, the pilot plant will incorporate Henkel Alodine®5200 with Protech Chemicals LTD ES542N49 powder epoxy topcoat as supplied by Almond Products, Inc., Spring Lake, MI. Experimental coating systems include Henkel's "MgC" for magnesium only structures and Atotech, Inc. Interlox® 5705 for 3-metal systems (steel, Mg, aluminum). A detailed test matrix to explore variations of coatings to self-piercing rivets for joining die-cast magnesium to extruded 6082 aluminum was devised and implemented, as well as a matrix to examine the several coating alternatives for friction-stir welded aluminum to magnesium upper rail joints. Evaluation of surface effects on pretreatment using the MAGPASS-COAT® process was completed at Ohio State University. This work confirmed suspicions that residual lubricating oils exposed to "warm forming" operations for AZ31 sheet material, could not readily be removed by the recommended processing sequence for MAGPASS-COAT® which had otherwise shown superior performance as a pretreatment for magnesium. New research on self-piercing

rivet galvanic corrosion and the effects of mitigating coatings to rivets was begun at Missouri University of Science and Technology and North Dakota State Universities, respectively. Research on possible hydrogen embrittlement effects on hardened steel fasteners (e.g., rivets) was undertaken at the Ohio State University.

**Task 6—Extrusion.** This task is responsible for procuring extruded plates and rails (of both aluminum and magnesium) for studies by other task teams as well as production of MFERD demonstration structures. Extruded aluminum 6082 in the T4 condition was recommended for the lower crush rail applications (cf Figure III-82). Kaiser Aluminum was commissioned to produce a die and provide 6082 T4 in coupon form for initial studies of joining and surface treatment. These coupons were distributed to the Task 9 (Joining) Team and Canadian Partners. Extruded 6082 T4 lower rails will be produced in January, 2014.

The task team also selected and provided a novel Mg alloy for improved ductility. Mag Specialties Inc., Denver, CO produced the billet material for ZE20 (Mg-2wt%Zn-0.2wt % Ce) at their plant in China. The chemical composition is shown in Table III-9. The billet was shipped to North America and 96 extruded rails were produced (see Figure III-87). Slices of the billet material were also distributed to the ICME team for further characterization of billet microstructure and deformation behavior.

**Table III-9: Composition of ZE20 novel Mg alloy billet stock produced by Mag Specialties Inc.**

| Alloy | Al    | Zn      | Ce      | Mn      | Si    | Fe     | Cu     | Ni     |
|-------|-------|---------|---------|---------|-------|--------|--------|--------|
| ZE20  | <0.01 | 1.6–2.4 | 0.1–0.4 | 0.2–0.5 | <0.10 | <0.005 | <0.005 | <0.003 |

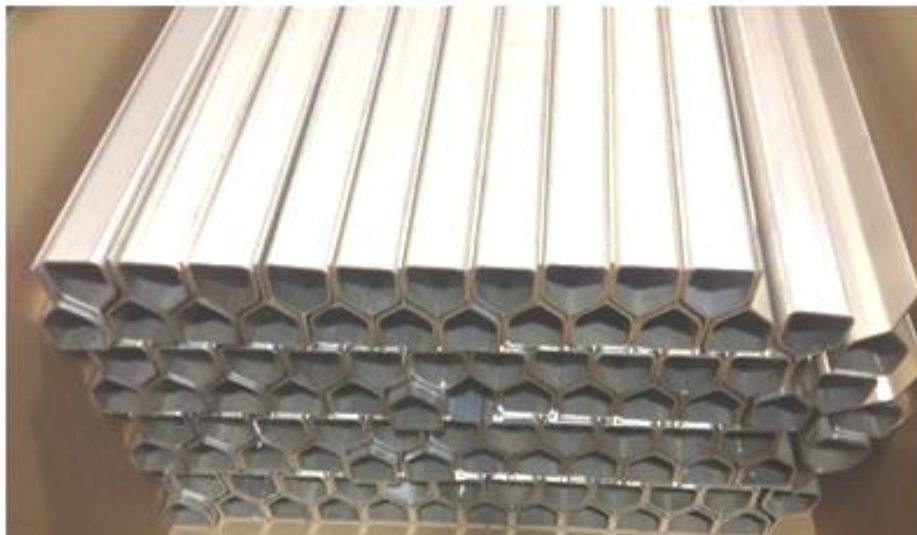


**Figure III-87: ZE20 novel Mg alloy lower rails produced by Mag Specialties.**

**Task 7—Low-cost Sheet and Forming.** The production and performance assessment of advanced sheet grades of magnesium (e.g., ZEK100) was deemed unlikely for the demonstration structures, given the relatively minor and unchallenging deformation requirements of the upper rail sheet component (cf Figure III-82). The task team has opted instead to follow progress on these advanced grades through the Canada partners, as might eventually be employed by U.S. Original Equipment Manufacturers (OEMs) in more demanding sheet-forming applications. The team has, however, actively engaged in the production of the upper rail sheet component pieces in galvanized steel and 6022-T4 E40 aluminum by the supplier, Duggan Manufacturing, Shelby Township, MI.

**Task 8—High-integrity Casting.** The task team arranged for donation of 15,000 lbs of AM60B magnesium from U.S. Magnesium LLC for consignment to CANMET Materials Technology Laboratory (CANMET), Hamilton, ON and ACT Test Panels, Hillsdale, MI for use in production of “top hat” and shock tower die castings as well as test plates for the various coupon studies of joining, durability and corrosion. Inputs for redesign of the shock tower for purposes of improved metal flow and strength in weaker areas were provided as well as assistance to the Canadian tooling supplier (Cana-Datum Moulds LTD, Toronto, ON) in re-working of the shock-tower and top hat tools. An initial supply of approximately 15 shock towers was obtained for comparison to CAD renderings and use in crashworthiness (Task 3) studies. Practical advice on magnesium die-casting idiosyncrasies and improvements was provided to CANMET as part of an ongoing dialog. All SVDC die castings employed by the project will be produced at CANMET. While the high pressure die-cast (HPDC) test coupons produced by ACT do not employ high vacuum in the processing, and thus may have lesser mechanical properties than SVDC materials, the HPDC material was felt to provide adequate representation for the comparative coupon joint, durability and corrosion testing for which they are to be used.

**Task 9—Joining.** The goal of this task is to identify and demonstrate joining technologies compatible with the selected dissimilar material combinations incorporated in the demonstration structures, with strength, durability (i.e., fatigue resistance) and corrosion behavior that meet or exceed established criteria for such structural applications.

**Self-piercing rivets (SPR).** Supplier Henrob Corp., Livonia, MI assessed the feasibility of SPRs for joining 6111 Al sheet, HSLA350 steel sheet and 6082 T4 Al extrusion to AM60 Mg die castings. They determined that it was feasible to produce sound joints at room temperature for Mg casting (top element) to the 6082 Al extrusion (bottom element). However, even with preheat, they were not able to produce sound joints for the other combinations. Hardened bare steel rivets were obtained through Henrob and aluminum coatings were applied by ion vapor assist deposition (IVAD). Some rivets so treated also received a secondary ceramic coating using Henkel Corporation’s ElectroCeramic Coating (EC<sup>2®</sup>) process for laboratory evaluation.

More than a hundred Al-Mg coupon specimens have now been assembled with conventionally (Sn-Zn) coated rivets, and more than 200 specimens have been assembled with the aluminized rivets, both with and without intervening adhesive bonding for evaluation by the Durability (Task 4) and Corrosion (Task 5) teams.

**Friction-stir welding.** In conjunction with supplier Hitachi America Ltd., the feasibility of friction-stir welding of Mg to Al (specifically 3.1-mm AM60 to 1.5-mm AA6022-T4) utilizing both friction stir spot welding (FSSW) and FSLW was established for both stack orders (i.e., Al(top)/Mg and Mg(top)/Al). More than 150 lap-shear samples were tested to optimize the process parameters and to establish the range of supported loads for the above stackups. Typical maximum lap-shear loads were 2.5 kN for FSSW and 3.3 kN for FSLW. The Joining team decided to use FSLW to attach the aluminum upper rails to the Mg shock towers in the demonstration structures (cf Figure III-82). The FSLW process was used to produce several hundred specimens to fully assess the corrosion and mechanical performance of this joint.

**Adaptable Inserts.** The team engaged supplier AET Integration, Inc., Wixom, MI to develop a novel technique for joining the steel upper rails to the Mg shock tower. The technique employs an adaptable insert placed in a hole in the dissimilar material to capture that dissimilar material as shown in Figure III-88. Based on preliminary success, the plan is to use a Mg insert welded to the Mg shock tower, using conventional resistance spot welding (RSW) equipment, to capture and secure the steel sheet.

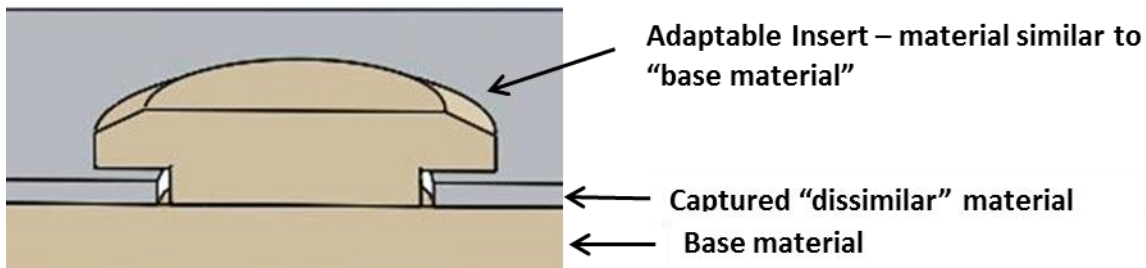


Figure III-88: Adaptable insert concept.

**Task 10—Integrated Computational Materials**

**Engineering.** The overall objectives of the ICME task for the past year were to complete the development of local property models and to develop the linkage procedure to apply the ICME approach on the “demonstration” structures, focusing on the die-cast magnesium shock tower to predict the performance under static, fatigue and crash loading. The following are highlights of achievements during this period.

**1. Quantitative Characterization of Evolution of Continuous Precipitates in SVDC AZ91 Alloy and Yield Strength Model Development.**

The distribution of three-dimensional (3D) sizes of continuous  $\beta$  precipitates after aging treatment at 168°C for three different times 5 hours, 10 hours and 50 hours, was measured using scanning transmission electron microscopy. Two kinds of morphology of continuous  $Mg_{17}Al_{12}$  were observed: asymmetrical lozenge shape and lath shape. The length and width of continuous precipitates were measured on BF-STEM images taken along [0001] direction. The thickness of precipitate was measured on Bright Field–Scanning Transmission Electron Microscopy (BF-STEM) images captured along [12-10] direction. Around 400 measurements were made for each dimension of precipitate

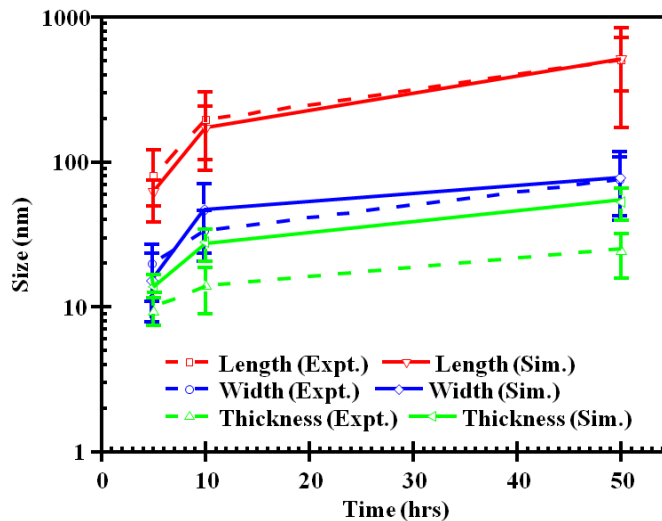
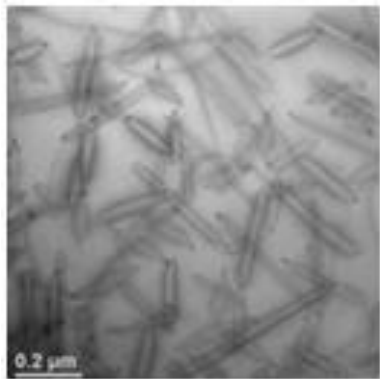


Figure III-89: Electron micrograph of developing  $\beta$ -phase precipitates in AZ91D magnesium and 3D platelet growth characteristics deduced from such observations as a function of ageing time. The results are compared with predictions from phase field simulations and show good correlation.

**Technology Transfer Path**

Increased use of magnesium alloys as lightweighting material alternatives in automotive structural designs is faced with both economic and technical challenges including material cost, perceived durability concerns, receding supplier base (particularly for die castings—the most common form of the material) and manufacturing issues such as joining and surface treatment. The precursor efforts to this project showed, in principle, the weight reduction opportunity (approaching 45% relative to baseline mild steel) for large, integrated magnesium-intensive substructures. Primarily

size under each aging condition. The evolution of three dimensional sizes of continuous precipitates with aging time is shown in Figure III-89. The growth rate of the length of  $Mg_{17}Al_{12}$  is much faster than other two dimensions under current aging condition. The aspect ratio of precipitate also continues varying with aging time. Those quantitatively measurements have been used to calibrate hybrid Density Functional Theory (DFT)/ Phase Field simulation and used for precipitation strengthening model.

**2. Integrating Local Property into the Performance Analysis for Shock Tower.**

The Internal State Variable (ISV) and Multi-Scale Fatigue (MSF) models have been integrated into the ABAQUS® finite element code for AZ91. The mapping of the spatial distribution and size of pores for the die-cast AZ91D shock tower has been accomplished. Two cases of ISV-Finite Element Analysis (FEA) simulations have been conducted for both homogeneous material and heterogeneous pore size state. Finite element simulation using ABAQUS® that integrate the static and cyclic material models based on processing-structure-property (PSP) relationship for heterogeneous dendrite cell size (DCS), heterogeneous pore size, and heterogeneous porosity are being conducted.

based on die castings, such substructures are the most economical and practical implementation of magnesium for the automotive sector.

Over the course of its existence, “MFERD” has engaged the various constituencies of the technology transfer framework as detailed below:

**OEMs.** An ongoing theme for the ensemble of MFERD projects is the generation of design, manufacturing and performance data for the various forms of magnesium, sufficient in its quality and robustness to be employable by vehicle designers and engineers using the various computer-aided engineering tools for structural design and material

deformation simulations. Material and joint performance information for new grades of magnesium (e.g., ZE20) will also be of use to designers. Understanding of material performance improvements associated with processing—SVDC and ICME methodologies will permit assessment of local material properties from inputs such as casting simulations and material deformation in wrought processing. Improved confidence in designing with magnesium and robustness of its performance from an engineering standpoint will aid in increasing acceptance and utilization of the material. The project has already contributed new material models for die-cast magnesium for the LS-DYNA® structural deformation code, and will expand this in the current phase from shell to solid elements typical of large castings.

**Supply Base.** Over the course of the broader MFERD initiative, USAMP has enlisted over three dozen distinct suppliers of materials, technologies and services relating to the design, production and incorporation of magnesium components in automotive structures. Through its committee structure, web-based tools (viz. “Vroom”) and various technical meetings, suppliers are both engaged in discussion of magnesium technologies as well as in providing often unique adaptations of existing technologies for deployment with magnesium. Suppliers are thus engaged in understanding the particular technical challenges facing expanded use of magnesium in vehicle lightweighting. Suppliers are also educated in peculiarities of working with magnesium—e.g., requirements for special fire extinguishers as a safety item, and ventilation requirements associated with aqueous processing.

**Universities.** A long-range goal of the MFERD initiative, originally set forth by its architects, has been the fostering of greater magnesium technology education and innovation through the university system. To this end, eleven universities have been engaged in the overall project with nine in the current embodiment, focusing on ICME, durability, metal deformation and corrosion. Such sponsored university research was intended to instill a greater interest in magnesium science and technology among students, as well as providing a means for linking knowledgeable graduating students with possible opportunities in supplier or OEM organizations.

## Conclusion

In its first full fiscal year of operation, the project has completed the design of the demonstration structures, determined and obtained materials of construction and proposed manufacturing methods for the individual components, as well as joining and finishing technologies. Ongoing team efforts have continued for the knowledge-based and experimental disciplines of crashworthiness, fatigue and corrosion measurements of the anticipated demonstration structures, planned for delivery in 2014. Efforts in ICME are targeted at strengthening mechanisms and their measurement for heat-treatable magnesium alloys, as well as next-generation grain-refined and texture-resistant wrought grades such as ZE20. A major shift in project emphasis has been toward mixed-metal construction as might be employed for the

integration of large-scale magnesium alloy die-castings with other materials of automotive construction—principally wrought aluminum and galvanized high-strength, low-alloy steel. Addressing the challenges of mixed-metal joining and corrosion is seen as being more timely for greater implementation of magnesium in automotive manufacturing, than the longer-range vision for more extensive use and lower cost of wrought magnesium grades or fully integrated all-magnesium structures employing these materials. The project team continues its involvement in the international collective project with Canada and China who have the same overall focus of magnesium-intensive, front-end substructures.

## Presentations/Publications/Patents

1. Castano, C., O’Keefe, M., and Fahrenholtz, W., “Photo-assisted reduction in nanostructured cerium-based coatings”, *Scripta Materialia*, 69, 489 (2013).
2. Forsmark, J.H., Li, M., Wagner, D., Su, X., Zindel, J., Luo, A. A., Quinn, J.F., Verma, R., Wang, Y.-M., Logan, S.D., Bilkhu, S., and McCune, R.C., “The USAMP Magnesium Front End Research & Development Project: Results of the Magnesium “Demonstration” Structure,” presented at the Magnesium Technologies Symposium, TMS Annual Meeting, San Antonio, TX, March 4, 2013.
3. Miao, J, Li, M, and Allison, J (2012). “Microstructural Evolution During Heat Treatment of Super Vacuum Die Cast AZ 91”, *Proceeding of 9th International Conference on Magnesium Alloys and Their Applications*, July 8-12, 2012, Vancouver, BC, Canada.
4. Wang, J, Li, M, Ghaffari, B, Chen, L, Miao, J, and Allison, J (2012). “A Hybrid Kinetic Evolution Model for Mg17Al12 Precipitates in AZ91”, *Proceeding of 9th International Conference on Magnesium Alloys and Their Applications*, July 8-12, 2012, Vancouver, BC, Canada.
5. Miao, J., Marquis, E., Li, M. and Allison, J., “Quantitative Characterization of Precipitate Microstructure for Use in ICME Models for Magnesium Alloys”, presented at the 2nd ICME World Congress, July 7-11, 2013, Salt Lake City, Utah.
6. Wang, J., Li, M., Ghaffari, B., Miao, J. and Allison, J., (2012). “Phase Field Model for Mg17Al12 Precipitates Kinetics and Yield Strength Model Development in AZ91” presented at the 2nd ICME World Congress, July 7-11, 2013, Salt Lake City, Utah.

## Reference

Luo, A. A., Quinn, J.F., Wang, Y.-M., Lee, T.M., Verma, R., Wagner, D.A., Forsmark, J.H, Su, X., Zindel, J., Li, M., Logan, S.D., Bilkhu, S., and McCune, R.C., “The USAMP Magnesium Front End Research and Development Project,” *Light Metal Age*, April 2012, 54-58.

## III.8. Integrated Computational Materials Engineering Approach to Development of Lightweight 3GAHSS Vehicle Assembly (ICME 3GAHSS)

### **Dr. Louis Hector, Jr. (Principle Investigator)**

General Motors R&D Center  
RML 1-120  
Mail Code 480-106-224  
30500 Mound Road  
Warren, MI 48090-9055  
Phone: (586) 651-2628  
E-mail: [Louis.hector@gm.com](mailto:Louis.hector@gm.com)

### **Mr. Ron Krupitzer (Principle Investigator)**

American Iron and Steel Institute  
Vice President Automotive Applications  
2000 Town Center, Suite 320  
Southfield, MI 48075  
Phone: (248) 945-4761  
E-mail: [rkrupitzer@steel.org](mailto:rkrupitzer@steel.org)

### **David Ollett, Technology Project Officer**

National Energy Technology Laboratory  
DOE/NETL/PMC/VTO Division  
626 Cochran Mill Road  
Pittsburgh, PA 15236-0940  
Phone: (412) 386-7339  
E-mail: [david.ollett@netl.doe.gov](mailto:david.ollett@netl.doe.gov)

### **William Joost, Technology Development Manager**

U.S. Department of Energy  
1000 Independence Avenue, S.W.  
Washington, DC 20585  
Phone: (202) 287-6020  
E-mail: [william.joost@ee.doe.gov](mailto:william.joost@ee.doe.gov)

Contractor: United States Automotive Materials Partnership  
Contract No.: DOE DE-EE0005976

### **Abstract/Executive Summary**

The goal of the program is to successfully demonstrate the applicability of Integrated Computational Materials Engineering (ICME) for the development and deployment of third generation advanced high strength steels (3GAHSS) for immediate weight reduction in passenger vehicles. The ICME approach will integrate results from well-established computational and experimental methodologies to develop a suite of material constitutive models (deformation and failure), manufacturing process and performance simulation modules,

a properties database, as well as the computational environment linking them together for both performance prediction and material optimization. The project officially started on February 1, 2013.

The project has six technical co-dependent tasks (as listed in the "Approach"). The bulk of this period's work was focused on model development and validation, with five universities (Brown University (BU), Clemson University (CU), Colorado School of Mines (CSM), Michigan State University (MSU), and the University of Illinois at Urbana Champaign (UIUC) and Pacific Northwest National Lab (PNNL). Initial efforts were to modify existing length scale material models for steel and to develop the constitutive material parameters to run these models and predict the steel chemistries and microstructures that will enable 3GAHSS. This information will be used by participants from the steel industry to manufacture steel coupons for model validation and refinement.

During this period of performance, General Motors, LLC (GM) provided Baosteel Group Corporation (BAO) QP980 steel (a near third generation steel made from the quench and partitioning (QP) process developed by the Advanced Steel Products and Process Research Center (ASPPRC) at the CSM, for the purpose of adapting material models for steel, defining the needed constitutive material parameters, and gathering material properties data for the execution of these models. The BAO QP980 steel is a reasonable baseline material because the QP process is one of the potential process pathways to developing 3GAHSS. The BAO QP980 steel chemistry and its mixed microstructure, consisting of ferrite, martensite and retained austenite, provide sufficient information for early model adaptation.

On August 15, 2013 a steel experts meeting was held with representation from the steel industry, automotive original equipment manufacturers (OEMs) and CSM with the objective of defining the steel processing pathways that would enable a third generation steel. During the meeting, several possible steel processing pathways were discussed. The medium manganese transformation induced plasticity steel (TRIP) and enhancement of the QP process were preliminarily identified as those pathways that have the highest probability of achieving the mechanical properties specified in the Funding Opportunity Announcement (FOA) for the two Department of Energy (DOE) proposed 3GAHSS targets, i.e., exceptional strength, high ductility and high strength, exceptional ductility.

A significant amount of test data has been gathered on the BAO QP980 steel, which includes but is not limited to uniaxial, bulge, bilinear, micro-hardness, and micro-pillar compression testing. One significant development is the creation of three dimensional (3D) representative volume elements (RVEs) for the BAO QP980 steel. This marks the first known time that 3D RVEs have been used in ICME

development and will improve model accuracy, especially forming simulation, by accounting for natural and processed induced anisotropy of sheet steels. This work is an excellent demonstration of how integration is occurring between the Task 2 sub-recipients.

The side structure of a 2008 Model Year (MY) sedan was selected to demonstrate the weight savings potential and associated costs with the proposed 3GAHSS. During this period, the Engineering + Design AG (EDAG) firm under the leadership of GM, generated finite element models (FEM) of the entire Body-in-White (BIW) and a bill of materials with alloy chemistries for each component, defined the overall body structure performance including the contribution of the body side structure load paths, and generated a preliminary technical cost model. Once fully characterized, the baseline assembly will be contrasted against design optimized assemblies using gauge optimization first to show the 3GAHSS material impact on weight savings and later to shape optimization and demonstrate how 3GAHSS will enable more efficient designs. The project assumed an optimized spot welding and adhesive bonding joining strategy.

The project team produced a flowchart of the model assembly and integration process, which will be used to assemble the length scale material models and integrate them with the forming, design optimization and technical cost model. Increased emphasis on assembly of the material models and forming simulations as 3GAHSS designs mature are planned for the 2014 Fiscal Year (FY). The project is on track to meet all deliverables for the first budget period and all subsequent years.

### Accomplishments (2013 FY)

- General Motors, LLC transferred the design package for a 2008 model year sedan to EDAG. EDAG processed the design package to generate finite element analysis (FEA) models for the entire 2008 sedan BIW design.
- A bill of materials was generated for the 45 components that make up the side structure and alloy chemistries for each component were identified.
- On September 30, 2013 the project team met Milestone #1 'Selection of body structure components/subassembly and identification of baseline materials'. The project team identified the side structure from a 2008 model year sedan as the baseline subassembly from which the four or more targeted AHSS components will be selected to demonstrate that the 3GAHSS will reduce weight in structural automotive components and assemblies.
- The team produced a preliminary technical cost model for the baseline design and future 3GAHSS designs.
- The project team approved the use of spot welding with adhesive bonding for the baseline and 3GAHSS sub-assembly designs.
- EDAG established a computer aided engineering (CAE) method and load cases for analysis of the baseline and 3GAHSS assemblies and created LSDYNA format material cards.
- The UIUC computed the elastic constants, lattice parameters, and force constants of body centered cubic (bcc) and face centered cubic (fcc) iron, which serve as inputs into the lattice Green function method for dislocation core structures and, ultimately critical resolve shear strengths for each 3GAHSS phase to be used with the crystal plasticity modeling.
- The Combined Constraint Crystal Plasticity (CCCP) was modified to include a dislocation density-based hardening model and to account for the non-Schmid law.
- In close cooperation with BU, and under the leadership of Dr. Louis Hector, Jr., MSU has completed an initial 3D RVE for the BAO QP980 steel. This marks the first known implementation of 3D RVEs in ICME modeling and will be a fundamental component of the steel crystal plasticity model.
- The CSM completed a comprehensive literature review on metallurgical paths that can be further exploited leading to the property targets aimed in this project. The literature review and initial results of composite modeling were presented in the Steel Experts Meeting held at the Auto/Steel Partnership (A/SP) office in Southfield, Michigan on August 15, 2013. Quench and partitioning and medium manganese TRIP steel were proposed as two possible steel pathways that would enable 3GAHSS with the mechanical properties of the two DOE proposed 3GAHSS.
- BU generated electron backscatter diffraction (EBSD) patterns of the as-received BAO QP980 steel to determine the volume fraction of retained austenite and its distribution at interfaces. BU ran micro-pillar compression tests to generate flow properties of the ferrite, martensite and austenite in BAPQP980. BU also applied EBSD at various levels of plastic tensile strains until fracture to determine the change in the volume fraction of retained austenite with strain and especially beyond the ultimate tensile strength (UTS). BU provided the data to MSU to enable the generation of 3D RVEs.
- CU completed all uniaxial tensile testing on the starting material (BAO QP980) at room temperature and a selected quasi-static rate ( $2 \times 10^{-3} \text{ s}^{-1}$ ), covering seven orientations with respect to rolling direction (0, 15, 30, 45, 60, 75 and 90°). CU established a testing linkage with the National Institute of Standards and Technology (NIST), Gaithersburg, MD for testing over the low dynamic range for vehicle impact and completed a first set of high strain rate tensile testing using Kolsky Bar achieving a strain rate of  $\sim 850 \text{ s}^{-1}$  as the lowest strain rate. Flow curves were generated for three orientations (0, 45 and 90°) with respect to the rolling direction.
- CU completed material deformation studies using digital image correlation (flow stress/strain curves, mechanical properties, plots of strain hardening exponent with strain, evolution of the R-value with strain.)
- CU completed temperature measurements of material samples deformed at room temperature and quasi-static rate; plots of temperature increase as a function of plastic strain have been generated.

### Future Directions

- Complete the characterization of BAO QP980 steel and derive relevant constitutive parameters for input into the crystal plasticity model.
- Complete and assemble material length scale models and provide initial meso-scale computational predictions for 3GAHSS chemistries and microstructures (Project Milestone #2).
- Manufacture AHSS and 3GAHSS steel coupons for testing and model calibration and validation.
- Identify, adapt, and apply forming and fracture simulation to baseline and 3GAHSS designs in the third year of the program (Project Milestones #4 and #3 respectively).
- Complete characterization of the baseline assembly (Project Milestone #1). Evaluate the potential weight savings that can be achieved by substituting the two target 3GAHSS on the baseline assembly weight using gauge optimization. Once actual 3GAHSS materials are devised conduct full design optimization, including shape optimization, of the baseline assembly to determine the cost impact and weight savings of using 3GAHSS on automotive structural assemblies.
- Integrate material length scale models with the forming model, fracture model, technical cost model with design optimization. Provide a user manual for the ICME model and data repository for material property data.

grades. Once 3GAHSS coupons are made available, full design optimization, including shape optimization, will be performed to determine if optimized 3GAHSS designs can achieve the desired weight savings while meeting strength requirements.

- Gap: This program will not assess the manufacturability of the shapes proposed during design optimization. Forming simulations may mitigate this risk but shape optimization may generate shapes that may not be easily manufacturable. Technical cost modeling may provide a qualitative assessment of manufacturability where the cost of the proposed components may exceed the \$3.18 per pound weight-saved target.
- Target: Two different 3GAHSS are defined by the FOA, exceptional strength and high ductility (>1500 MPa UTS, >1200 MPa YS, >25% elongation) and high strength and exceptional ductility (>1200 MPa UTS, >800 MPa YS, >30% elongation).
- Gap: The ICME model will predict the necessary chemistry and steel microstructure needed to meet the target mechanical properties but process development (melting, rolling, intermediate heat treatments, finishing, etc.) may be needed to produce sheet steel with the predicted microstructure. The project will leverage the expertise of steel industry participants to guide process development using laboratory size heats to develop a process that can achieve the predicted microstructure.

### Technology Assessment

- Target: Model elements must be within 15% of experimental results and the optimized 3GAHSS assembly must achieve 35% weight savings at no more than \$3.18 cost per pound of weight savings.
- Gap: There is no existing ICME framework that ties together all length scale computer models with forming simulation, fracture modeling and design optimization, especially with low and high level optimization loops. Although a linear input/output connectivity can be achieved between the length scale material models, optimization loops will require significant coding that may be complicated by disparate codes used in the individual models.
- Gap: Boundary conditions have been applied to model elements to facilitate assembly and integration within the project four year duration. For example, the number of solutes to be evaluated has been limited, inclusions and precipitates are largely ignored, and dislocation dynamics are superficially treated. These are all opportunities for future work and model improvement but these boundary conditions may adversely affect model accuracy.
- Gap: The weight savings targets are aggressive and it is not known if these targets can be achieved with the selected sub-assembly using the two proposed 3GAHSS grades as defined in the FOA. An optimized joining strategy of spot welding with adhesive bonding was selected for the baseline and 3GAHSS design optimization studies. The project will first assess the potential weight savings through material substitution and gauge optimization using the two proposed 3GAHSS



### Introduction

The goal of the program is to successfully demonstrate the applicability ICME for the development and deployment of 3GAHSS for immediate weight reduction in passenger vehicles. The ICME approach used in this project will accelerate the development and widespread deployment of 3GAHSS through modeling of multi-scale metallurgical, thermal and mechanical processes in coil sheet development to automotive part and assembly manufacturing and ultimate in-vehicle performance. By integrating a suite of comprehensive, science-based computational models at different length scales in the ICME environment, this project will demonstrate to end users in both the automotive and steel industries that immediate cost-effective weight savings can be achieved with 3GAHSS, and that the ICME framework will support a reduced development to deployment lead time in all lightweight materials systems. The product of this proposed effort will be a simulation toolset and computational infrastructure composed of material models and associated validation data at different length scales together with the software and application programming interfaces developed by the project team.

The project faces three distinct challenges, 1) to develop an ICME model, 2) to develop a viable 3GAHSS and 3) to optimize an automotive design concept for a material that does not yet exist. As shown in Figure III-90, there are no commercial 3GAHSS and no U.S. steel company currently markets a 3GAHSS. Figure III-90 also illustrates the relative

values for BAO QP980 and the two DOE targets for 3GAHSS. Although the manufacturing of 3GAHSS is not a deliverable of this program, the DOE proposed two 3GAHSS grades with mechanical properties listed in Table III-10 as targets for the program. The project began the task of adapting existing material models for steel by selecting an AHSS grade, BAO QP980, which has mechanical properties on the cusp of the 3GAHSS envelope. In the absence of the 3GAHSS, the BAO QP980 with its mixed martensite and retained austenite microstructure will 1) facilitate the identification of relevant constitutive parameters for each length scale material model 2) provide a means to validate these models and 3) help

define the microstructural elements that will be needed for a 3GAHSS.

The first year of the program will develop the framework to assemble the length scale material models. Starting in the second year of the program, the project team anticipates that the developed and assembled models will provide early 3GAHSS predictions of steel chemistries and microstructures that will enable a 3GAHSS. These early predictions will be used by the six steel industry participants to guide the manufacturing of steel coupons with mechanical properties that will evolve toward the DOE targets as the models mature and are validated.

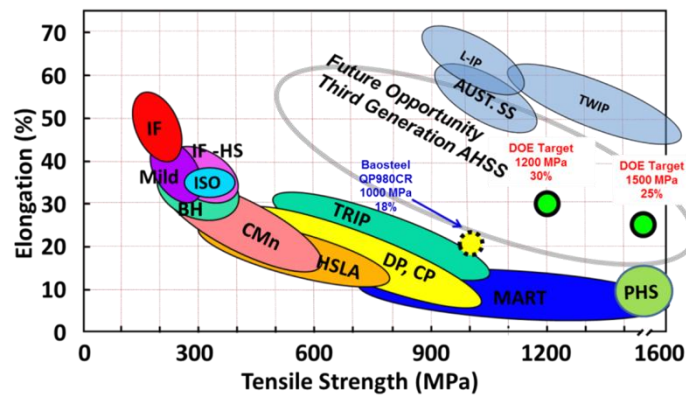


Figure III-90: Target 3GAHSS Properties.

Table III-10: 3GAHSS Types.

| Ferrous Sheet Metal Type             | Yield Strength (MPa) | Tensile Strength (MPa) | Total Elongation (Uniaxial Strain to Failure) | Uniform Elongation |
|--------------------------------------|----------------------|------------------------|---|--------------------|
| High Strength, Exceptional Ductility | ≥800                 | ≥1200                  | ≥30%  | ≥20%               |
| Exceptional Strength, High Ductility | ≥1200                | ≥1500                  | ≥25%  | ≥8%                |

As the models are being adapted and assembled, a baseline will be established to demonstrate the potential benefits of the 3GAHSS to reduce automotive assembly weight. An automotive assembly will be identified which must contain a minimum of four 3GAHSS components extracted from a 2008 MY or later production vehicle. Initially, the baseline assembly will be fully characterized in terms of the weight, cost and performance criterion. An iterative design optimization process of gauge and shape optimization will be applied to the baseline assembly substituting 3GAHSS for AHSS and developing a 3GAHSS design that can meet the proposed weight savings target listed in Table III-11. Coupled with design optimization are forming modeling and simulation, fracture modeling and simulation and technical cost modeling to assess the manufacturability, performance and cost of the different design iterations with the goal of achieving the cost targets listed in Table III-11 without compromising component and assembly performance.

Table III-11: DOE FOA Weight and Cost Targets.

| Vehicle System | System Definition                                    | Weight Reduction Target | Cost per Pound of Weight Saved (\$/lb. saved) |
|----------------|--|-------------------------|---|
| Body           | Body-In-White, Closures, Windows, Fenders, & Bumpers | ≥35%                    | ≤3.18/lb.                                     |

Work to integrate the material, forming, fracture, and cost models with design optimization will span the entire length of the program. The primary project deliverable includes an ICME model and user guide to enable users to run the model. The objective is to create an ICME model capable of predicting part and assembly properties from the sheet properties and the process history within 15% accuracy at all length scales that will enable the baseline structure to meet the specified weight and cost targets.

The challenges of this program require significant academic and cross-industry expertise, and regular communication and collaboration between these parties to

make the integration component of the project successful. The project is highly leveraged with expertise from the participants shown in Table III-12 supporting the entire life cycle of material, process and product development. Prior

collaboration between these project participants through the United States Automotive Materials Partnership (USAMP) and the A/SP provides a unique and successful foundation for addressing the technical challenges of this program.

**Table III-12: Project Participants.**

| Universities/National Labs                     | Industry                                  |
|--|---|
| Brown University                               | Chrysler Group LLC                        |
| Clemson University                             | Ford Motor Company                        |
| Colorado School of Mines                       | General Motors Company                    |
| Michigan State University                      | AK Steel Corporation                      |
| Pacific Northwest National Lab                 | ArcelorMittal                             |
| University of Illinois                         | Nucor Steel Corporation                   |
| <b>Consortiums</b>                             | Severstal NA                              |
| Auto/Steel Partnership                         | ThyssenKrupp USA                          |
| United States Automotive Materials Partnership | U. S. Steel                               |
|  | EDAG, Inc.                                |
|  | Livermore Software Technology Corporation |

### Approach

The project has been structured with seven tasks as follows:

- Task 1: Project Management and Planning
- Task 2: Model Development and Model-Level Validation
- Task 3: Forming: Component-Scale Performance Prediction and Validation
- Task 4: Assembly
- Task 5: Design Optimization
- Task 6: Integration
- Task 7: Technical Cost Modeling

#### Budget Period 1:

During the first year, the program achieved the following:

- Completed numerous experiments to characterize the behavior of BAO QP980 steel as a baseline for adapting well-established computational material models for AHSS.
- Completed the first phase of the atomistic calculations which includes the development of a Density Functional Theory (DFT) based solid-solution strengthening model for iron crystal structures relevant for 3GAHSS: bcc Ferrite, fcc Austenite, and body-centered tetragonal (bct) Martensite.
- Developed 3D RVEs for input into the Crystal Plasticity Finite Element Model (CPFEM).
- Defined steel processing paths which will likely produce a 3GAHSS and will assist in developing a plan to produce steel coupons for the purpose of model validation (Project Milestone #1).
- Defined and flow charted a process in which the material constitutive models will be assembled and integrated with manufacturing process and performance simulation

modules, performance prediction, and material optimization.

- Identified the side structure of a 2008 high volume production sedan as the target sub-assembly from which 3GAHSS will be substituted for a minimum of four AHSS parts to demonstrate the weight saving potential and cost of using 3GAHSS in structural automotive assemblies (Project Milestone #7).
- Identified the joining methodology to be used for the baseline assembly and 3GAHSS assemblies (Project Milestone #6).
- Defined a technical cost model which will be used to compare the baseline assembly costs against the two DOE proposed 3GAHSS targets.

#### Budget Period 2:

The second year of the program will begin the transition from model adaptation to model validation. At this time, AHSS coupons with microstructures different from BAO QP980 will be manufactured for testing and model validation. The model inputs and outputs will be defined to facilitate the process of assembling the constitutive material models. By the end of the second year, the material models should have some limited predictive capability and enable the first iteration of 3GAHSS simulation and prediction (limited to the ability to propose steel chemistries and microstructures that may generate steels with the DOE proposed mechanical properties for 3GAHSS (Project Milestone #2)).

The baseline sub-assembly identified in the prior period will be fully characterized, which will include a FEA model, defined load paths based upon established vehicle performance criteria, a bill of materials for the vehicle sub-assembly, and a preliminary cost model. Using the joining criteria defined in the prior period, the project will apply gauge optimization to determine the cost and weight savings potential of substituting the two proposed DOE 3GAHSS

grades for the four or more AHSS components. This will enable a preliminary determination of the weight and cost of the sub-assembly with the DOE 3GAHSS grades applied. An estimate can then be made as to whether the DOE mass reduction targets can be achieved from the optimal 3GAHSS materials.

Forming simulation will begin during this period coupled with design optimization as the project measures the manufacturing feasibility of the 3GAHSS components. This work is expected to reveal opportunities for part commonization as well as component designs that can best respond to applied load paths.

### Budget Period 3:

The third year of the program will begin with the assembly of the constitutive materials models and refinement in their predictive capability. By this time, the 3GAHSS designs will be complete providing an assessment of the cost and weight savings potential of 3GAHSS. Fracture modeling will begin during this period utilizing the constitutive models fit to the mechanical properties of the 3GAHSS materials and the known forming requirements of the sub-assembly. This work is scheduled to be completed by the end of the budget period (Project Milestone #4).

Integration of the material models with the forming, fracture, performance and cost models will be accelerated during this period using the flow charts defined in Budget Period One. By the close of the budget period the project is expected to have a rudimentary ICME model (Project Milestone #3). Key to this work will be the framework that enables the ICME model to execute 3GAHSS simulations.

Based on Budget Period Two 3GAHSS model simulations, steel coupons will be produced, tested and characterized using tests applied to the baseline BAO QP980 steel. These samples are not expected to have the target mechanical properties of the two proposed 3GAHSS in the FOA, but rather these samples will be representative of microstructures with properties closer to the targets for the purpose of correcting and/or validating the length scale material models.

The project will continue to improve the individual models and the linkage between the models, and optimize the integration of the ICME model (Project Milestone #9) during this period. Upon completion of the program, a final forming model (Project Milestone #5), a completed technical cost model (Project Milestone #11), an ICME user guide and data repository (Project Milestone #10) will be developed as part of the final project deliverables.

Steel coupons will continue to be manufactured using more accurate predictions from improved material model simulations. The project has assumed that proposed material chemistries can be successfully processed to achieve the proposed microstructures. If the resulting coupons have the properties of or near the two proposed 3GAHSS targets, the project will utilize the mechanical properties derived from the 3GAHSS coupons for the final stage of design optimization. The final 'actual' 3GAHSS design (Project Milestone #8) will be contrasted against the baseline assembly weight and cost

as well as results derived from the two theoretical DOE 3GAHSS targets. The final design will provide a better means to assess the potential of 3GAHSS to meet proposed cost and weight targets as well as the potential design flexibility from proposed and actual 3GAHSS.

## Results and Discussion

The UIUC is applying existing first principal DFT methodologies and other atomistic-scale methodologies to compute relevant parameters of the crystal plasticity model of the 3GAHSS (e.g., various hardening parameters of the different phases in the steel microstructure, critical resolved shear strengths) and to compute accurate geometries of relevant defect structures (e.g., dislocation cores) in the various phases of the 3GAHSS. The atomistic-scale methodologies will serve as a computational means for calibration of the microstructural models following the ICME approach. This will enable the prediction of flow curves, yield criteria and stress / strain curves. The atomistic approach will also define relevant parameters that can be computed with discrete dislocation dynamics modeling which is not part of the present project.

BU is evaluating austenite stability as a function of strain to better predict the flow properties of third generation steels. Part of this work is the development of test procedures to evaluate the submicron properties (e.g., flow behavior) of austenite, which include microhardness and micro-pillar compression testing, which is significantly complicated by sheet steel's highly anisotropic properties due mostly to processing.

CU is conducting coupon-level mechanical tests on the BAO QP980 and eventually the 3GAHSSs to provide flow behavior, anisotropy, formability, adiabatic heating and failure/fracture data as inputs to the crystal plasticity and state variable models at MSU and PNNL. During this reporting period CU continued the characterization of the starting material BAO QP980, and received additional material from GM. Testing activities covered quasi-static tensile testing, bake hardening behavior, temperature increase due to tensile deformation, measurements of volume fraction of retained austenite, high strain rate testing (Kolsky Bar), preliminary high strain rate testing (servo-hydraulic), and preliminary bulge testing.

MSU is applying and integrating the atomistic and microstructural scale material models to generate material models that can be used in the crystal plasticity material models and state variables models to enable the prediction of flow curves, and stress / strain curves for 3GAHSS. This work will enable automotive forming process engineers as well as automotive CAE engineers to accurately model the material response of steel, advanced high strength steel (AHSS), and 3GAHSS. The development of the first ever three dimensional representative volume elements (3D RVEs) is included in this work and will enable improved accuracy in predicting material properties over the two dimensional RVEs. Figure III-91 is a pictorial of the 3D RVE generated for BAO QP980 steel.

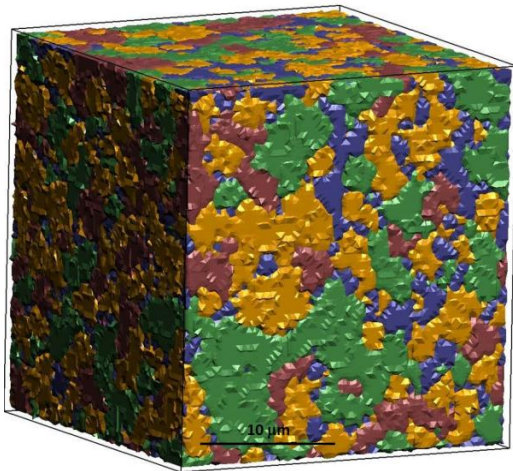


**Figure III-91: Three Dimensional Representative Volume Element of BAO QP980 Steel—(Green = Martensite, Blue = Austenite and Red + Yellow = Ferrite).**

PNNL is adapting single phase state variable models to accommodate multiphase third generation steels. PNNL is supporting advanced experimentation involving synchrotron radiation measurements at the Argonne National Lab Advanced Photon Source and has offered the use of its atom probe tomography capability to measure solute concentration and partitioning in the various 3GAHSS phases (needed by the atomistic and crystal plasticity components of the project). PNNL has also transferred their implementation of a transformation kinetics model to enable GM to begin forming simulations of steels with TRIP chemistries. PNNL also established a Sharepoint site that is serving as a *de facto* data repository for the project.

General Motors (GM) provided a vehicle data package for a 2008 MY sedan from which the baseline assembly was extracted. The baseline assembly will be used to demonstrate

the potential weight and cost impact of third generation steels on automotive structures and assemblies. EDAG processed this vehicle data to generate representative finite element models from which the side structure was chosen for the baseline assembly, see Figure III-92. The joining criteria, load cases, and the framework for the technical cost model were defined. GM is also providing computational support to the atomistic, crystal plasticity, and forming components of the project.

During this budget period, the model assembly and integration process was flow-charted which will be used to assemble the length scale material models and integrate them with the forming, design optimization, and technical cost model.

### Technology Transfer Path

The primary deliverable of this program is an integrated computer model with a user guide that will enable users to develop 3GAHSS. The software will include a high level description of the integrated models along with a description of input variables, output variables, state variables, and relational databases implemented within the final software deliverable. The user's manual will provide an overall description of the user implementation approach for the software.

During the development of the ICME model, the project will be developing test methodologies for evaluating and characterizing 3GAHSS such as nano-hardness testing, micro-pillar, bulge testing, sheet tension-compression, etc. If the results from these tests can be correlated to macroscopic bulk materials properties testing then these tests are expected to be adopted for future work and potentially industry standardization.

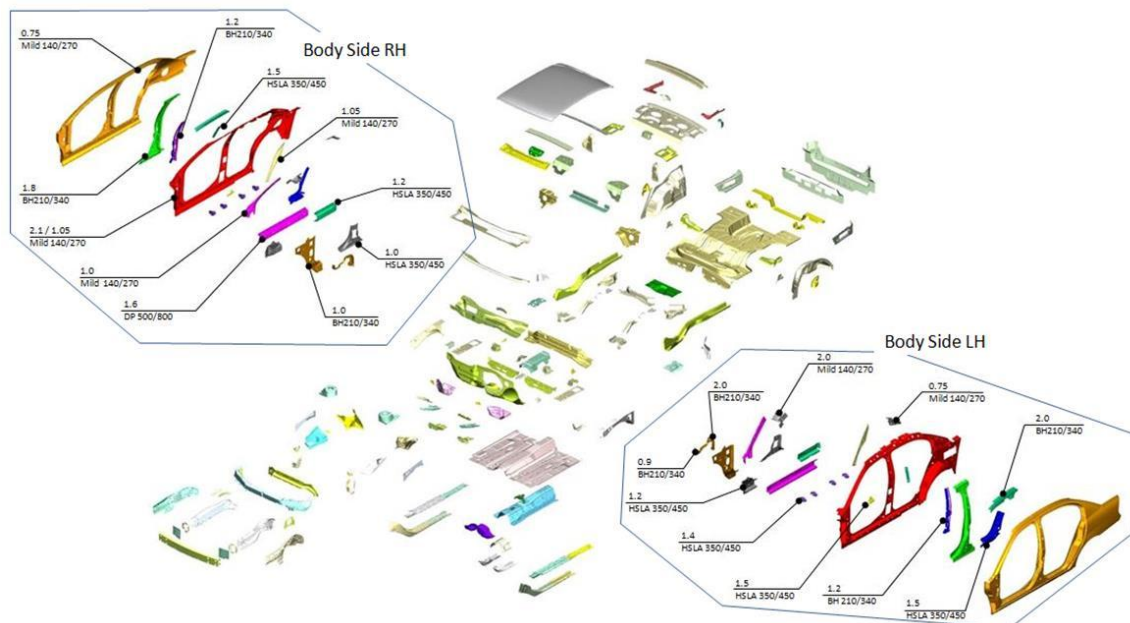


**Figure III-92: Baseline Assembly: Side Structure Part Details.**

Additionally, if the individual length scale material models show a high degree of accuracy then these models will be adopted by industry and academia for expansion and refinement to cover additional steel processing paths. Primary users of the technology are the partners that are engaged in this project which is expected to speed the implementation of results and lessons learned.

## Conclusion

Although still in the early stages (first eight months), the project is on track to meet the first period deliverables. The task teams were still able to better define the scope of work for the tasks such as flow charting the assembly and integration of the models, flow charting the co-dependent work of forming simulation with design optimization, and defining a technical approach to selecting a focal sub-assembly that can best utilize 3GAHSS with respect to applied load paths as determined from applied vehicle performance criterion. This work facilitated the development of supplier statements of work (SoWs) and improved the ability of the project to coordinate co-dependent tasks thereby increasing the likelihood that the project will successfully achieve the objectives and proposed deliverables.

Task 2 is fully launched and is focused on adapting length scale computer models for 3GAHSS and deriving representative constitutive parameters for the BAO QP980 steel. The project has identified several potential processing paths for making 3GAHSS, which include carbide free bainite, stainless steel, medium and high manganese TRIP steel and further enhancement of the quench and partitioning processing pathway. The project is working on developing a plan, due January 31, 2014 (Project Milestone #1), to make sample coupons for model validation.

The effect of solute upon elastic constants and dislocation dynamics has been completed for both ferrite and austenite with work continuing in the 2014 FY on martensite. Test results from uniaxial, bilinear, tension/compression, microhardness, bulge, and micro-pillar testing will shortly be passed to the crystal plasticity and forming component models to facilitate model validation. Work to evaluate the effect of strain and temperature on austenite stability will continue in the 2014 FY with emphasis on contrasting and validating test methodologies. Work in the 2014 FY will focus on correlation of test results with bulk material properties, and between crystal plasticity model predictions against state variable model predictions, and bulk materials properties test results.

Significant effort was needed to develop 3D RVEs for AHSS using BAO QP980 steel as a starting microstructure. The results should improve the predictive ability of the crystal plasticity model by being able to better assess the natural and processing induced material anisotropy of sheet steels. This appears to be the first time that 3D RVEs have been derived for ICME work, which is especially noteworthy considering the multiphase nature of steel versus more homogenous materials such as aluminum.

The side structure from a 2008 model year sedan was selected as the assembly from which four or more AHSS

components will be selected to evaluate the potential of 3GAHSS to reduce weight in automotive structural assemblies. The performance criterion for the side structure was defined, a bill of materials generated for all side structure components and a preliminary technical cost model developed. Full characterization of the side structure is underway with a January 31, 2014 deliverable date.

Flow charts were developed to coordinate the co-dependent tasks of forming simulation, design optimization and technical cost modeling. During the 2014 FY, the project will continue to adapt existing material models and transition from development to testing and validation as steel coupons are made available. Also during this period, the materials contribution of substituting 3GAHSS for AHSS on the weight of the side structure using only gauge optimization will be assessed. This work will also initiate the identification and application of forming models.

Flow charts were developed during this period to coordinate both assembly and integration of the computer models. Work to assemble the material models will increase throughout the 2014 FY with emphasis on documenting the inputs and outputs of each model and establishing the necessary linkages and optimization loops to facilitate assembly and eventual integration into the ICME model.

## Presentations/Publications/Patents

1. Hector Jr., L.G. The Next Generation of Advanced High Strength Steels—Computation, Product Design and Performance. Presentation given at the Great Designs in Steel Symposium, Livonia, Michigan, U.S.A., May 1, 2013; AISI/SMDI, Southfield, Michigan
2. Hector Jr., L.G.; Integrated Computational Materials Engineering Approach to Development of Lightweight 3GAHSS Vehicle Assembly. Presentation given at the 2013 DOE Annual Merit Review, Crystal City, Virginia, U.S.A. May 16, 2013
3. Hector Jr., L.G.; Krupitzer, R.; Sachdev, A.K. Integrated Computational Materials Engineering (ICME) for Third Generation Advanced High-Strength Steels: A New Four-year Project. In Proceedings of the International Symposium on New Developments in Advanced High-strength Steels, Vail, Colorado, U.S.A, June 23-26, 2013, pp. 341-349; AIST, Warrendale, PA.
4. Shen, Y.F.; Wang, Y.D.; Liu, X.P.; Sun, X.; Peng, R. Lin; Zhang, S.Y.; Zuo, L.; Liaw, P.K. Deformation Mechanisms of a 20Mn TWIP steel Investigated with In situ Neutron Diffraction and TEM. To appear in *Acta Mat.* 2013.
5. Shen, Y.F.; Liu, Y.D.; Sun, X.; Wang, Y.D.; Zuo, L.; Misra, R.D.K. Improved Ductility of a Transformation-Induced-Plasticity Steel by Nanoscale Austenite Lamellae. To appear in *Materials Science and Engineering A*, 2013.

6. Taylor, M.D.; Choi, K.S.; Sun, X.; Matlock, D.K.; Packard, C.E.; Xu, L.; Barlat, F. Relationship between Micro- and Macro- Properties for Eight Commercial DP980 Steels. Submitted to *Materials Science and Engineering A*, 2013.

## Reference

Coryell, J; Savic, V.; Mishra, S.; Hector, Jr., L.G.; Temperature Effects on the Deformation and Fracture of a Quenched-and-Partitioned Steel. Society of Automotive Engineers (SAE), 2013; Paper #2013-01-0610.

---

## IV.0 CARBON FIBER AND POLYMER COMPOSITES

### IV.1. Low-Cost Carbon Fiber Development—Oak Ridge National Laboratory

**C. David Warren, Field Technical Monitor**

Oak Ridge National Laboratory  
1 Bethel Valley Road  
Oak Ridge, TN 37831  
Phone: (865) 574-9693; Fax: (865) 574-6098  
E-mail: [warrencd@ornl.gov](mailto:warrencd@ornl.gov)

**Carol Schutte, Technology Area  
Development Manager**

U.S. Department of Energy  
1000 Independence Avenue, S.W.  
Washington, DC 20585  
Phone: (202) 287-5371; Fax: (202) 856-2476  
E-mail: [carol.schutte@ee.doe.gov](mailto:carol.schutte@ee.doe.gov)

Contractor: Oak Ridge National Laboratory  
(ORNL)  
Contract No.: DE-AC05-00OR22725

The cost of producing carbon fiber (CF) is the single most important factor controlling its incorporation in future automotive systems. According to a cost study [1], 51% of the cost of producing CF is attributable to the cost of the precursor, 43% of the cost of CF is attributable to the conversion of the precursor into CF and activating the surface

for resin compatibility, and the remaining 6% of the cost is for spooling and handling. Significant effort is being expended on developing lower-cost, higher-rate production technologies. Conversion work includes development of a higher-speed, lower-cost oxidative stabilization process and development of a microwave-assisted plasma (MAP) process carbonization method.

The first task is aimed at developing an atmospheric plasma processing technique to rapidly and inexpensively oxidize polyacrylonitrile (PAN) precursor fibers. Conventional oxidation is a slow thermal process that typically consumes more than 80% of the processing time in a conventional CF conversion line. A rapid oxidation process could dramatically increase the conversion line throughput and appreciably lower the fiber cost. The second project has already demonstrated the potential for significantly accelerating carbonization while simultaneously reducing the after treatment cost of effluent mitigation.

The strategy for transitioning each of these technologies to industry is to involve industry as early in the development process as is practical to reduce investment risk. The advanced oxidation task is nearing a maturity stage to start involving oxidation oven manufacturers within the next 18 months. The advanced carbonization project already has an industrial partner involved.

## ACTIVITY AND DEVELOPMENTS

### Advanced Oxidative Stabilization of Carbon Fiber Precursors

#### Felix Paulauskas (Principal Investigator)

Oak Ridge National Laboratory  
Phone: (865) 576-3785; Fax: (865) 574-8257  
E-mail: [paulauskasfl@ornl.gov](mailto:paulauskasfl@ornl.gov)

#### RMX Technologies:

Truman Bonds, Jeremy Jackson, Corey Bounds,  
Sergio Couttolenc  
Phone: (865) 777-2741; Fax: (865) 671-0650  
E-mail: [tbonds@rmxtechnologies.net](mailto:tbonds@rmxtechnologies.net)

#### Accomplishments

- Successfully processed textile-grade PAN with new advanced oxidation technique to required density levels in under 35 min (33 min). Achieved 364 Ksi breaking strength and 25 Msi tensile modulus, exceeding program requirements of 250 Ksi and 25 Msi, respectively. (FY 2013)
- Continued construction of the 1 ton/year plasma oxidation oven (large reactor), which is the next scale-up step in the plasma oxidation process. (FY 2013)
- Conducted chemical characterization using Fourier transform infrared spectroscopy techniques, correlating chemical properties to physical and mechanical properties to understand the relationship between process parameters and final properties. (FY 2013)
- Designed and implemented a robust plasma generation electrode configuration that is more durable than previously used equipment. (FY 2013)
- Installed and made operational the four-zone stretcher system for the large reactor. (FY 2013)
- Applied for one new patent and awarded another patent based on advanced plasma-processing technique. (FY 2012)

#### Future Directions

- Complete construction and make operational the 1 ton/year plasma oxidation oven (large reactor).
- Complete performance analysis of laboratory-scale plasma oxidation (small reactor) operations to establish starting basis for large reactor.
- Determine optimal operating conditions and CF processing parameters for the large reactor.
- Establish an industrial partnership with a commercial company for commercialization of advanced plasma oxidation technologies.

#### Technology Assessment

- Target: Develop higher throughput (approximately 3X faster) oxidation of CF, thus lowering the manufacturing costs of CF and increasing material throughput and production rate.
- Gap: Conventional oxidation methods require 80–120 min, thus limiting CF production rates. Faster oxidation could reduce the cost per pound of downstream processes for manufacturing CF, such as the carbonization, surface treatment, and sizing, because of increased mass throughput rates.
- Gap: Conventional oxidation methods contribute \$1.78/lb to the cost of CF and, more importantly, are the rate limiting and mass throughput limiting steps because of the long residence times required. Increasing the mass throughput will decrease the cost per pound attributable to oxidative stabilization for the CF.
- Gap: The advanced oxidative stabilization process has been successfully demonstrated in the laboratory but has not yet been demonstrated while integrated with other parts of the CF conversion process or at speeds and reliability levels required for industrial adoption of the technology.



#### Introduction

The purpose of this project is to develop a plasma processing technique to rapidly and inexpensively oxidize PAN precursor fibers. Conventional oxidation is a slow thermal process that typically consumes more than 80% of the processing time in a conventional CF conversion line. A rapid oxidation process could dramatically increase the conversion line throughput and appreciably lower the fiber cost. Atmospheric pressure plasma is a new and relatively inexpensive technology to implement in industrial processes [2]. A related project has already demonstrated the potential for significantly accelerating carbonization. The oxidation residence time must be greatly reduced to effect fast conversion and match the speed of the advanced carbonization technology. This project is developing an atmospheric plasma oxidation technology that could be used in line with conventional conversion equipment or be integrated with other advanced fiber conversion processes to produce low-cost CF with properties suitable for use by the automotive industry. Critical technical criteria include (1)  $\geq 25$  Msi tensile modulus,  $\geq 250$  Ksi tensile strength, and  $\geq 1.0\%$  ultimate elongation in the finished fiber (U.S. Department of Energy [DOE] programmatic goals); (2) uniform properties over the length of the fiber tow; (3) repeatable and controllable

processing; and (4) significant unit cost reduction compared with conventional processing. This effort is aimed at further developing those technologies to be able to continuously process 12–50K tows of fiber and achieve properties meeting program minimum property requirements with tow-to-tow and along-the-tow property variation within  $\pm 15\%$ . The goals also include significantly reducing the time required for oxidative stabilization (conventionally 90–120 min), which will permit greater fiber production rates and improved economics.

## Approach

For this project, the researchers are investigating PAN precursor fiber oxidation using nonthermal plasma at atmospheric pressure. As illustrated in Figure IV-1, conventional oxidative stabilization produces “core-shell” geometry with a distinct interphase between the (slowly growing) fully oxidized shell and the (shrinking) stabilized inner core. Plasma processing enhances oxygen diffusion and chemistry in the PAN oxidation process, accelerating the oxidized layer growth rate and oxidizing the fiber more uniformly, with a considerably less pronounced interface between the two regions. Previous work at ORNL has shown that this approach can reduce the required residence time for complete oxidation.

The overall project approach is to develop and validate the plasma-based process at the laboratory scale. Development was completed in previous years, and validation was accomplished in 2013 using a 24,000 filament (24K) PAN precursor. The construction of the large reactor will now scale the technology to a level where continuous operation at a pilot scale can be demonstrated. Once that is completed a pre-production scale prototype unit will be designed. Construction of the pre-production scale prototype unit, in collaboration with an industrial partner, will be funded separately from this effort.

In FY 2013, the research effort focused on successfully processing textile-grade PAN precursor (24k) and construction

of the large reactor. The textile grade fiber was successfully processed early in the second quarter, so the attention turned to a post-experimental analysis of the fiber and data produced, as well as continuing construction of the large reactor. Towards the end of FY 2013 rapid progress was made on construction of the large reactor.

## Results and Discussion

FY 2013 saw the successful completion of using textile-grade PAN with plasma oxidation, verifying that the two are compatible. This work was completed using the small reactor. A summary table of the mechanical properties is shown in Table IV-1.

The previous generation small reactor had several shortcomings that are being addressed in the design of the large reactor. Those shortcomings were as follows:

1. **Thermal control:** Proper precursor oxidation takes place in a thermal gradient. The best way to establish this gradient is with discrete, independent oven modules that can independently control temperature. In large-scale industry, the number of modules is usually four to eight. The small reactor only had one module, so a thermal gradient was established ad hoc with multiple heaters. The large reactor will have four fully independent thermal modules and so will conform to industry standards.
2. **Tension control:** During oxidation, the precursor relaxes in proportion to its temperature. Therefore, along with independent temperature control, independent fiber tension control is also a must. The small reactor only had one tension zone, despite it having a “virtual” thermal gradient. The large reactor will have four fully independent tension/stretching zones, corresponding to the four thermal modules.

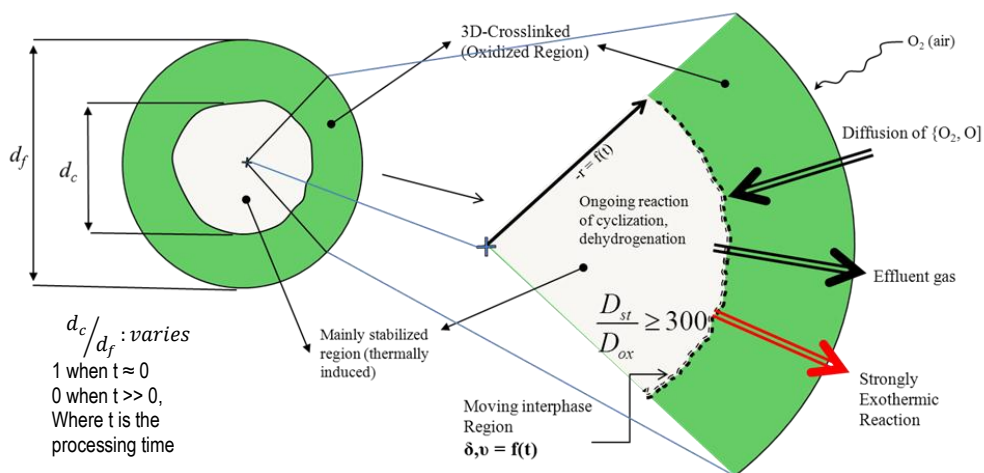


Figure IV-1: Single filament cross section during conventional oxidative stabilization process. [3, 4]

Table IV-1: 24k Textile PAN Results. Plasma oxidized (33 min), conventionally carbonized.

| Treatment    |               | Adv. Oxidized                |   |               |                    | Carbonized          |                   |               |                    |
|--------------|---------------|------------------------------|---|---------------|--------------------|---------------------|-------------------|---------------|--------------------|
| Sample       | Date Oxidized | Density (g/cm <sup>3</sup> ) | Peak Stress (ksi)                                   | Modulus (Msi) | Strain @ Break (%) | Fiber Diameter (um) | Peak Stress (ksi) | Modulus (Msi) | Strain @ Break (%) |
| Conventional | 7/17/2008     | 1.370                        | 60.1  | 0.9           | 11.72              | 6.36                | 409.1             | 25.5          | 1.48               |
| SR629        | 10/9/2012     | 1.383                        | N/M   | N/M           | N/M                | N/M                 | 345.4             | 22.3          | 1.33               |
| SR638        | 11/26/2012    | 1.377                        | 25.9  | 1             | 5.4                | 5.6                 | 363.5             | 25.1          | 1.47               |
| SR646        | 12/11/2012    | 1.380                        | N/M   | N/M           | N/M                | 5.72                | 302.2             | 22            | 1.2                |
| SR654        | 3/7/2013      | 1.367                        | 23.6  | 0.86          | 5.34               | N/M                 | N/M               | N/M           | N/M                |
| SR655        | 3/27/2013     | 1.371                        | In Evaluation for Process Correlation (Milestone 4) |               |                    |                     |                   |               |                    |
| SR656        | 3/28/2013     | 1.385                        |   |               |                    |                     |                   |               |                    |
| SR657        | 4/9/2013      | 1.364                        |   |               |                    |                     |                   |               |                    |
| SR660        | 4/23/2013     | 1.377                        |   |               |                    |                     |                   |               |                    |
| SR661        | 4/25/2013     | 1.346                        |   |               |                    |                     |                   |               |                    |
| SR662        | 5/01/2013     | 1.361                        |   |               |                    |                     |                   |               |                    |

- Plasma control:** The small reactor's plasma generation system only allowed for one power setting for the entire process. Along with independent thermal and tension control, independent plasma control in each module is anticipated to be the optimal condition. The large reactor will have such an arrangement.

The large reactor's design addresses all the known shortcomings of the small reactor design and should provide improved performance and results. Four modules are used that utilize independent thermal, fiber, plasma, and flow control. The oven is heavily instrumented to allow for maximum diagnostic and learning of the process. The development team will continue into FY 2014 working as rapidly as possible to get the large reactor operational as soon as possible. Figure IV-2 indicates the project status toward design and construction of the large reactor.

### Technology Transfer Path

RMX Technologies has obtained an exclusive option to license ORNL's rights to the intellectual property (IP) covering plasma oxidation (RMX already has rights to this IP through co-invention). RMX will therefore lead the commercialization effort and has already executed a plan to win industry commitments to support scaling this technology to industrial levels. Once the large reactor is operational and optimized, RMX will invite CF producers to provide precursor to process on this device. The resulting oxidized PAN fiber will be returned to the producer so that they can analyze and make prototype parts from it. Industry interest in this technology is high, thus successful demonstration of the large reactor might provide a direct path of technology transfer.

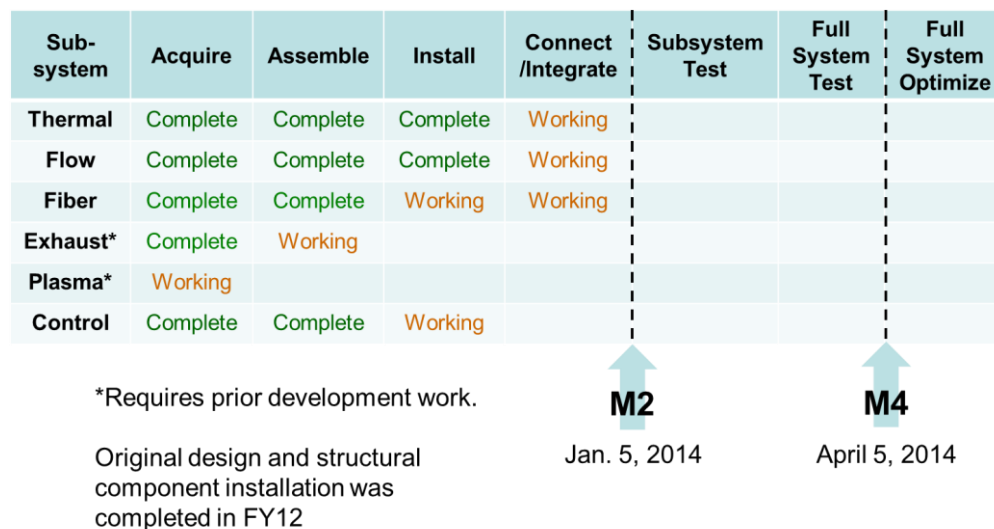


Figure IV-2: Progress on the construction of the 1 ton/year plasma oxidation oven (large reactor).

## Conclusion

The technology has been proven at the laboratory scale and is now being scaled to the pilot scale. Once demonstrated at the pilot scale, it will then be scaled to the preproduction scale in collaboration with industrial partners. The goal of the research team is to establish a clear path of technology transfer to industry by the end of FY 2014. At the conclusion of Phase II of this project (projected to be the end of FY 2015), the researchers will be positioned to procure, install, test, and operate a pilot-scale (25 ton/year) plasma oxidation module in an advanced technology pilot line. The follow-on of this project will be the design and construction of an advanced technology pilot line that will then be installed at the Carbon Fiber Technology Facility (CFTF). The pilot line will be used to validate system performance and scalability as well as to produce the required quantities of advanced technology CFs to support the Lightweight Material Program's advanced development activities. The follow-on activity for scale-up will be a separate project from the current effort.

---

## Development and Demonstration of Advanced Carbonization

---

### Felix Paulauskas (Principal Investigator)

Oak Ridge National Laboratory

Phone: (865) 576-3785; Fax: (865) 574-8257

E-mail: [paulauskasfl@ornl.gov](mailto:paulauskasfl@ornl.gov)

### RMX Technologies:

Truman Bonds, Jeremy Jackson, Corey Bounds,  
Sergio Couttolenc

Phone: (865) 777-2741; Fax: (865) 671-0650

E-mail: [tbonds@rmxtechnologies.net](mailto:tbonds@rmxtechnologies.net)

### Accomplishments

- Completed upgrade to MAP line to process five tows continuously and demonstrated > 2-hour stable run with five tows. Mechanical properties meeting program requirements (250 KSI strength, 25 MSI modulus) were achieved, but inherent precursor uniformity limitations and tow-to-tow energy distribution within chamber resulted in a higher property variability than targeted.
- Guided by modeling results, implemented significant changes to fiber handling resulting in enhanced tensioning control and improved tow-to-tow energy distribution. The changes included horizontal tow spacing with vertical energy introduction and non-linear tow orientation in the processing chamber.
- Developed an alternative technique for focusing and controlling microwave energy deposition in the processing chamber. Hardware has been procured and installed for evaluation. Preliminary results show substantial energy efficiency improvements with indications that the technique can be deployed easily for larger-scale use, while likely making separation of low- and high-temperature carbonization approaches unnecessary.
- Completed evaluation of atmospheric plasma processing for portions of carbonization using RMX proprietary atmospheric pressure plasma technology coupled with an electromagnetic heating technique that is extremely energy efficient. The team concluded that this new technique is feasible for assisting in low-temperature carbonization but that it is not adequately advanced for implementation at this time.
- Developed techniques for investigating applicability of MAP processing to other precursors using short tow sections.
- Improved operational durability by implementing sealing approaches for both processing chamber tube connections and tow vacuum interfaces developed in FY 2012. These improvements were demonstrated by the ability to achieve stable vacuum with larger tube and more tows (e.g., the 2 hour run described previously) and by the enhanced ability to make configuration changes without significant downtime to resolve system interfaces related to sealing.

### Future Directions

- Characterize and optimize cost versus performance tradeoffs to facilitate commercial attractiveness.
- Use process stability and durability experience to make continuing improvements in operational stability.
- Incorporate alternative precursors such as textile PAN and polyolefins, as available in appropriate forms, into new process capability.
- Develop technical specification for a 25-tonne-per-year scale-up as the next step in the pathway to commercialization and cultivate industrial partnerships for technical collaboration in scale-up and commercialization.

### Technology Assessment

- Target: Develop and demonstrate alternative methods for carbonization of stabilized CF precursors having the potential to reduce energy and cost in carbonization by greater than 30%.
- Gap: Conventional carbonization requires significant expenditure of energy and requires extensive furnace maintenance resulting in high processing costs.
- Gap: High-temperature furnaces have significant thermal inertia requiring long start-up and shutdown times, limiting mid-process changes and adjustments and adding expense in resolving problems.



### Introduction

The objective of this project is to develop, demonstrate, and move toward commercialization a scaled energy-efficient advanced conversion technology to enable manufacturing of CF that is technically and economically viable in industrial markets. Industrial applications, critical to efficient energy production and use (transportation, wind energy, infrastructure, and oil drilling applications), are attractive for lower-cost applications where aircraft-grade CF properties are not required. Alternative fiber manufacturing processes could be implemented if the fiber performance requirements from these industries can be met while simultaneously achieving lower cost fiber. This project is co-funded by the Vehicle Technologies Program (VTO) and the Advanced Manufacturing Office in DOE's Office of Energy Efficiency and Renewable Energy. The project is aimed at further developing an advanced conversion processes. The advanced conversion process is based on previous ORNL work in MAP and related technologies for carbonization [4, 5]. The team is evaluating the overall energy usage of the hardware and materials systems to determine the energy and cost efficiency of the technology.

This work is building on substantial past research investments at ORNL funded through the DOE's VTO,

investigating a variety of alternative CF precursors and conversion processes. Conventional conversion employs a thermal pyrolysis process that is slow, energy intensive, and space intensive. ORNL has previously demonstrated that microwave energy combined with plasmas can be used as a means to rapidly convert PAN precursor fibers into finished CFs. The researchers demonstrated a residence time of approximately 1/2 (and in some cases up to 1/3) of the conventional residence time. This project is investigating and demonstrating the scale-up of advanced conversion technologies that are projected to reduce the manufactured cost of CFs and the energy used to produce them by up to 50%.

## Approach

In previous work, ORNL researchers carbonized a single 50,000 filament tow at 5 m/min, or  $< 1/2$  of conventional residence time, and 3 x 50,000 filament tows at 1 m/min, or  $< 2X$  conventional residence time. At the start of this project, the system was not robust and could not approach the required continuous operating time required by industry. This project is aimed at scaling and demonstrating the MAP carbonization process closer to industry requirements. The principal tasks of this project are as follows:

- Evaluate materials, sealing, and atmospheric pressure solutions.
- Estimate the energy requirement for various scales.
- Develop system modeling to guide hardware design and process development.
- Determine the preferred microwave/plasma parameters and profiles necessary to minimize residence time.
- Scale to  $\geq$  five large tows of 24,000 or more filaments.
- Demonstrate non-stop operation of at least 8 hours, indicating the potential for week-long production scenarios.
- Develop information necessary to produce a robust advanced technology carbonization unit to be built and operated in the ORNL CF demonstration line.

The targeted outcome for this project is to have technical specifications for scaling this technology to semi-production scale consistent with the 25-tonne-per-year capability at the Oak Ridge CFTF. Plans are to have demonstrated adequate hardware improvements, operational experience, production performance in meeting fiber property targets and uniformity, system robustness in continuous operation, and scalability in going from one to three tow operations to  $\geq$  five large tows with a strategy for scaling to production levels. Plans are under way to project the economic feasibility in production to pursue partner interest and sponsor opportunities to take this technology to the next step in the commercialization process.

## Results and Discussion

As reported in FY 2012, a number of hardware upgrades have been completed on the MAP line, the experimental campaign to demonstrate acceptable fiber properties is showing good results, and preparations for the major upgrade to five-tow operation were under way at the conclusion of the

reporting period. The upgrade to five-tow operation is now completed and includes fiber-handling equipment for the five tows with enhanced tensioning. The most significant upgrade of the MAP line was the installation of a 25% larger vacuum tube. The purpose of the larger tube is to allow an increased number of tows in the plasma chamber without an interaction (dragging) with the wall. With five tows in the applicator, the plasma was stable over a larger operating space than under three-tow operation. Reflected power was on average several percent lower than in one- or three-tow operations as well, which raises the efficiency of the process. However, initial experiments demonstrated that tow-to-tow processing is not as uniform as had been hoped. The outer tows seem to be processed more than the inner tows, but the variance is not as drastic as was seen in the three-tow experiments with the radio frequency (RF) coupling from the side. Also, as had been seen in previous experiments, the horizontal tows are not processed evenly, with the tow farthest from the coupled RF being inadequately processed. The solution to this issue was to rotate the RF applicator itself so that the tows are still horizontal to avoid gravity effects but with all the tows a similar distance from the RF source. Early in FY 2013, this rotation was completed; the new configuration is shown in Figure IV-3. The larger tube and vertical energy introduction also provided the capability to change tow orientation geometry to make improvements in tow-to-tow property uniformity. After completion of these configuration changes, a stable two-hour MAP run with five tows was demonstrated.

Figure IV-4 provides a compilation of representative results from three- and five-tow test runs. Shortly after the system upgrades, the team successfully ran five tows but found variations in properties with tow position. A run under these operating parameters, but at 50% more speed, shows some degradation of properties, but the property levels were in ranges comparable with earlier experiments where relatively small modifications to processing parameters allowed achievement of target properties. Indeed, by altering the operating parameters at the lower speed, the tensile strength and modulus were increased to a point where the target specification for all tows was met, as shown by the cyan points in Figure IV-4. Several actions are under way to increase the line speed at the newer operating conditions and attempt to maintain the better properties.

As improving processing uniformity was a key focus of this recent reporting period, the modeling effort was revisited to understand the cause and effect relationship between changing process parameters and the resulting carbon fiber properties. If the plasma is treated as a poor conductivity metal, the plasma current density profile can be modeled, which corresponds to the processing power as function of location. Figure IV-5 shows two simulations of a plasma column in an applicator analogous to the MAP. At a different conductivity the current profile changes shape considerably in the right panel to become hollow. This may explain the relatively lower level of processing of the interior tows.

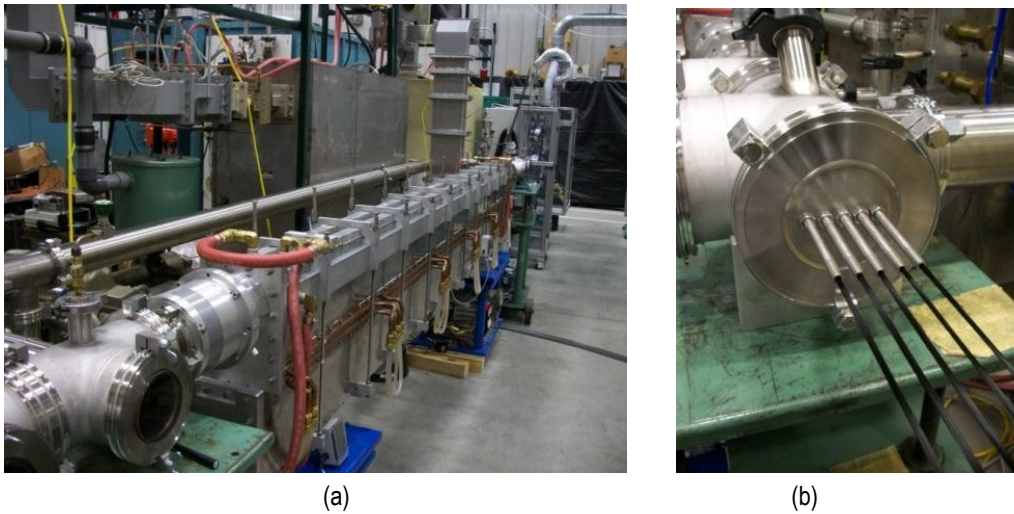


Figure IV-3: (a) The MAP line after rotating the applicator. Microwave coupling is now from below. (b) The MAP line exit feed-throughs shown fully strung with five tows in the horizontal configuration.

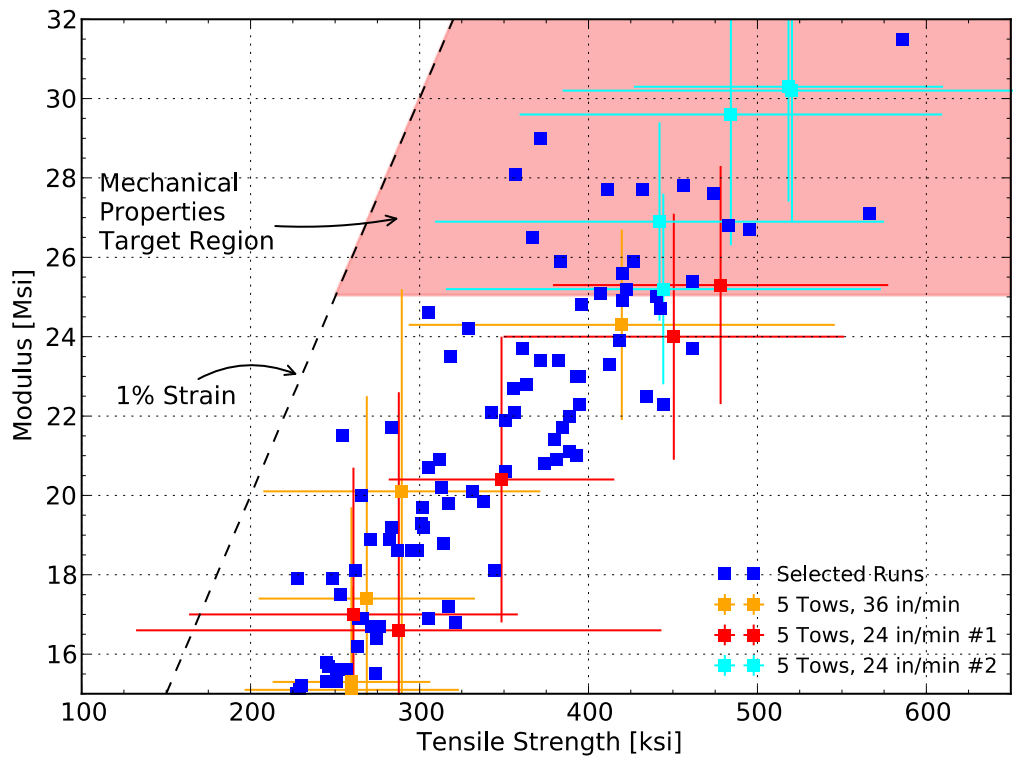


Figure IV-4: Mechanical properties from selected MAP runs. The orange, red, and cyan points are from three 5-tow runs. Fiber properties in the shaded region meet or exceed programmatic targets. The large variance is the result of single-filament mechanical testing.

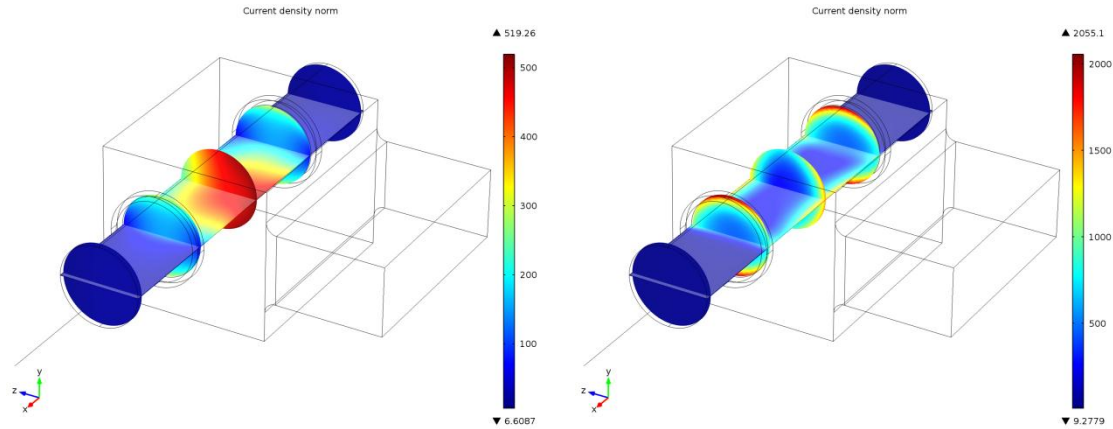


Figure IV-5: Current density shown inside the plasma column for two different values of plasma conductivity.

To counteract this difference in conductivity, the geometry of the tows in the plasma can be modified as in Figure IV-6(c). By modifying the hardware, tows can be moved out of the center where the current density is lowest. This approach has now been implemented.

As part of the broader low-cost CF initiatives, ORNL continues to seek opportunities to evaluate alternative precursor formulations and tow configurations, and these materials are typically available initially in very small quantities—usually small tow sizes (filament count) of very short lengths. In addition to evaluating the precursor “convertibility” to carbon fiber, needs exist to project applicability of advanced processing techniques to these alternative forms. During this reporting period, preparations were made for processing small samples in the MAP line. To maximize the number of experiments, an experiment was conducted by running a fully carbonized 12k tow through the MAP. This experiment was a success, and the fully carbonized tow will be used as a carrier to eventually tie short lengths of polyolefin into the process. The fully carbonized tow

did not appear to change the plasma at all, and knots tied into the tow survived without apparent ill effect. This approach will be used to process smaller samples of alternative precursors as future needs arise.

ORNL and long-term partner RMX have completed a feasibility study of a low-cost carbonization method. This technique used RMX’s proprietary atmospheric pressure plasma technology coupled with an electromagnetic heating technique that is extremely energy efficient. Work began in July 2012 and finished at the end of July 2013. Results confirmed that, at the very least, this technique accomplishes “low-temperature” carbonization (conventionally in the 500–700°C range of processing). During this study, a variety of techniques and equipment were evaluated. A final design was determined at the end of the project and has been termed the Close-Proximity Plasma Electromagnetic-Heating (CP<sup>2</sup>E) carbonization technique. The project team concluded that the new technique is feasible for assisting in low-temperature carbonization but that it is not adequately advanced for implementation at this time.

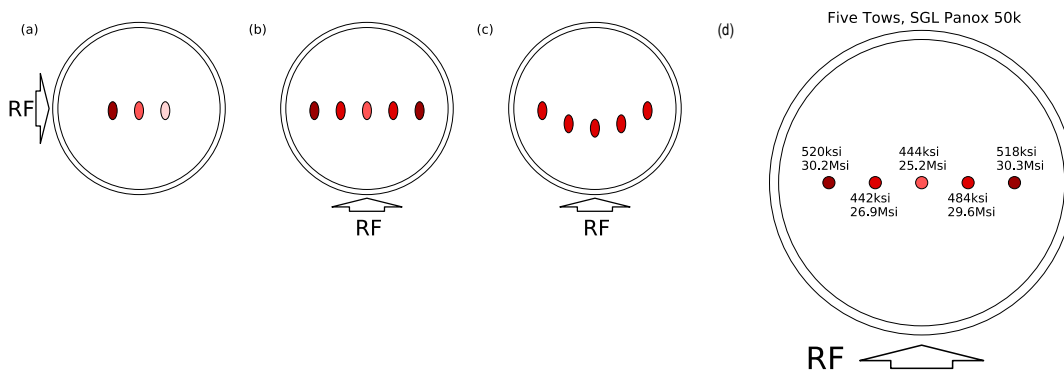


Figure IV-6: Tow orientations within MAP applicator. (a) Orientation in pre-2012 multi-tow experiments. Heating is very uneven. (b) Tow orientation after applicator rotation for five-tow experiment. Inner tows are processed less than the outer tows. (c) Current tow orientation. (d) Recent data at each position before reconfiguration.

Plasma stability and reproducibility has been a focus in moving the MAP line to a dependable industrial process. The number of zones and relative power and location of the multiple plasma zones in the current MAP applicator are highly interdependent. System stability is a function of the input power and pressure as well as the location and presence of the CF in the applicator. If the plasma zones could be uncoupled from each other, then the heating profile could be more easily tailored and the plasma made more stable under a variety of operating conditions. ORNL has developed a concept for a multi-chamber applicator method that uses commercially demonstrated equipment to replace the current driving/driven coupled waveguide design for the MAP. Each chamber is driven separately and can be matched to provide the desired chamber-to-chamber heating profile. A single chamber has been procured and integrated into the MAP line taking advantage of the existing processing chamber and microwave generator. As this reporting period is coming to a close, the initial experiment with this approach has been completed, and preliminary data indicate that this approach does indeed focus the microwave energy and creates an intense and effective plasma (see Figure IV-7) that efficiently carbonizes stabilized precursor. Additional units are on order to complete what will be the final demonstration unit for this project.



**Figure IV-7: Improved microwave energy and enhanced plasma hardware. This approach, here demonstrated with a single unit, should allow improved energy deposition control for industrial scale-up.**

### Technology Transfer Path

The team has identified microwave generator and vacuum system suppliers who could be potential partners. The team also has fielded inquiries from existing manufacturers of CF conversion equipment and others interested in entering this business regarding potential partnerships for scaling up carbonization systems. At this point, it is not appropriate to commit to specific partners, especially considering that the issues regarding the potential for atmospheric plasma approaches and specifics of multi-chamber versus single chamber MAP approaches have not yet been resolved. A formal request for expressions of interest requiring potential partners to outline their proposed approaches is being

planned. This activity will be completed during the first half of FY 2014.

During the latter portion of this work, ORNL will formally evaluate potential partners and partnership arrangements for scaling the technology to the pre-production scale demonstration comparable with the 25-tonne-per-year scale currently being implemented at the CFTF in Oak Ridge. A deliverable of this project is technology documentation adequate for specifying the equipment in this size range. Equipment and process details can be demonstrated and discussed with potential partners allowing for development of collaborative proposals for moving to the next scale level and eventual commercialization. ORNL will solicit input from various commercial sources as to interest in this area and will work with the program office(s) to formalize planning for acquiring adequate resources for the following phases of this work.

### Conclusions

Significant progress continues in understanding and addressing issues associated with the durability and scaling of the MAP process. Appropriate tools have been put in place to assist with the hardware development, including a system model complemented with dielectric measurement capability as a function of temperature. The optimization of plasma parameters for conversion will continue to focus on improving process economics and uniformity since the process has been shown capable of meeting performance targets. The team will continue to review the energy balance data to refine the data as well as to prioritize the balance of system priorities. Progress is continuing on improvement of the current hardware transition regions, sealing approaches, and effluent handling.

The targeted outcome for the advanced carbonization portion of the project is to have technical specifications for scaling this technology to semi-production scale consistent with the 25-tonne-per-year capability at the Oak Ridge CFTF. The CFTF initiative will enhance demonstration of CF technologies at near-production scale to facilitate commercialization of these technologies. Future plans are to demonstrate adequate hardware improvements, operational experience, production performance in meeting fiber property targets and uniformity, system robustness in continuous operation, and scalability in going from one- to three-tow operation to  $\geq$ five large tows with a strategy for scaling to production levels. Plans are under way to project the economic feasibility in production to pursue partner interest and sponsor opportunities to take this technology to the next step in the commercialization process.

### Conclusions

Two advanced conversion processes are currently under development: advanced oxidative stabilization and MAP carbonization. Both technologies have previously been proven effective at the laboratory bench scale by processing PAN-based precursors into carbon fibers, which exceeded the

program minimum requirements of 250 KSI breaking strength and 25 MSI tensile modulus. Both technologies are currently being scaled to demonstrate continuous operation, in a reliable manner, while processing multiple large tows of precursor. At the conclusion of the current phase for each of these technologies, sufficient knowledge will be gained and specifications written to allow for development of continuously operating preproduction scaled units intended to match the speeds and throughput of the CFTF line. That next scale-up step will be done in collaboration with industrial partners who are capable of taking those technologies to full commercialization. The partnerships for that next scale-up step are being sought and developed.

### Presentations/Publications/Patents

1. Paulauskas, F. L., et al., *Apparatus and Method for Carbon Fiber Surface Treatment*. U.S. Patent 8,227,051 B1, issued July 24, 2012.
2. Paulauskas, F. L., et al., *Rapid Oxidation of Polymeric Fibers for Producing Flame Retardant Fibers*. 13/163,134 filed in June 2011.

### References

1. Friedfeld, B. Cost Assessment of Lignin-and PAN-Based Precursor for Low-Cost Carbon Fiber, Presentation for the Automotive Composites Consortium, 17 January 2007.
2. Roth, J. R. *Industrial Plasma Engineering, Volume 2: Applications to Nonthermal Plasma Processing*; Institute of Physics Publishing: Philadelphia, 2001; Chapter 15.
3. Paulauskas, F. L. Advanced Oxidation & Stabilization of PAN-Based Carbon Precursor Fibers. Presented at the *DOE Annual Merit Review*, Washington, June 9, 2010; LM-006.
4. Paulauskas, F. L. Temperature-Dependent Dielectric Measurements of Polyacrylonitrile Fibers. Presented at *SAMPE 2004*, Long Beach, CA, May 16–20, 2004.
5. White, S. M.; Spruiell, J. E.; Paulauskas, F. L. Fundamental Studies of Stabilization of Polyacrylonitrile Precursor, Part 1: Effects of Thermal and Environmental Treatments. Presented at *SAMPE 2004*, Long Beach, CA, May 16–20, 2004.

## IV.2. Carbon Fiber Technology Facility—Oak Ridge National Laboratory

### Lee McGetrick (Principle Investigator)

Oak Ridge National Laboratory  
PO Box 2008  
Oak Ridge, TN 37830-6186  
Phone: (865) 574-6549  
E-mail: [mcgetricklb@ornl.gov](mailto:mcgetricklb@ornl.gov)

### Carol Schutte, Technology Area Development Manager

U.S. Department of Energy  
1000 Independence Avenue, S.W.  
Washington, DC 20585  
Phone: (202) 287-5371; Fax: (202) 856-2476  
E-mail: [Carol.Schute@ee.doe.gov](mailto:Carol.Schute@ee.doe.gov)

Contractor: Oak Ridge National Laboratory  
(ORNL)  
Contract No.: DE-AC05-00OR22725

### Abstract/Executive Summary

In March 2009 the U.S. Department of Energy's (DOE's) Office of Energy Efficiency and Renewable Energy (EERE) issued a competitive call for proposals to construct and operate a highly flexible, highly instrumented low-cost carbon fiber technology demonstration facility for demonstrating and evaluating new low-cost manufacturing technologies at a pilot scale. Oak Ridge National Laboratory responded to the call and was awarded the project. Construction of the Carbon Fiber Technology Facility (CFTF) began in March 2011, and the facility was commissioned for operations in March 2013.

The CFTF offers a unique, highly flexible, highly instrumented carbon fiber line for demonstrating advanced technology scale-up and for producing market-development volumes of prototypical carbon fibers. The CFTF has unique capabilities, with the flexibility to process a range of feed stocks and product forms that are unmatched anywhere in the world. The CFTF bridges the "valley of death" between laboratory research and commercial scale deployment of low-cost carbon fiber technologies, thus filling a critical need for promoting industrial competitiveness for the manufacture of carbon fiber in this nation.

The objective of this project is to accomplish the safe and reliable operations of the CFTF and to further DOE's objectives for large-scale commercialization of low-cost carbon fibers (LCCF). Operating funds covered under this project are co-funded by the Vehicle Technologies Program (VTO) and the Advanced Manufacturing Office (AMO) and support EERE's efforts towards transitioning technologies to industry, specifically, with respect to cost-effective carbon fiber for composite materials in high-volume energy applications.

Activities funded under this project include the development and implementation of management systems to ensure safe, compliant, and reliable facility operations; the production of sufficient quantities of carbon fibers from lower-cost precursor materials to place LCCF in the hands of industry partners for the development of prototypical composite applications; and establishment of a skilled workforce and a training system that can be leveraged to assist industry in the development of the future carbon fiber and composites workforce.

### Accomplishments

- The CFTF transitioned to operations in March 2013, following a series of independent readiness assessments including a "readiness to operate" assessment by the DOE Oak Ridge Site Office. The project was completed six months ahead of schedule and almost \$2M under budget. (FY 2013)
- Operations during this period primarily focused on converting carbon fibers in a variety of formats in anticipation of supporting projects approved by AMO and VTO. Approximately 2,000 kilograms were produced during the period from a variety of traditional polyacrylonitrile precursor and textile acrylic fiber precursor materials in small tow (12K), medium tow (24K and 48K) and large tow (601K) formats. (FY 2013)
- Notable progress was made in the conversion of the textile acrylic fibers that are being supplied by the Kaltex Group, a large textile fiber producer located in northern Mexico. Between July 8, 2013, and September 20, 2013, eight production lots of oxidized acrylic fibers and carbon fibers were produced from the Kaltex precursor material. Analytical test results from these production runs indicate increasingly improving properties in tensile strength and modulus, indicating that this material might be a good candidate for full-scale production of lower-cost carbon fibers. (FY 2013)
- During the first year of start-up and operation the CFTF exhibited a perfect record of safety and environmental compliance. (FY 2013)

### Future Directions

- Continue the safe and reliable operation of the carbon fiber conversion line and the melt spinner, with a focus in FY 2014 on providing lower-cost carbon fibers produced from textile acrylic fibers to industry partners for development of prototypical composite applications. The primary objective for this activity is to create industry "pull" for carbon fibers from this textile material with the outcome of large-scale investment by industry to build production lines for mass producing lower-cost carbon fiber to supply automotive and other markets. A goal for FY 2014 is to transfer at least 51% of oxidized fibers and

carbon fibers produced at the CFTF to industry partners, academia, or research institutes for use in downstream projects or applications which further DOE EERE clean energy mission and goals.

- Scale-up other alternative precursor materials including lignin-based carbon fibers, cellulosic paper carbon materials, and polyolefin-based carbon fibers.
- Engage industry partners and identify projects, including one-to-one cost share projects and work-for-others projects.

### Technology Assessment

- Target: Scale up alternative, low-cost precursors and processing technologies for the manufacture of low-cost carbon fibers. Alternative materials include textile acrylic fiber (FY 2013), lignin for functional applications (FY 2014), and polyolefin (FY 2015).
- Gap: Development of processing recipes for stabilization and carbonization of these materials requires significant effort including the collection of process data and correlation of large amounts of data sets to outcomes (e.g., material properties) to determine optimum run conditions. For lignin-based carbon fibers the melt spinability and stabilization times remain technical challenges.
- Target: Scale up alternative, lower-cost processing methods for converting precursors into carbon fiber. Alternative processing methods include advanced oxidation and microwave-assisted plasma carbonization, as well as other processes that are under development.
- Gap: New processes can be developed as individual units at the laboratory. Interfacing of these new processes can be demonstrated for short-term operation at the pilot scale with 1-6 tows being simultaneously processed for 1-2 hours. Without the CFTF facilities, it would not be possible to scale the technologies to the level of continuous operation for days or weeks, which is a necessary step for the new technologies to be commercialized by private industry.
- Target: Reduce the process development time for new precursor materials by 50% from typically three months to six weeks, increase throughput by 25%, and reduce waste by 20%.
- Gap: Conventional carbon fiber conversion technology measures process parameters associated with the environment in which the precursor material is exposed (e.g., temperature of the atmosphere in stabilization ovens and carbonization furnaces). There is no current use of technology to measure the material itself during conversion to correlate end-product carbon fiber properties with actual material in-process properties. Introducing in-process measurement and feedback on material properties such as color, sheen, density, and modulus would enable improvement in process development time and increase process efficiency.



### Introduction

The objective of this project is the safe and reliable operations of the Carbon Fiber Technology Facility (CFTF) for the purpose of furthering the U.S. Department of Energy's (DOE's) objectives for large-scale commercialization of LCCFs. The tasks covered under this project are co-funded by the Vehicle Technologies Program and the Advanced Manufacturing Office and support the Office of Energy Efficiency and Renewable Energy's efforts towards transitioning technologies to industry, specifically with respect to cost-effective carbon fiber for composite materials in high-volume energy applications. Key strategies to be implemented by the project are (1) develop and implement management systems that will ensure environmental, health, safety, and consistency of operations; (2) develop and implement inspection, testing, and maintenance programs to protect the DOE's investment in the CFTF; and (3) develop a skilled workforce for the carbon fiber and composites industries. To implement these strategies, Oak Ridge National Laboratory (ORNL) will deliberately transition from plant start-up and commissioning into operation of the CFTF. Specific tasks to be executed include staffing, process and procedures development, training, readiness assessments, and safe, reliable operation of the CFTF.

### Approach

To ensure a smooth transition to operations during FY 2013, the CFTF management team worked with a number of ORNL subject matter experts to prepare and issue several *facility-specific* program plans and procedures:

- Environment, Safety, and Health Plan
- Quality Assurance Plan
- Technology Control Plan
- Post-construction Fire Hazards Analysis document (Draft)
- Training Program Plan
- Work Control Policy for CFTF Operations and Maintenance
- Emergency Action Plan

Each of these documents describes how the CFTF will implement applicable requirements outlined in ORNL's Standards Based Management System (SBMS). SBMS contains the set of contractual requirements that must be implemented by ORNL projects and facilities based on DOE directives and applicable technical standards.

The CFTF officially transitioned to operations in March 2013. Early operations have focused on running a series of test matrices using standard polyacrylonitrile (PAN) precursor fiber as a baseline material. These test matrices have helped the operations team establish and understand key process parameters (e.g., temperature profiles, dwell times, tensions, and air flow) and how they affect the properties of the carbon fibers being produced. This will enable the CFTF to produce specific carbon fibers with targeted properties for use in future technical collaboration projects with industry partners, as well to develop a better understanding of the equipment to improve

effectiveness in executing future trials with more experimental precursor materials.

With operations under way, several systems necessary to support operations were developed and implemented. The operations teams, led by the shift managers and senior technicians (who have previous experience with the production of carbon fibers), completed development of operational procedures and checklists for each unit operation on the production line. These procedures were incorporated into CFTF's "paperless" work control system and are available on the production floor via hand-held electronic tablets.

A comprehensive set of quality laboratory procedures were developed using analytical test methods based on standards from the American Society for Testing and Materials. These procedures define the requirements and methods that are being used to test carbon fibers produced at the CFTF for tensile strength, modulus, elongation at break (strain), density, and denier. Test methods and equipment calibrations were validated by using an outside, independent, ISO-certified laboratory to compare and verify test results using a variety of sample sets.

A computer-based, commercially available maintenance management system, "Bigfoot," was implemented. Bigfoot has been populated with scheduled inspections, calibrations, and preventive maintenance activities and is being used to track and manage both scheduled and unscheduled maintenance activities. A program goal is to demonstrate at least 95% compliance to preventive maintenance schedules during each quarterly reporting period. Reporting will include milestone

schedule reports generated from the Bigfoot equipment history database.

A manual Excel-based inventory tracking system was implemented for raw materials and finished products, both for carbon fiber conversion and melt-spun and melt-blown precursor fiber materials. In the coming year, this system (because of the large amount of data and information being captured and reported) will transition to an automated system.

## Results and Discussion

CFTF management took an aggressive approach in scaling up the conversion of a textile acrylic fiber to carbon fiber. The team established availability of textile acrylic fiber manufactured in northern Mexico by The Kaltex Group, a large textile fiber producer located 200 miles south of Brownsville, Texas. Notable progress is being made in the conversion of these textile acrylic fibers. Between July 8, 2013, and September 20, 2013, eight production lots of oxidized PAN and carbon fibers were produced from the Kaltex precursor material. Analytical test results from these production runs indicate increasingly improving properties in tensile strength and modulus (Figure IV-8), indicating this material might be a good candidate for full-scale production of lower-cost carbon fibers. The availability of the Kaltex fibers is fortuitous since, in April 2013, Bluestar Fibres announced the closure of their PAN precursor production facility located in Grimsby, UK, creating a need by several U.S. producers for a replacement source of precursor.

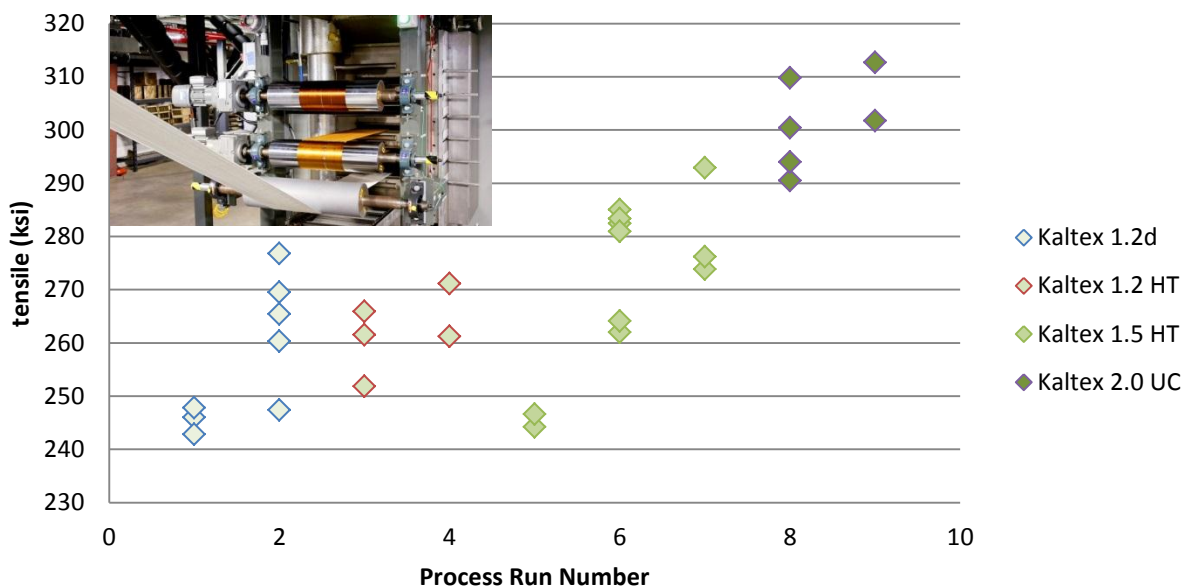


Figure IV-8: Kaltex strand tensile strength. Each diamond symbol represents a set of test data for a sample set processed during different weeks. The photo is the Kaltex tow in the first oxidation oven.

Several independent assessments of CFTF operations took place throughout the course of FY 2013. The CFTF director organized an ORNL internally led, independent management assessment of operational readiness. The independent management assessment team reported, "...the CFTF is ready to begin commissioning activities with minor recommendations. The CFTF staff displayed a remarkable knowledge and understanding of all process hazards and controls. There exists an active safety culture with a very strong commitment to empowering workers to seek out safety improvements and take personal responsibility for their safety and the safety of others. The hard work, dedication, and teamwork of the CFTF Team are outstanding."

A second assessment was performed by the DOE Oak Ridge Site Office (OSO) before recommendation of Critical Decision 4 (CD-4) and transition to operations. There were five recommendations in the OSO, which were promptly addressed, and on March 21, 2013, OSO issued their final report recommending approval of CD-4.

During July through September 2013 the DOE Office of the Inspector General performed an audit of the CFTF. The audit was completed with no findings.

Successful commercialization of low-cost carbon fiber technology for achieving U.S. energy and economic benefits is the overarching objective of CFTF. Toward that end, we have identified a number of potential partners with whom the CFTF is establishing effective partnerships with emphasis on industry partners with interest in using the CFTF to scale up their new precursor materials as well as carbon fiber composites manufacturers to generate market pull in high-volume energy applications. ORNL's leadership in the carbon fiber efforts will continue to engage potential industrial partners with interest in use of the CFTF.

## Conclusion

Since the official transition into operations in March 2013 the CFTF has continued to meet or exceed goals for safe, efficient, and compliant operations and production of lower-cost carbon fibers. In a relatively short amount of time the CFTF has demonstrated that a lower-cost carbon fiber can be produced from a textile-grade acrylic fiber, an accomplishment that has resulted in many inquiries from industry partners. A process was implemented in June 2013 by which these lower-cost carbon fibers and other products, such as oxidized PAN fibers, can be placed in the hands of industry for the development of prototypical composite applications to prove the value of these fibers.

## Presentations/Publications/Patents

### Presentations:

1. "The Human Factor in Carbon Fiber Manufacturing," presented November 5, 2013, at the National Educators' Workshop on at Ivy Tech Community college in Fort Wayne, Indiana.
2. "The Human Factor in Carbon Fiber Manufacturing," presented December 5, 2012, at Carbon Fibers 2012 Conference in San Diego, California.
3. "The Carbon Fiber Technology Facility," presented March 7, 2013, at the SAMPE 2013 conference in Long Beach, California.
4. "Development of Low-cost Carbon Fibers," presented to the American Composites Manufacturers Association (ACMA) Symposium for Business Owners, Senior Managers, and Market Leaders, May 22, 2013, Washington, DC.
5. "Carbon Fiber Technology Facility, Commercialization of Low-cost Carbon Fibers," presented at Harper, International Workshop in Buffalo, New York on July 25, 2013.

## References

None.

## IV.3. Development and Commercialization of a Novel Low-Cost Carbon Fiber—Zoltek Companies, Inc.

### **George Husman (Principle Investigator)**

Zoltek Companies, Inc  
Chief Technology Officer  
3101 McKelvey Road  
St. Louis, MO 63044  
Phone: (314) 291-5110  
E-mail: [george.husman@zoltek.com](mailto:george.husman@zoltek.com)

### **William Joost or Carol Schutte, Technology Area Development Managers**

U.S. Department of Energy  
1000 Independence Avenue, S.W.  
Washington, DC 20585  
Phone: (202) 287-6020; Fax: (202) 856-2476  
E-mail: [william.joost@ee.doe.gov](mailto:william.joost@ee.doe.gov)

Contractor: Zoltek Companies, Inc.  
Contract No.: DE-EE0005394

### **Abstract/Executive Summary**

The objectives of this project are to develop and commercially validate a low cost carbon fiber meeting the target cost of \$5.00 / lb. and target properties of strength > 250,000 pounds per square inch (psi), modulus of elasticity > 25,000,000 psi, and strain-to-failure > 1%. This project is a joint development effort of Zoltek Companies, Inc. and Weyerhaeuser Company. The bases of this development are innovative, patent pending technology for wet-spinning of Lignin / polyacrylonitrile (PAN) blended polymer precursor fibers combined with modifications to existing commercial precursor and carbon fiber manufacturing processes. This approach, which combines the fiscally conservative use of existing carbon fiber infrastructure, with the innovative development of a new low cost, renewably based lignin precursor material, provides the greatest chance of near term commercial adoption and a line of sight to low cost carbon fiber suitable for light-weighting automotive structures as well as other energy efficient applications.

The objectives of Phase 1 were to optimize the precursor technology and carbon conversion parameters to achieve a precursor fiber with maximum lignin content that converts to a carbon fiber exceeding the defined property requirements. The final objective of Phase 1 was to validate the scale up of this technology to full scale commercial production using existing spinning and carbon fiber manufacturing facilities. Phase 1 of the project was essentially completed during the current fiscal year, and objectives were achieved.

Many technical issues were encountered and much knowledge was gained during the Phase 1 commercial scale trials. This is setting a new focus and technical plan for Phase 2. New Phase 2 objectives are (1) to develop and optimize precursor polymer and spinning parameters for commercial product that eliminate technical and production problems identified in Phase 1, maximize lignin content to  $\geq 35\%$ , and achieve lowest possible precursor cost; (2) develop and optimize oxidation and carbonization parameters for lowest cost, highest performance carbon fiber; (3) identify & implement improved manufacturing concepts and equipment that will further drive down costs toward project objective of \$5.00 / pound. The final objective of Phase 2 is to validate the scale up of the improved precursor and carbon fiber manufacturing technologies to full scale commercial production using manufacturing facilities that have been modified for operational efficiency and energy reduction.

### **Accomplishments**

- Over 100 pilot scale spinning trials were completed to evaluate various blends of lignin and PAN polymers, various solution parameters, and various spinning conditions in order to define best polymer and spinning conditions to achieve precursor fibers that can convert to carbon fibers meeting project objectives. (FY 2012–2013)
- Over 150 pilot oxidation trials were completed to establish processing parameters required to fully stabilize the pilot precursor fibers so that they can survive the carbonization process. A small number (< 25) of these pilot oxidized fibers have been successfully carbonized into carbon fiber exceeding project objectives. These results defined the polymer, precursor spinning, and oxidation parameters to be used for the Phase 1 full scale commercial validation. (FY 2012–2013)
- These pilot scale precursor fibers, oxidized fibers, and carbon fibers were fully characterized for physical, chemical and mechanical properties and have also been examined using scanning electron microscopy to assess fiber morphologies. (FY 2012–2013)
- A large data base of thermal properties was generated to determine the chemical reaction behavior of Lignin / PAN precursor fibers to understand the oxidation / stabilization process required to produce carbon fiber. This data includes differential scanning calorimetry (DSC), thermal gravimetric analysis (TGA), and dynamic mechanical analysis (DMA). (FY 2012–2013)
- In preparation for the Phase 1 commercial scale validation of the Lignin / PAN precursor and carbon fiber technologies, 10,000 pounds of high purity Lignin polymer were produced, commercial scale polymer mixing equipment was developed and readied for production

operation, and a commercial scale spinning line was prepared for the commercial trial to be accomplished in FY 2013. (FY 2012)

- The Phase 1 commercial scale precursor spinning trial was completed in March, 2013, producing a total of 13 metric tons of lignin / PAN precursor with lignin contents of 25% and 35%. Precursor fiber spools with acceptable quality and sufficient spool lengths, approximately 9 metric tons, were shipped to Zoltek Hungary plant for carbon conversion. (FY 2013)
- The Phase 1 commercial scale lignin / PAN carbon fiber production was completed in June, 2013. Various problems were encountered during this first commercial scale trial, resulting in a lower than expected volume of carbon fiber produced. 1000 kilograms of the 25% lignin / PAN carbon fiber was successfully spooled. (FY 2013)
- The commercial carbon fibers produced were tested and properties exceeded project targets. Subsequently, the fibers were used to produce prepreg tapes, pultruded bars, unidirectional stitched fabrics, and carbon sheet molding compounds (SMC). The prepreg tapes were molded into panels and tested with results indicative of expected properties. The pultruded bars were also tested with similar results. Tests on composites made from fabrics and SMC will be completed in early FY 2014, completing all Phase 1 efforts. (FY 2013)

### Future Directions

- Pilot scale development of precursor polymer and spinning will continue in Phase 2 to optimize materials and process parameters for commercial product that eliminate technical and production problems identified in Phase 1, maximize lignin content to  $\geq 35\%$ , and achieve lowest possible precursor cost. In addition, development and optimization of oxidation and carbonization parameters will be continued to achieve lowest cost, highest performance carbon fiber possible.
- Commercial spinning line modifications will be made to correct production problems identified in Phase 1. In addition, equipment modifications to a commercial carbon line will be made to further reduce cost of producing the lignin based carbon fiber.
- Multiple industrial scale reactor runs will be performed to develop and validate scale up of high molecular weight PAN required. This will lead to multiple commercial scale spinning trials to fully validate polymer and precursor spinning prior to final product production validation in late 2014.
- Approximately 20,000 pounds of high purity lignin polymer will be produced in the Weyerhaeuser pilot facility. This will be used for the commercial scale spinning trials as well as the final product production validation. Final validation of commercial scale process and product will be accomplished during 4<sup>th</sup> calendar quarter of 2014. This will include development of final cost model as well as commercial product implementation plan.
- Final task of the project will be complete characterization of commercial carbon fiber produced from Lignin / PAN

precursor fiber, including putting the fiber into various intermediate product forms for composite testing. Some of these products will be distributed to various automotive original equipment manufacturers (OEMs) and Tier 1 suppliers for their evaluations and part demonstrations.

### Technology Assessment

- Target: Achieve \$5.00 / pound carbon fiber from renewable (non-petroleum based) raw materials.
- Gap: The approach of this project is to develop precursor fibers from lignin / PAN polymer blends utilizing existing wet spinning technologies and commercial equipment. Solution chemistry limits this approach to 45% Lignin (renewable) content, but this is a significant step forward toward using renewable materials for producing carbon fiber. This will also result in lower energy consumption and CO<sub>2</sub> emissions for carbon fiber production.
- Gap: Material substitution alone cannot achieve the cost target. Phase 2 of this project will focus on carbon fiber manufacturing and additional energy consumption efficiencies to further reduce costs and approach the cost target.
- Target: Achieve a low cost carbon fiber with tensile strength > 250,000 PSI and tensile modulus > 25,000,000 PSI.
- Gap: Precursor spinning behavior with Lignin / PAN polymer blends is significantly different than 100% PAN. Phase 1 of this project has demonstrated the ability to spin the Lignin containing precursor fibers, but achieving good morphologies in these fibers (no macro-voids) capable of achieving carbon fibers with target properties has proven technically challenging.
- Gap: Achieving good precursor fiber morphology with lignin contents as high as 40% has been demonstrated at pilot scale. This requires using higher than standard molecular weight PAN. Going from pilot scale reactor to industrial scale reactor for producing the needed PAN polymer has been difficult. This must be resolved during Phase 2.



### Introduction

The objectives of this project are to develop and commercially validate a low cost carbon fiber meeting the target cost of \$5.00 / lb. and target properties of strength > 250,000 pounds per square inch (psi), modulus of elasticity > 25,000,000 psi, and strain-to-failure > 1%. This project is a joint development effort of Zoltek Companies, Inc. and Weyerhaeuser Company. The bases of this development are innovative, patent pending technology for wet-spinning of Lignin / PAN blended polymer precursor fibers combined with modifications to existing commercial precursor and carbon fiber manufacturing processes. This approach, which combines the fiscally conservative use of existing carbon fiber infrastructure, with the innovative development of a new low cost, renewably based lignin precursor material, provides the

greatest chance of near term commercial adoption and a line of sight to low cost carbon fiber suitable for light-weighting automotive structures as well as other energy efficient applications.

Initial feasibility of technology was demonstrated during Phase 0 in FY 2011, prior to award of this project. The objectives of Phase 1 were to optimize the precursor technology and carbon conversion parameters to achieve a precursor fiber with maximum lignin content that converts to a carbon fiber exceeding the defined property requirements. The final objective of Phase 1 was to validate the scale up of this technology to full scale commercial production using existing spinning and carbon fiber manufacturing facilities. Phase 1 of the project was essentially completed during the current fiscal year, FY 2013, and objectives were achieved.

Many technical issues were encountered and much knowledge was gained during the Phase 1 commercial scale trials. This has set a new focus and technical plan for Phase 2. New Phase 2 objectives are (1) to develop and optimize precursor polymer and spinning parameters for commercial product that eliminate technical and production problems identified in Phase 1, maximize lignin content to > 35%, and achieve lowest possible precursor cost; (2) develop and optimize oxidation and carbonization parameters for lowest cost, highest performance carbon fiber; (3) identify and implement improved manufacturing concepts and equipment that will further drive down costs toward project objective of \$5.00 / pound. The final objective of Phase 2 is to validate the scale up of the improved precursor and carbon fiber manufacturing technologies to full scale commercial production using manufacturing facilities that have been modified for operational efficiency and energy reduction. Phase 2 was initiated in FY 2013 in parallel with completion of Phase 1 and will continue through FY 2014. The project is moving forward aggressively to accomplish the Phase 2 objectives, with full scale commercial validation of process and product scheduled for 1<sup>st</sup> quarter FY 2015.

## Approach

The approach used for this project consists of a logical sequence of series and parallel tasks focused on achieving the project objectives. These tasks develop and validate the required technologies through a classical building block approach from lab scale through pilot scale to full scale commercial demonstration. Descriptions of tasks performed during the Phase 1 of project are outlined below:

**Task 1–Cost Model Development:** An initial spreadsheet cost model was developed early in Phase 1 based on Zoltek standard costs to produce PAN precursor and resulting carbon fiber and using estimated material substitution cost savings replacing various percentages of PAN with lignin polymer. This cost model will be refined based on process improvements achieved during Phase 2.

**Task 2–Polymerization and Solution Studies:** Solution studies have been done throughout the project to assess solubility, stability, and spin-ability of lignin / PAN spinning solution dopes. Phase 1 identified that PAN polymers with

higher molecular weights would be required to achieve needed spinning viscosities for the blended polymer solutions. Significant technology development in this area will be continued in Phase 2 to resolve scale up issue identified in Phase 1.

**Task 3–Lab and Pilot Scale Spinning:** Develop and validate spinning parameters at lab scale leading to spinning of larger tow precursor fibers at pilot scale for batch and continuous oxidation studies. Approximately 100 pilot scale precursor trials have been performed throughout Phase 1 and early stages of Phase 2. This will continue in Phase 2 to define optimum parameters for commercial product validation.

**Task 4–Pilot Scale Oxidation and Carbonization Development:** Perform pilot oxidation and carbonization studies leading to selection of candidate product and process conditions for full scale development and validation. Approximately 150 pilot oxidation trials have been performed throughout Phase 1 and early stages of Phase 2. This will continue in Phase 2 to define optimum parameters for commercial product validation.

**Task 5–Analytical Studies:** Perform thermal analysis, chemical analysis, microscopy, mechanical and physical property testing at all stages of development. Hundreds of analytical tests have been performed throughout the program and this will continue through evaluations of final product validation. In addition, hundreds of scanning electron microscope images have been generated on precursor fibers, oxidized fibers, and carbon fibers. Microscopy is a primary tool for assessing morphologies and quality of the development products.

**Task 6–Large Scale Lignin Production:** In Phase 1, 10,000 pounds of high purity lignin polymer was produced at Weyerhaeuser pilot facility to be used for full commercial scale validation of Lignin / PAN precursor fiber and resulting carbon fiber. In Phase 2, approximately 20,000 pounds of lignin polymer will be produced to allow for more large scale studies prior to final commercial validation and to allow for larger quantity of carbon fiber production during the validation trial.

**Task 7–Commercial Scale Equipment:** In Phase 1, large scale Lignin / PAN mixing equipment was developed to provide the blended polymer dope mixing for commercial scale trial. Zoltek commercial spinning line 1 required some slight modifications and preparation for the commercial scale trials. A standard Zoltek commercial carbon fiber line was used for the Phase 1 carbon fiber commercial scale trial. In Phase 2, commercial spinning line 1 will require further modifications to resolve production problems identified in Phase 1. Also, based on carbon fiber process studies, modifications will be made to a commercial carbon fiber line to reduce energy consumption and increase production efficiencies of the lignin / PAN fiber to try to achieve target cost goal of the project.

**Task 8–Commercial Scale Validation:** Each Phase of the project is completed with a commercial scale validation of process and product technologies. Phase 1 commercial scale validation was completed in FY 2013, successfully producing 25% Lignin / Pan carbon fiber with properties exceeding target requirements. This Phase 1 commercial validation also

identified process and product issues that needed further development and resolution during Phase 2. The Phase 2 commercial ready process and product validation is scheduled for 1<sup>st</sup> quarter FY 2015.

## Results and Discussion

### Phase 1 Summary Results and Discussions

Phase 1 of the project has been successfully completed with the validation of commercial scale production of lignin / PAN precursor fiber and conversion of that precursor fiber into carbon fiber with properties exceeding the project targets.

The commercial scale precursor spinning was completed in March, 2013, producing a total of 13 metric tons of lignin / PAN precursor with lignin contents of 25% and 35%. Precursor fiber spools with acceptable quality and sufficient spool lengths, approximately 9 metric tons, were shipped to Zoltek Hungary plant for carbon conversion. Precursor spools ready for shipment are shown in Figure IV-9.

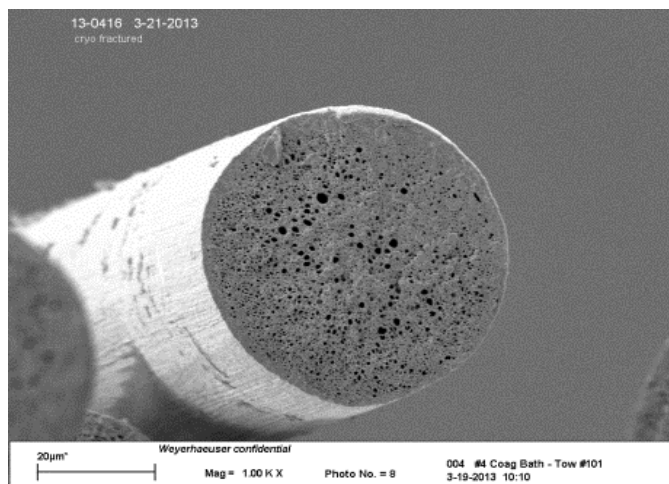
Morphology of the commercially produced lignin / PAN precursor had mixed quality. Some of the fibers, as seen in Figure IV-10, had desired morphology with uniform micro-porosity. However, much of the precursor fibers produced showed morphologies with numerous macro-voids, seen in Figure IV-11, which will likely not convert into carbon fiber.



**Figure IV-9: Lignin / PAN precursor fiber spools.**

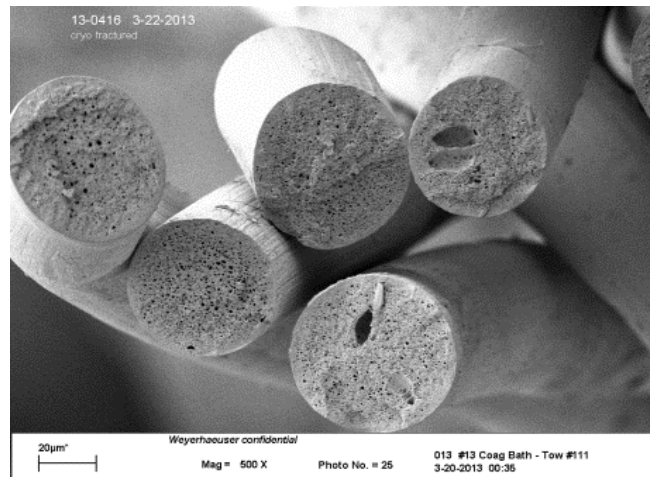
Morphology SEM images shown are taken from the coagulation bath during the spinning process. This does not represent the final fully collapsed precursor fiber. The SEM morphology analyses are made at this stage of the spinning process because morphology at this stage relates to performance in carbon fiber conversion process.

One problem encountered during the commercial scale spinning of the lignin / PAN precursor fiber was the loss of some lignin (2.5–3%) during the spinning process creating deposits in the spinning line and creating problems with continuous production. This will need to be addressed in Phase 2 of the project. This deposit problem is shown in Figure IV-12.



25% Lignin / PAN

**Figure IV-10: Commercial Precursor Fiber Sample.**



25% Lignin / PAN

Figure IV-11: Commercial Precursor Fiber Sample.



Figure IV-12: Heater coil in pre-stretching bath saturated with non-soluble residue during commercial spinning trial.



Figure IV-13: Lignin / PAN precursor color changes during oxidation.

The commercial scale lignin / PAN carbon fiber production was completed in June, 2013. Various problems were encountered during this first commercial scale trial, resulting in a lower than expected volume of carbon fiber produced. Only 1000 kilograms of the 25% lignin / PAN carbon fiber was successfully spooled. Figure IV-13 shows the lignin / PAN precursor going through color changes in the commercial oxidation oven, and Figure IV-14 and Figure IV-15 shows spooled lignin / PAN carbon fiber.

The most significant problem encountered was filament sticking that resulted in weakness and failure during carbonization. This problem was suppressed with the application of additional spin finish, but a complete evaluation of the precursor properties and behavior during oxidation and carbonization will be initiated to determine improvements required for the next commercial trial to be accomplished during Phase 2 of the project.

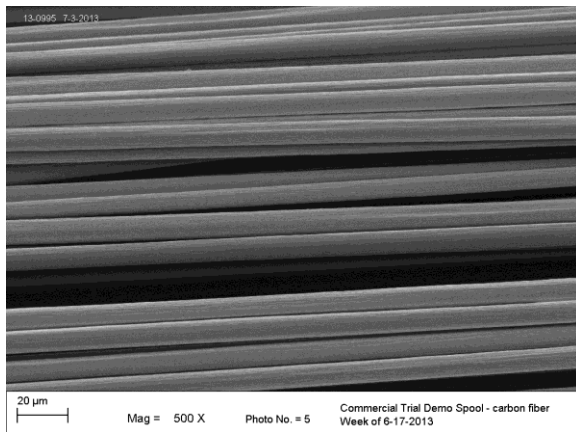


Figure IV-14: Spools of lignin / PAN carbon fiber.



**Figure IV-15: 1500 meter spools of lignin / PAN carbon fiber ready for shipment.**

The visual quality of the carbon fibers that were successfully spooled was very good. SEM pictures of the lignin / PAN fibers are shown in Figure IV-16 and Figure IV-17.



**Figure IV-16: SEM of 25% lignin / PAN carbon fiber**

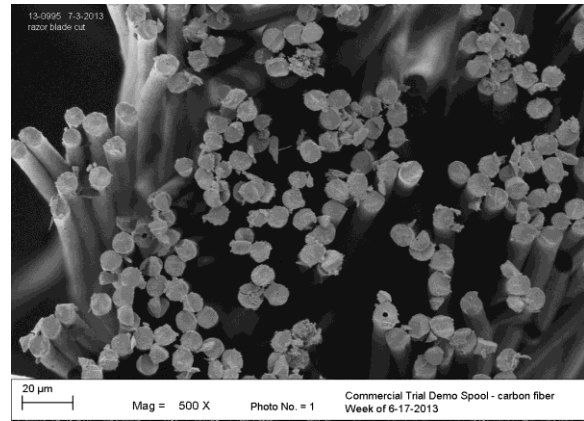


**Figure IV-17: SEM of 25% lignin / PAN carbon fiber.**

Properties of the successfully spooled lignin / PAN carbon fibers were very good, exceeding project targets. A summary of these properties is shown in Table IV-2, listing average property value and standard deviation (SD) and coefficient of variation (CV).

The carbon fibers produced were used to make epoxy prepreg tapes, which were molded into panels for mechanical properties testing. Results of the mechanical properties tests are shown in Table IV-3.

This data represents > 72% of fiber strength translation in the composite and > 90% translation of fiber modulus. Over all, these composite properties are considered good. Tensile data on unidirectional pultruded composite strips showed similar fiber tensile strength translation and modulus translation > 95%. These results are very consistent with anticipated composite properties. Additional tests on fabric composite panels and sheet molding compound composite panels will be completed early in FY 2014, completing Phase 1.

**Table IV-2: Properties of 25% lignin / PAN carbon fiber.**

| Parameter         | Tensile Strength (Ksi) | Tensile Modulus (Msi) | Strain (%) | Density (g/cc) | Tow Mass (g/m) | Moisture (%) | Resistivity ( $10^{-3} \Omega\text{-cm}$ ) | Sizing (%) |
|-------------------|------------------------|-----------------------|------------|----------------|----------------|--------------|--|------------|
| AVERAGE           | 325                    | 31.5                  | 0.98       | 1.780          | 3.99           | 0.045        | 1.61                                       | 1.30       |
| SD                | 49                     | 2.2                   | 0.09       | 0.013          | 0.10           | 0.027        | 0.09                                       | 0.10       |
| CV                | 15.0                   | 7.1                   | 9.6        | 0.7            | 2.6            | 59.6         | 5.6  | 8.0        |
| Number of Samples | 20                     | 20                    | 20         | 20             | 20             | 20           | 3  | 20         |

**Table IV-3: Mechanical Property Data from Prepreg Composite Panels**

|                                   | Panel 1 | Panel 2 |
|-----------------------------------|---------|---------|
| <b>Tensile Strength (Ksi)</b>     | 137     | -       |
| <b>Tensile Modulus (Msi)</b>      | 16.7    | -       |
| <b>Compressive Strength (Ksi)</b> | -       | 187     |
| <b>Compressive Modulus (Msi)</b>  | -       | 17.2    |
| <b>ILSS (Ksi)</b>                 |         | 11.2    |
| <b>FVF (%)</b>                    | 58      | 58      |
| <b>Void Content (%)</b>           | 2.36    | 2.08    |

**Phase 2 Summary Results and Discussions**

The results and issues defined in Phase 1 have set a new course of actions and technical objectives to be accomplished in Phase 2. Initial efforts for Phase 2 were started in FY 2013, but most of Phase 2 will be performed in FY 2014–FY 2015.

**Phase 2 Objectives**

- Develop and optimize precursor polymer and spinning parameters for commercial product
  - Eliminate problems identified in Phase 1
  - Maximize lignin content;  $\geq 35\%$
  - Achieve lowest possible cost
- Develop and optimize oxidation and carbonization parameters for lowest cost, highest performance carbon fiber
- Identify and implement improved manufacturing concepts and equipment that will further drive down costs toward project objective of \$5.00 / pound
- Validate full commercial scale, production ready processes and products
- Define and initiate commercialization implementation plan

**Technology Development**

Initial Phase 2 efforts in technology development have been focused on optimizing the PAN chemistry to provide higher molecular weight and leading to precursor fibers with higher lignin content and excellent morphologies. SEM image of 35% lignin precursor with good morphology using the new PAN polymer is shown in Figure IV-18.

Other technology approaches are being pursued, including changes to spinning parameters, use of alternative solvents, and the development of air gap spinning. None of these studies are far enough along to report at this time.

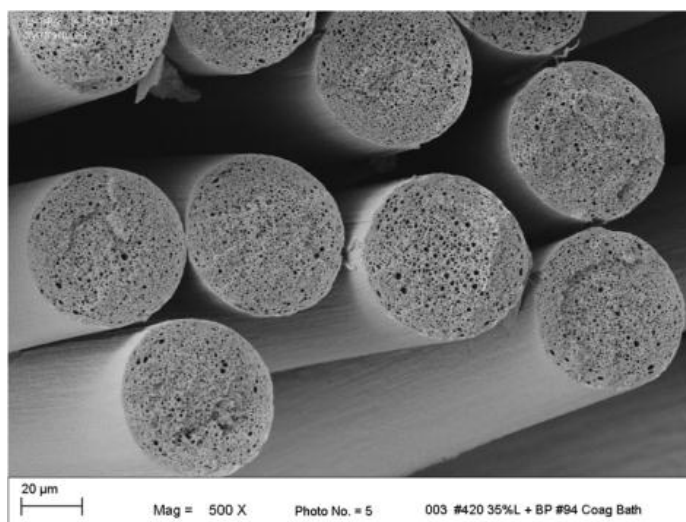
**Operational Efficiencies Concepts Development**

Increasing process throughput represents the greatest potential for reducing unit conversion costs. Improved performance from the current oxidation ovens is required to enable this objective. A computational fluid dynamics (CFD) analysis of the oven air flow, initiated early in FY 2013, has identified the required oven modifications.

The proposed modifications will (1) increase the overall recirculation air flow and (2) distribute the air so as to achieve improved vertical and horizontal air flow uniformity within the heated chamber and across the oxidizing tows. The result should be an increase in the effective heated length of the oven, improved energy efficiency of the oxidation process, and reduced potential for destructive exotherms.

**Modifications to Commercial Equipment**

Detailed designs are being developed for the modifications to the oxidation ovens for the commercial carbon fiber line planned for use in the lignin / PAN commercial product. Current schedule is to approve these plans and begin the equipment modifications early in FY 2014. Detailed schedule and budget for these modifications are also under development.



35% Lignin / PAN precursor fiber from BP # 94

**Figure IV-18: Precursor Fiber Sample # 420.**

Preliminary designs have been developed to modify commercial spinning line 1 to be able to filter the lignin that is leached and capture it for reuse. The equipment modifications will include recirculation and filtering as well as putting heat exchangers on the outside of the hot-stretching bath rather than inside the bath. Detailed designs are being developed for these commercial equipment modifications, and current plans are to approve these designs and begin equipment modifications early in FY 2014.

### Technology Transfer Path

The Phase 1 commercial scale precursor spinning trial was completed in March, 2013, producing a total of 13 metric tons of lignin / PAN precursor with lignin contents of 25% and 35%. Commercial scale conversion of this precursor fiber to carbon fiber was completed in June, 2013. Various problems were encountered during this first commercial scale trial, and the knowledge gained is driving the technical plan for Phase 2 development and process and product commercialization.

The commercial carbon fibers produced were tested, and properties exceeded project targets. Subsequently, the fibers were used to produce prepreg tapes, pultruded bars, unidirectional stitched fabrics, and carbon sheet molding compounds (SMC). The prepreg tapes were molded into panels and tested, indicating expected properties. The pultruded bars were also tested with similar results. Tests on composites made from fabrics and SMC will be completed in early FY 2014, finishing all Phase 1 efforts.

A similar validation will be done at the end of Phase 2 of the project demonstrating the performance of the fully commercialized Lignin / PAN precursor and carbon fiber technology. The culmination of Phase 2 will validate the fully commercially robust process and product for lignin / PAN based carbon fiber. After successful validation of the Phase 2 commercial product, this innovative low cost, high performance Lignin / PAN carbon fiber product will be available for sale to the worldwide automotive industry, as well as for use in other markets such as wind energy.

### Conclusions

During FY 2013, Phase 1 of the project was successfully completed. In March, 2013 the commercial scale precursor spinning trial was completed, demonstrating the ability to produce Lignin / PAN precursor on commercial spinning equipment in high volume manufacturing process. This precursor was subsequently converted to carbon fiber on a commercial carbon fiber line in June, 2013. The carbon fibers produced exceeded the structural properties targets of the project. The Lignin / PAN carbon fibers were used to produce prepreg tapes that were molded into composite panels for testing. Composite properties demonstrated expected results. Pultruded plates were also produced giving similar composite properties. Testing of composite panels made from fabrics and sheet molding compounds will be completed early in FY 2014.

There were a number of issues identified in the Phase 1 commercial scale trials that have set the direction for Phase 2 of the project. Phase 2 of the project was started in FY 2013 in parallel with completion of Phase 1. The objectives of Phase 2 are to optimize the polymer and spinning parameters as well as the carbon fiber conversion process and production equipment and validate commercial ready Lignin / PAN precursor and carbon fiber process and products.

A high level of interest has been expressed by automotive OEM and Tier 1 and Tier 2 manufacturers. Completion of Phase 1 in FY 2013 and successful development and validation of commercial manufacturing technologies in Phase 2 during FY 2014–2015 will allow immediate and wide scale production implementation for automotive and other applications.

### Presentations/Publications

#### Presentations:

1. A one slide status of this project was presented at the SAE 2012 World Congress & Exhibition on April 24, 2012.
2. Project status presentation was given at the DOE Vehicle Technologies Program Annual Merit Review on May 16, 2012.
3. A presentation on this project was presented at the International Lignin Biochemicals Conference in Toronto, Canada on June 21, 2012.
4. Project status presentation was given at the Society of Plastics Engineering / Advanced Composites Conference and Exhibition, SPE / ACCE on September 13, 2012.
5. Project status presentation was given at the JEC Americas Composites Show and Conference on November 8, 2012.
6. Project status presentation was given at the DOE Vehicle Technologies Program Annual Merit Review on May 15, 2013.
7. Two slides on project status were included in presentation given at the Plastic Modification for Automotive and Durable Goods Conference, Chicago, IL September 4, 2013.

### Patent

Patent application # 12828054, **Lignin/polyacrylonitrile-containing dopes, fibers, and methods of making same**, filed June, 2010, published on January 5, 2012. This patent covers base technology developed at Weyerhaeuser prior to contract.

## IV.4. Predictive Engineering Tools for Injection-Molded Long-Carbon-Fiber Thermoplastic Composites—Pacific Northwest National Laboratory

### **Ba Nghiep Nguyen (Principal Investigator)**

Pacific Northwest National Laboratory  
P.O. Box 999  
Richland, WA 99352  
Phone: (509) 375-3634  
E-mail: [ba.nguyen@pnnl.gov](mailto:ba.nguyen@pnnl.gov)

### **Kevin L Simmons (Principal Investigator)**

Pacific Northwest National Laboratory  
P.O. Box 999  
Richland, WA 99352  
Phone: (509) 375-3651  
E-mail: [kevin.simmons@pnnl.gov](mailto:kevin.simmons@pnnl.gov)

### **Aaron Yocum, Contract Manager**

National Energy Technology Laboratory  
3610 Collins Ferry Road  
Morgantown, WV 26507  
Phone: (304) 285-4852  
E-mail: [Aaron.Yocum@netl.doe.gov](mailto:Aaron.Yocum@netl.doe.gov)

### **Carol Schutte, Technology Area Development Manager**

U.S. Department of Energy  
1000 Independence Avenue, S.W.  
Washington, DC 20585  
Phone: (202) 287-5371  
E-mail: [carol.schutte@ee.doe.gov](mailto:carol.schutte@ee.doe.gov)

Contractor: Pacific Northwest National Laboratory (PNNL)

Contract No.: DE-AC05-00OR22725 & DE-AC06-76RLO1830

### **Abstract/Executive Summary**

This project proposes to integrate, optimize, and validate the fiber-orientation and length-distribution models previously developed and implemented in the Autodesk Simulation Moldflow Insight (ASMI) package for injection-molded, long-carbon-fiber thermoplastic composites. In a previous U.S. Department of Energy (DOE)-funded project titled: “*Engineering Property Prediction Tools for Tailored Polymer Composite Structures*,” the Pacific Northwest National Laboratory (PNNL) partnered with the University of Illinois and Autodesk, Inc. That team developed a unique assembly of computational algorithms that provided a state-of-the-art process and constitutive models to enhance the capabilities of

commercial software packages to predict fiber orientation and length distributions (Phelps and Tucker 2008, Phelps 2009), as well as subsequent mechanical properties of injection-molded, long-fiber thermoplastic composites (Nguyen et al., 2008, Nguyen et al., 2009, Nguyen and Kunc 2010). These predictive capabilities were validated using data generated at Oak Ridge National Laboratory on generally two-dimensional (2D) structures of edge-gated plaques or center-gated disks injection-molded from long-glass-fiber/polypropylene or long-glass-fiber/polyamide 6,6 pellets. The current project aims to render those previously developed models more robust and efficient to achieve weight savings and cost reductions in automotive parts design. This will be achieved by optimizing the developed models, improving and integrating their implementations in ASMI (Jin and Wang 2011, Autodesk 2013), and validating them for a complex three-dimensional (3D) long-carbon fiber thermoplastic automotive part. Local fiber orientation and length distributions at the key regions on the part will be measured for the model validation based on the 15 percent accuracy criterion. The project outcome will be the ASMI package enhanced with computational capabilities to accurately predict fiber orientation and length distributions in automotive parts designed with long-carbon fiber thermoplastics.

### **Accomplishments**

In FY 2013, the team was in the planning phase, working to complete the legal and contract documents required for establishing subcontracts and a cooperative research and development agreement (CRADA) with Autodesk, Inc. (Autodesk), Toyota Motor Engineering and Manufacturing North America (Toyota), and Magna Exterior and Interiors Corporation (Magna).

- Established non-disclosure agreements (NDAs) with all project partners
- Established statements of work (SOWs) for all subcontracts
- Established legal documents for the CRADA, including the CRADA SOW
- Established a Gantt chart for the project

### **Future Directions**

- The internal project-team kickoff meeting with the project participants was scheduled for November 13, 2013.
- Phase I will begin with the injection moldings of long-carbon-fiber/polypropylene (PP) and long-carbon-fiber/polyamide 6,6 (PA6,6) plaques by PlastiComp, Inc.

- Once the CRADA is in place, Autodesk, Inc. will deliver a research version of ASMI to PNNL for process modeling of PlastiComp plaques
- Samples from molded plaques will be shipped to Purdue University for fiber orientation and length measurements
- PNNL will perform process modeling of PlastiComp plaques using ASMI to predict fiber orientation and length distribution at selected locations

### Technology Assessment

- Target: Predicted fiber orientation and length distributions at selected locations on PlastiComp plaques will be compared to the corresponding measured data based on the 15 percent accuracy criterion
- Gap: Current process models for injection molding simulations were only validated for fiber orientation and length predictions for long-glass-fiber thermoplastic structures and not for complex 3D part shapes
- Target: Achieve well-dispersed carbon fibers with the mean residual length equal to or higher than 2 mm in long-carbon-fiber thermoplastic plaques using conventional injection molding or direct injection molding ("Direct" long-fiber thermoplastic or D-LFT) processes. The 2-mm length target is to ensure large fiber aspect ratios for enhanced mechanical properties
- Gap: Conventional injection molding processes degrade fiber length significantly. In many long-fiber thermoplastic structures, the mean residual fiber length is less than 2 mm.



### Introduction

The objective of this project is to advance the predictive engineering (PE) tool to accurately predict fiber orientation and length distributions in injection-molded long-carbon fiber thermoplastic composites for optimum design of automotive structures using these materials to meet weight- and cost-reduction requirements defined in DE-FOA-0000648 (Area of Interest 1). The project period is divided in two phases with a 12-month duration for each phase.

#### Phase 1 Objective and Scope:

The first step toward achieving the overall project objective is to integrate, optimize, and validate the fiber-orientation and length-distribution models previously developed and implemented in the ASMI package for injection-molded, long-carbon-fiber/PP and long-carbon-fiber/PA6,6 plaques. The Phase 1 objective is the achievement of the advanced ASMI package as a PE tool to accurately predict fiber orientation and length distributions in these plaques within 15 percent of experimental results.

#### Phase 2 Objective and Scope:

Following completion of Phase 1, the team will have the PE tool needed to achieve the overall project objective. Therefore, Phase 2 objective is to validate the advanced ASMI

package achieved in Phase 1 for a complex three-dimensional (3D) Toyota automotive part (Figure IV-19), injection molded from long-carbon-fiber/PP and long-carbon-fiber/PA6,6 to predict flow-induced fiber orientation and length distributions. Predicted fiber orientation and length distributions for key locations on the complex part will be compared with the experimental results within 15 percent of the experimental results to validate the PE tool. At the end of Phase 2, the ASMI tool will be interfaced with structural analyses of the complex part to perform weight and cost savings for the part.

### Approach

This project will build on the predictive capabilities developed under the previous PE efforts and will integrate, optimize, and validate injection-molded, long-carbon-fiber thermoplastic composite PE tools. Past PE work at PNNL identified a series of areas that will be investigated, strengthened, and rendered more efficient to model the injection molding of long-carbon fiber thermoplastic composites to accurately predict flow-induced fiber orientation and length distributions, allowing more accurate mechanical properties predictions. The latter will guide the weight reduction effort to make cost-effective and optimum design parts. The areas relevant to the present work are the following:

- 1) Improve the ASMI solver for 3D modeling to more accurately capture flow velocity gradients in complex 3D parts for more accurate fiber orientation and length predictions.
- 2) Implement the improved fiber length attrition model in ASMI (termed the reduced-order fiber length model). This model should enable fiber length modeling a practical engineering tool for mold and part designers.
- 3) Perform process modeling of injection-molded, long-carbon-fiber composite structures, including plaques and Toyota's complex 3D automotive structure using the improved research versions of ASMI, which incorporates an improved 3D solver and a reduced-order fiber length model. Both mid-plane/dual domain and 3D ASMI models of plaques and of the complex 3D structure will be built for process simulations. Figure IV-19 shows the Toyota complex 3D part which has representative features of Toyota proprietary automotive components. Figure IV-20 shows the potential applications of the proprietary components in automotive structures.
- 4) Validate the ASMI fiber orientation and length predictions for plaques and for the complex 3D structures at selected locations within 15 percent of the experimental results.
- 5) Once the predictions are validated within 15 percent, the improved ASMI package will serve as a tool for complex 3D structure design to meet the weight- and cost-reduction targets. Weight savings are first estimated by comparing the weight of the long-carbon-fiber/PA6,6 structure with that of the equivalent steel structure. In addition, this task will require the prediction of the local elastic stiffness of the complex 3D structure made of long-carbon-fiber/PA6,6 to be compared with the local

stiffness of the same complex 3D structure made of long-glass-fiber/PA6,6 to evaluate the weight savings achieved and to substantiate the long-term benefits of long-carbon-fiber thermoplastics.

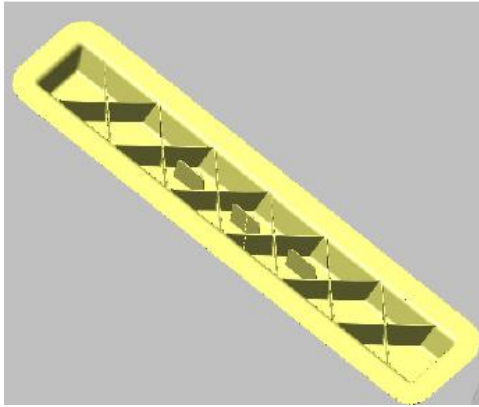


Figure IV-19: Toyota’s complex 3D automotive structure that will be injection-molded from long-carbon-fiber/PP and long-carbon-fiber/PA6,6 compounds.

### Technology Transfer Path

The participation of industrial partners (i.e., Autodesk, PlastiComp, Toyota, and Magna) ensures that the PE tool and research results will be transferred to the American automotive and plastics industries.

### Conclusion

During FY 2013, the team was in the planning phase for the project, awaiting finalization of the CRADA with Autodesk, Toyota, and Magna. This CRADA must be in place so that the project can start technically. All legal and contractual requirements needed for all the subcontracts and the CRADA have been completed. The project is expected to technically launch in November 2013, once DOE approves the CRADA.

### Presentations/Publications/Patents

None.

### Results and Discussion

There is nothing to report on the technical work in FY 2013 as the project was awaiting the finalization of the CRADA with Autodesk, Toyota, and Magna.

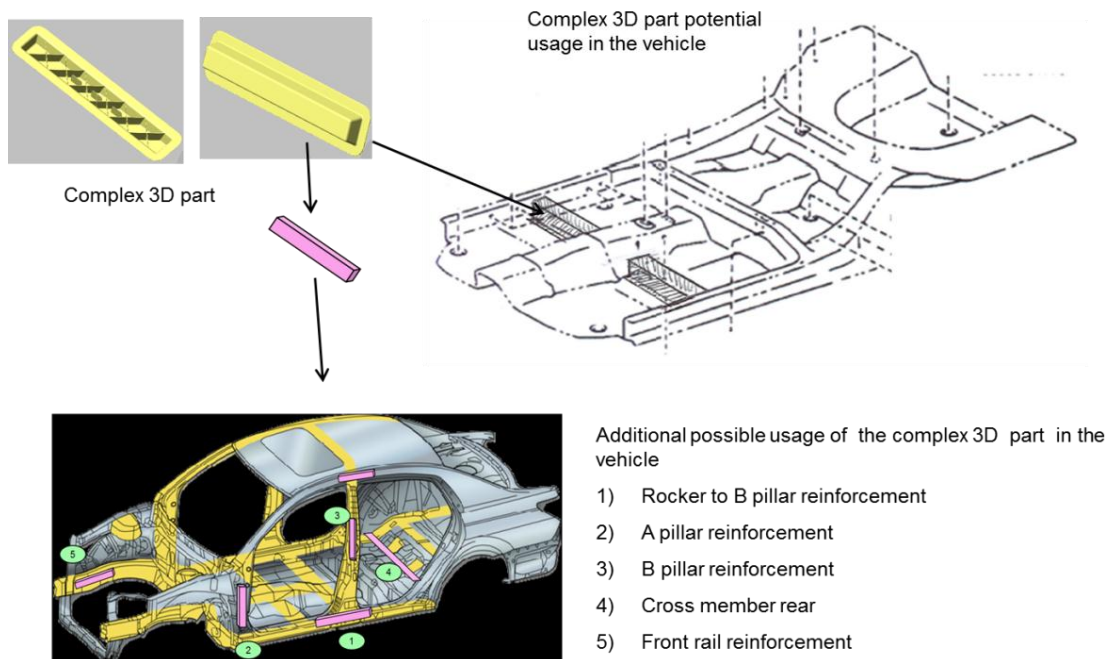


Figure IV-20: Potential applications of components with features represented by the complex part (Figure IV-19) in an automotive body structure.

## References

1. Phelps, J.H. and C.L. Tucker III. An Anisotropic Rotary Diffusion Model for Fiber Orientation in Short- and Long-Fiber Thermoplastics. *J. Non-Newt. Fluid Mech.*, 2009, **156**(3), pp165-176.
2. Phelps, J.H. Processing-Microstructural Models for Short- and Long-Fiber Thermoplastic Composites. Ph.D. Thesis, University of Illinois at Urbana-Champaign, 2009, Urbana, IL.
3. Nguyen, B.N., S.K. Bapanapalli, J.D. Holbery, M.T. Smith, V. Kunc, B.J. Frame, J.H. Phelps, and C.L. Tucker III. 2008. "Fiber Length and Orientation Distributions in Long-Fiber Injection-Molded Thermoplastics—Part I: Modeling of Microstructure and Elastic Properties," *J. Compos. Mater.*, 2008, pp 1003-1029.
4. Nguyen, B.N., S.K. Bapanapalli, V. Kunc, J.H. Phelps, and C.L. Tucker III. Prediction of the Elastic-Plastic Stress/Strain Response for Injection-Molded Long-Fiber Thermoplastics. *J. Compos. Mater.*, 2009, **43**, pp 217-246
5. Nguyen, B.N. and V. Kunc. An Elastic-plastic Damage Model for Long-Fiber Thermoplastics," *Intl J. Dam. Mech.*, 2010, **19**(6):691-725.
6. Jin, X. and J. Wang. Fiber Breakage Calculation for Injection Molded Long Fiber Composites. In *Proceedings of ANTEC 2011*, 2011, Society of Plastics Engineers.
7. Autodesk, Inc. "Validation of Long Fiber Breakage and Composite Property Calculation." Validation Report, 2013.

## IV.5. Low Cost Carbon Fiber Composites for Lightweight Vehicle Parts— Materials Innovation Technologies LLC

### Mark Mauhar (Principle Investigator)

Chief Operating Officer  
Materials Innovation Technologies, LLC  
320 Rutledge Road  
Fletcher, NC 28732  
Phone: (828) 651-9646  
E-mail: [mmauhar@mitrcf.com](mailto:mmauhar@mitrcf.com)

### Carol Schutte, Technology Area Development Manager

U.S. Department of Energy  
1000 Independence Avenue, S.W.  
Washington, DC 20585  
Phone: (202) 287-5371  
E-mail: [carol.schutte@ee.doe.gov](mailto:carol.schutte@ee.doe.gov)

Contractor: Materials Innovation Technologies, LLC  
Contract No.: DOE-EE0004539

### Executive Summary

The goal of the project is to commercialize one or more of the candidate parts being developed during this Phase III program utilizing a Materials Innovation Technologies, LLC (MIT-LLC) patented 3-DEP<sup>®</sup> technology and related extensions of this technology. Successful commercialization will create high paying manufacturing jobs to produce these parts and will result in lightweight passenger vehicles with greater efficiencies. The main technical focus of the project is investigating new material systems utilizing reclaimed carbon fiber (CF), making component parts from those material systems, and demonstrating the commercialization potential of these new component parts.

To achieve the overall goal of this project, the 3-DEP<sup>®</sup> technology was demonstrated to: (1) develop rapid processing technologies for carbon fiber reinforced polymers (CFRPs) for use in primary and secondary structures of passenger vehicles; and (2) show that the concept(s) can be cost-effectively incorporated into the high-rate, high volume manufacturing of commercial passenger vehicles. At the completion of this Phase III SBIR, MIT-LLC will have laid the foundation for successful entry into the transportation industry as a supplier to Tier 1 automotive suppliers and an electric bus original equipment manufacturer (OEM). A key element of this cost-effective approach is the use of recycled CF. MIT-LLC is a leader in the emerging industry of CF recycling.

To make the Phase III project as relevant to commercialization as possible, MIT-LLC is partnered with five companies: Proterra, LLC, an electric bus and truck OEM; Innovative Composite Solutions LLC (ICS), a small business

with extensive experience in processing thermoplastic matrix composites and with particular experience in making composite parts for transit buses; International Automotive Components (IAC), a Tier 1 automotive supplier to all major automotive OEMs; Molded Fiber Glass Companies (MFG), a Tier 1 supplier to General Motors (GM) and others; and GM/Corvette, an automotive OEM.

Specifically, the technical objectives of our Phase III project were to:

1. Develop a process for producing roll goods (in flat sheet form) consisting of reclaimed CF, either alone or in conjunction with other materials including thermoplastics (Co-DEP<sup>™</sup>).
2. Develop and select the appropriate material(s) and manufacturing process(es) for each of the three (3) candidate parts for commercialization.
3. Develop process capabilities to include material handling, preform and roll goods formation, preform and roll goods drying, improving preform and roll goods uniformity and final part molding of the resulting preforms and roll goods material(s).
4. Build process cost models for each material/process route.
5. Complete the required Production Part Approval Process (PPAP) for each respective automotive OEM or Tier 1 Supplier.
6. Document all Standard Operating Procedures (SOP's) and Work Instructions (WI).
7. Produce commercial quantities of component parts at the projected run rates and cost standards while meeting our customers' expectations for product quality and delivery.

### Accomplishments

- Completed initial roll goods (up to 200 feet in length) trials on a pilot-scale 26 inch width machine using reclaimed CF alone along with Co-DEP<sup>™</sup> consisting of CF in combination with various thermoplastic fibers such as polypropylene (PP), polyethylene (PE), polyethylene terephthalate (PET), polyamide (PA) and polyphylene sulfide (PPS). (FY 2011)
- Designed, constructed, installed and successfully commissioned a 50-inch wide production roll goods line capable of producing areal basis weights ranging from 50 grams per square meter (gsm) up to 1,200 gsm in a wide range of material systems that incorporate reclaimed (and/or virgin) CF. (FY 2012)
- Produced roll goods totaling over 4 miles in overall length. (FY 2013)
- Successfully demonstrated thermoforming of our Co-DEP<sup>™</sup> roll goods materials in CF/PPS (for an aircraft

- seatback demonstration part and for aircraft interior panels), CF/PET (for a Proterra Bus rocker panel) and CF/Natural Fiber (NF)/PP (for a door bolster for the Ford Escape). (FY2011)
- Compression molded several dozen prototype parts made of CF/PET roll goods for evaluation as a rocker panel on the Proterra electric bus resulting in a 25% weight reduction over the incumbent vacuum thermoformed acrylonitrile butadiene styrene (ABS) sheet material with improved stiffness and cold impact performance. (FY 2011)
- Optimized a Co-DEP™ roll goods material for use on automotive “soft trim” applications such as door bolsters, package trays or headliners resulting in a 40% weight reduction over incumbent materials. (FY 2013)
- Produced several hundred upper door trim pieces using CF/NF/PP compositions on production tooling at the Tier 1 supplier’s plant while completing a final, “run-at-rate” trial to validate our reclaimed CF roll goods as “production ready”. (FY 2013)
- Designed, constructed, installed and successfully commissioned a large-scale production 3-DEP® machine capable of producing three-dimensional engineered preforms up to six feet by six feet in size in a one minute cycle time. (FY 2012)
- Optimized resin, CF volume fraction, molded part thickness, and molding conditions to allow successful molding of a reclaimed CF preform using a thermoset resin system (vinyl ester). (FY 2012)
- Successfully produced two commercially-viable semi-structural parts (upper plenum and lower plenum) with a 35% weight savings over the same parts made using fiberglass. (FY 2013)
- Produced several dozens of reclaimed CF preforms for the lower plenum for qualification testing at GM/Corvette through their Tier 1 supplier, MFG. (FY 2013)
- Completed Computational Fluid Dynamics (CFD) modeling work on large 3-DEP® machine while incorporating the preform forming tool for the lower plenum preform. (FY 2013)
- Completed process cost models for each material/process route.

### Future Directions

- Continue to investigate a variety of pre-consolidation techniques for both roll goods and 3-DEP® applications.
- Continue to explore heated and cooled tooling for compression molding applications.
- Commercialize automotive interior Co-DEP™ material system at a major OEM in 2014.
- Commercialize 3-DEP® lower plenum on C7 Corvette in 2014 and 2015.
- Develop cored composites applications using our reclaimed CF roll goods such as floor boards or load floors.
- Conduct additional CFD modeling work to further our understanding of our patented 3-DEP® process.

### Technology Assessment.

- Target: Commercialize one or more of the candidate parts being developed during this Phase III program utilizing our company’s patented 3-DEP® technology and related extensions of this technology such as Co-DEP™ and roll goods forming processes utilizing wet-laid forming of discontinuous fibers.
- Gap: Despite demonstrated weight savings of 25%–30% for an electric bus lower body panel, the molding techniques required to use our Co-DEP™ roll goods made of CF/PET made the tooling cost prohibitive for a low volume application such as electric buses.
- Gap: Despite demonstrated weight reductions of 40% for an automotive interior “soft trim” application, most OEM’s are reluctant to be the first company to introduce reclaimed CF into a higher volume automotive vehicle. Future sales are expected to be easier to achieve once this aversion to being “the first adopter” is overcome.
- Gap: Despite demonstrated weight savings of one pound per part (35%) for a molded lower plenum versus the incumbent fiberglass-reinforced part, the OEM involved will be moving cautiously and will start with introduction on a smaller volume vehicle variant in order to more fully validate the design change before going across the board on the entire vehicle platform.



### Introduction

MIT-LLC has developed a variety of processes for reclaiming CF from all portions of the industrial waste stream and for converting those reclaimed CFs into wet-laid non-woven preforms and roll goods for re-use as CF reinforced composite parts.

MIT-LLC proposes to use its Three Dimensional Engineered Preform (3-DEP®) chopped fiber composite technology to address the need for cost-effective, high volume, lighter weight components for automobiles and other vehicles. 3-DEP® was initially developed under DOE Small Business Innovation Research (SBIR) Phase I and II projects. At the end of the Phase II project, the 3-DEP® technology could make thermoset composite parts, at pilot scale, that met the stringent requirements of an automotive OEM.

The new Corporate Average Fuel Economy (CAFE) standards for automotive and light truck fuel economy are a major driver for the future of automotive design. By 2016, the CAFE standard for automobiles will rise from the current 27.5 mpg to 37.8 mpg. CFRP composites can help manufacturers meet the requirements for weight reduction and they have the structural integrity required for many secondary structural applications.

Today, however, CF reinforced components are only used in high-end vehicles because the cost is too high and the production rates are too low for general vehicle production. There is a need for (1) manufacturing approaches that incorporate cost-effective CFs and cost-effective processing

methods; and, (2) composite part molding approaches that can be incorporated into high-rate, high volume manufacturing systems for commercial passenger vehicles.

This SBIR Phase III project was to demonstrate that the 3-DEP® technology can be used to: (1) develop rapid processing technologies for CFRPs for use in primary and secondary structures of passenger vehicles; and (2) show that the concept(s) can be cost-effectively incorporated into the high-rate, high volume manufacturing of commercial passenger vehicles. Further, MIT-LLC will have laid the foundation for its successful entry into the transportation industry as a supplier to Tier 1 automotive supplier at the conclusion of this project. A key element of this cost-effective approach is the use of recycled CF.

The base technology for this project is the 3-DEP® process which makes near-net-shaped, chopped fiber preforms for thermoset composite molding. A logical extension of the 3-DEP® process was also used in this project: Co-DEP™. Co-DEP™ employs a blend of structural fibers (e.g., carbon or glass) and thermoplastic polymeric fibers (e.g., polypropylene or nylon) to make a near-net-shape preform that can be compression molded to form a thermoplastic composite. The use of these two, complimentary, technologies brings the best composite solution to bear in almost all situations.

A significant output from the Phase II SBIR project was the demonstration that the 3-DEP® process can utilize reclaimed CF. This finding opened the door for high volume parts production with mass savings and developed a new market for a material that is currently being landfilled. Considerable time and resources have been invested by MIT-LLC to develop reclamation processes for all forms of CF scrap. Currently active reclamation campaigns are in place with the aerospace, automotive and recreational industries, fiber manufacturers, and fiber processing companies. MIT-

LLC commissioned a new, 50,000 square foot, state of the art fiber reclamation facility in 2010. The objective of this facility is to re-engineer and re-purpose CFs into high value and advanced performance components. The new operating division MIT-RCF (Re-engineered CF), with current capacity to reclaim up to 5 million pounds of CF annually, was capitalized by investments of over \$14 M.

**Background in materials substitution for automotive applications**

Choosing to substitute a composite part (or system of parts) for a metal part (or parts), or one composite form for another one depends on the following among other things:

1. Physical and chemical properties (strength, stiffness, corrosion resistance, density)
2. Formability of the competing materials, and
3. The potential for part consolidation (and the resulting reduction in the cost of assembly operations) offered by using composites

Most analyses of this type start with a "direct substitution" of one material for another based on the desire to improve the performance of a particular component relative to one or more physical or chemical performance criteria. Table IV-4 lists the strength, specific strength, stiffness and specific stiffness of four composite materials and three metallic alloys. In general, the resistance to aqueous corrosion of polymer-matrix composites is far superior to that of metallic alloys.

Based on these properties alone, one might choose to build a structure out of carbon fiber or glass fiber-reinforced polymer instead of one of the alloys due to the lower density of the composite and having similar mechanical properties and better corrosion resistance.

**Table IV-4. Comparison of Cured Composite Properties with those of Metals.**

| Material              | Density<br>(g/cm3) | Tensile Strength |        | Specific Strength<br>(MPa / g/cm3) | Tensile Modulus |        | Specific Modulus<br>(GPa / g/cm3) |
|-----------------------|--------------------|------------------|--------|------------------------------------|-----------------|--------|-----------------------------------|
|                       |                    | (MPa)            | (kpsi) |                                    | (GPa)           | (Mpsi) |                                   |
| E-glass               | 2.1                | 1103             | 160    | 530                                | 44.8            | 6.5    | 22                                |
| S-glass               | 2.0                | 1931             | 280    | 970                                | 51.7            | 7.5    | 26                                |
| Kevlar-49             | 1.4                | 1448             | 210    | 1049                               | 75.8            | 11.0   | 55                                |
| Carbon                | 1.6                | 1724             | 250    | 1112                               | 138             | 20.0   | 89                                |
| Aluminum<br>(7075-T6) | 2.8                | 572              | 83     | 206                                | 68.9            | 10.0   | 25                                |
| Titanium<br>(6Al-4V)  | 4.4                | 1103             | 160    | 249                                | 114             | 16.5   | 26                                |
| Steel<br>(4130)       | 8.0                | 1379             | 200    | 172                                | 200             | 29.0   | 25                                |

*Additional issues to be considered beyond properties—* However, for most substitutions of composites for metallic materials one not only needs to compare nominal properties,

but also the cost of producing the part as a function of production volume. Figure IV-21 shows that the cost of producing a body-in-white (BIW) automobile body is

dependent not only on the material of construction (steel vs. carbon fiber composite), but also on the production volume (low volumes favor the composite largely because of higher tooling and assembly costs for steel) and simultaneously on the cost of the carbon fiber. Therefore, a simple "which is a more cost effective solution" has to be considered within the context of what is being manufactured and how much of it is being made.

*Formability and Cost Considerations*—In addition to the issue of production volumes, one also needs to include the issue of formability. Consider the following situation encountered by one of our customers. This customer manufactures parts in aluminum, titanium, and thermoplastic carbon fiber composites. Once the decision is made to use composite instead of metal (based on mechanical properties, corrosion resistance, and part weight), the choice of which composite route to take is largely based on formability and cost.

As an example, consider a letter we received from this customer. The letter emphasizes the fact that MIT-LLC

thermoplastic materials (LFT and Co-DEP™) provide the customer with paths to manufacturing a wide range of composite parts that were not previously open to them. Those new composite manufacturing paths are based on the following factors:

1. The MIT-LLC LFT thermoplastic raw materials provide the customer with the ability to form parts having geometries that are not within the scope or range of unidirectional thermoplastic tape (which is the standard raw material used by the customer). Many of the parts listed in the communication from the customer contain compound curves, sharp corners, and deep draws which cannot be formed using unidirectional prepreg tape.
2. The cost associated with MIT-LLC's LFT materials made from recycled carbon fiber makes it attractive for the customer to commercialize parts that were previously too expensive for them to even quote.

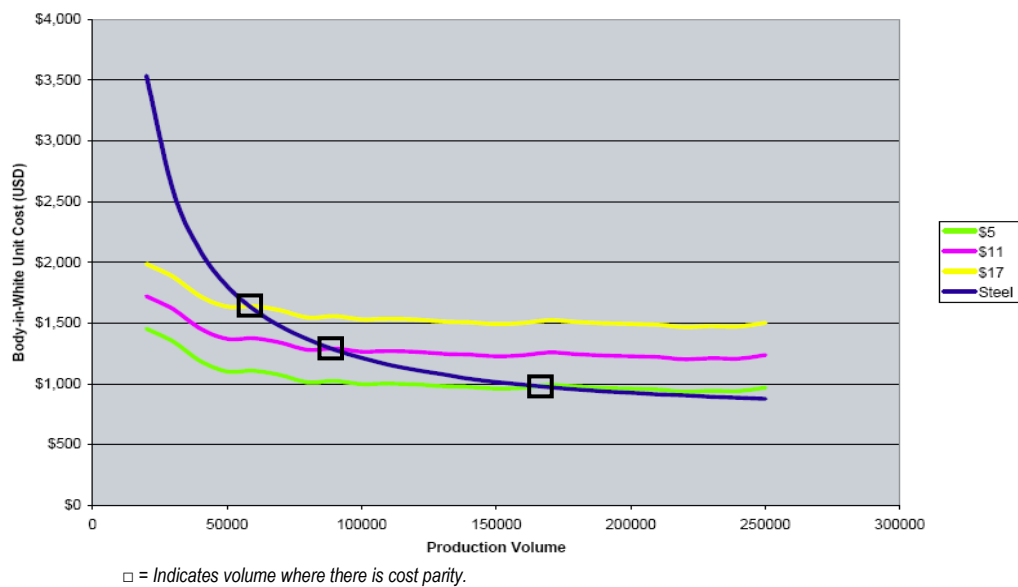


**Figure IV-21: The body-in-white (BIW) unit cost of an automobile body is dependent on the materials of construction (steel vs. carbon fiber composite), the cost of carbon fiber, and the production volume.**

Reference: ERH Fuchs, FR Field, R Roth, RE Kirchain, "Strategic materials selection in the automobile body: Economic opportunities for polymer composite design," *Composites Sci Tech*, **68**, 1989–2002 (2008).

## Approach

The approach used for this project consisted of selecting three candidate parts for potential commercialization—two for automobiles and one for an electric bus— and then partnering with a strong team of companies including the two current Tier 1 suppliers of two of the three candidate parts. The target parts are a rocker panel for a transit bus, door trim support for the Ford Fusion/Mercury Milan (or similar volume vehicle), and a lower plenum for the Corvette. The potential weight savings for these parts in CF composite compared with current materials are in the range of 30 to 50%, depending on the improvement in mechanical properties that can be achieved with CF, the volume saved by using thinner carbon composite materials, and the type of materials currently in use.

The work necessary to achieve commercialization in one or more of the candidate parts was broken up into the following Tasks:

**Task 1—Roll Goods Development:** Fabricate roll goods materials necessary for completing Task 2 and Task 3.

**Task 2—Rocker Panel:** Perform resin selection, material property testing, successfully mold rocker panels and establish business case for conversion to reclaimed CF Co-DEP™ roll goods.

**Task 3—Door Trim:** Select reinforcing fiber(s) and resin(s), successfully mold door trim parts, complete all material verification and validation testing and demonstrate successful run-at-rate production speeds to pave the way for commercialization of the part in a medium- to high-volume vehicle platform.

**Task 4—Large 3-DEP® Machine:** Design, build and install and successfully complete start-up and shakedown of a production-scale 3-DEP® suitable for producing a part up to 6 feet x 6 feet.

**Task 5—Lower Plenum:** Design and build lower plenum preform tool, optimize the resin and fiber selection, complete CFD modeling work, successfully mold parts for Tier 1 and OEM acceptance trials and demonstrate suitability for commercialization.

## Results and Discussion

### Task 1—Roll Goods Development:

Producing a continuous flat sheet of nonwoven material using a vacuum-based, water-borne deposition process similar to that used in our patented 3-DEP® process is a logical extension of our current technology. This new process offers an opportunity to produce a large volume of material at a low manufacturing cost for less complex final part geometries. The objective for this task was to develop and demonstrate the production of continuous flat sheets of roll goods materials using both reclaimed CF by itself as well as reclaimed CF in conjunction with other material (including various thermoplastics).

As highlighted in the FY 2011 annual report, this task was completed three months ahead of schedule. The early roll goods development work was deemed so successful that MIT-LLC decided to design and build a 50-inch wide production roll goods line shown in Figure IV-22, which was completed early in FY 2012 using Rotoformer technology. This production line was successfully commissioned and has been selling some limited commercial quantities of roll goods material using reclaimed CF shown in Figure IV-23 as one of the principle components. Areal basis weights of between 50 gsm and 1,200 gsm have been produced to date and higher areal basis weights are possible. Roll goods sheet uniformity (both across the width and from end to end of the roll) has been improved over the course of this funded development grant with a Coefficient of Variation of less than 4% currently being achieved. Both 100% reclaimed CF as well as various blends of both reclaimed CF and thermoplastic fiber (Co-DEP™) roll goods have been successfully produced and sold during the last two years of this grant.



Figure IV-22: Fifty-inch wide production roll goods line.



Figure IV-23: Typical roll of nonwoven roll goods material made from reclaimed CF.

### Task 2—Rocker Panel:

The second task involved replacing an existing exterior lower protective bumper piece (“rocker panel”) on Proterra’s electric and hybrid urban commuter buses shown in Figure IV-24. The existing part is vacuum-thermoformed out of 5 mm thick ABS thermoplastic sheets. This forming method has the advantage of using very low cost tooling for the final part molding step. Unreinforced ABS, while quite heavy, is easily vacuum thermoformed. This particular family of parts (there are several different sizes of rocker panels to protect the entire lower perimeter of the bus) are quite heavy and offer the opportunity for significant weight reduction. This is very important to Proterra since the range of a fully-charged electric bus relates directly to the overall mass of the bus.

An optimized composite structure consisting of 20% reclaimed CF together with 80% PET fibers comingled into a nonwoven roll goods material was successfully molded into lower “rocker panels” for the Proterra bus during FY 2011/FY 2012.

The task was a resounding technical success in that a much lighter weight rocker panel (up to a 50% weight reduction versus the incumbent material system) was successfully constructed using reclaimed CF in conjunction with the thermoplastic resin, PET and is shown in Figure IV-25. However, due to the very low production volumes associated with the Proterra bus program, these particular parts are not commercially feasible at this time. The cost of the compression molding tools necessary to form each of the twelve different rocker panel parts on the Proterra bus cannot be amortized across a large enough volume of parts to justify their expense.

The only technical disappointment encountered during Task 2 was the inability to find a way to vacuum thermoform consolidated sheets of our Co-DEP™ roll goods. Successful vacuum thermoforming of reclaimed CF roll goods would have led directly to commercial success on the Proterra bus rocker panels. The stiffness of the reclaimed CF together with the random orientation of the fibers as they are formed in wet-laid processes results in a “lofting” or fluffing up of the pre-consolidated roll goods during heating and prior to vacuum thermoforming. This “lofting” prevents an acceptable vacuum from being pulled against the material and leads to poor part formation.

However, the significant weight reduction achieved during the completion of this task through the use of reclaimed CF may justify the use of this (or similar) Co-DEP™ roll goods materials in similar applications for higher volume bus, over-the-road truck, local delivery van, and/or light rail applications.



Figure IV-24: Proterra electric bus for urban transit market.

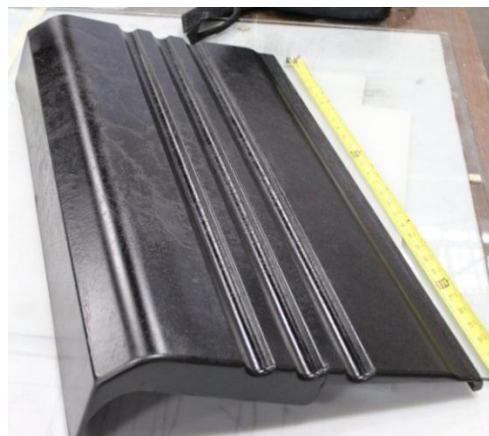


Figure IV-25: Molded rocker panel made from reclaimed CF and PET fiber roll goods.

### Task 3—Door Trim:

Typical interior door trim parts made by North American vehicle manufacturers are constructed of injection-molded ABS in a areal basis weight of between 1,600 gsm and 1,800 gsm. North American OEM’s are beginning to follow the lead of their European counterparts by investigating compression molding of natural fiber reinforced PP in an effort to help achieve the vehicle weight reduction necessary to meet aggressive upcoming CAFE fuel economy standards. The natural fiber-based composites have the additional advantage (at least in public perception) of being a more environmentally friendly and sustainable material option.

The goal of Task 3 was to offer another alternative to direct natural fiber thermoplastics by introducing small amounts of reclaimed CF (5–20 weight %) to current materials systems in an effort to achieve significant reductions in molded part thickness and final part weight without a commensurate increase in final part manufacturing cost while maintaining minimum strength requirement. The goal was to develop a novel family of material systems that incorporate reclaimed CF while still remaining compatible with the current compression molding equipment, tooling and standard operating procedures in use today.

IAC is considering several different vehicle platforms for the introduction of our Co-DEP™ materials in roll goods form for interior door trim pieces. These include the Ford Escape/Mazda Tribute, the GM full size truck family and several new launch vehicle programs by other OEM's. All of these vehicle platforms are high volume (over 500,000 door trim pieces per year).

Fiber/resin selection was completed iteratively using several types of Co-DEP™ materials in a series of molding trials at IAC's Sheboygan, WI molding plant as well as at IAC's molding development and validation center in Troy, MI. Materials testing and evaluation were completed concurrently with a very broad range of different material systems.

To summarize our results to date in the words of our Tier 1 customer/partner (International Automotive Components) to the vehicle OEM (Ford Motor Company): "We have demonstrated a lighter weight, cost neutral and greener composite construction for automotive interiors. We believe this game-changing technology is implementation ready for volume production. The Door Bolster for the current model year Ford Escape may offer a great opportunity to implement this innovative material."

In addition to material property testing, "component product testing" or "full construction testing" of actual door trim parts was also completed FY 2012. In this validation process, actual complete finished part constructions were molded using production and development tooling for the Ford Escape complete with the surface "cover stock" that typically covers the door trim piece and is seen by the purchaser of the finished vehicle (see Figure IV-26 and Figure IV-27). A full round of component product testing was completed including limited side impact testing, sag under high temperature and high humidity conditions as well as odor testing in order to fully validate the material system for use by the vehicle OEM.

FY 2013 efforts consisted of further optimization on the material system in order to further improve (lower) water absorption and reduce subsequent odor. In addition, further validation work was completed in order to ensure full compatibility between our reclaimed CF roll goods materials and the existing semi-automated production equipment at IAC's manufacturing facility currently producing the Ford Escape door trim piece. Finally, detailed cost models are currently being developed and these will be presented to vehicle OEM's to facilitate a final "go/no go" materials substitution decision in early 2014. Our expectation is that our roll goods using reclaimed CF will be on a production vehicle platform in the first half of 2014.

The impact of going to production is very significant. In addition to the expected 10–16 new jobs created in Lake City, SC, the mass reduction on just the Ford Escape/Mazda Tribute family of vehicles would equate to over 300,000 lbs. per year. Each subsequent model year at the same expected 500,000 vehicle unit volume will have an additional mass savings of 300,000 lbs. each year. The potential weight savings across the entire vehicle (other interior parts) and across all vehicle platforms is tremendous.



**Figure IV-26: Molded upper door trim for Ford Escape front door made from reclaimed CF/natural fiber/polypropylene roll goods.**



**Figure IV-27: Molded upper door trim with cover stock.**

#### **Task 4—Large 3-DEP® Machine:**

Our large 3-DEP® machine shown in Figure IV-28 was successfully designed, built, installed and commissioned in FY 2012. Start-up and shakedown testing was completed in the first half of FY 2013.

Most of the tool base, the tool holder and the 3-DEP™ forming tools are made using our reclaimed CF roll goods vacuum-infused with epoxy resin. Making these components out of virgin woven CF would have been prohibitively expensive and making them out of fiberglass would not have been feasible due to the increase in weight for these components.

Baseline Computational Fluid Dynamics (CFD) modeling work was completed in FY 2013. Figure IV-29 is an example of the CFE modeling showing fluid flow fields in the large 3-DEP® forming tank.



Figure IV-28: Large 3-DEP<sup>®</sup> machine.

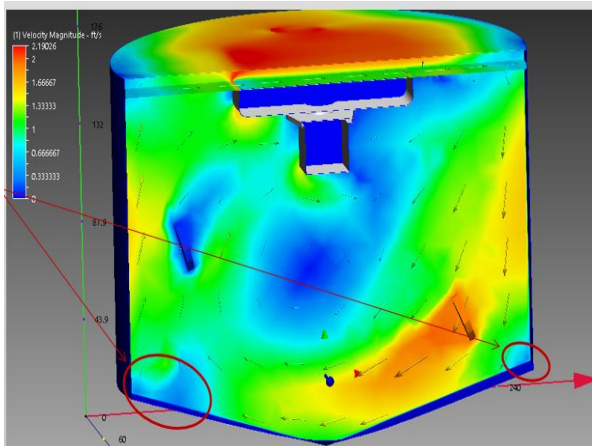


Figure IV-29: CFD model showing fluid flow fields in large 3-DEP<sup>®</sup> forming tank.

#### Task 5—Lower Plenum:

Several defined project milestones have been met including: (1) the confirmation that vinyl ester resin is highly compatible with MIT-LLC reclaimed CF; (2) the formulation and development of an optimized, VE LCM (vinyl ester–liquid compression molding) paste formulation for compression molding with both 3-DEP<sup>®</sup> reclaimed CF preforms and reclaimed CF roll goods mat; and, (3) the development of a set of molding parameters for our attempts to successfully mold Corvette Upper Plenum and Lower Plenum parts (see Figure IV-30) at a significant weight and thickness reduction over current fiberglass SMC production parts. These achievements were made within the constraints of current preform/LCM production molding and processing “best practices” requirements.

As a result of these achievements, The first technical objective of this Phase III project to “develop rapid processing technologies for CF reinforced polymers that can be used in primary and secondary structures of passenger cars” has been attained and completed.

From the data generated thus far, the overall objective of reducing vehicle mass by incorporating reclaimed CF in our 3-DEP<sup>®</sup> preforms for use in molded parts for automotive applications is achievable. In the case of the Corvette Upper Plenum and Lower Plenum parts, the physical properties of the incumbent compression molded fiberglass/vinyl ester resin SMC are easily surpassed by the 3-DEP<sup>®</sup> preform molded parts even at significantly lower fiber loadings. By taking advantage of the increased stiffness of the reclaimed CF and molding the parts thinner than today’s parts, part mass will be reduced commensurately.

FY 2013 efforts have been focused on successfully producing acceptable Lower Plenum preforms made from reclaimed CF for subsequent liquid compression molding into finished parts at MFG with the ultimate goal being commercialization of this opportunity. MFG and Corvette both remain committed to achieving the goal of having reclaimed CF incorporated onto the new C7 Corvette as a means of reducing overall vehicle mass and our results to date have only enhanced their commitment to achieving this goal.

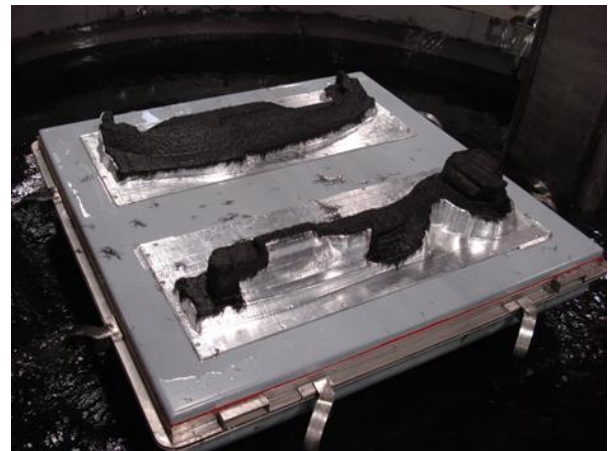


Figure IV-30: Upper and lower plenum preforms made of reclaimed CF after 40-second forming cycle.

#### Technology Transfer Path

MIT-LLC has been successfully selling small quantities of roll goods and 3-DEP<sup>®</sup> preforms containing reclaimed CF into the automotive industry during FY 2013. Sales of our reclaimed CF roll goods have been made to Tier 1 molders and directly to OEM’s. Successful commercialization on one or more high volume vehicles is expected during the first half of 2014; however, many of the automotive OEM’s are reluctant to be “first adopters” of a new material or technology.

For MIT-LLC, the technology transfer path is quite clear—sell the reclaimed CF products we have developed and are offering to the market today at attractive prices and in the required volumes. One difficulty facing our company is that we do not currently have molding capability in-house and are therefore relying on Tier 1 molders to help bring our products to market (and they generally have less aggressive time schedules than we do).

## Conclusion

Through the work funded by this grant, MIT-LLC has successfully demonstrated that the use of reclaimed CF in both roll goods and in our patented 3-DEP® process can lead to very significant weight savings (25%–50%) in a range of molded parts suitable for the transportation industry. This project designed, constructed, installed and successfully commissioned a large-scale production 3-DEP® machine capable of producing three-dimensional engineered preforms up to six feet by six feet in size in a one minute cycle time. The business case justification for conversion to a reclaimed CF reinforced composite part must be done on a case-by-case basis, accounting for the incumbent part material and processing costs, vehicle production volumes, part complexity and the value of weight savings on each particular vehicle platform. However, in many cases, conversion to a part that utilizes reclaimed CF can be economically justified.

## Presentations/Publications/Patents

1. Mauhar, M. Low Cost Carbon Fiber Composites for Lightweight Vehicle Parts. Presented at the 2013 DOE Vehicle Technologies Office Annual Merit Review, May 13–17, 2013, Arlington, VA.
2. Mauhar, M.; Janney, M.; Vaidya, U.; Johnson, R. Thermoplastic Composites for Transportation Applications from Recycled Carbon Fiber. *Proceedings SAMPE 2012*, May 21-24, 2013, Baltimore, MD.
3. Mauhar, M. Low Cost Carbon Fiber Composites for Lightweight Vehicle Parts. Presented at the 2012 DOE Vehicle Technologies Office Annual Merit Review, May 14–18, 2012, Washington, D.C.
4. Mauhar, M. Low Cost Carbon Fiber Composites for Lightweight Vehicle Parts. Presented at the 2011 DOE Vehicle Technologies Office Annual Merit Review, May 9–13, 2011, Crystal City, VA.

## IV.6. Validation of Carbon Fiber Composite Crash Models Via Automotive Crash Testing—USAMP, LLC

### **Omar Faruque, PhD. (Principal Investigator)**

Passive Safety Department  
Ford Motor Company Research and Innovation  
Center  
PO Box 2053  
Dearborn, MI 48121  
Phone: (313) 322-1044  
E-mail: [ofaruque@ford.com](mailto:ofaruque@ford.com)

### **Libby Berger, Ph.D. (Principal Investigator)**

Chemical Sciences & Material Systems Lab  
General Motors R&D Center  
MC 480-106-710  
30500 Mound Road  
Warren, MI 48090  
Phone: (248) 930-5018  
E-mail: [libby.berger@gm.com](mailto:libby.berger@gm.com)

### **Aaron Yocum, Project Manager**

National Energy Technology Laboratory  
PO Box 880  
3610 Collins Ferry Road  
Morgantown WV 26507-0880  
Phone: (304) 285-4852  
E-mail: [aaron.yocum@netl.doe.gov](mailto:aaron.yocum@netl.doe.gov)

### **Carol Schutte, Ph.D., Technology Area Development Manager**

U.S. Department of Energy  
1000 Independence Avenue, S.W.  
Washington, DC 20585  
Phone: (202) 586-1022  
E-mail: [carol.schutte@ee.doe.gov](mailto:carol.schutte@ee.doe.gov)

Contractor: United States Automotive Materials  
Partnership, LLC  
Contract No.: DE-EE0005661

### **Abstract/Executive Summary**

The objective of this project is to validate physics-based crash models for simulating primary load carrying automotive structures made of production-feasible carbon fiber composites for crash energy management. This will include the two Automotive Composites Consortium/USAMP-developed meso-scale models from the University of Michigan (UM)<sup>1,2,3</sup> and Northwestern University (NWU)<sup>4,5</sup>, as well as existing composite crash material models in four major

commercial crash codes (LS-DYNA<sup>6-10</sup>, RADIOSS<sup>11-13</sup>, PAM-CRASH<sup>14,15</sup>, ABAQUS<sup>8, 16-18</sup>.) The models will be used to predict quasi-static and dynamic crash behavior of vehicle front end sub-system made of carbon fiber composites. The project goal is to validate the models for simulating crash of a lightweight carbon-fiber composite front bumper and crush can (FBCC) system. In order to do this, we are determining the crash behavior of a reference steel FBCC, designing, building, and crash testing a composite FBCC predicted to have equivalent crash behavior, and comparing the predictions with the physical crash tests. The crash performance of the composite FBCC should be equivalent to the steel FBCC under various crash-loading modes. The successful validation of these crash models will allow the use of lightweight carbon-fiber composites in automotive structures for significant mass savings.

For the past several years, USAMP has collaborated extensively on research with academia, materials suppliers and engineering design software vendors in order to accelerate the development of advanced computational tools for predicting the crash response of composites in vehicle structures. Two material models in particular, UM's representative unit cell (RUC) meso-scale model and NWU's RUC micro-plane model, are complete and comprehensive enough to be used for crash simulation of composite structures. In addition, crash simulation software developers have also implemented many advanced material models to characterize highly nonlinear crash response of composite structures in the four major commercial crash codes— i.e., LS-DYNA, RADIOSS, ABAQUS and PAM-CRASH. The material models in these commercial crash codes also require validation for automotive carbon fiber composites.

During Year 1, the project team, comprised of USAMP automotive original equipment manufacturer (OEM) technical staff, as well as multiple academic and engineering suppliers, was organized into four functional sub-teams. Work began by sub-awardees and vendors in accordance with the Statement of Project Objectives. In order to determine the targets that a representative carbon-fiber composite FBCC will need to meet, the team selected and procured a baseline production steel FBCC. Crash testing with six load cases and corresponding predictive modeling with steel FBCCs began in order to develop and correlate experimentally-determined crash test data with the predictive data from commercial models. At the end of FY 2013, nearly two-thirds of the planned 40 steel FBCC crash tests were completed and the crash data analyzed. Work also began on preliminary carbon-fiber composite crush can design concepts and computer-aided engineering (CAE) for innovative FBCC designs. The team determined material property data requirements and critical design criteria in order to support the extensive

composite material modeling required for the crash predictions. Plaque samples of candidate thermoset composite (polymer and reinforcement) material samples were procured from an automotive composite Tier 1 supplier for initial property testing and for non-destructive evaluation (NDE).

### Accomplishments

- Developed a list of minimum material property data required to support crash model validation for a high-volume composite FBCC that will meet crash criteria.
- Released contracts and technically engaged all key vendors.
- Successfully molded and distributed the first round trials of thermoset carbon fiber plaques for initial testing of mechanical properties and screening using three NDE methods. These included compression molding unidirectional pre-impregnated (prepreg) and twill weave fabric prepreg in several orientations as well as chopped carbon fiber sheet molding compounds (SMC).
- Initiated design of a composite FBCC by analysis of a variety of crush can concepts, and initial selection of bumper/crush can structures.
- Test fixtures were fabricated for all high-speed test modes. Load cells were purchased, calibrated and incorporated into as many test modes as physically possible.
- Baseline steel FBCC tests were conducted in the following modes: Full-frontal impact simulating the New Car Assessment Program (NCAP), 40% rigid frontal offset simulating the Insurance Institute for Highway Safety (IIHS) frontal deformable barrier impact, center 10 inch diameter rigid pole frontal impact, and 30 degree frontal rigid angular impact. Observations from various data streams showed good correlation and repeatability within each test mode. Data analysis is complete for the full-frontal while analyses are underway for the other three impact modes.

### Future Directions

- Complete all six load cases for the baseline steel FBCC crash testing and analyze results for validity and reproducibility. Compare with predictive modeling results using the selected commercial codes. From the steel crash data analysis, the performance targets for composite FBCC will be established.
- Obtain detailed material property test data as inputs for the various modeling strategies and computational codes and select composite material and process system.
- Using the findings from baseline steel crash tests and CAE with down-selected composite FBCC concepts, complete the design of a composite FBCC such that it is predicted to perform at least as well as the steel FBCC in the six crash modes.
- Procure tooling and fabricate thermoset carbon fiber composite FBCCs for crash testing and correlation with targets determined from the crash of the steel FBCCs;

identify opportunities for thermoplastic composite materials and lower-cost carbon fiber reinforcements.

### Technology Assessment

- Target: Assess the validity of material models for crash performance of carbon-fiber composites. Design, fabricate and crash-test a composite FBCC to provide equivalent crash performance to a steel FBCC, while demonstrating a 33% (or better) weight savings over the baseline steel structure.
- Gap: Unvalidated meso-scale material models developed by the UM and NWU through Automotive Composites Consortium (ACC)/USAMP support for crash-critical carbon fiber composite structures.
- Gap: Unknown failure modes and composite material properties for micro- and meso-scale material models.
- Gap: Unproven NDE methods for detection of crash damage.
- Gap: Error band for steel FBCC not established, defaulting to “industry best practice” of  $\pm 10\%$ .



### Introduction

Several new material models for predicting the behavior of carbon-fiber composites were developed by academic collaborators over the last decade under the oversight of USAMP, sponsored by the DOE. These included micro-scale and meso-scale models of braided carbon fabric composite materials, as well as random fiber composites<sup>19-22</sup> Of these, two models in particular—UM’s RUC-based meso-scale material model<sup>1-3</sup> and NWU’s micro-plane RUC model<sup>4,5</sup>—are promising enough to be used for crash simulation of composite structures. In addition, several engineering design houses and commercial crash software developers have also implemented many advanced constitutive models to characterize highly nonlinear crash response of composite structures in the four major finite element-based commercial crash codes—i.e., LS-DYNA, RADIOSS, ABAQUS and PAM-CRASH. To enable ongoing lightweighting initiatives incorporating advanced materials such as carbon fiber composites, these models require validation and are the subject of the USAMP VMM Project.

### Approach

Our approach to validating these models consists of selecting a production steel FBCC, utilizing commercial crash codes to predict its crash performance, crashing it and comparing the crash predictions to the crash results to determine the appropriate targets. These targets will be utilized to design the carbon fiber composite FBCC. A carbon fiber composite FBCC will then be fabricated, crash behavior predicted (using commercial codes and the UM and NWU material models), experimentally crash tested, and the predictions will be compared to the crash results.

The USAMP Project is organized into seven main tasks to be executed over the 48-month period with results and discussion at the end of Year 1 discussed below—the status of active tasks is indicated:

**Task 1:** Project Administration/Management—ongoing

**Task 2:** Experimental/Analytical Characterization of Crash Performance of a Baseline Steel FBCC—in progress

**Task 3:** Design and Crash Performance Predictions of a Composite FBCC—in progress

**Task 4:** Manufacture/Assembly of the Composite FBCC—begins in Year 2.

**Task 5:** Crash Test Composite FBCC—begins in Year 4.

**Task 6:** Non-Destructive Evaluation (NDE) of Composite Structure—in progress

**Task 7:** Compare Experimental Results with Analytical Predictions—begins in Year 4.

## Results and Discussion

### Task 1: Project Administration/Management

Members from the USAMP companies organized a vertically integrated research and management team. The team includes leading academic researchers proficient in modeling, automotive design/engineering service suppliers, composite manufacturers, and crash test vendors. The National Center for Manufacturing Sciences, an experienced research and technology management organization, coordinates the technical and management tasks for this project.

### Task 2: Experimental/Analytical Characterization of Crash Performance of a Baseline Steel FBCC

Crash tests for four of the required six crash load cases for the baseline steel FBCC were completed by Wayne State University (WSU). In parallel, prediction runs were conducted using a selected commercial code to estimate the energy absorption of the steel crush cans.

Steel FBCCs were run in each of the four high-speed impact modes (full-frontal, 40% frontal offset, frontal center pole and 30° frontal angular), and the velocities were tracked. Within each test mode, the velocity of impact had a low coefficient of variation (CoV). Table IV-5 demonstrates the consistency of measured velocity results for the sled. These tests are used as a baseline to determine the accuracy of the commercial crash software models (PAM-CRASH, LS-DYNA, ABAQUS and RADIOSS) for predicting each crash mode.

For all test modes, a sled-on-sled setup was employed (Figure IV-31). The following measurements were recorded to use in comparing crash model predictions: accelerations using accelerometers, force using the accelerometers and load cells, overall system displacement using high-speed video analysis and accelerometers, and crush can deformation using potentiometers and high-speed video analysis. Data acquisition systems (DAS) were used on the sled and

impacting load wall to collect outputs from the aforementioned transducers. Due to the test setup, potentiometers were only used in the full-frontal impact test mode, and load cells could only be used for the full-frontal and front center pole impact tests.

**Table IV-5: Impact velocities for the 40% frontal offset test mode.**

| Bumper #          | Velocity (mph) |
|-------------------|----------------|
| 15                | 26.5           |
| 16                | 26.17          |
| 17                | 26.73          |
| 18                | 27.18          |
| 19                | 26.5           |
| 20                | 26.17          |
| <b>Average</b>    | <b>26.54</b>   |
| <b>Stand Dev.</b> | <b>0.38</b>    |
| <b>CoV</b>        | <b>1.43</b>    |

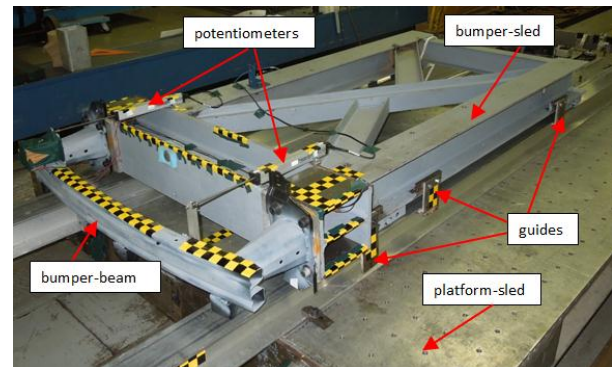


**Figure IV-31: Set-up of sled-on-sled system used for all high-speed test modes.**

Redundant measures were used in case of DAS failure or for any unforeseen test failure as well as to compare data recorded vs. data calculated, such as sled system displacement vs. double integration of acceleration from accelerometers. A pressure trigger located on the struck structure was used to trigger high-speed cameras located above and to the sides of the struck structure. The term “struck structure” is used to describe either a load wall or FBCC as each crash test mode had a different setup. Test setups are illustrated in Figure IV-32 and Figure IV-33. Additionally, thermal images of the crush cans were captured with the use of an infrared (IR) camera.

Post processing analysis for the full-frontal impact test is complete, and discrete and calculated measurements demonstrate good correlation.

- Mass-acceleration compared with force measured from load cells (Figure IV-34)
- High-speed film analysis system displacement compared with double-integrated acceleration (Figure IV-35)

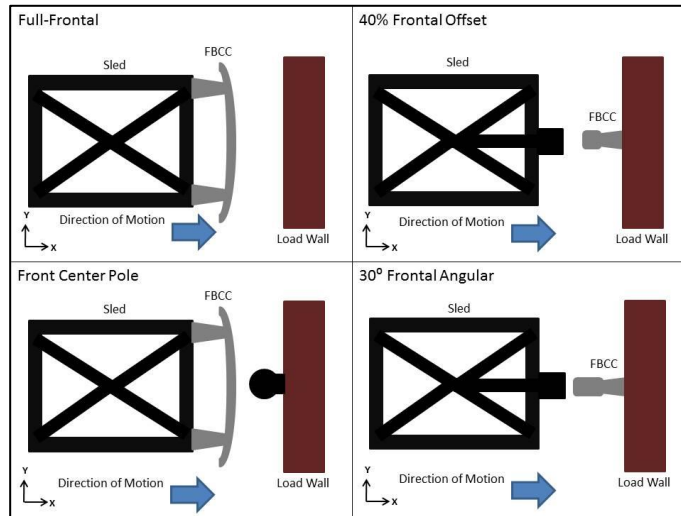


Figure IV-32: Schematic of top-view of four completed high-speed tests.

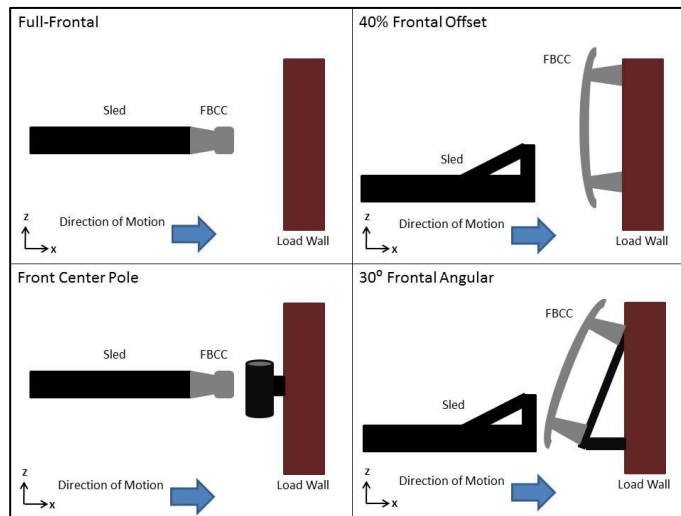


Figure IV-33: Schematic of side view of four completed high-speed tests.

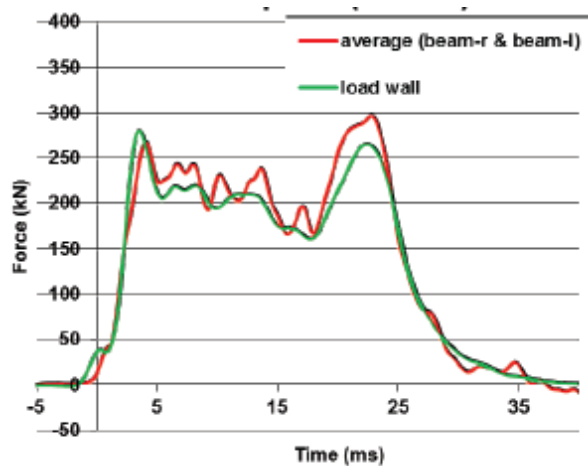


Figure IV-34: Impact force vs. time comparing discrete measurements from load cells with calculated force using Newton's Second Law from mass and acceleration.

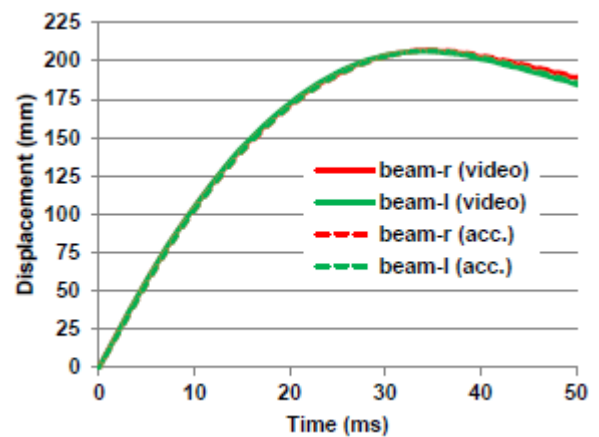


Figure IV-35: Graph of sled system displacement vs. time, comparing film analysis with double integrated acceleration from accelerometers for a full-frontal impact test.

Analysis is complete for the full-frontal impact tests, and preliminary analyses are underway for the remaining three high-speed impact modes for the baseline steel FBCCs. At present, 10% variability is an acceptable and common correlation between predictive models and actual physical tests. However, a new ISO standard is currently being proposed called “Objective Rating Metrics for Dynamic Systems”. This standard looks at time histories of measured and predictive responses and assigns/qualifies a value normalized to 1.0 to evaluate and quantify how good the predictive model is compared to the physical tests. The leadership team and the crash team are evaluating this standard in place of the 10% variability. Preliminary evaluation of the full-frontal impact tests shows good comparison with preliminary predictive models.

**Task 3 Design and Crash Performance Predictions of a Composite FBCC**

**Task 3.1 Material and Process Selection:**

In the second quarter of 2013, the Material and Process Selection (MPS) Team did the first thermoset carbon fiber plaque molding trial, compression molding unidirectional prepreg and 2x2 twill weave fabric prepreg in several orientations, as well as chopped carbon fiber SMC. Plaques were all molded successfully, and distributed for initial testing. Additionally, the team continued its efforts to find a thermoplastic molding source, as the initial selected source

was found unacceptable during the negotiation and sub-contract discussions.

The results of the initial tensile testing of the plaques for the woven and SMC are shown below in Figure IV-36. These are results consistent with literature values for these materials. Note that the 0/90 layups of the woven are quite anisotropic for the 45° angle, as would be expected. Also notice that the SMC, which is nominally a quasi-isotropic material, shows considerable anisotropy between the 0°, the 90°, and 45° directions when all of the nominally-random plies are laid in one direction. This indicates a high degree of orientation in the compounded material. When the plies are crossed during molding, the results are much more isotropic.

Extensive USAMP collaborations with NWU, UM, and Engineered Solutions, Inc. (ESI)—the selected design/CAE source—have resulted in a consolidated list of critical material properties which will give all of the required data for the commercial codes and the university codes. This includes tensile, compression, shear, and flexural testing, as well as cyclic tension, interlaminar fracture toughness [ $G_{1c}$  (Double Cantilever Beam) and  $G_{2c}$  a(End Notch Flex)] at 3 thicknesses, notched tension at 3 sizes, and micrography analysis of the geometry of the woven samples<sup>23-29</sup>. The MPS team is presently finalizing the scope of material test requirements of all these properties as inputs to the crash models being used to develop the composite FBCC design.

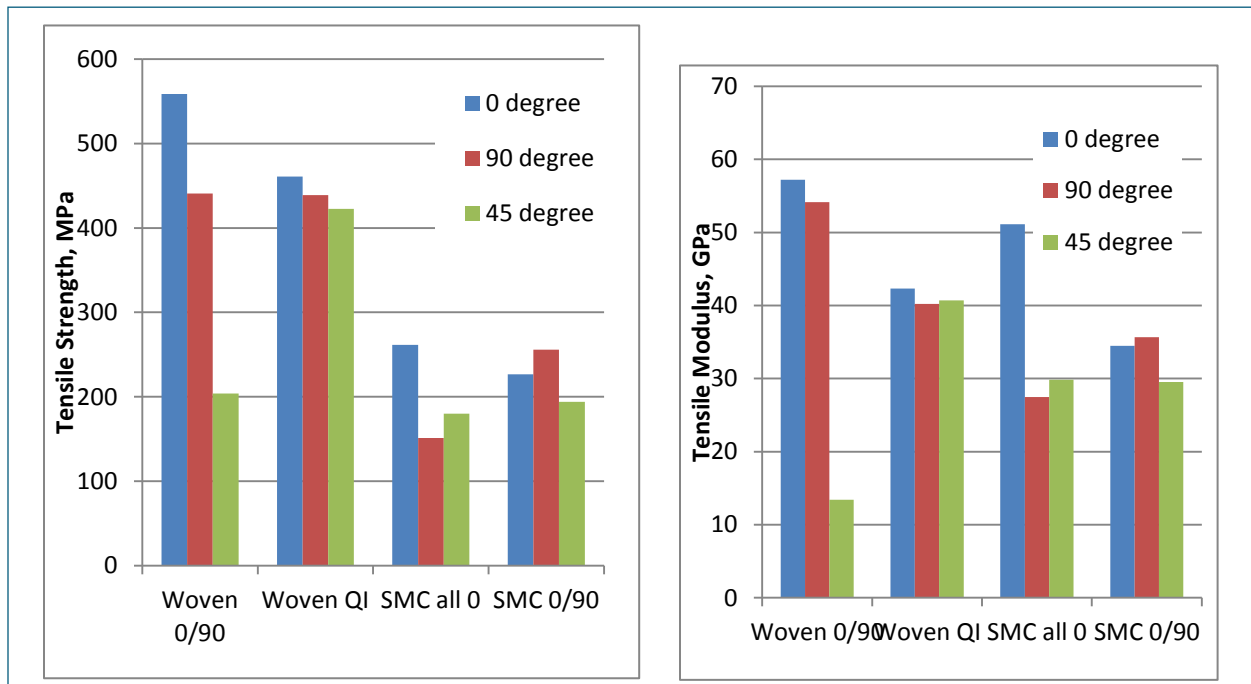


Figure IV-36: Tensile strength and modulus for 2x2 twill fabric at 0/90 orientation and quasi-isotropic orientation, and for carbon fiber SMC with all plies at 0° and with plies crossed at 0 and 90°.

Plans are underway for another plaque molding trial, which will include molding in the inserts needed for  $G_{1c}$  and  $G_{2c}$ , as well as additional “molded-in flaws” for NDE development. The team will also be molding a closed hat section part that will enable us to determine the deformation behavior of the materials being considered for a shaped part.

The following is a brief discussion of the attributes and material data requirements of the two prototype analytical crash models and the four crash material models implemented in commercial codes that the USAMP project is evaluating for their capacity to predict quasi-static and dynamic crash behavior of a designed vehicle front end sub-system using carbon fiber composites. The USAMP team worked with each modeling group to identify material properties across these codes, and to compile a coordinated list of required data.

#### *UM's Meso-scale RUC-based Material Model:*

Textile composites dissipate energy through matrix cracking and fracture of tows. Thus, both of these mechanisms must be captured in any continuum model that aims to predict energy absorption and management of crashworthy structures made from textile composites. In references 1 through 3, a RUC based model of braided fabric composite crush response was developed. The outcomes of this modeling effort have been extended in the present project to model an 8-ply, satin-weave material as a damaging (through matrix cracking) and fracturing (through tow and matrix fracture) shell element material model. To do this, the non-linear shear response of the material is measured through coupon tests. This test captures non-linearity in stress-strain response due to shear (the matrix cracking mechanism). Furthermore, single edge notch fracture tests are carried out to measure fracture initiation strength and fracture toughness of the 8-ply, shell-element material model. These tests (shear non-linearity measurement, and fracture toughness measurement) and basic coupon level tests to get elastic moduli (such as  $E_{11}$ ,  $E_{22}$ ,  $G_{12}$  and  $\nu_{12}$ ) serve to characterize the material for purposes of implementing a finite-element-based model of crash energy management.

#### *NWU's Micro-Plane RUC Models and Material Tests to Support Model Validation:*

In order to accurately calibrate and validate the constitutive models<sup>4,5</sup> developed by the NWU team, a test matrix was developed for the mechanical and fracture properties of woven composites (twill 2x2) which are to be used for the crush cans. For the unidirectional composites, which are to be used in the demonstration composite bumper beam, only the main mechanical properties (tension, compression, shear and flexural) were requested by NWU, while the remaining parameters will be estimated from literature. Both of the models developed by the NWU team can be calibrated against the mechanical properties of a lamina and then used to predict the behavior of a laminate of any arbitrary stacking sequence. This allows the flexibility to study the effects of different lay-ups on the final properties of the crush can. Accordingly, mechanical test data were requested for the [0/90] woven laminates (to calibrate the models) and for the quasi-isotropic (QI) laminates (to validate the models). For the unidirectional laminates, tests on the [0]<sub>8</sub>

laminates were requested to obtain the mechanical properties of the lamina (for model calibration) while tests on the [0/90] and QI configurations were intended for validation.

Due to the anisotropy of composites, uniaxial tests, either in tension or compression, were requested to get elastic moduli and strength along the directions of orthotropy. Shear tests were requested by NWU in order to obtain the in-plane shear modulus and strength (the out-of-plane shear properties will be estimated). All of the above-mentioned material tests are required due to the anisotropy of the mechanical properties of composites as well as their failure mode behavior. This is true even for the simplest models available in the literature, e.g., the Tsai-Wu criterion<sup>12</sup>. All of the requested material tests follow the appropriate ASTM standards. (e.g., ASTM 7078 for the V-Notched Rail Shear test for shear properties<sup>25</sup>).

Since polymer composites are viscoelastic materials with strain rate sensitive mechanical and fracturing behavior<sup>29</sup>, consideration of strain rate effects is essential to accurately predict the crushing behavior under different speeds. Accordingly, to explore the rate effects NWU has requested that each test be performed at two different strain rates: one as fast as possible (suggested 0.1 sec to peak load), and the other, according to the standards (5 to 10 minutes to peak load).

An important differentiator of the crash model formulations developed by the NWU team compared to most models in the literature (e.g., the Tsai-Wu criterion<sup>12</sup>) is the capability of modeling the correct energy dissipation pattern during fracture. This is accomplished by taking into consideration the quasi-brittle character of composites that leads to a size effect on the mean nominal strength, i.e., a nominal strength which depends on the structure size<sup>30-33</sup>. This aspect must be taken into consideration if crush cans of different sizes and geometries are to be studied. To calibrate the models, size effect tests were requested. These represent the only practical way to uniquely determine the intra- and inter-laminar fracture properties of the laminates. Unfortunately, these are not regulated by ASTM standards so the main specifications of the tests were suggested by the NWU team based on their extensive experience in the characterization of quasi-brittle materials. For the intra-laminar fracture properties, tests on single-notched specimens of at least 3 different radially scaled sizes were suggested<sup>30</sup>. As for the characterization of the mode I inter-laminar fracture behavior, double cantilever beam specimens of different thicknesses were suggested. Except for the thicknesses, all the other specifications for the tests can be found in the related standard<sup>22</sup>. Tests on mode II inter-laminar fracture behavior were requested as well with the same scaling of the thicknesses. In this case, end notch flexure specimens were suggested.

#### *PAM-CRASH Material Models:*

PAM-CRASH material model 131 is for multi-layered composite shell elements. Within this model different ply types can be used for different fiber reinforcements and damage laws. (1) Ply type 1 for uni-directional composites (shell elements). (2) Ply type 7 for woven type composites (shell elements).

**Ply Type=1:** Ply Model *TYP* =1 is based on a paper by P. Ladevèze and E. Ledantec<sup>14</sup> and modified to include transverse shear. This model corresponds to a homogenized, global description of the fiber and matrix phases. The Ladevèze model is dedicated to the numerical simulation of unidirectional continuous fiber reinforced composite materials. The Ladevèze model does not treat the two phases separately (fibers and matrix). Instead the composite ply is described using homogeneous continuum mechanics.

**Ply Type=7:** Ply Model *ITYP* = 7 is based on a paper by A.K. Johnson, A.K. Pickett and P. Rozycki<sup>15</sup>. This model corresponds to a homogenized, global, description of the fibers and matrix phases. The Ladevèze fabric model is defined from unidirectional global model as an extension for fabric described using homogeneous mechanics. The two fiber directions defined for this fabric remain perpendicular throughout the run. A damage mechanics formulation is used in which ply degradation parameters are internal state variables that are governed by damage evolution equations.

#### *LS-DYNA Material models:*

Two kinds of material models in LS-DYNA can be used to model composite crash simulations; “Progressive Failure models (PFM)”, which use a ply discount method to degrade material properties, and “Continuum Damage Mechanics (CDM) models”. MAT 54 is a PFM, while MAT58/59 and MAT158 are based on CDM.

LS-DYNA MAT54 adopts the Chang-Chang failure criterion<sup>6</sup> and has been observed to work well in the simulation of composites that shown brittle fracture at the crush front, like unidirectional tape composites, woven fabric and chopped fiber composites. A good reference is [7].

MAT58 in LS-DYNA is based on the continuum damage mechanics model proposed by Matzenmiller, Lubliner and Taylor<sup>9</sup>. This material model has been seen to work well for crush simulations where the material at the crush front formed continuous fronds, as seen in braided composites<sup>9</sup>. An update to this material model<sup>10</sup>, including strain rate effects, is present in MAT158.

#### *RADIOSS Material models:*

RADIOSS has two composite material models available for shell structural analysis<sup>11,13</sup>. The first is Law 25. This uses either the Tsai-Wu model plasticity formulation or the CRASURV formulation.

The second, LAW 15, uses plastic behavior based on the Tsai-Wu criteria, but uses the Chang failure criteria. This law is not recommended by Altair, the developing company of RADIOSS, but instead recommends the LAW 25 model with a separate Chang failure definition.

#### *ABAQUS Material models:*

For composite materials, Abaqus/Explicit offers the capability to predict the onset of damage and model the evolution of elastic-brittle damage, which is typically seen in unidirectional tape and woven composites. The damage initiation is based on the Hashin’s failure criterion<sup>16</sup>. The damage evolution capability assumes a progressive

degradation of material stiffness leading to failure as suggested by Matzenmiller *et. al.*<sup>8</sup>. In Abaqus, the evolution of the damage variable is based on the energy dissipated due to failure<sup>17</sup>. Multi element models with cohesive elements defining the inter-laminar response of these composites can be defined to model the delamination failure<sup>18</sup>.

#### **Task 3.2 Design/CAE Analysis of Composite FBCC:**

The primary focus of Year 1 activity for the Design/CAE Team was to generate design concepts for the composite FBCC, and in particular to evaluate the energy absorption characteristics and the crush mode of different crush can geometries in the front impact and angular impact. In doing this, the results of the steel FBCC crash testing reported above are utilized as targets.

#### *Composite Crush-Can Development—Flat Frontal Load Case*

Using the length of the steel crush can (196 mm) as a starting point, 12 different sections (shown in Figure IV-37) were evaluated for the energy absorption, crush mode and average load. The team agreed that in order to meet the steel FBCC performance, the composite crush-can should have similar energy absorption and a progressive crush mode (front to rear). There was some discussion about the nature of the crush mode (circumferential peel or axial crushing) which will continue to be debated and assessed until the most robust model is identified across all frontal impact load cases.

The crush-can models were crushed at 35mph with a 150 kg mass applied to the sled. This represents an input load that a single crush-can would be required to manage in the full system with a 300 kg mass. The crush-can was constructed in CAE from a quasi-isotropic, symmetric laminate with 8 layers 0.2375 mm pre-preg at [0/45/-45/90] orientation. The total thickness of the laminate for each crush-can shape was 1.9 mm.

The Force-Displacement curve for each of the concepts is shown in Figure IV-38. The Force-Displacement characteristics are shown for a single steel crush can for reference. Table IV-6 compiles the energy absorption of each concept. Although all of the composite concepts showed higher specific energy absorption (energy absorbed per unit mass) compared to the steel design, each had lower total energy absorption than the steel crush-can (for the given material and laminate assumptions). There was also a significant variation in the crush mode and force curves between the geometries. Profiles P4, P7 and P10 exhibited unstable crush or a crush mode that was not axially progressive front to rear (Figure IV-39). Such behavior results in unstable crush force and leads to lower energy absorption. These unstable geometries were ruled out.

The results indicated that P12 had the highest Force-Displacement average and energy absorption. This profile also exhibited a stable, progressive crush mode, as shown in Figure IV-40. The study also showed that the internal stiffeners of P12 increased the average force and improved the stability of the crush mode compared with P8 or P11.

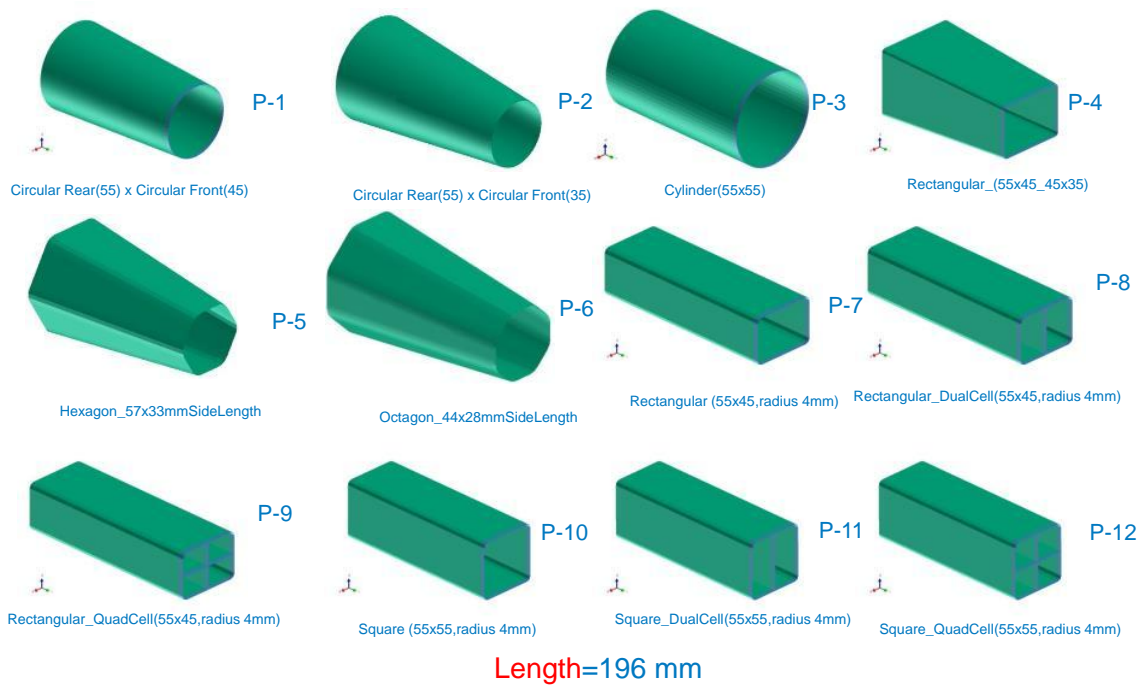


Figure IV-37: Crush Can Shape Concepts.

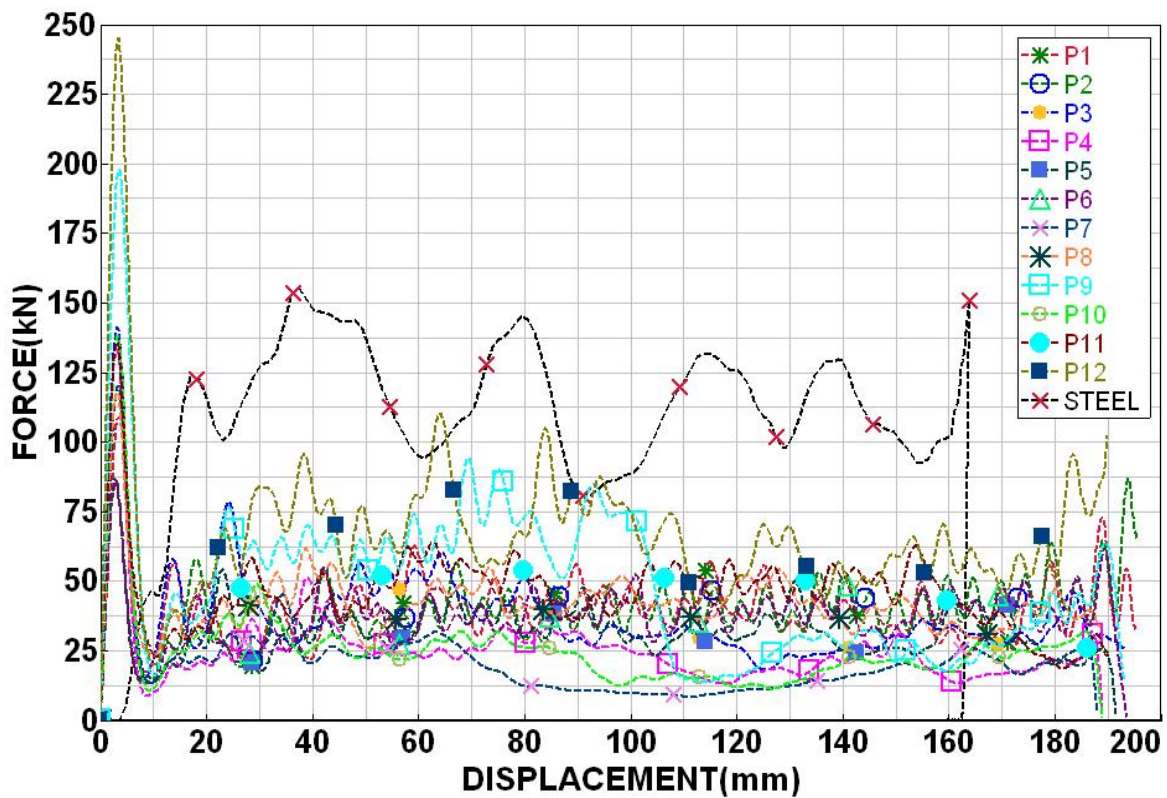


Figure IV-38: Force-Displacement Curves for the 12 Composite Concepts.

Table IV-6: Energy Absorption Comparison (35 mph Flat Frontal).

| Profiles     | Energy (KJ)  | Specific Energy Absorption (SEA) (kJ/Kg) |
|--------------|--------------|--|
| P1           | 7.63         | 35.03                                    |
| P2           | 7.42         | 37.61                                    |
| P3           | 7.06         | 29.43                                    |
| P4           | 4.76         | 19.57                                    |
| P5           | 6.09         | 28.83                                    |
| P6           | 7.12         | 34.79                                    |
| P7           | 3.90         | 20.51                                    |
| P8           | 7.29         | 31.45                                    |
| P9           | 9.34         | 32.31                                    |
| P10          | 4.77         | 21.55                                    |
| P11          | 7.05         | 25.30                                    |
| <b>P12</b>   | <b>12.85</b> | <b>34.34</b>                             |
| <b>STEEL</b> | <b>17.65</b> | <b>19.45</b>                             |

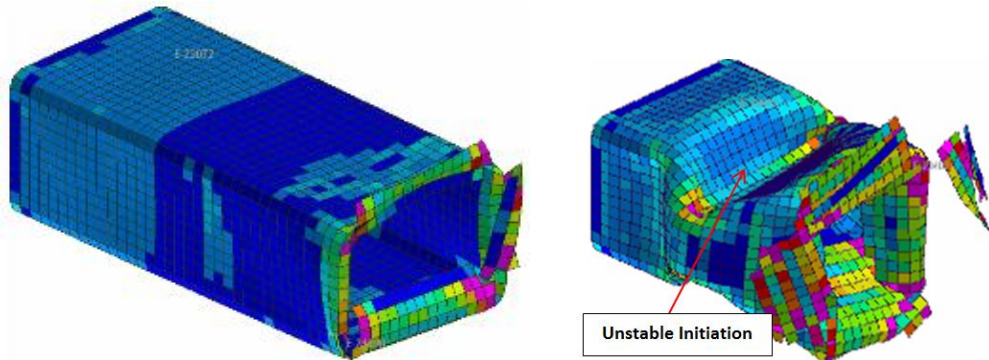


Figure IV-39: P7 Unstable Crush Mode a) Initial Crush b) Unstable Crush.

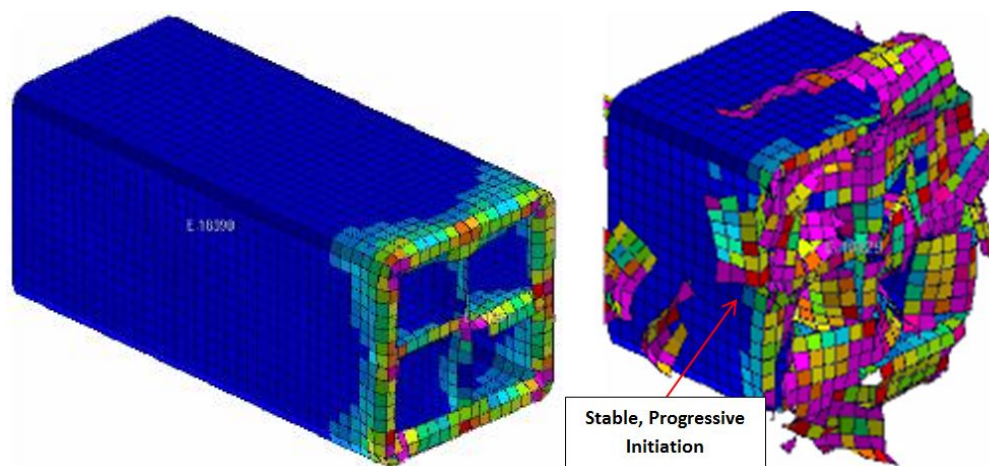


Figure IV-40: P12 Crush Mode.

Further studies were performed on the P12 concept to increase the energy absorbed by increasing the mass, and softening the front portion of the crush can to reduce the peak load and further improve initial crush stability. It was found that increasing the thickness from 1.9 mm to 2.5 mm enabled the P12 crush-can to meet the steel energy absorption requirement. Although the average force is lower, the energy absorption can be met as the composite material crush characteristics allow the can to crush the full length, whereas the folding crush mechanism of the steel design allows a smaller crush length until the can is completely compressed.

*Composite Crush-Can Development—30 mph Angular Load Case*

The 30 mph angular impact load case was also assessed to identify the robustness of P12 to load input angle, and determine if another concept proved to be more robust across the different impact loadcases. Force-Displacement results of all geometry concepts are compared with the single steel crush-can as shown in Figure IV-41. Again, P12 and P9 show to have the highest energy absorption and most consistent crush mode. The energy absorbed for each concept in this impact mode is tabulated in Table IV-7.

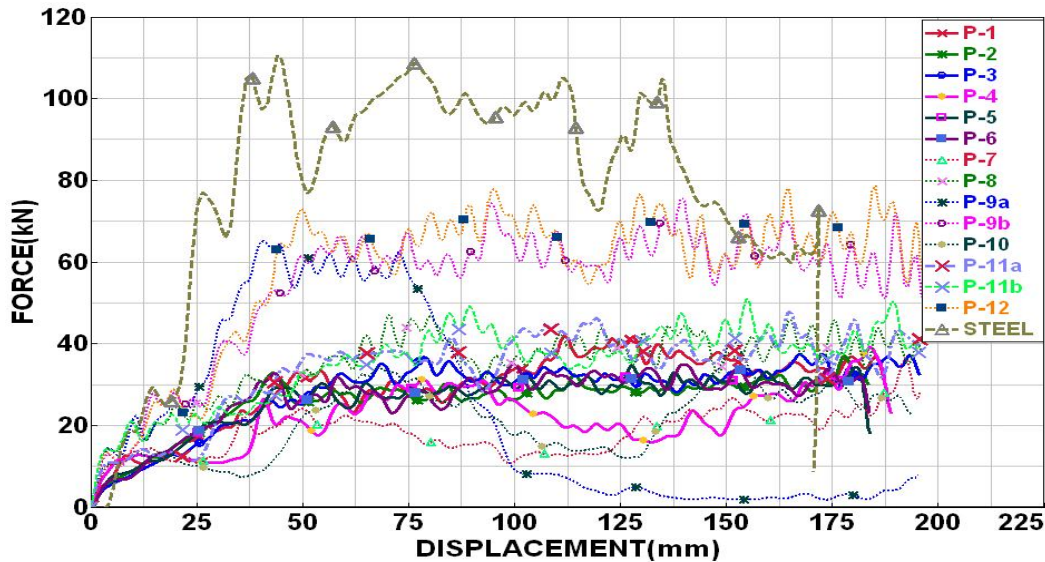


Figure IV-41: Force-Displacement Curves for 30 mph Angular Impact.

Table IV-7: Energy Absorption Comparison (30 mph Angular Impact).

| Profiles     | Energy (KJ)  | Specific Energy Absorption (SEA) (kJ/Kg) |
|--------------|--------------|--|
| P1           | 5.49         | 25.20                                    |
| P2           | 4.75         | 24.08                                    |
| P3           | 5.50         | 22.92                                    |
| P4           | 4.16         | 17.10                                    |
| P5           | 4.80         | 22.72                                    |
| P6           | 4.91         | 23.99                                    |
| P7           | 3.59         | 18.88                                    |
| P8           | 6.86         | 29.59                                    |
| P9a          | 4.42         | 15.29                                    |
| P9b          | 10.67        | 36.91                                    |
| P10          | 4.09         | 18.47                                    |
| P11a         | 6.57         | 23.57                                    |
| P11b         | 6.85         | 24.58                                    |
| <b>P12</b>   | <b>11.29</b> | <b>30.17</b>                             |
| <b>STEEL</b> | <b>13.43</b> | <b>14.80</b>                             |

Table IV-8 shows a summary of both load cases and the energy absorbed. The P12 concept with 2.5 mm thickness performs very well under both load cases. This concept could be manufactured by a pultrusion process (a high-volume fabrication process), which will be further investigated by the MPS team.

**Table IV-8: Energy Absorption Summary.**

| Profiles                              | NCAP (KJ)    | Angular (KJ)          |
|---------------------------------------|--------------|-----------------------|
| P1                                    | 7.63         | 5.49                  |
| P2                                    | 7.42         | 4.75                  |
| P3                                    | 7.06         | 5.50                  |
| P4                                    | 4.76         | 4.16                  |
| P5                                    | 6.09         | 4.80                  |
| P6                                    | 7.12         | 4.91                  |
| P7                                    | 3.90         | 3.59                  |
| P8                                    | 7.29         | 6.86                  |
| P9                                    | 9.34         | (a) 4.42<br>(b) 10.67 |
| P10                                   | 4.77         | 4.09                  |
| P11                                   | 7.05         | (a) 6.57<br>(b) 6.85  |
| <b>P12</b>                            | <b>12.85</b> | <b>11.29</b>          |
| <b>P12 (Thicker Laminate, 2.5 mm)</b> | <b>17.91</b> | —                     |
| <b>STEEL</b>                          | <b>17.65</b> | <b>13.43</b>          |

The Design/CAE team also considered analysis of different failure modes of the crush-can. The NWU representatives provided strong arguments for an alternate crush based on a circumferential “peeling” of the laminate. Assuming the presence of a crush initiator, the main crushing modes as shown in Figure IV-42 were found to be:

- Intra-laminar cracking (splitting)
- Inter-laminar cracking (Mode I and II)
- Fracturing of lamina bundles

Based on the experience of the NWU team, the presence of a crush initiator was highly recommended to guarantee high energy dissipation and the developing of a relatively gradual crushing mode. Without a crush initiator, the main crushing modes are expected to be:

- Buckling
- Inter-laminar cracking (Mode I and II)

However the team agreed that this mode was not a requirement for correlation of the ACC models, and that the ACC models could predict the failure and energy absorbed under other modes with correct input of material properties obtained from the prescribed testing. Additionally, while this may be the optimum mode for the flat frontal impact and provides the most efficient energy absorption, some concern was raised as to the effectiveness under an angular impact.

**Tasks 4 and 5: No effort in FY2013**

**Task 6: Non-destructive Evaluation ((NDE) of Composite Structure**

Robust NDE methods are essential for determining both, the quality and the actual construction characteristics of composite structures. Because long-fiber composites are constructed from multiple plies that are first stacked and then compressed, there may be situations where delaminations, voids, and foreign material that reduce material strength are introduced. Draping issues may alter fabric orientation from design specifications. Identification of these discrepancies and variations allow predictive models to perform more accurately and our interpretation of material property testing data to improve. Structural health monitoring is also a critical issue for automotive composites where parking lot and other low velocity impacts may compromise the performance of CFRP's without any visible indications.

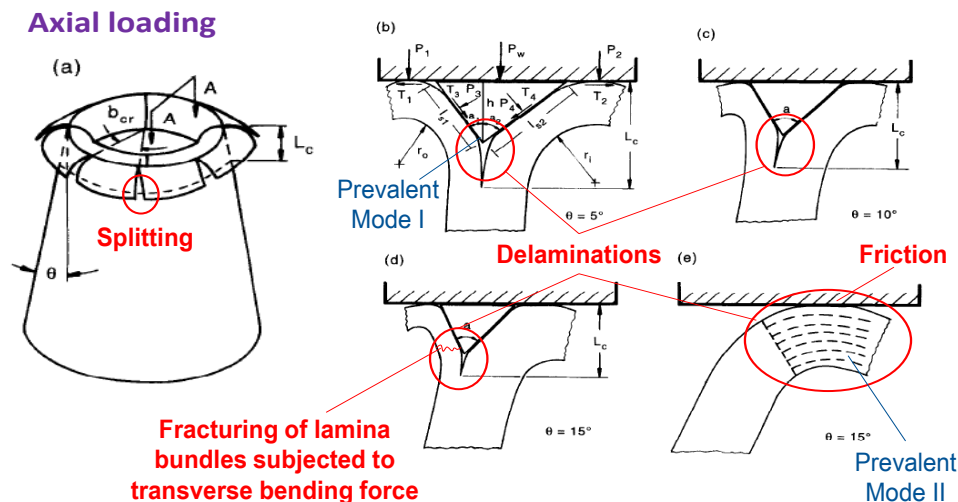


**Figure IV-42: "Peel" Crush Can Failure Mode (Adapted from Mamalis et al., 1997).**

The NDE Round 1 analysis activity was focused on flat plaques. Plaque layout was specified with a variety of inserts to simulate disbands (polytetrafluoroethylene (PTFE) film) and foreign matter (aluminum foil). To determine depth sensitivity, PTFE inserts were located at varying inter-ply locations. Eight of the Round 1 flat plaques made with 8 plies of various carbon fiber/epoxy prepregs and layups were received for NDE. These included one of each type of prepreg (unidirectional, 2x2 twill fabric, and SMC). The plaques were examined both with low energy radiography (20 KeV) and high-frequency, pulse-echo ultrasonics (15-50 MHz). The plaques were found to have low porosity and only a few foreign objects. The low porosity and thinness of the samples mean that relatively high frequencies (15-20 MHz) can be used for the ultrasonic inspections. All the inserts could be seen with both NDE methods.

The NDE team has also begun closer collaboration with the other task teams to better understand current material and fiber configuration concerns and crash/impact performance, and to provide feedback on material quality and properties and on “inspectability” of designs. Since at least 40 composite FBCCs are required for crash testing under 6 load cases in Task 5, work is in progress for development of an inspection procedure for the composite FBCC components and assemblies, both before and after crash.

### Technology Transfer Path

The FBCC was selected because it represents the primary energy absorbing structural members in frontal crashes and is a challenging structural application of composites for crash energy management. Two USAMP-facilitated material models and four major commercial crash codes (LS-DYNA, RADIOSS, PAM-CRASH and ABAQUS) are being evaluated for the crush cans and bumper beam application in predictive modeling followed by validation with fabricated structures via crash and physical testing and analyses. At all levels, a broad group of technology stakeholders are involved so as to help accelerate the evaluation of the models and for early identification of key knowledge gaps. Advances made in crash modeling will be quickly implemented by the respective crash code vendors into the major commercial crash codes for crash analyses of carbon composite structures.

Successful demonstration of such challenging structures opens new lightweighting application opportunities for composites in passenger vehicles and light trucks, with the near-term potential to drive U.S. industrial capacity and economies of scale in carbon-fiber production. The project outcomes are expected to advance the readiness levels of composite material modeling, and crash-modeling technologies so as to prove their feasibility for broader application of primary automotive composite structures. Periodically, the research will be reported by the OEM, vendor and academic experts in subject-matter reports, as well as disseminated through publications in the open literature and/or subject-matter conferences.

### Conclusion

During the year following kick-off, considerable progress has been made to complete the majority of baseline steel FBCC crash testing with detailed analysis of crash responses in progress. Definitions of equivalency were developed that can be incorporated in crash models to help drive the design of innovative composite structures that leverage the strength and lightweighting potential of carbon fiber product forms. Ten composite FBCC design concepts were evaluated, and the feasibility of each design will be evaluated to develop a short-list of viable composite FBCCs for detailed design in Year 2. Development of methodologies suitable for evaluation of complex composite structures was initiated.

### Presentations/Publications/Patents

Several papers or presentations have been submitted by the USAMP team members:

1. A. Seyed Yaghoubi, G. Newaz, P. Begeman, D. Board, Y. Chen, O. Faruque. "Rigid Full Frontal Response of Generic Steel FBCC Samples". SAE 2014 World Congress.
2. A. Seyed Yaghoubi, G. Newaz, P. Begeman, D. Board, Y. Chen, O. Faruque. "Generic Steel FBCC Samples Subjected to Rigid Offset Frontal Impact". SAE 2014 World Congress.
3. A. Seyed Yaghoubi, G. Newaz, P. Begeman, D. Board, Y. Chen, O. Faruque. "Load History Assessment of Generic Steel FBCC Samples Subjected to Rigid Center Pole Impact". 2014 Society of Experimental Mechanics' Conference & Exposition on Experimental and Applied Mechanics.
4. A. Seyed Yaghoubi, G. Newaz, P. Begeman, D. Board, Y. Chen, O. Faruque. "Rigid Angular Impact Response of Generic Steel FBCC Samples: Correlation of Multiple Velocity-Measurement Techniques". 2014 Society of Experimental Mechanics' Conference & Exposition on Experimental and Applied Mechanics.

### References

1. Song S, Waas AM, Shahwan KW, et al., Braided textile composites under compressive loads: Modeling the response, strength and degradation, *Composites Science and Technology*, **67**(15-16), 3059-3070, 2007.
2. Quek, S C, A M Waas, K W Shahwan, and V Agaram, "Analysis of 2D Flat Triaxial Braided Composites", *Int.J. Mechanical Sciences*, **45**(6-7): 1077-1096, 2003.
3. Shunjun Song, A.M. Waas, K. W. Shahwan, O. Faruque, X. Xiao, "Compression response, strength and post-peak response of an axial fiber Reinforced tow," *International Journal of Mechanical Sciences*, **51**, 491–499, 2009

4. Caner, F.C., Bazant, Z.P., Hoover, C.G., Waas, A.M., Shawan, K.W., "Microplane Model for Fracturing Damage of Triaxially Braided Fiber-Polymer Composites," *Journal of Engineering Materials and Technology*, **133**, 021024-1-12, April 2011.
5. Cusatis, G., Beghini, A., Bazant, Z.P., "Spectral Stiffness Microplane Model for Quasibrittle Composite Laminates—Part 1: Theory," *Journal of Applied Mechanics*, **75**, 021009-1-6, 2008.
6. Chang, F.K., and Chang, K.Y., 'A progressive damage model for laminated composites containing stress concentrations', *Journal of Composite Materials*, 21: 834-855, 1987.
7. Feraboli, P., Wade, B., Deleo, F., Rassian, M., Higgins, M., and Byar, A., 'LS-DYNA MAT54 modeling of the axial crushing of a composite tape sinusoidal specimen', *Composites (Part A)*, 42, 1809-125, 2011.
8. Matzenmiller, A., J. Lubliner, and R. L. Taylor, "A Constitutive Model for Anisotropic Damage in Fiber-Composites," *Mechanics of Materials*, vol. 20, pp. 125–152, 1995.
9. Xiao, X., 'Simulation of Composite Tubes Axial Impact with a Damage Mechanics Based Composite Material model'. In 10th International LS-DYNA Users Conference (2008), 43-54.
10. Goldberg, R.K., and Carney, K.S., 'Modeling the Nonlinear, Strain Rate Dependent deformation of Shuttle Leading Edge Materials with Hydrostatic Stress Effects Included'. In 8th International LS-DYNA Users Conference (2006), 3, 45-56.
11. Gatti, M., Vescovi, L., Sperati, M., Pagano, P. and Ferrero, L., "Characterization of Composite Materials, Unidirectional and Fabric Samples," *Autosim Technology Workshops & CSC*, Paris, France, July 5-6, 2007.
12. Tsai, S. W., and Wu, E. M., (1971), A general theory of strength for anisotropic materials *J. Compos. Mater.*, 5(1), 58–80, 1971.
13. Daniel, I.M., Ishai, O. (2006). *Engineering Mechanics of Composite Materials*. (2nd Edition. pp 122-147). New York, NY: Oxford University Press
14. Ladevèze P, Le Dantec E, "Damage Modelling of the elementary ply for laminated composites", *Composites. Science and Technology*, Vol. 43, Issue 3, 1992, pp. 257-267.
15. A.K. Johnson, A.K. Pickett and P. Rozycki, "Computational methods for predicting impact damage in composite structures", *Composites Science and Technology*, Vol-61 (15), pp. 2183-2192, 2001
16. Hashin, Z., "Failure Criteria for Unidirectional Fiber Composites," *Journal of Applied Mechanics*, vol. 47, pp. 329–334, 1980.
17. Abaqus Analysis Users Manual, v6.11. Dassault Systemès Simulia Corp.
18. Heimbs, S., 'Bird Strike Simulations on Composite Aircraft Structures'. In 2011 Simulia Customer Conference, 2011.
19. Yi Pan, Lucian Iorga, Assimina A. Pelegri, "Numerical generation of a random chopped fiber composite RVE and its elastic properties," *Composites Science and Technology*, **68**, 2792–2798, 2008.
20. Flesher, N.D.; Chang, F-K. *Effect of Cross-Section Configuration on Energy Absorption of Triaxially Braided Composite Tubes*. 18th Annual Technical Conference American Society for Composites. Oct. 19-22, University of Florida, 2003.
21. Z. Yuan and J. Fish, "Hierarchical Model Reduction at Multiple Scales," *International Journal for Numerical Methods in Engineering*, 2008.
22. ASTM D3039, Standard Test Method for Tensile Properties of Polymer Matrix Composite Materials.
23. ASTM D6856, Standard Guide for Testing Fabric-Reinforced "Textile" Composite Materials
24. ASTM D5379, Standard Test Method for Shear Properties of Composite Materials by the V-Notched Beam Method
25. ASTM D7078, Standard Test Method for Shear Properties of Composite Materials by V-Notched Rail Shear Method
26. ASTM D3410, Standard Test Method for Compressive Properties of Polymer Matrix Composite Materials with Unsupported Gage Section by Shear Loading
27. ASTM D5528, Standard Test Method for Mode I Interlaminar Fracture Toughness of Unidirectional Fiber-Reinforced Polymer Matrix Composites
28. ASTM E132, Standard Test Method for Poisson's Ratio at Room Temperature
29. Hsiao HM, Daniel IM, "Strain rate behavior of composite materials," *Composites Part B* 29, 521–533, 1998.
30. Bažant, Z. P., Daniel I. M., Li Z., "Size effect and fracture characteristics of composite laminates," *ASME J. Eng. Mater. Tech.*, 118: 317-324, 1996.
31. Bažant, Z.P., "Scaling theory for quasibrittle structural failure," *Proc., National Academy of Sciences*, 101(37), 13400-13407 (inaugural article), 2004.
32. Bažant, Z. P., Kim, J. -J. H., Daniel, I. M., Becq-Giraudon, E., and Zi, G., "Size Effect on Compression Strength of Fiber Composites Failing by Kink Band Propagation," *Int. J. Fract.*, **95**, 103–14, 1999,
33. Bazant, Z.P., Zhou, Y., Novak, D., and Daniel, I.M., "Size effect on flexural strength of fiber-composite laminate." *J. of Engrg. Materials and Technology ASME*, **126**, 29–37, 2004.

## V.0 CROSSCUTTING

### V.1. Demonstration Project for Multi-Material Lightweight Prototype Vehicle as Part of the Clean Energy Dialogue with Canada—Vehma International of America, Inc. and Ford Motor Company

**Tim Skszek (Principle Investigator)**

Vehma International of America, Inc.  
1807 East Maple Road  
Troy, MI 48084  
Phone: (248) 786-2584  
E-mail: [tim.skszek@vehmaintl.com](mailto:tim.skszek@vehmaintl.com)

**Matthew Zaluzec, Ph.D. (Principle Investigator)**

Ford Motor Company, Research and  
Innovation Center  
2101 Village Road  
Dearborn, MI 48121  
Phone: (313) 337-1098  
E-mail: [mzaluzec@ford.com](mailto:mzaluzec@ford.com)

**Carol Schutte, Ph.D., Technology Area  
Development Manager**

U.S. Department of Energy  
1000 Independence Avenue, S.W.  
Washington, DC 20585  
Phone: (202) 287-6020; Fax: (202) 856-2476  
E-mail: [carol.schutte@ee.doe.gov](mailto:carol.schutte@ee.doe.gov)

Contractor: Vehma International of America, Inc.  
Contract No.: DE-EE0005574

#### Abstract/Executive Summary

The Multi-Material Lightweight Vehicle (“MMLV”) includes engineering/design, prototype vehicle build and component- and vehicle-level validation testing of a “new passenger vehicle design architecture” which facilitates extensive use of lightweight and high strength materials, resulting in environmental and fuel economy benefits associated with up to a 50% reduction in weight relative to a CY-2002 baseline FMVSS-compliant steel vehicle architecture.

The MMLV project includes the design of two (2) vehicle variants:

- The Mach-I design is comprised of materials and processes that are commercially available and focuses on an aluminum and steel intensive MMLV body structure.

- The Mach-II design is comprised of advanced materials and manufacturing processes that have known potential but require further research and development to resolve processing and materials-related issues required for commercialization. The Mach-II design will demonstrate the potential mass reduction benefits that can be achieved, if the promising new materials and process technologies are successfully commercialized.

Both the Mach-I and Mach-II design variants maintain the vehicle attributes associated with the Ford Motor Company (“FORD”) production 2014 C/D segment passenger car (Fusion) and represent all of the comparative elements associated with the baseline vehicle. Each MMLV subsystem and vehicle is designed to perform within the acceptable range of the functional safety requirements of a passenger vehicle, using original equipment manufacturer (OEM) standard experimental procedures.

Vehma International of America (Vehma) completed the Mach-I vehicle design in Q1-2013. Vehma is currently integrating the lightweight body structure, chassis, bumper and closure components prototyped by Vehma with the 2014 Ford Fusion donor vehicles and lightweight vehicle subsystems developed by FORD. The Ford-developed subsystems include a lightweight advanced powertrain, suspension, interior, seating, Heating, Ventilation and Air Conditioning (HVAC), steering, occupant safety, lighting, glass, wheels and braking systems. The Mach-I prototype vehicles will be tested by Ford during Q1 and Q2 of 2014. Testing will include a subset of vehicle validation test protocols, accessing corrosion, durability, noise, vibration and harshness (NVH) and crash performance of the Mach-I Vehicle. The results associated with the physical tests will be compared to the Computer Aided Engineering (CAE) predictive models to access correlation.

The Mach-II concept design was released in Q3-2013. The MMLV body-in-white (BIW) architecture comprised of cast aluminum body structure and ultra-high strength steels (UHSS) safety cage is common to both the Mach-I and Mach-II vehicle designs.

During Q3-2013, Oakridge National Laboratory (ORNL) was contracted to conduct weight assessment and Life Cycle Analysis (LCA) associated with the Mach-I and Mach-II vehicle designs per the Canadian Standards Association LCA protocol.

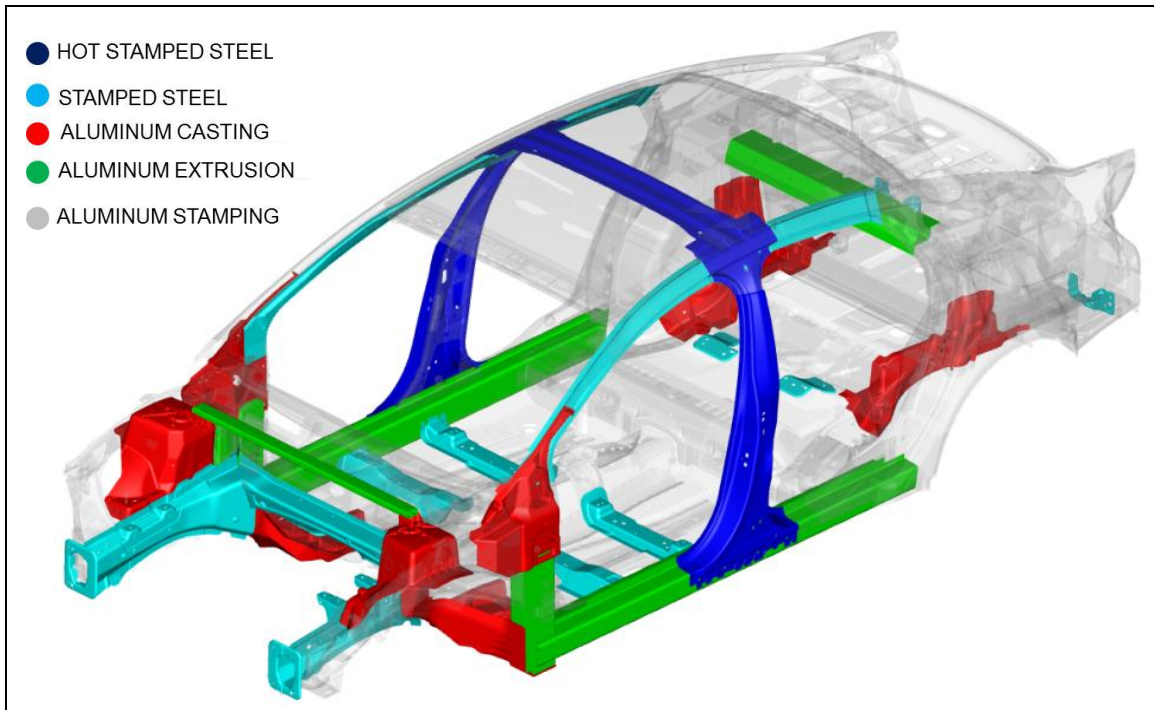


Figure V-1: MMLV BIW cast node architecture, common to both Mach-I and Mach-II vehicle designs.

## Accomplishments

FY2013 (October 2012 thru September 2013)

### *Mach-I and Mach-II Generic Activities*

- BIW Vehicle Architecture—Developed an advanced vehicle design architecture which facilitates the use of multiple lightweight materials and manufacturing processes for high volume applications (+200,000 vehicles/yr).
- Manufacturing Strategy—Developed a vehicle assembly sequence (Bill of Process) and MMLV corrosion mitigation strategy (E-coat, secondary sealing, paint) compatible with the advanced vehicle design architecture and lightweight materials.
- Joining Strategy—Developed and tested several multi-material joint designs characterized by material type, gauge, adhesive type and mechanical/fusion joining process.

### *Mach-I Activities*

- Prototype Design Release—Released CAD models, as well as component-level and full-vehicle CAE predictive models associated with the Mach-I vehicle.
- Bill of Material—Released BOM illustrating material selection and mass distribution of the MMLV vehicle. A mass reduction of 364kg (22% reduction in curb weight) relative to the 2002 Ford Taurus baseline vehicle was achieved.

- Testing—Commenced performance testing of MMLV joint designs.
- Completed the Mach-I CAE-based analytical evaluation at a 22% curb weight reduction from the 2002 Ford Taurus baseline vehicle, while meeting critical 2013 safety requirements, meeting durability performance and meeting most of the NVH metrics.
- Prototype Build—Released tooling, fixtures and material specifications for build of Mach-I prototype vehicles in Q1-2013. Completion status as of Q3-2013 is shown graphically in Figure V-2.

### *Mach-II Activities*

- Concept Design Release—Completed “Concept Design Release” for Mach-II vehicle design Q3-2013. The Mach-II vehicle integrates carbon fiber structures and magnesium materials with the generic BIW architecture comprised of aluminum cast nodes and UHSS safety cage as previously illustrated in Figure V-1 above.
- CAE Modeling—Commenced modeling associated with the Mach II concept design. Completion scheduled in Q1 2014.
- Vehicle Mass Objective—761 kg curb weight for a C/D segment passenger vehicle, representing 50% reduction in mass relative to 2002 Ford Taurus baseline vehicle.

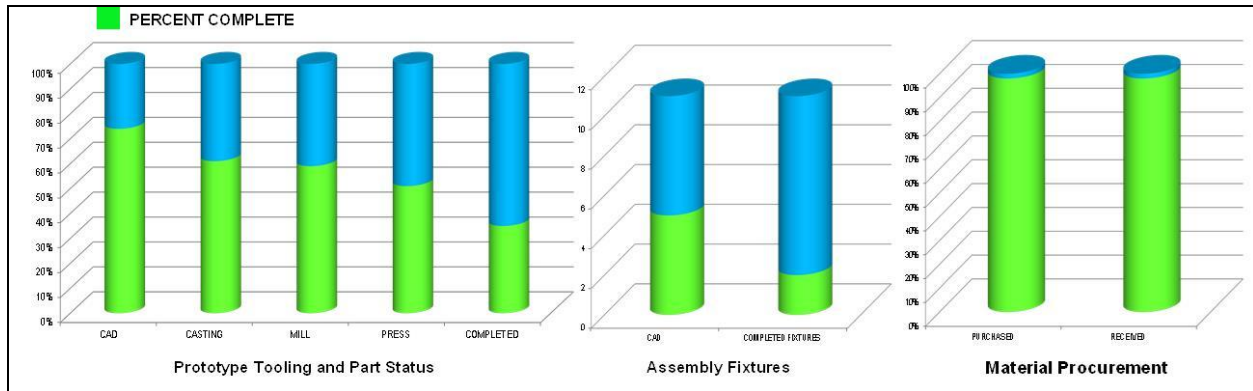


Figure V-2: Mach-I Prototype Vehicle Build Status.

### Future Directions

- Mach-II Design Release—Complete design to achieve a 50% mass reduction (761 kg curb weight) relative to the 2002 Ford Taurus baseline vehicle, while meeting the 2013 safety requirements. Scheduled Completion: Q1-2014.
- Mach-I Prototype Vehicle Build—Complete build of six Mach I prototype vehicles. Scheduled Completion: Q2-2014.
- Mach-I Vehicle Testing—Perform physical testing of Mach I prototype vehicles for Noise, Vibration, and Harshness (NVH), durability, corrosion, and safety. Scheduled Completion: Q3-2014.
- Mass and Environmental Assessment—Complete LCA analysis by Oak Ridge National Laboratories (ORNL) of the Mach-I and Mach-II designs. Scheduled completion by Q4-2014.

### Technology Assessment

- Target: Achieve 37% weight reduction for the Mach-I design from the 2002 Ford Taurus baseline vehicle.
- Gap: Mach-I design using materials and processes that are commercially available or demonstrated using currently available materials and manufacturing processes delivered a 328 kg (22%) weight reduction compared to the 2002 Ford Taurus baseline vehicle. The gap is partially attributed to the increased safety requirements between 2002 and 2013 model year vehicles. Additionally, weight reduction was limited due to packaging constraints imposed by the use of existing 2014 Fusion donor vehicle and the increased vehicle content associated with evolution in consumer preferences since 2002 (power windows, 6-Way power seats, dual zone HVAC temperature control, as examples).
- Technology Target: Magnesium sheet was considered but not deployed in the MMLV Mach-I vehicle design due to limited formability at room temperature and processing time/cost associated with elevated temperature forming processes (QPF, SPF...). Anisotropy and asymmetry challenges prohibit use of magnesium castings in multi-axial loading and safety critical applications. Magnesium

sheet is the primary candidate for Class A surface applications associated with the Mach-II vehicle. The technology gap which exists includes the need to develop non-rare earth magnesium wrought alloys, capable of being formed at or near room temperature. Prior to commercialization by the automotive community, the application of magnesium sheet for Class A surface applications requires further development and validation testing.

- Technology Target: The use of carbon fiber reinforced plastics, although offering significant weight savings, suffers from materials supply and infrastructure issues, thus not meeting the +200k units per annum (UPA) volume criteria as a material of choice for the MMLV Mach I design. However, the potential for future lightweight vehicle architectures for both Class A surfaces and body structure application makes it an ideal candidate and is incorporated into the MMLV Mach II design. Ongoing efforts to reduce the cost of producing low cost carbon fiber, and high volume manufacturing process development is needed to reduce the process cycle time to improve the business case for high volume application.
- Technology Target: Packaging constraints inherent to current vehicle architecture necessitate the use of high modulus material (steel) to meet stiffness targets associated with BIW, closure and suspension components, resulting in a stiffness-driven architecture. The development of a stiffness-driven BIW, closure and suspension architecture would enable further weight reduction opportunities using high strength lightweight alloys (aluminum, magnesium and titanium).
- Target: Produce Mach-I prototype vehicles for verification of the Mach-I designs for safety, durability and NVH attribute performance.
- Gap: Noise transmission is known to be a function of material density, stiffness and the use of interior blanket materials which mitigate sound transmission. CAE-models predict that the interior noise level associated with the lightweight MMLV Mach-I prototype vehicle will be higher than current vehicles. The lightweight Mach-I prototypes will be instrumented and tested to determine correlation between the Mach-I CAE models and actual NVH performance. CAE-based evaluations indicate that the

MMLV Mach-I prototype will meet critical durability and safety performance metrics such as rough road durability and New Car Assessment Program (NCAP) frontal impact.

- Gap: Industrial Capacity—The MMLV vehicle design architecture incorporates several high integrity aluminum castings in the BIW and chassis portions of the vehicle. High integrity aluminum castings are an enabling component of the lightweight multi-material automotive design architecture. Global capacity to manufacture high integrity aluminum cast components, using high pressure vacuum die cast (HPVDC) and low pressure semi-permanent mold (LPSPM) casting processes, is VERY limited and may limit the production of lightweight vehicles.



## Introduction

In recent years, many vehicle light-weighting applications have been demonstrated by the OEM community. Light-weight and high strength materials including 5xx, 6xxx and 7xxx series grade aluminum alloys, magnesium sheet and castings, and various steels such as dual phase (DP), transition-induced plasticity (TRIP), ultra-high strength steel (UHSS) and press hardened steel (PHS) have resulted in a significant incremental mass reduction of specific vehicle body, body structure, bumper and chassis components. Powertrain components have also become lighter weight due to the use of lightweight materials and increased efficiency associated with the development of boosted engine technology and transmission components. Ironically, the mass of vehicles has not been reduced since 2002, primarily due to the evolution of safety compliance standards and consumer demand for telematics and comfort features such as; navigation and power-assist windows, seating and lift gates. Existing manufacturing and corrosion protection infrastructure to manufacture steel body and body structure has limited the commercial application of lightweight materials to “bolt-on components” such as closures, chassis and bumper components. Further, the cost differential between aluminum and steel components has limited applications to premium and luxury vehicles.

Recent advancements in corrosion protection, adhesive materials, and joining processes have enabled the development of multi-material lightweight vehicles. The MMLV project incorporates many of the demonstrated lightweight multi-material technologies and advanced powertrain developments into the design of high volume production vehicle.

## Approach

The scope associated with the MMLV program includes the development of two (2) multi-material lightweight vehicle designs referred to as Mach-I and Mach-II. The Mach-I vehicle includes the design, manufacture and testing of production

intent prototype vehicles, incorporating materials and manufacturing processes which are commercially available and have been demonstrated for production use.

The Mach-II vehicle design includes the development of a production intent vehicle design comprised of advanced materials and manufacturing processes, presumed to be available in the 2025 timeframe, to achieve a 50% mass reduction relative to a 2002 equivalent vehicle.

The design intent for both the Mach-I and Mach-II vehicle designs include compliance to 2013 U.S. safety standards. The materials and processes evaluated for the MMLV vehicle design are listed below:

### Materials

- Wrought aluminum (5xxx, 6xxx & 7xxx series)
- Wrought magnesium (ZEK100, AZ31)
- Cast Aluminum (A356, Aural2)
- Cast magnesium (AM60, AZ91)
- Martensitic Steels (PHS & UHSS)
- Advanced High Strength Steels (DP, TRIP, Twinning Induced Plasticity (TWIP))
- Titanium
- Carbon Sheet Molded Composite (SMC) (with/without local unidirectional (UD) reinforcement, braided infused, and Non-Crimped Fabric(NCF)Chopped Fiber–Infused/Wet Pressed–P4 or similar

### Processes

- Injection molding
- Stamping (warm forming and conventional)
- Roll forming
- Casting, high pressure vacuum die cast (HPVDC)
- Casting, low pressure semi-permanent mold (LPPM)

### Fasteners

- Self-piercing rivets
- Adhesives (UV and heat cure)

### Corrosion Protection

- Alodine
- Keronite
- MgC (Henkel)
- Electrophoretic Painting Process (E-Coat)

BIW—As part of the MMLV program, Vehma developed an Advanced Lightweight Vehicle architecture which is common for both the Mach-I and Mach-II vehicle designs. The BIW architecture is based on the use of eight (8) vacuum die cast aluminum body castings, which integrate aluminum extrusions and aluminum stampings. UHSS is used where higher yield strength materials are needed to meet vehicle crash and roll-over requirements. Joining technologies include the use of SPR's as the primary joining method for assembly of both Al/Al and Al/steel material joints. Flow drills screws, RIVTAC®, and single-sided rivets are used where SPR access is not available.

**Vehicle Assembly Sequence and Corrosion Mitigation—**  
 The unique material combinations associated with the MMLV necessitated the development of a unique vehicle assembly and corrosion mitigation process illustrated in Figure V-3. The development of a corrosion mitigation strategy addressing potential galvanic corrosion inherent to multi-material joints and the modular assembly process concept addresses the temperature sensitivity associated with the various metallic and composite substrates, adhesive and sealing materials. The corrosion mitigation strategy includes use of both a ultraviolet (UV)-cured and temperature-cured adhesive material, as well as pretreatment and E-Coat of steel and Class A aluminum surfaces.

## Results and Discussion

### Mach-I Vehicle

In FY2012, the MMLV Advanced Lightweight Vehicle architecture and the design concept for the BIW, closures, and structural chassis component was developed. The mass goals and performance targets associated with each subsystem were established based on the 2014 Ford production C/D (Fusion) sedan. Development of the MMLV architecture included an assembly/corrosion strategy, dimensional plan,

slip plane, and multi-material joining strategy. CAE virtual analysis of the baseline vehicle was conducted to identify load paths and optimize material gauge and sectional properties of the design concept, resulting in a Concept Design Release of the prototype lightweight vehicle.

In FY2013, CAE virtual analysis was completed to finalize a prototype release design for the BIW, closures, and structural chassis. Figure V-4 presents an overall review of the finalized Mach I design with material distribution and weight reductions for the BIW, closures, and chassis structures.

**BIW—**The MMLV BIW architecture is comprised of eight (8) cast aluminum structural castings and a press-hardened steel safety cage shown in Figure V-5. The Mach-I vehicle design includes extruded aluminum rail, as well as AHSS and aluminum stampings. A total mass reduction of 84kg (24%) was achieved relative to the baseline vehicle components.

**Body Panels—**The Mach-I vehicle design includes the use of 6xxx, 5xxx series aluminum body panels. Typically, 6xxx material is used for outer panels to address dent resistance and 5xxx material is used for roof and inner panels which addresses the need for increased formability.

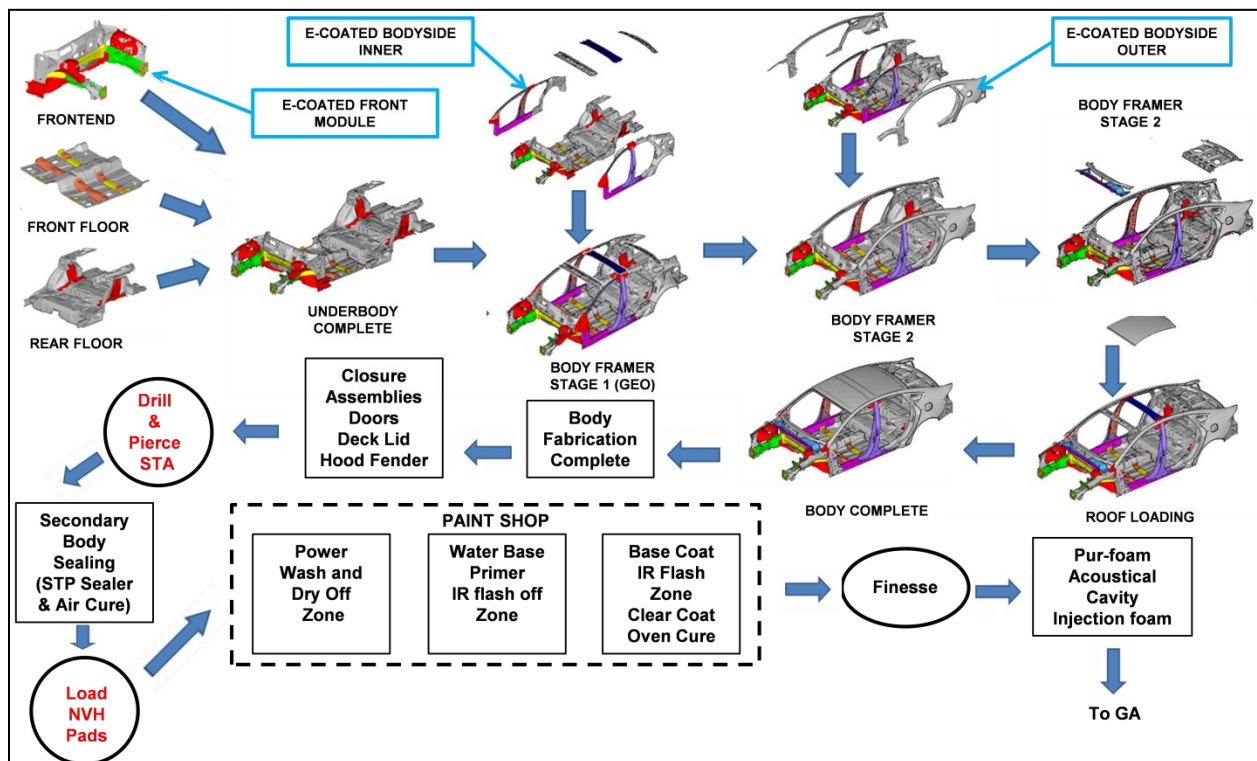


Figure V-3: Vehicle Assembly enables utilization of an existing body shop that integrates pre-coated subassemblies processed independent of the Class A components.

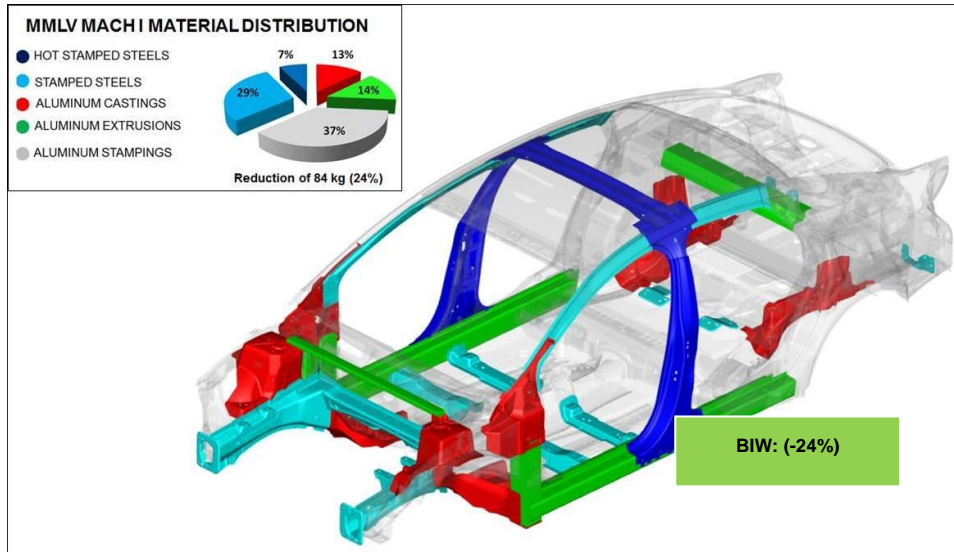


Figure V-4: Mach-I BIW.

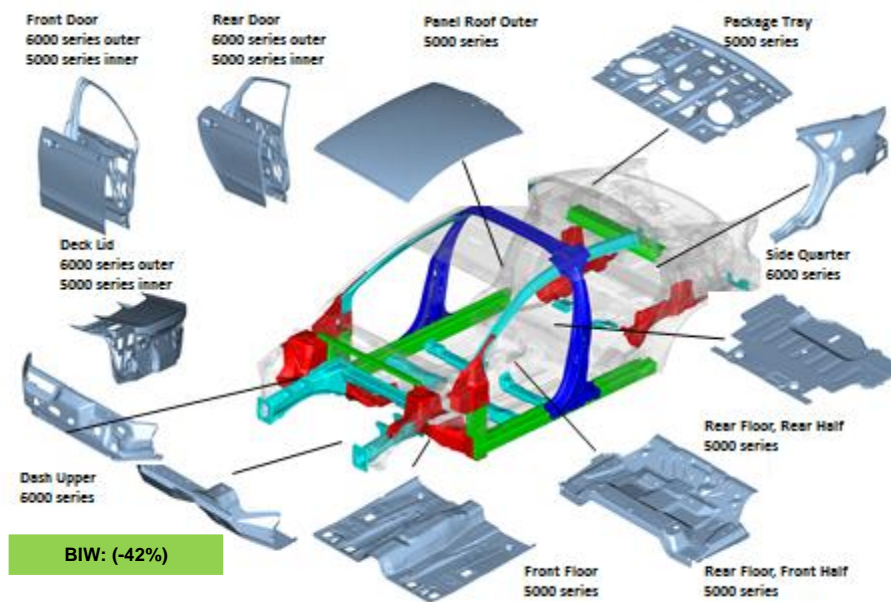


Figure V-5: Mach-I Body Panels.

Chassis and Bumper Components— Front and rear cradles are comprised of aluminum Low Pressure Permanent Mold (LPPM) castings and aluminum extrusions shown in Figure V-6. The aluminum components are joined using a metal inert gas (MIG) fusion-welding process. The LPPM casting and extrusion manufacturing processes enable incorporation of hollow sections, providing an efficient lightweight opportunity to meet the product stiffness requirements, while maintaining packaging constraints. Front and rear bumpers are comprised of 6xxx roll formed aluminum. A total mass reduction of 30kg (50%) was achieved for the chassis components and 12kg (24%) mass reduction

for bumper components relative to the baseline vehicle components.

Powertrain—The powertrain associated with the Mach-I vehicle includes the down-sized and boosted 1.0 liter three-cylinder Ford EcoBoost engine and a reduced torque capacity six-speed automatic transmission. Both the engine and transmission designs include weight savings through material substitutions. The engine design includes an aluminum cylinder block with Compacted Graphite Iron (CGI) bulkhead inserts which features fractured split main bearing caps, a composite/aluminum front cover, and a composite oil pan. Weight savings for each component are shown in Figure V-7.

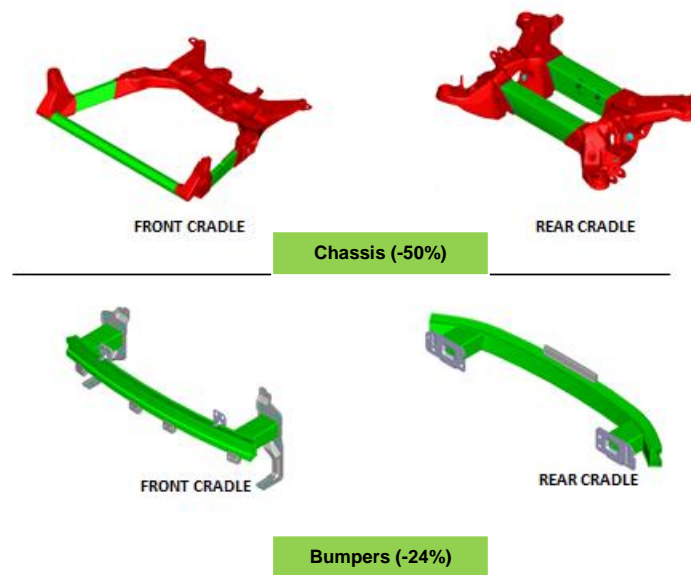


Figure V-6: Mach-I Chassis and Bumper Components.



Figure V-7: Engine weight savings investigations.

The transmission design for Mach-I envisions a lighter, reduced torque capacity six-speed automatic transmission with an magnesium case, aluminum pump support, magnesium valve body, aluminum side cover, aluminum clutch hub and aluminum bolts. Weight savings for each area of the transmission are shown in Figure V-8. Finite element analysis (stress, thermal, vibration, deflection, clamp load, formability) were completed for all planned components. The Mach-I driveline is front-wheel drive with carbon fiber drive shafts and lightweight constant velocity joints.

Interior Components—The Mach-I design for the interiors includes carbon fiber seat structures and a carbon fiber instrument panel cross-car beam as well as foamed plastic interior trim parts shown in Figure V-9. Taken together these design actions yield approximately a 20 kg weight savings over the 2002 Taurus.

Front seat-back structural design was completed and ready for tooling. Weight savings is 1.3 kg per vehicle for the seat back structure. Initial seat cushion design was completed and is currently undergoing CAE analysis and optimization. Initial design yields 1.8 kg weight savings per vehicle. Additional weight savings will be realized in the foam and trim (1~2kg) and in the mechanisms and motors (1~2kg).

Instrument Panel (IP) Beam—Design iteration resulted in a carbon fiber reinforced nylon instrument panel/cross car beam that meets design targets for vibration and strength performance shown in Figure V-10. Optimization for additional weight savings is ongoing. Current weight savings is 3.9 kg with a reduction in part count from 71 parts to 21 parts. Manufacturing feasibility and design validation to be demonstrated with the surrogate design. Mach-I design parts will be produced for the vehicle builds using low-cost prototyping methods.

NVH—The Mach-I design includes improved performance interior sound package, without weight impact. This offsets some of the sound transmission loss degradation from the lightweight body panels.

Glazing—The lightweight glazing include a polycarbonate (PC) backlite (rear window on the sedan) and a hybrid laminated chemically strengthened glass for the windshield and the side doors. The weight of the 5.0 mm thick PC backlite is 6.2 kg resulting in a 3.3 kg (35%) weight savings for the Mach-I prototype vehicle. Testing has confirmed that the lightweight backlite glazing system meets critical Federal safety requirements against Federal Motor Vehicle Safety Standards (FMVSS) 205. Side door glass bending, chemical

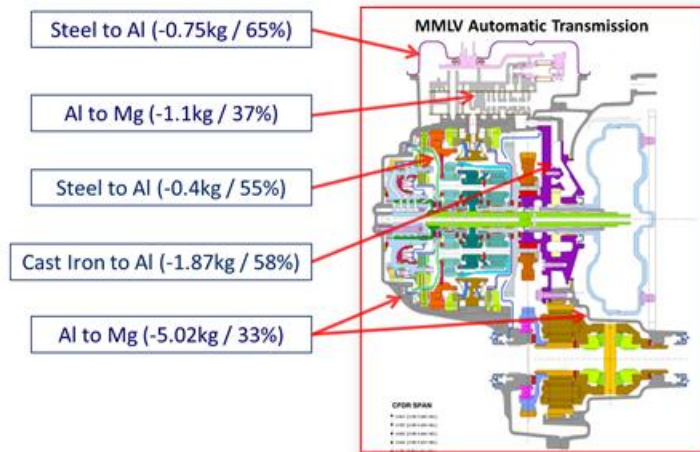


Figure V-8: Transmission weight savings investigations.



Figure V-9: Carbon Fiber seat back and cushion structures.

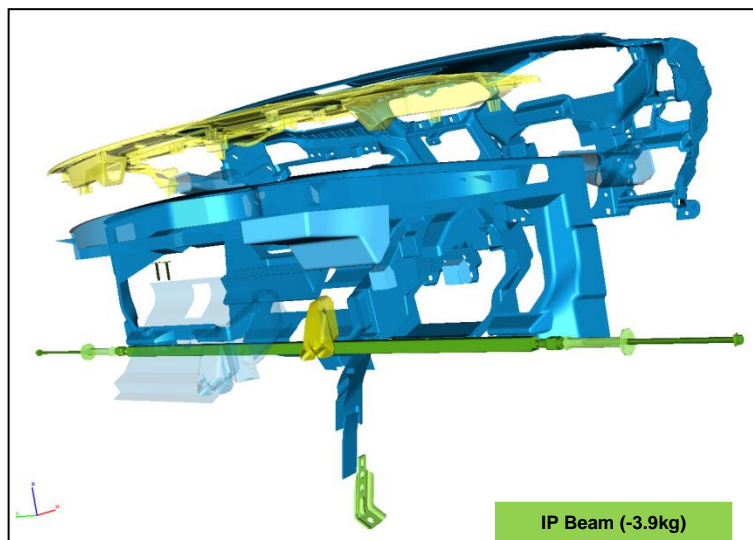


Figure V-10: Carbon fiber instrument panel cross-car beam.

strengthening and lamination for the prototypes were completed. Windshield glass bending trials are ongoing. Dimensional analysis of formed (not laminated) windshield glass is within +/- 1.0 mm after chemical strengthening. Further process investigations will be conducted to produce the prototype windshields for the Mach-I drivable vehicles. Urethane adhesive verification testing to insure adequate adhesion of all the glazing's systems into the Mach-I was validated.

**Rotors**—The Mach-I design incorporates lightweight brake rotor comprised of a cast aluminum A356 rotor that is thermally-sprayed with a stainless steel alloy to create a lightweight, wear-resistant rotor having the proper frictional values. An engineered Fe-Mn-Cr-Al austenitic steel alloy was found to have the optimum combination of coefficient of thermal expansion (CTE), corrosion resistance, friction, and wear-resistance. The rotor surfaces are sprayed with the austenitic steel alloy using a twin-wire arc-spraying method. The rotors are then ground to finished dimensions. Three (3)

rotors have undergone a series of friction durability tests (see Figure V-11) on a brake dynamometer to determine their response to operating conditions. These tests have shown that the thermal spray coating has friction equivalent to cast iron rotors.

**Tires and Wheels**—Ford has collaborated with Michelin to develop and evaluate lightweight tires based upon a unique, tall and narrow design, 155/70R19, shown in Figure V-12 for the Mach-I prototypes. The Mach-I prototype tires will be matched to a lightweight wheel. During initial testing, the lightweight, summer tread tires exhibited equivalent or preferred performance as compared to the all-season, control tire for most of the tested criteria. The testing included ride, subjective noise, steering, and wet handling, curb handling, dry braking and wet braking assessments.

Both a cast aluminum and a carbon fiber wheel are under development that is expected to provide an 8.0 kg (3.6 kg, 30% weight save) prototype tire.



Figure V-11: Aluminum brake under test.



Figure V-12: Photographs of tall/narrow prototype tire.

Coil Springs and Suspension- Three (3) lightweight coil springs have been designed and produced for the Mach-I prototype build; the composite front spring, the titanium rear spring, and the hollow steel rear spring. All three springs met the rate/load design targets and tolerance requests. The weight savings of the springs are 57%, 53%, and 37% respectively. Dry fatigue test for all three spring designs were

completed. The corrosion fatigue tests will be completed in 1Q14. The composite springs will undergo additional tests with mixed fatigue plus environmental exposure and resistance to automotive fluids. Figure V-13 shows the rate/load test for composite springs with all three required loading positions, normal, rebound, and jounce.

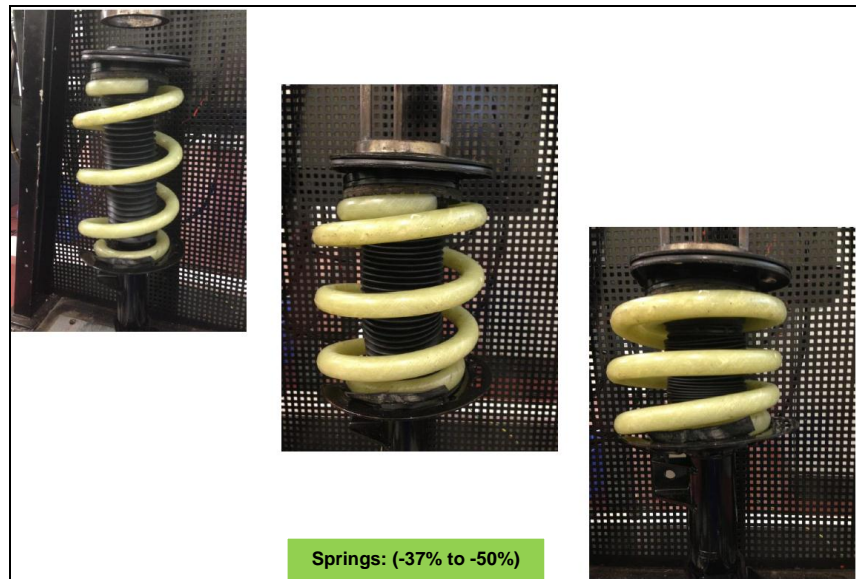


Figure V-13: Composite front spring at different loading conditions.

The design and development of the hollow steel front and rear stabilizer bars for Mach-I are proceeding. The load and stiffness testing proved the designs meet specifications. Initial fatigue testing is underway.

### Mass Summary

#### Mach-I Vehicle

Component masses associated with the MMLV Mach-I vehicle design have been sorted into the 73 bins from the DOE investigations of the “average 2002 model year sedan”. The data presented in Table V-1 is an illustrative example of potential weight savings for the MMLV. The comparisons of any single line item prove difficult, since the details of the assumptions behind assigning components into each of the 73 bins are not clearly defined. However, all the 1195-kg weight of the MMLV has been distributed into the 73 bins.

*NOTE: The “Average Sedan” is **not** associated with the 2002 Ford Taurus, or the 2014 Ford Fusion C/D segment baseline vehicle.*

#### Mach-II Vehicle

In Q3-2013, the Mach-II design concept was released for the BIW, Closure, and Chassis assemblies and targeted the

50% mass reduction criteria associated with the Mach II design. The Mach-II design includes CF composites, magnesium and aluminum to achieve the weight optimization of the BIW, closures, and chassis structure. Joining techniques for these multi-material designs will be finalized after the initial weight reduction exercise is complete.

Body Panels—The Mach-II vehicle design will incorporate aluminum or magnesium sheet products for the Class A panels. Carbon fiber and composites were deemed not feasible for “Class A” applications, due to appearance requirements and process cycle time requirements potentially available in the 2025 timeframe.

BIW- The Mach-II BIW design retains the aluminum and UHSS components in the impact related areas of the vehicle. Aluminum is being evaluated, to replace steel for the front module rails. Roof Crossmember and B-Pillar inner and outer components were released as press-hardened steels (yield 2000 MPa) to address roof crush and side impact requirements. The conceptual design is shown in Figure V-14. Mach-II design release is scheduled for completing in Q1-2014.

**Table V-1: MMLV Mach-I Weight Comparison by System Against the DOE 2002 Baseline Average Sedan.**

| Mass Distribution of Major Components in a 2002 Baseline Vehicle (based on DOE averages) |                              | 2002 DOE Average Baseline | MMLV Mach-I Design |
|--|------------------------------|---------------------------|--------------------|
|  |                              | Mass (kg)                 | Mass (kg)          |
| <b>Powertrain</b>  |                              | <b>483.1</b>              | <b>253.2</b>       |
| Engine   | Crankshaft                   | 18.3                      | 6.5                |
|  | Cylinder Head                | 21.8                      | 9.0                |
|  | Cylinder Block               | 41.3                      | 14.6               |
|  | Oil Pan Assembly             | 5.5                       | 5.9                |
|  | Camshafts                    | 3.6                       | 3.5                |
|  | Valve Roller Rocker          | 1.6                       | 3.2                |
|  | Other                        | 62.4                      | 12.2               |
| Energy Storage   | Energy Storage               | 17.7                      | 8.0                |
| Fuel System  | Fuel Tank                    | 58.3                      | 52.2               |
|  | Other                        | 5.5                       | 7.1                |
| Transmission   | Case                         | 27.3                      | 13.2               |
|  | Gears and Shaft              | 22.7                      | 8.0                |
|  | Clutch                       | 33.6                      | 6.0                |
| Driveshaft/Axle  | Other                        | 25                        | 49.8               |
|  | Driveshaft assembly          | 8.7                       | 6.6                |
| Differential   | CV joint                     | 19                        | 8.1                |
|  | Drive bearings               | 3.2                       |                    |
| Cradle   | Case                         | 4.5                       |                    |
|  | Gears                        | 5                         |                    |
|  | Other                        | 32.3                      | 15.0               |
| P/T Thermal  | Radiator                     | 4.8                       |                    |
|  | Radiator fan assembly        | 6.6                       |                    |
|  | Radiator fan motor           | 1.5                       |                    |
|  | Other                        | 5.5                       | 1.7                |
| Exhaust System   | Exhaust manifold             | 7.3                       | 0.8                |
|  | Catalytic converter          | 3.2                       | 5.8                |
|  | Muffler                      | 5.1                       | 9.7                |
|  | Other                        | 6.7                       |                    |
| Powertrain Electrical  | Engine control module        | 1.4                       | 1.8                |
|  | Power electrical             | 4.4                       |                    |
|  | Alternator                   | 6                         |                    |
| Emission Control Electronics   | Emission Control Electronics | 1.2                       | 0.6                |
| Oil and Grease   | Oil and Grease               | 12.1                      | 4.0                |
| <b>Body</b>  |                              | <b>447.2</b>              | <b>404.2</b>       |
| BIW  | BIW                          | 320.5                     | 250.2              |
|  | Panels                       | 60                        | 68.8               |
| Front/Rear Bumper  | Impact module                | 5.5                       | 11.6               |
|  | Other                        | 4.5                       | 14.3               |
| Glass  | Glass                        | 21.8                      | 24.9               |
| Paint  | Paint                        | 12                        | 7.7                |
| Exterior Trim  | Exterior Trim                | 10.9                      | 21.4               |
| Body Hardeners   | Body Hardeners               | 10                        |                    |
| Body Sealer & Deadners   | Body Sealer & Deadners       | 2                         | 5.3                |

| Mass Distribution of Major Components in a 2002 Baseline Vehicle (based on DOE averages) |                          | 2002 DOE Average Baseline | MMLV Mach-I Design |
|--|--------------------------|---------------------------|--------------------|
|  |                          | Mass (kg)                 | Mass (kg)          |
| <b>Chassis</b>   |                          | <b>301.7</b>              | <b>251.0</b>       |
| Corner Suspension  | Upper front control arms | 15.9                      |                    |
|  | Lower front control arms | 11.4                      | 7.6                |
|  | Rear control arms        | 7.7                       | 31.8               |
| Braking Systems  | Other                    | 98.6                      | 61.7               |
|  | Steering Knuckle         | 6.2                       | 4.7                |
|  | Rotor                    | 27.2                      | 17.0               |
| Wheels and Tires   | Assembly Calliper        | 15.6                      | 21.6               |
|  | Other                    | 20.6                      | 20.9               |
| Steering System  | Wheel                    | 28.2                      | 31.0               |
|  | Tires                    | 29.3                      | 35.0               |
| Steering System  | Steering column assembly | 39.2                      | 16.9               |
|  | Steering wheel w/ airbag | 1.8                       | 2.8                |
| <b>Interior</b>  |                          | <b>245.1</b>              | <b>286.4</b>       |
| Instrument Panel   | IP Cockpit               | 15.6                      |                    |
|  | Beam assembly            | 9.3                       | 13.7               |
|  | Bracket assembly         | 4.5                       | 6.5                |
|  | Other                    | 2.3                       | 11.5               |
| Trim and Insulation  | Accessories              | 6.1                       | 20.3               |
|  | Carpet                   | 19.5                      | 13.6               |
|  | Overhead trim            | 15.2                      | 4.5                |
| Door Modules   | Door trim assembly       | 18.3                      | 38.1               |
|  | Garnish                  | 11.4                      | 4.4                |
| Seating and Restraints   | Seat assembly            | 65.5                      | 41.8               |
|  | Airbag assembly          | 14.9                      | 8.0                |
|  | Restraints               | 7.3                       | 8.6                |
| HVAC   | HVAC system              | 9.1                       | 20.4               |
|  | Radiator                 | 4.8                       | 15.3               |
| Electrical   | Other                    | 7.3                       | 4.9                |
|  | Interior                 | 3.1                       | 25.1               |
| Assembly   | Chassis                  | 3.1                       | 19.0               |
|  | Exterior Lighting        | 17.7                      | 8.9                |
| Assembly   | Assembly                 | 10.1                      | 21.9               |
|  | <b>Total (kg)</b>        | <b>1477</b>               | <b>1195</b>        |

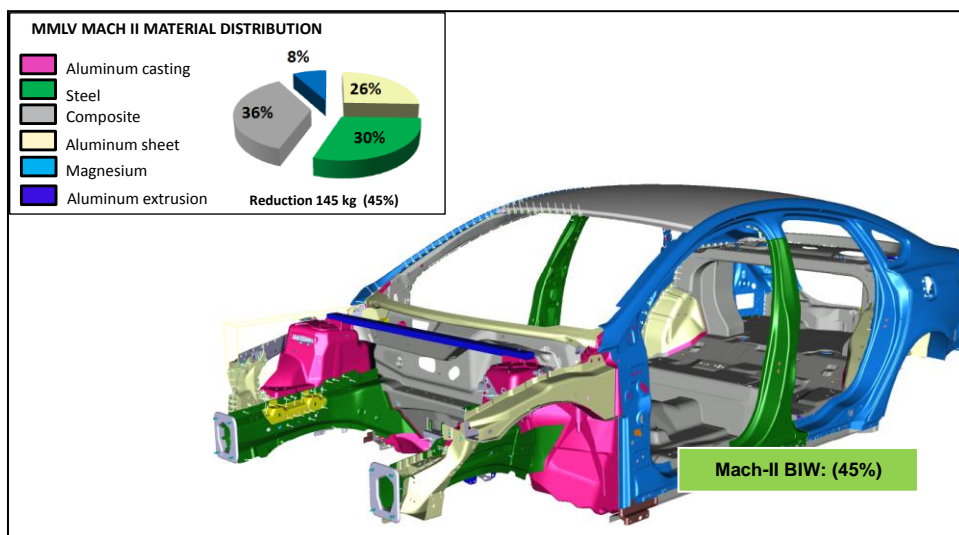


Figure V-14: Mach-II BIW “Concept Release.”

**Powertrain**—The Mach-II design includes a naturally-aspirated, direct-injection, one-liter, and three-cylinder gasoline engine. A number of investigations have begun to further reduce the engine weight from the Mach-I design. Along with removing the turbocharger and associated content, alternative materials are being investigated for the engine block and other major components. The transmission selection has been narrowed to two candidates and will be completed in Q1-2014.

**Interior Components and Other Components**—The Mach-II design team is considering increasing the use of carbon fiber and magnesium for the interiors, suspension and other vehicle systems, as well as reductions in vehicle content/features which include motorized seats and windows.

### Technology Transfer Path

The technology integration of this project will transition and be applied by Ford Motor Company on near future product platforms. Additionally, this technology will be applied by Magna International on future OEM development projects and production intent designs for automotive and heavy truck designs.

### Conclusions

The MMLV Mach-I vehicle design resulted in a 22% reduction in weight as compared to the 2002 Taurus baseline vehicle. Weight reduction barriers included evolution of FMVSS standards from 2002 to 2012, donor vehicle architecture packaging constraints and project scope limitations to peruse further mass reduction opportunities such as lightweighting the transmission and driveline. Mach-I prototype vehicle results are currently being integrated with 2014 donor vehicles designs with completion scheduled for Q2-2014. Physical testing associated with Mach-I vehicles will be completed in Q3-2014.

### Presentations/Publications/Patents

1. Kotagiri, Swamy (Magna EVP) and Zaluzec, Mathew (Ford), MMLV Project, Automotive Day Detroit, LanXess, August 7, 2013.
2. Conklin, Jeff; Multi-Material Lightweight Vehicle (MMLV) Project, DOE Vehicle Technologies Program 2013 Annual Merit Review and Peer Evaluation, May 15, 2013
3. Multi-Material Lightweight Vehicle (MMLV) Project, Magna Executive Board Technical Review (EBTR) Meeting, October 30, 2012. (Note: Vice President of Ford Motor Company and Chief Engineer representatives were present)
4. Multi-Material Lightweight Vehicle (MMLV) Project, Global Technology Meeting (GTM), October 23, 2012 (Note: Raj Nair, Senior VP for Product Development of Ford Motor Company and six other VPs in Ford Product Development were present.)

### References

No references during this reporting period.

## V.2. Safety Data and Analysis—Lawrence Berkeley National Laboratory

### **Tom Wenzel (Principal Investigator)**

Lawrence Berkeley National Laboratory  
1 Cyclotron Road, 90R4000  
Berkeley, CA 94720  
Phone: (510) 486-5753  
E-mail: [TPWenzel@lbl.gov](mailto:TPWenzel@lbl.gov)

### **Carol Schutte, Technology Area Development Manager**

U.S. Department of Energy  
1000 Independence Avenue, S.W.  
Washington, DC 20585  
Phone: (202) 287-5371  
E-mail: [carol.schutte@ee.doe.gov](mailto:carol.schutte@ee.doe.gov)

Contractor: Lawrence Berkeley National  
Laboratory (LBNL)  
Contract No.: DE-AC02-05CH11231

### **Abstract/Executive Summary**

In FY2013 LBNL summarized its results of the relationship between vehicle mass and size on U.S. societal fatality risk per vehicle mile traveled in three articles submitted to journals; two have been published, and one is still under review. LBNL also conducted several analyses to test the sensitivity of the results obtained in FY2012 on the estimated effect of vehicle mass or size reduction on U.S. societal fatality risk per vehicle mile traveled. First, similar to the method developed by Dynamic Research, Inc. (DRI), we created a two-stage logistic regression model to simultaneously estimate the relationships on vehicle crash frequency and crashworthiness/compatibility. We used the model to assess the sensitivity of several changes in the DRI approach. Second, using data obtained by the Environmental Protection Agency (EPA) from Consumer Reports, we estimated the effect of vehicle braking and handling test results on crash frequency. Third, we modeled the relationship of total fatalities by vehicle model and calendar year with vehicle mass or size, after including vehicle miles of travel (VMT) as an independent explanatory variable (that is, on the right-hand side of the regression equation). Fourth, we used linear regression to estimate the effect vehicle, driver, and crash characteristics have had on fatality risk per VMT in each U.S. state over 18 years. Fifth, we added driver seat belt and alcohol/drug use to the National Highway Traffic Safety Administration (NHTSA) database, and estimated the effect of adding these two variables to the estimated relationship between vehicle mass and size and U.S. societal fatality risk. We prepared several draft reports summarizing our findings for these analyses. Finally, we began assembling data on vehicle miles traveled for individual

vehicles and households, using odometer readings and vehicle registration data over several years in California and Texas, to begin estimating what effect recent changes in gasoline prices and economic conditions have had on vehicle miles traveled. This analysis will include examination of trends in police-reported crashes over time in 18 states to better understand what vehicles and drivers may have reduced their travel in response to changing fuel prices and economic conditions.

### **Accomplishments**

- Conducted research on the relationship between vehicle weight/size and safety, in support of federal agency rulemakings on fuel economy/greenhouse gas emission standards for new light-duty vehicles. Prepared three journal articles summarizing the results of this research; two have been published, and one is under review.
- Presented results at TRB UTC conference, two-day NHTSA workshop on relationship between vehicle weight/size and safety, DOE Annual Merit Review, and National Research Council (NRC) fuel economy committee meeting.
- Reviewed a report by Dynamic Research, Inc. which uses a simultaneous two-stage regression model to estimate the two components of fatality risk per mile traveled: crash frequency (crashes per mile traveled), and fatality risk per crash. Replicated the DRI regression model, and updated the model to include the same data NHTSA used in its regression analyses.
- Analyzed 13 tests of vehicle braking and handling for 491 vehicles that EPA obtained from Consumer Reports. Tested the effect of including 3 of these test results in LBNL's Phase 2 regression model of crash frequency per vehicle mile traveled.
- Conducted two new analyses of the sensitivity of the results obtained in FY2012 on the estimated effect of vehicle mass or size reduction on U.S. societal fatality risk per vehicle mile traveled: including vehicle miles of travel by vehicle model as an independent explanatory variable; and including whether the driver was wearing a seat belt or using alcohol or drugs at the time of the crash.
- Conducted a new linear regression analysis of state-level data estimating the effect vehicle, driver, and crash characteristics have on fatality risk per VMT in each U.S. state over the last 18 years.
- Began assembling seven years of vehicle odometer and registration data from California and Texas to assess how changing gasoline prices and economic conditions have influenced consumer vehicle purchase decisions and vehicle use, by household.

## Future Directions

- Continue to examine several aspects of the relationship between vehicle mass or footprint, and fatality risk per VMT, crash frequency per VMT, and fatality risk per crash.
- Analyze annual vehicle odometer data from the Texas vehicle emission inspection program to understand how driving activity changed in response to the economic downturn, and increased gas prices, in 2008. The reduction in driving likely contributed to the large decline in fatalities in 2008.



## Introduction

Reducing vehicle mass is perhaps the easiest and least-costly method to reduce fuel consumption and greenhouse gas emissions from light-duty vehicles. However, the extent to which government regulations should encourage manufacturers to reduce vehicle mass depends on what effect, if any, light-weighting vehicles is expected to have on societal safety. As part of an interagency analysis effort between NHTSA, EPA, and DOE, LBNL has been examining the relationship between vehicle mass and size and U.S. societal fatality and casualty risk, using historical data on recent vehicle designs. This research effort informs the agencies on the extent to which vehicle mass can be reduced in order to meet fuel economy and greenhouse gas emissions standards, without compromising the safety of road users.

The final versions of the safety analyses LBNL conducted in support of the federal rulemakings for fuel economy and greenhouse gas emissions standards for model year 2017 to 2024 were published in late 2012 (Wenzel 2012a and b). In FY2013, LBNL summarized the results of these analyses in several journal articles (Wenzel 2013b, c, and g) and presentations (Wenzel 2012c, Wenzel 2013d, e, f), replicated and evaluated DRI's two-stage logistic regression model (Wenzel 2013a), and conducted several additional analyses of the sensitivity of the results to including additional control variables in the regression models.

## Results and Discussion

The approach taken, results, and conclusions from each of the additional analyses LBNL conducted are discussed separately below.

### 1. Review of DRI 2-stage regression model

DRI developed a 2-stage regression model that simultaneously estimates the effect of mass or footprint reduction on the two components of fatality risk per VMT: crash frequency (crashes per VMT) and crashworthiness/compatibility (fatalities per crash; Van Auken and Zellner 2012a). LBNL replicated the DRI 2-stage model, but was not able to exactly replicate its results (Wenzel 2013a). LBNL noted discrepancies in how DRI and LBNL classified the state police-reported crash data into crash types;

in particular, DRI appeared to underestimate the number of crashes of all types in Pennsylvania. In addition, LBNL identified more vehicles involved in crashes with a heavier-than-average truck, but fewer vehicles involved in crashes with a heavier-than-average car than DRI. This suggests either that DRI and LBNL are using different average curb weights to define lighter- and heavier-than-average cars and light trucks, or that DRI is classifying certain light truck models as cars (or alternatively LBNL is classifying certain car models as light trucks).

LBNL compared the results from the NHTSA 2012 and DRI 2012a reports with five alternate regression models: using the 10 states DRI used and decimated crash data based on DRI's method; using the 10 states and an alternative sample of decimated crash data; using the 13 states NHTSA used and decimated crash data; using the 13 states and all crash data; and using the 13 states and all crash data, including duplicated data for missing calendar years in three states and only including cases where reported model year matches the model year decoded from the vehicle identification number (VIN). The top section of Table V-2 shows the comparison for fatality risk per crash, the middle section shows the comparison for crashes per VMT, and the bottom section shows the comparison for fatality risk per VMT.

In general, Table V-2 suggests that the estimated associations between mass or footprint reduction and crash frequency, fatality risk per crash, and fatality risk per VMT can be sensitive to changes in what data are used in the analysis, or even the particular vehicles included in the decimation sample (comparing the results from LBNL models 1 and 2).

DRI argued that using non-culpable vehicles in two-vehicle crashes as a proxy for all vehicles travelling on road may understate the risk exposure measured by VMT of vehicle/driver combinations that could have avoided a two-vehicle crash. DRI proposed using stopped vehicles struck by another vehicle, rather than the vehicle determined not to be at fault, as a proxy for the distribution of vehicle/driver combinations on the road to be used for induced exposure. While this proposal makes sense, it must be recognized that using stopped rather than non-culpable vehicles dramatically reduces the number of vehicles in the police-reported crash data available for the induced exposure data: there are 2,242,871 non-culpable vehicles in the NHTSA dataset, while there are only 610,689 (73% fewer) stopped vehicles in the alternate dataset NHTSA developed on DRI's recommendation.

LBNL demonstrated that there are slightly smaller fractions of crashes at night, in rural counties, on high-speed roads, and with male, young, or old drivers in stopped vehicles than in non-culpable vehicles. This suggests that stopped vehicles are less influenced by these risky crash or driver characteristics than non-culpable vehicles; there are much larger fractions of vehicles characterized by these risk factors in the entire database of police-reported crashes than in the two subsets used for the induced exposure. However, there are slightly higher fractions of crashes involving risky sporty or

**Table V-2: DRI 2-stage and alternate LBNL 2-stage estimates of the effect of mass or footprint reduction on U.S. societal fatality risk per crash (crashworthiness/compatibility), crashes per VMT (crash frequency), and fatality risk per VMT.**

|                      | Variable            | Case vehicle type | A. NHTSA 1-stage estimate | B. DRI 2-stage estimate | C. Alternate LBNL 2-stage estimates  |  |                                    |                              |   |
|----------------------|---------------------|-------------------|---------------------------|-------------------------|--------------------------------------|--|------------------------------------|------------------------------|---|
|                      |                     |                   |                           |                         | 1. 10 states, decimated crash data * | 2. 10 states, alternate decimated crash data | 3. 13 states, decimated crash data | 4. 13 states, all crash data | 5. 13 states, all crash data, duplicated data, where MY matches |
| Fatalities per crash | Mass reduction      | Cars < 3106 lbs   | —                         | -0.51%                  | -0.35%                               | -0.29%                                       | -0.55%                             | -0.53%                       | -0.65%  |
|                      |                     | Cars > 3106 lbs   | —                         | 0.42%                   | 0.65%                                | 0.65%  | -0.16%                             | -0.51%                       | -1.12%  |
|                      |                     | LTs < 4594 lbs    | —                         | -0.80%                  | -1.46%                               | -1.11%                                       | -0.97%                             | -0.96%                       | -1.03%  |
|                      |                     | LTs > 4594 lbs    | —                         | -1.17%                  | -1.15%                               | -1.01%                                       | -1.11%                             | -1.56%                       | -1.59%  |
|                      |                     | CUV/minivan       | —                         | -0.96%                  | -1.34%                               | -1.35%                                       | -1.02%                             | -1.42%                       | -1.53%  |
|                      | Footprint reduction | Cars              | —                         | 0.20%                   | -0.45%                               | -0.48%                                       | 0.57%                              | 0.95%                        | 1.25%   |
| LTs                  |                     | —                 | -1.81%                    | -1.57%                  | -1.84%                               | -1.63%                                       | -1.46%                             | -1.37%                       |   |
| CUV/minivan          |                     | —                 | 1.64%                     | 1.65%                   | 1.60%                                | 1.49%  | 2.41%                              | 2.57%                        |   |
| Crashes per VMT      | Mass reduction      | Cars < 3106 lbs   | —                         | 2.10%                   | 1.83%                                | 1.86%  | 1.95%                              | 1.84%                        | 1.96%   |
|                      |                     | Cars > 3106 lbs   | —                         | 0.16%                   | -0.10%                               | -0.05%                                       | 0.75%                              | 0.77%                        | 1.41%   |
|                      |                     | LTs < 4594 lbs    | —                         | 1.41%                   | 1.81%                                | 1.50%  | 1.30%                              | 1.29%                        | 1.41%   |
|                      |                     | LTs > 4594 lbs    | —                         | 0.83%                   | 0.76%                                | 0.67%  | 0.71%                              | 1.04%                        | 1.08%   |
|                      |                     | CUV/minivan       | —                         | 0.52%                   | 0.86%                                | 0.83%  | 0.62%                              | 0.80%                        | 0.89%   |
|                      | Footprint reduction | Cars              | —                         | 1.20%                   | 2.26%                                | 2.25%  | 1.27%                              | 1.08%                        | 0.81%   |
| LTs                  |                     | —                 | 1.59%                     | 1.28%                   | 1.45%                                | 1.35%  | 1.20%                              | 1.09%                        |   |
| CUV/minivan          |                     | —                 | 0.31%                     | 0.15%                   | 0.29%                                | 0.25%  | -0.44%                             | -0.58%                       |   |
| Fatalities per VMT   | Mass reduction      | Cars < 3106 lbs   | 1.56%                     | 1.58%                   | 1.48%                                | 1.57%  | 1.40%                              | 1.31%                        | 1.30%   |
|                      |                     | Cars > 3106 lbs   | 0.52%                     | 0.58%                   | 0.55%                                | 0.59%  | 0.59%                              | 0.27%                        | 0.29%   |
|                      |                     | LTs < 4594 lbs    | 0.52%                     | 0.61%                   | 0.36%                                | 0.39%  | 0.33%                              | 0.33%                        | 0.38%   |
|                      |                     | LTs > 4594 lbs    | -0.34%                    | -0.34%                  | -0.39%                               | -0.34%                                       | -0.40%                             | -0.52%                       | -0.51%  |
|                      |                     | CUV/minivan       | -0.37%                    | -0.45%                  | -0.48%                               | -0.52%                                       | -0.40%                             | -0.62%                       | -0.64%  |
|                      | Footprint reduction | Cars              | 1.89%                     | 1.40%                   | 1.80%                                | 1.78%  | 1.84%                              | 2.03%                        | 2.06%   |
| LTs                  |                     | -0.07%            | -0.23%                    | -0.29%                  | -0.38%                               | -0.28%                                       | -0.25%                             | -0.28%                       |   |
| CUV/minivan          |                     | 1.73%             | 1.96%                     | 1.80%                   | 1.89%                                | 1.74%  | 1.96%                              | 1.99%                        |   |

Estimates that are statistically significant at the 95% level based on regression model standard errors are shown in red. Using a jack-knife method to estimate uncertainty, NHTSA found that only the mass reduction in lighter-than-average cars is statistically significant.

\* DRI estimates using decimated data for 10 states. Estimates for track width and wheelbase reductions in cars and light trucks are the weighted average DRI estimates by crash partner weight based on the number of fatalities.

all-wheel drive (AWD) cars using stopped rather than non-culpable vehicles. On balance, stopped vehicles, and their drivers, are slightly less risky than non-culpable vehicles/drivers, and therefore may better represent the actual population of on-road vehicles. However, using stopped rather than non-culpable vehicles substantially reduces the sample of vehicles available for the induced exposure dataset.

LBNL estimated the sensitivity of the combination of the two changes suggested by DRI, replacing footprint with wheelbase and track width, and using stopped rather than non-culpable vehicles as the basis for induced exposure, as shown in Table V-3. The table compares NHTSA's 1-stage fatality risk per VMT estimates with the DRI and LBNL 2-stage estimates for fatality risk per VMT, as well as for fatality risk per crash and crash frequency per VMT. The LBNL estimates are from model 5 in Table V-2, which uses all crash data from 13 states (including an internal control variable for each state except Florida), as well as duplicate data for four state/CY combinations with missing data, while excluding vehicles where the model year reported in the state crash data did not match the decoded VIN. This dataset most closely resembles the methodology NHTSA used in its analyses.

Comparing columns A, D, and G in Table V-3, the three estimates for fatality risk per VMT, the DRI estimates more closely match the NHTSA estimates for mass reduction in cars and crossover utility vehicles (CUVs)/minivans, track width reduction in CUVs/minivans, and wheelbase reduction in cars; all of these estimates are small, and none are statistically-significant. On the other hand, the LBNL estimates more closely match the NHTSA estimates for mass reduction in light trucks, track width reduction in cars and light trucks, and wheelbase reduction in light trucks and CUVs/minivans; five of these six estimates are statistically-significant.<sup>3</sup>

In terms of fatalities per crash (comparing columns B and E), LBNL estimates a more beneficial effect than DRI from mass reduction in cars, heavier-than-average light trucks, and CUVs/minivans; from track width reduction in light trucks; and from wheelbase reduction in CUVs/minivans. In terms of crash frequency per VMT (comparing columns C and F), LBNL estimates a more beneficial effect than DRI from mass reduction only in lighter-than-average light trucks, from track width reduction only in CUVs/minivans, but from wheelbase reduction in all three types of vehicles. LBNL estimates a fairly large (1.37%) statistically-significant reduction in crash frequency per VMT from track width reduction in CUVs/minivans.

## 2. Analysis of vehicle handling and braking ratings from Consumer Reports

In its analyses of the relationship between vehicle mass and fatality risk, NHTSA has noted that crash frequency tends to increase as vehicle mass decreases. This runs counter to the expectation that lighter, and perhaps smaller, vehicles have better handling and shorter braking distances, and thus

should be able to avoid crashes that heavier vehicles cannot. NHTSA has speculated that additional differences in who drives lighter vehicles, other than their age and gender, and how they are driven, may explain this somewhat unexpected result. LBNL's analysis of 13-state casualty risk per crash (Wenzel 2012b, as well as DRI and LBNL analyses of U.S. fatalities per police-reported crash using a simultaneous two-stage regression model (Van Auken and Zellner 2012a and Wenzel 2013a) confirms this phenomenon; vehicles of lower mass are associated with increased crash frequency for all three types of vehicles, with larger increases in crash frequency for lighter-than-average cars or light trucks. Understanding this phenomenon is important because the LBNL and DRI analyses indicate that any increases in risk per VMT associated with mass reduction are the result of the association of mass reduction with crash frequency and not with risk once a crash has occurred (crashworthiness/compatibility i.e., fatalities per crash).

A combination of vehicle design (other than mass, footprint, or safety features installed) and driver behavior (other than age and gender) may influence the relationship between reduced mass and increased crash frequency. Vehicle design may influence both crash frequency and risk per crash; however, driver behavior most likely only influences crash frequency. Handling and braking test results should account for the vehicle design influence on crash frequency; initial vehicle purchase price may account for the influence of vehicle design on both crash frequency and risk per crash. Alcohol/drug use, poor or risky driving behavior, driver income, and seat belt use are likely to influence driver behavior. Adding these variables to the regression model may change the estimated relationship between vehicle mass and crash frequency. In the LBNL 2012 Phase 2 report (Wenzel 2012b), adding vehicle purchase price to the regression model substantially reduced the estimated increase in crash frequency from mass reduction for all five vehicle types. On the other hand, adding median household income had essentially no effect on the estimated increase in crash frequency from mass reduction. These results suggest that vehicle parameters may be influencing the somewhat unexpected increase in crash frequency from mass reduction.

LBNL examined what effect vehicle braking and handling characteristics have on the relationship between mass reduction and crash frequency. Consumer Reports provided EPA a database of braking and handling test results for 491 vehicles, from model years 2000 to 2007. LBNL added three of the Consumer Reports tests, maximum speed obtained during the avoidance maneuver test, acceleration time from 45 to 60 mph, and dry braking distance, to the database used to estimate the effect of mass reduction in cars on crash frequency, from Wenzel 2012b. (We did not extend this regression analysis to CUVs/minivans or light trucks because nearly half of the CUV/minivan models could not be matched with Consumer Reports data, and Consumer Reports did not test any heavy-duty truck models, and did not report the drive configuration, cab or bed size of the pickup and sport utility vehicle (SUV) models it did test.)

<sup>3</sup> NHTSA used a jack-knife method to estimate uncertainty and found that only the mass reduction in lighter-than-average cars is statistically significant.

**Table V-3: Comparison of DRI and LBNL estimated effect of mass, track width, or wheelbase reduction on U.S. societal fatality risk per crash, crash frequency per VMT, and fatality risk per VMT.**

| Variable              | Case vehicle type | A. NHTSA 1-stage (fatalities per VMT) | DRI 2-stage estimate*                                   |                                      |                                  | LBNL 2-stage estimate**                                 |                                      |                                  |
|-----------------------|-------------------|---------------------------------------|---|--------------------------------------|----------------------------------|---|--------------------------------------|----------------------------------|
|                       |                   |                                       | B. Crashworthiness/compatibility (fatalities per crash) | C. Crash avoidance (crashes per VMT) | D. Combined (fatalities per VMT) | E. Crashworthiness/compatibility (fatalities per crash) | F. Crash avoidance (crashes per VMT) | G. Combined (fatalities per VMT) |
| Mass reduction        | Cars < 3106 lbs   | 0.26%                                 | -1.05%  | 1.42%                                | 0.36%                            | -1.26%  | 1.71%                                | 0.45%                            |
|                       | Cars > 3106 lbs   | -0.90%                                | -0.36%  | -0.12%                               | -0.48%                           | -2.19%  | 1.87%                                | -0.32%                           |
|                       | LTs < 4594 lbs    | -0.10%                                | -0.70%  | 0.75%                                | 0.06%                            | -0.54%  | 0.42%                                | -0.12%                           |
|                       | LTs > 4594 lbs    | -0.97%                                | -1.34%  | 0.50%                                | -0.84%                           | -1.68%  | 0.83%                                | -0.85%                           |
|                       | CUV/minivan       | -0.14%                                | -0.61%  | 0.39%                                | -0.22%                           | -1.39%  | 0.92%                                | -0.47%                           |
| Track width reduction | Cars              | 6.04%                                 | 1.34%   | 1.03%                                | 2.37%                            | 3.66%   | 1.11%                                | 4.78%                            |
|                       | LTs               | 0.90%                                 | -0.82%  | 1.23%                                | 0.41%                            | -2.14%  | 2.81%                                | 0.68%                            |
|                       | CUV/minivan       | -0.55%                                | -0.44%  | 0.13%                                | -0.31%                           | 0.33%   | -1.37%                               | -1.04%                           |
| Wheelbase reduction   | Cars              | 0.38%                                 | -0.43%  | 0.81%                                | 0.38%                            | 0.30%   | 0.18%                                | 0.47%                            |
|                       | LTs               | -0.09%                                | -1.12%  | 0.77%                                | -0.35%                           | -0.44%  | 0.21%                                | -0.23%                           |
|                       | CUV/minivan       | 1.45%                                 | 2.20%   | 0.45%                                | 2.65%                            | 1.82%   | 0.04%                                | 1.86%                            |

Estimates that are statistically significant at the 95% level based on regression model standard errors are shown in red. Using a jack-knife method to estimate uncertainty, NHTSA found that only the mass reduction in lighter-than-average cars is statistically significant.

\* DRI estimates using decimated data for 10 states. Estimates for track width and wheelbase reductions in cars and light trucks are the weighted average DRI estimates by crash partner weight based on the number of fatalities.

\*\* LBNL estimates using all non-fatal crash data for 13 states (with 12 internal control variables), duplicated data for missing state/CY combinations, and where the MY reported in state crash data matches the decoded VIN.

Table V-4 compares the results of five alternative regression models estimating the effect on overall car crash frequency (crashes per vehicle mile traveled, or VMT), to NHTSA's baseline model (from LBNL Phase 2 report). For each of the models in the table, a single regression is run across all nine types of crashes (rather than running a separate regression for each of the nine crash types, and then reweighting the estimated regression coefficients by the number of fatalities in each type of crash assuming full penetration of Electronic Stability Control (ESC) technology; see Kahane 2012 and Wenzel 2012b. For simplicity, the regression estimates presented here are not converted from odds to probabilities, as they were in Wenzel 2012b). Estimates in the expected direction (i.e., where a better handling or braking test result is associated with lower crash frequency) are shown in green text in Table V-4, while estimates in the opposite direction as expected are shown in red text.

The first model limits the analysis to those car models that could be matched to Consumer Reports test results; almost 90% of cars involved in crashes were matched to Consumer

Reports data. Limiting the analysis to matched car models has little effect on the estimated effect of mass or footprint reduction on crash frequency. Model 2 adds MANEUVER, the maximum speed (in miles per hour) the vehicle obtained on the avoidance maneuver test; a higher value indicates better handling. Model 2 estimates that for each additional mile per hour achieved on the test, overall crash frequency increases 0.53%; this suggests that better results on this handling test increases crash frequency, an unexpected result. Model 3 adds the ACC45TO60 test result, the time (in seconds) for the vehicle to accelerate from 45 to 60 miles per hour; here the higher the value (i.e., more time), the worse the vehicle handling in emergency situations. Model 3 suggests that for each additional second to achieve 60 miles per hour, a vehicle's crash frequency is reduced 1.27%; this suggests that faster acceleration is associated with higher crash frequency. This result is not entirely unexpected, as drivers of vehicles with faster acceleration may tend to take advantage of their vehicles' capabilities and drive them more recklessly. Model 4 includes the DRYBRAKE test result, the stopping distance (in feet) on a dry surface; a higher value for DRYBRAKE

**Table V-4: Estimated effect of mass or footprint reduction on 13-state crash frequency (crashes per VMT), under alternative regression model specifications.**

|                      | Variable  | NHTSA baseline model<br>(crashes per VMT) | 1. Using only vehicles<br>with CR test results | 2. Including MANEUVER<br>(max speed on<br>avoidance maneuver<br>test) | 3. Including<br>ACC45TO60 (seconds<br>to accelerate from 45 to<br>60 mph) | 4. Including DRYBRAKE<br>(stopping distance in feet<br>on dry surface) | 5. Including<br>MANEUVER,<br>ACC45TO60, and<br>DRYBRAKE |
|----------------------|-----------|---|--|---|---|--|---|
| All crashes          | UNDRWT00  | 2.00%*                                    | 1.97%*   | 1.87%*  | 2.11%*  | 1.96%*   | 2.04%*  |
|                      | OVERWT00  | 1.50%*                                    | 1.40%*   | 1.27%*  | 1.33%*  | 1.35%*   | 1.25%*  |
|                      | FOOTPRNT  | 0.64%*                                    | 0.72%*   | 0.70%*  | 0.85%*  | 0.73%*   | 0.83%*  |
|                      | MANEUVER  | —   | —  | 0.53%*  | —   | —  | 0.27%*  |
|                      | ACC45TO60 | —   | —  | —   | -1.27%*   | —  | -1.13%*   |
|                      | DRYBRAKE  | —   | —  | —   | —   | -0.07%*  | -0.03%*   |
| Crashes with objects | UNDRWT00  | 1.24%*                                    | 1.33%*   | 0.86%*  | 1.66%*  | 1.28%*   | 1.25%*  |
|                      | OVERWT00  | -0.10%                                    | -0.54%*  | -1.21%*   | -0.73%*   | -0.83%*  | -1.27%*   |
|                      | FOOTPRNT  | 2.45%*                                    | 2.75%*   | 2.68%*  | 3.05%*  | 2.81%*   | 2.96%*  |
|                      | MANEUVER  | —   | —  | -2.65%*   | —   | —  | -1.64%*   |
|                      | ACC45TO60 | —   | —  | —   | 3.04%*  | —  | 2.20%*  |
|                      | DRYBRAKE  | —   | —  | —   | —   | 0.43%*   | 0.27%*  |

\* Statistically significant at the 95% level based on regression model standard errors.

Note: All are single regression model across all nine types of crashes (Alternative model 2 in LBNL 2012b), rather than estimated coefficients from nine regression models by crash type reweighted by the number of fatalities by type of crash after assuming full penetration of ESC technology (NHTSA baseline model). Estimates not converted from odds to probabilities.

indicates that the vehicle has relatively lower braking effectiveness. Model 4 suggests that every one-foot increase in braking distance, or decrease in braking capability, is associated with a 0.07% reduction in crash frequency, which also is in the unexpected direction. Therefore for each of the three test results, an improvement in handling or braking capability is associated with a statistically-significant increase in crash frequency. Model 5 adds all three of these variables to the regression model; the signs of the estimated coefficients do not change, although the estimated effect of each is reduced slightly from Models 2 through 4.

The bottom half of Table V-4 shows the results only for crash frequency in crashes with stationary objects, which reduces the effect of the driver of another vehicle on whether a crash occurs. In contrast to those in the top of Table V-4, for all crashes, the coefficients for the three handling/braking variables in the bottom of Table V-4, for only crashes with stationary objects, are in the expected direction, and are substantially larger. For example, an increase in maximum maneuver speed is associated with a 2.65% reduction, an increase in the time to reach 60 miles per hour is associated with a 3.04% increase, and an increase in braking distance is associated with a 0.43% increase in the likelihood of a crash with a stationary object.

Note that adding one or all of the three handling/braking variables has relatively little effect on the estimated relationship between mass reduction in lighter-than-average cars (UNDRWT00) or footprint reduction and crash frequency. However, adding one or all three of the handling/braking variables increases the beneficial effect of mass reduction in heavier-than-average cars (OVERWT00) on crash frequency with stationary objects, from a not statistically-significant 0.10% reduction in crash frequency in the baseline model to as much as a 1.27% reduction in crash frequency in Model 5.

In summary, inclusion of three measures of a car's handling or braking capabilities has a small effect on the estimated relationship between mass or footprint reduction and crash frequency, either for all crashes or for crashes with stationary objects. Good scores on these tests are estimated to increase overall crash frequency, but reduce the frequency of crashes with objects.

**3. Analysis whether fatalities increase linearly with increasing VMT**

Several participants on a NRC committee evaluating the Corporate Average Fuel Economy standards suggested that an analysis be performed to test the assumption that the number of crashes increases linearly as VMT increases. There are reasons why fatalities may not increase linearly with

VMT, at least for individual vehicles; for example, there is evidence that drivers who have high VMT are better drivers than those with low VMT, probably due to more practice/experience, and may be involved in fewer crashes than drivers with low VMT. However, some measure of exposure must be used and VMT is probably better than vehicle registrations.

The NRC committee members proposed re-running the logistic regression models using fatalities (rather than fatalities per VMT) as the dependent variable, and including VMT on the right-hand side of the regression model as a control variable. It is not possible to do this using the logistic regression models, as the fatality cases and the non-fatality cases (the induced exposure cases) come from two separate sources of data: the Fatality Analysis Reporting System (FARS) for fatality cases, and the induced exposure cases from the 13 state crash databases for the non-fatality cases. The FARS cases do not have a VMT associated with them; only the induced exposure cases have a VMT weight, which summed across the induced exposure cases equals total national VMT.

In order to address the NRC committee members' suggestion, we reran the analysis for vehicle makes and models, rather than for individual vehicles. To accomplish this, the number of fatalities and VMT were summed by vehicle model year, make, and model, and a linear regression model was run using the number of fatalities by vehicle MY/make/model as the dependent variable and including VMT by MY/make/model as a control variable. Because the dependent variable is total fatalities, and not fatalities per VMT, we can use a linear rather than a logistic regression model.

Table V-5 shows the results from six linear regression models. For each of the six models in the table, a single regression is run across all nine types of crashes (rather than running a separate regression for each of the nine crash types, and then reweighting the estimated regression coefficients by the number of fatalities in each type of crash assuming full penetration of ESC technology; see Kahane 2012 and Wenzel 2012a). Model 1 uses fatalities by vehicle year, make, and model as the dependent variable, and does not include VMT as a control variable, for the three vehicle types (cars, light trucks, and CUVs/minivans). All of the other control variables used in the Kahane baseline regression models are included, but not shown in the table. Model 2 also uses fatalities by vehicle year, make and model as the dependent variable, but includes VMT as a control variable.

The most important point to take from Model 2 is that the three estimated coefficients for the VMT variable are positive (albeit very small) and statistically significant. This implies that the absolute number of fatalities increases as the number of miles driven increases, by 1.3% for cars, 1.8% for light trucks, and 1.1% for CUVs/minivans, for every additional 100 million miles driven. Note that the coefficients for the calendar year variables show the same trend in the logistic regression

models as well as the Model 1 linear models, with fatalities generally decreasing in later calendar years. The coefficients for the CY2008 variable are substantially lower, and statistically significant, than those for the CY2007 variable in Model 2, even after accounting for the reduced VMT in 2008 (in the VMTWTFa variable). This implies that something other than reduced VMT in 2008 accounts for the reduction in fatalities in that year. However, if NHTSA over-estimated VMT in 2008, as implied in Wenzel 2012a, then one would expect the coefficients for CY2008 to be lower than those for earlier calendar years even after accounting for the VMT as estimated by NHTSA.

#### 4. Analysis of societal fatality risk by state

Societal fatality risk (the number of total fatalities per 10 billion vehicle miles) varies substantially by vehicle make and model. This variance can be explained by a combination of vehicle design differences, driver behavior, and driving environment. Similarly, fatality rates vary considerably by state, from less than 65 (in California, Connecticut, Massachusetts, Minnesota, New Hampshire, New Jersey, and New York) in 2011 to over 150 (in Arkansas, Montana, North Dakota, and West Virginia) fatalities per billion vehicle miles, as shown in Figure V-15. Figure V-15 also shows how societal fatality risk has substantially declined in all states but one (North Dakota), and has declined nationwide from 146 to 92 fatalities per 10 billion vehicle miles, between 1994 and 2011. LBNL explored the possible causes of this variance in societal fatality risk by state, in order to shed light on how much of the variance is attributable to driver or environment variables, rather than vehicle differences.

For this analysis we use all non-pedestrian fatalities included in NHTSA's FARS, between 1994 and 2011. Car and light truck registrations and total vehicle miles traveled by state are obtained from the Highway Statistics series, published by the Federal Highway Administration, from data reported individually by states. The variables listed in Table V-6 were considered as independent control variables in the regression model. Only one value is available for each state for the first two variables in Table V-6, RURAL and HHINC; for all the other variables, the values vary not only for the 50 states but also for each of the 18 years in the analysis period (1994 to 2011). One variable, PCLT, is derived from annual vehicle registration data by state; all other variables are derived from the FARS database. None of the control variables listed in Table V-6 are strongly correlated with another, with correlation coefficients all less than 0.80; however, nine of the variables have a correlation coefficient between 0.60 and 0.80 with another variable. RURAL is fairly highly correlated with the percent of registered vehicles that are light trucks and the fraction of vehicles in FARS on high-speed roads, and highly negatively correlated with household income and the fraction of vehicles in FARS that are luxury cars. Household income is negatively correlated with whether the crash occurred in a red state, while the fraction of vehicles in FARS on a high-speed road is negatively correlated with the

**Table V-5: Estimates for selected control variables from two linear regression models of societal fatality risk, using different dependent variables.**

| Variable | Estimates for selected control variables from two linear regression models using different dependent variable |              |                   |  |              |                   |
|----------|---|--------------|-------------------|--|--------------|-------------------|
|          | Model 1: Fatalities   |              |                   | Model 2: Fatalities, including VMT as a control variable |              |                   |
|          | Cars  | Light trucks | CUVs/<br>minivans | Cars   | Light trucks | CUVs/<br>minivans |
| UNDRWT00 | 0.699   | 0.119        | —                 | -0.083   | -0.058       | —                 |
| OVERWT00 | 5.506   | -0.443       | —                 | 0.119  | 0.002        | —                 |
| LBS100   | —   | —            | -0.994            | —  | —            | 0.070             |
| FOOTPRNT | -5.102  | -0.279       | -0.998            | 0.002  | 0.072        | -0.137            |
| CY2002   | 14.820  | 34.913       | 6.563             | 0.284  | 1.418        | 0.244             |
| CY2003   | 7.433   | 32.096       | -13.047           | 0.174  | 1.121        | 0.169             |
| CY2004   | 0.948   | 21.881       | -5.001            | 0.020  | 0.863        | -0.231            |
| CY2005   | 0.135   | 5.586        | 11.832            | -0.149   | 0.428        | -0.044            |
| CY2007   | 0.281   | -10.657      | -6.962            | -0.097   | -0.162       | -0.127            |
| CY2008   | -15.692   | -34.398      | -4.698            | -1.235   | -1.151       | -0.889            |
| VMTWTF A | —   | —            | —                 | 1.3E-08  | 1.8E-08      | 1.1E-08           |

Note: estimates in red are statistically significant at the 95% level based on regression model standard errors.

Note: All are single regression model across all nine types of crashes (Alternative model 2 in LBNL 2012a), rather than estimated coefficients from nine regression models by crash type reweighted by the number of fatalities by type of crash after assuming full penetration of ESC technology (NHTSA baseline model). Estimates not converted from odds to probabilities.

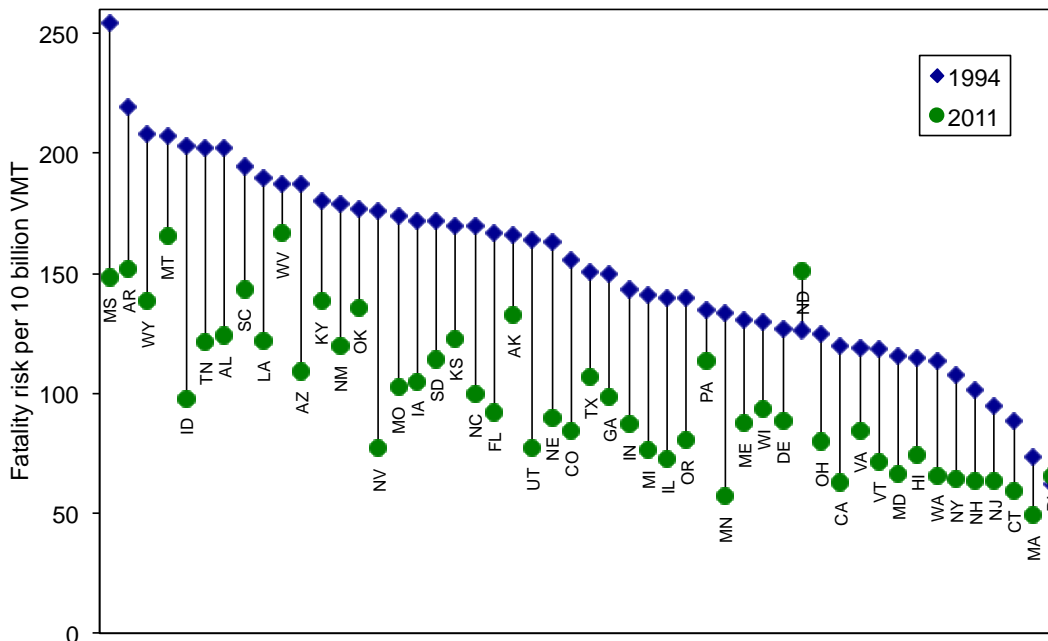


Figure V-15: 1994 and 2011 fatality risk per 10 billion miles traveled, by state.

**Table V-6: Control variables considered in the linear regression model.**

|           |  |
|-----------|--|
| RURAL     | Percent of vehicles in FARS that were involved in a crash in a county with a population less than 250 per square mile              |
| HHINC     | Average median household income by zip code weighted by the number of vehicles in FARS involved in a crash in that zip code        |
| PCTLT     | Percent of light-duty vehicle registrations that are light trucks  |
| PCTUNBELT | Percent of drivers in FARS that were reported as not wearing a safety belt   |
| PCTYOUNG  | Percent of drivers in FARS that were younger than 26 years old   |
| PCTOLD    | Percent of drivers in FARS that were between 70 and 96 years old   |
| PCTMALE   | Percent of drivers in FARS that were male  |
| PCTNIGHT  | Percent of vehicles in FARS that were involved in a crash at night   |
| PCTHISPD  | Percent of vehicles in FARS that were involved in a crash on a road with a speed limit of 55 mph or higher                         |
| PCTBAD    | Percent of drivers in FARS that were suspected of using alcohol or drugs, or had a previous conviction, or were driving recklessly |
| PCTRAIN   | Percent of vehicles in FARS that were involved in a crash in inclement weather (rain, mist, fog, snow, sleet, smoke, etc.)         |
| RED       | Whether the state voted Republican in the 2012 presidential election   |
| PCTTWODR  | Percent of vehicles in FARS that were two-door cars  |
| PCTMVAN   | Percent of vehicles in FARS that were minivans   |
| PCTLGPU   | Percent of vehicles in FARS that were large pickups with gross vehicle weight rating of 4,500 to 10,000 lbs                        |
| PCTLUXCAR | Percent of vehicles in FARS that were luxury cars (manufactured by Audi, BMW, Mercedes, Volvo, Acura, Infiniti, or Lexus)          |
| CY**      | Calendar year in which the crash occurred (2005 is the default)  |

percent of vehicles in FARS that are luxury cars. The fractions of vehicle registrations that are light trucks (PCTLT) are positively correlated with the fraction of vehicles in FARS that are large pickups (PCTLGPU) were on high-speed roads (PCTHISPD), and whether the crash occurred in a red state (RED).

Figure V-16 shows the results of a linear regression model with fatality risk per VMT as the dependent variable. Because annual miles traveled is not reported for the District of Columbia prior to 2004, we exclude it from the analysis. Factors that are associated with an estimated increase in fatality risk per vehicle mile are the fraction of crashes that occurred in rural counties, at night, and in a red state, and the portion of registrations that are light trucks; factors that are associated with an estimated decrease in fatality risk are increasing household income (in \$000s), the fraction of crashes that occurred in inclement weather, and the fraction of vehicles in FARS that are minivans or large pickups. Surprisingly, the fraction of drivers in FARS that are young or old are associated with high reductions in fatality risk per vehicle mile.

Almost all of the calendar year variables are statistically-significant, and, after 1994, estimate a steady reduction in fatality risk per mile traveled over time, from a 26 times greater fatality risk in 1995 than in 2005, to a 40 times lower fatality risk in 2011 than in 2005. This suggests that other changes in vehicles, drivers, and/or driving conditions not accounted for in

the regression model led to a substantial reduction in fatality risk per vehicle mile from 1995 to 2011.

The adjusted R-squared of the regression model in Figure V-16 is quite high, 0.80, suggesting that the control variables in the model explain the majority of the variability in societal fatality risk per mile traveled by state and year.

In summary, the analysis of societal fatality risk per VMT using annual state level data had similar results to the logistic regression analyses conducted at the vehicle level: driving in rural counties, at night, and in a light truck tends to increase societal risk. However the state level analysis suggests that the fraction of young or old drivers, or large pickups, in a state reduces societal fatality risk. Several variables that were statistically-significant in the vehicle-level analysis were not significant in the state-level analysis: notably the fraction of male drivers and driving on high-speed roads in a given state. Two variables not included in the logistic regression at the vehicle level are significantly associated with fatality risk: inclement weather reduces risk, while risk is increased in states that voted Republican in the last presidential election. And similar to the vehicle-level analysis, risk tends to decline over time. The high explanatory power of the state-level regression model suggests that the control variables included in the model capture the majority of the range in annual societal fatality risk across the states.

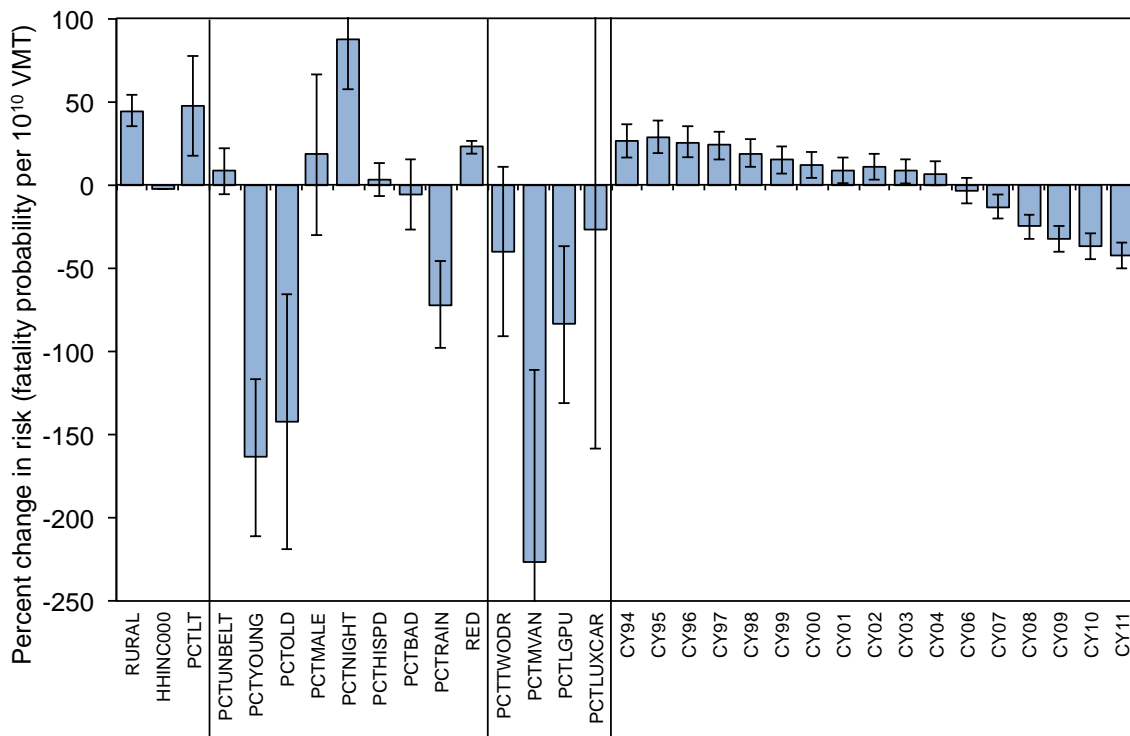


Figure V-16: Estimated effect of control variables on societal fatality risk per mile traveled.

**5. Analysis of driver alcohol/drug use or restraint use**

Some reviewers of the LBNL 2012 analyses suggested that two additional control variables be included in the regression model: whether the driver had been drinking or using drugs, or the driver was wearing his or her restraint system, at the time of the crash. NHTSA did not include alcohol/drug or restraint use in its baseline model for two reasons: not all of the 13 states consistently report these two parameters in their databases, and restraint use is often over-reported, even in FARS. In this analysis we add alcohol/drug and restraint use from the 13 state databases, and includes them in alternative regression models.

The fraction of non-culpable drivers in the 13 states that were suspected of using alcohol or drugs is extremely small, 0.17% overall, and ranges from 0.02% in Maryland and Wyoming to 0.56% in Florida (based on how Missouri determines which driver is at fault, by definition no non-culpable drivers in Missouri were suspected of being under the influence of alcohol or drugs). On the other hand, 38% of drivers involved in fatal crashes were suspected of being under the influence of alcohol or drugs (note that it was unknown whether nearly 60% of drivers in FARS were under the influence). The fraction of non-culpable drivers in the 13 states that were not properly wearing safety restraints (that is, RESTUSE=0) also is small, 2.5% overall, and ranges from 0.6% (in Michigan, New Jersey, and Washington) to nearly 10% (in Florida). Based on FARS, 27% of drivers involved in fatal crashes were not properly wearing safety restraints (for only 7% of drivers in FARS was the status of safety restraint use listed as unknown). These disparities are to be expected,

as non-culpable drivers are less likely, and drivers involved in fatal crashes are more likely, to be under the influence of alcohol or drugs, or not be wearing their safety restraints; however, the size of the disparities calls into question the accuracy of the belt use variable in the 13 state crash databases.

Table V-7 shows how adding the variables for whether the driver was suspected of being under the influence of alcohol or drugs, or was properly wearing his or her safety restraint, changes the estimated effect of mass or footprint reduction on societal fatality risk per VMT, by vehicle type. For each of the four models in the table, a single regression is run across all nine types of crashes (rather than running a separate regression for each of the nine crash types, and then reweighting the estimated regression coefficients by the number of fatalities in each type of crash assuming full penetration of ESC technology; see Kahane 2012 and Wenzel 2012a. For simplicity, the regression estimates presented here are not converted from odds to probabilities, as they were in Wenzel 2012a). The first model in Table V-7 is NHTSA's baseline model; Model 2 is the results we obtained after replicating the file NHTSA used for the 13 state crash data. (For several reasons, we were not able to exactly replicate NHTSA's induced exposure file. In the future we recommend that NHTSA include the state case number for each crash it uses in its induced exposure file, which will make it simpler to add data from the state crash databases for the cases NHTSA uses.) Model 3 shows the effect of adding the ALC\_DRUG variable to Model 2, while Model 4 shows the effect of adding the RESTUSE variable to Model 2.

**Table V-7: Estimated effect of including two additional variables on the NHTSA baseline model of societal fatality risk per VMT, by vehicle type.**

| Vehicle Type   | Variable | Model 1: NHTSA baseline model |        | Model 2: LBNL recreated induced exposure file |        | Model 3: including ALC_DRUG |        | Model 4: including RESTUSE |        |
|----------------|----------|-------------------------------|--------|---|--------|-----------------------------|--------|----------------------------|--------|
|                |          | Est                           | Sig    | Est   | Sig    | Est                         | Sig    | Est                        | Sig    |
| Passenger cars | UNDRWT00 | 1.27%                         | <.0001 | 1.26%   | <.0001 | 1.45%                       | <.0001 | 1.24%                      | <.0001 |
|                | OVERWT00 | 0.35%                         | 0.3377 | 0.31%   | 0.3870 | 0.39%                       | 0.3115 | 0.24%                      | 0.5003 |
|                | FOOTPRNT | 2.31%                         | <.0001 | 2.33%   | <.0001 | 1.78%                       | <.0001 | 2.42%                      | <.0001 |
|                | ALC_DRUG | —                             | —      | —   | —      | 190%                        | <.0001 | —                          | —      |
|                | RESTUSE  | —                             | —      | —   | —      | —                           | —      | 5.50%                      | <.0001 |
| Light trucks   | UNDRWT00 | 0.41%                         | 0.0404 | 0.41%   | 0.0422 | 0.73%                       | 0.0007 | 0.37%                      | 0.0645 |
|                | OVERWT00 | -0.42%                        | 0.0105 | -0.48%  | 0.0038 | -0.11%                      | 0.5276 | -0.50%                     | 0.0025 |
|                | FOOTPRNT | 0.22%                         | 0.1398 | 0.23%   | 0.1230 | 0.51%                       | 0.0013 | 0.25%                      | 0.0983 |
|                | ALC_DRUG | —                             | —      | —   | —      | 196%                        | <.0001 | —                          | —      |
|                | RESTUSE  | —                             | —      | —   | —      | —                           | —      | 4.74%                      | <.0001 |
| CUVs/minivans  | LBS100   | 1.27%                         | <.0001 | -0.76%  | 0.0811 | -1.67%                      | 0.0002 | -0.79%                     | 0.0716 |
|                | FOOTPRNT | 0.35%                         | 0.3377 | 2.31%   | <.0001 | 3.55%                       | <.0001 | 2.32%                      | <.0001 |
|                | ALC_DRUG | —                             | —      | —   | —      | 185%                        | <.0001 | —                          | —      |
|                | RESTUSE  | —                             | —      | —   | —      | —                           | —      | 8.56%                      | <.0001 |

Estimates that are statistically significant at the 95% level based on regression model standard errors are shown in red. Using a jack-knife method to estimate uncertainty, NHTSA found that only the mass reduction in lighter-than-average cars is statistically significant.

Note: All are single regression model across all nine types of crashes (Alternative Model 2 in LBNL 2012a), rather than estimated coefficients from nine regression models by crash type reweighted by the number of fatalities by type of crash after assuming full penetration of ESC technology (NHTSA baseline model). Estimates not converted from odds to probabilities.

Table V-7 indicates that, for all three types of vehicles, whether a driver is suspected of being under the influence of alcohol or drugs is associated with a large increase in societal fatality risk per VMT, from 185% for CUVs/minivans to 196% for light trucks, which is more than any other control variable in the regression models (not shown). And the driver's proper use of his or her restraint is associated with a small but statistically-significant increase in societal fatality risk per VMT, ranging from 4.7% for light trucks to 8.6% for CUVs/minivans.

Table V-7 also indicates that adding RESTUSE to the NHTSA baseline regression model has essentially no effect on the estimated relationship between vehicle mass or size and societal fatality risk. However, adding ALC\_DRUG to the baseline model in several cases results in substantial changes to the association between mass or footprint reduction and risk (indicated in red): including driver alcohol/drug use increases the beneficial effect of footprint reduction in light trucks and CUVs/minivans, and of mass reduction in lighter-than-average light trucks; reduces the detrimental effect of mass reduction in heavier-than-average light trucks; reduces the beneficial effect of footprint reduction in cars; and increases the detrimental effect of mass reduction in CUVs/minivans.

For all three vehicle types, there are only small changes in the estimated coefficients for most of the other control variables. The exception is when ALC\_DRUG is added to the model (Model 2), the estimated effect of a crash that occurs in a high fatality state substantially increases from that in the baseline model (from 0.26, 0.23, and 0.30 for cars, light trucks, and CUVs/minivans, respectively, to 13.85, 14.40, and 13.54).

The predictive power of Model 3 increases dramatically, from a model R<sup>2</sup> of 0.07 to 0.12, depending on vehicle type, to one of 0.32 to 0.58; however, the predictive power of Model 4 is the same as that of NHTSA's baseline model.

In FY14 the effect of adding ALC\_DRUG and RESTUSE variables to LBNL's regression models estimating crash frequency will be tested.

## Conclusion

In FY13 several analyses were conducted to better understand the relationship between vehicle mass and footprint and U.S. societal fatality risk per vehicle mile traveled. The estimated association of mass or footprint reduction with crash frequency, risk per crash, or risk per VMT using the two-stage simultaneous model is somewhat dependent on what data or sampling are used. Adding three braking and handling test results has little effect on the mass or size coefficients in the regression model estimating the frequency of all crashes, but substantially increases the estimated beneficial effect of mass reduction in heavier-than-average cars in crash frequency with objects. And adding whether a driver properly used his or her restraint system also has little effect on the association between mass or size reduction and societal fatality risk; however, driver alcohol or drug use in some cases does change the estimated effects. Our analysis indicates that total fatalities do increase as VMT increases. The state-level analysis suggests that the control variables used, including new variables for statewide household income, seatbelt use, bad driving behavior, inclement weather, and political affiliation tendency, explain much of the variability in societal fatality risk per VMT over time across the states.

## Presentations/Publications/Patents

1. Wenzel, Tom. 2012c. *Relationships Between Vehicle Mass, Footprint, and Societal Risk*. Poster presented at the TRB UTC Spotlight Conference on Sustainable Energy and Transportation: Strategies, Research, and Data, Washington DC, November 8-9, 2012. LBNL-6276E.
2. Wenzel, Tom. 2013a. *Assessment of DRI's Two-Stage Logistic Regression Model Used to Simultaneously Estimate the Relationship between Vehicle Mass or Size Reduction and U.S. Fatality Risk, Crashworthiness/Compatibility, and Crash Avoidance*. Peer review submitted to International Council for Clean Transportation, and draft report prepared for EERE, U.S. DOE. January.
3. Wenzel, Tom. 2013b. "The Effect of Recent Trends in Vehicle Design on U.S. Societal Fatality Risk per Vehicle Mile Traveled, and Their Projected Future Relationship with Vehicle Mass." *Accident Analysis and Prevention* 56, 71-81. LBNL-6277E.
4. Wenzel, Tom. 2013c. "The Estimated Effect of Mass or Footprint Reduction in Recent Light-Duty Vehicles on U.S. Societal Fatality Risk per Vehicle Mile Traveled." *Accident Analysis and Prevention* 59, 267-276.
5. Wenzel, Tom. 2013d. *Relationships between Mass, Footprint, and Societal Risk in Recent Light-Duty*

*Vehicles*. Presentation at NHTSA Mass-Size-Safety Workshop, Washington DC, May 13-14, 2013. LBNL-6343E.

6. Wenzel, Tom. 2013e. *Relationships between Vehicle Mass, Footprint, and Societal Risk*. Presentation at the DOE 2013 Annual Merit Review, Washington DC, May 15, 2013.
7. Wenzel, Tom. 2013f. *Relationships between Mass, Footprint, and Societal Risk in Recent Light-Duty Vehicles*. Presentation to the NRC Committee Meeting: Assessment of Technologies for Improving Fuel Economy of Light-Duty Vehicles: Phase 2, Washington DC, June 25, 2013.
8. Wenzel, Tom. 2013g. "The Relationship between U.S. Societal Fatality Risk per Vehicle Mile Traveled and Vehicle Mass, by Vehicle Type and Model." Under review for publication in *Traffic Injury Prevention*.

## References

1. Kahane, C.J. 2012. *Relationships Between Fatality Risk, Mass, and Footprint in Model Year 2000-2007 Passenger Cars and LTVs*. Final report prepared for the National Center for Statistics and Analysis, National Highway Traffic Safety Administration. August. DOT HS 811 665.
2. Van Auken, R.M. and J.W. Zellner. 2012a. *Updated Analysis of the Effects of Passenger Vehicle Size and Weight on Safety, Phase II: Preliminary Analysis based on 2002 to 2008 Calendar Year Data for 2000 to 2007 Model Year Light Passenger Vehicles*. Revision 2, November. DRI-TR-12-01-2.
3. Van Auken, R.M. and J.W. Zellner. 2012b. *Updated Analysis of the Effects of Passenger Vehicle Size and Weight on Safety: Supplemental Results on the Sensitivity of the Estimates for 2002 to 2008 Calendar Year Data for 2000 to 2007 Model Year Light Passenger Vehicles to Induced-Exposure Data and Vehicle Size Parameters*. Revision 2, November. DRI-TR-12-03-2.
4. Wenzel, Tom. 2012a. *Assessment of NHTSA's Report "Relationships Between Fatality Risk, Mass, and Footprint in Model Year 2000-2007 Passenger Cars and LTVs"*. Final report prepared for the Office of Energy Efficiency and Renewable Energy, U.S. Department of Energy. Lawrence Berkeley National Laboratory. August. LBNL-5698E.
5. Wenzel, Tom. 2012b. *An Analysis of the Relationship between Casualty Risk per Crash and Vehicle Mass and Footprint for Model Year 2000-2007 Light-Duty Vehicles*. Final report prepared for the Office of Energy Efficiency and Renewable Energy, U.S. Department of Energy. Lawrence Berkeley National Laboratory. August. LBNL-5697E.



DOE/EE-1039 February 2014  
Printed with a renewable-source ink on paper containing  
at least 50% wastepaper, including 10% post consumer waste.

U.S. DEPARTMENT OF  
**ENERGY** | Energy Efficiency &  
Renewable Energy

For more information  
[eere.energy.gov](http://eere.energy.gov)